# Biomineralization of hydroxyapatite in the presence of amino acids dissolved in solution or bound to a carboxylated graphene oxide surface

#### Maryam Tavafoghi Jahromi

Department of Mining and Materials Engineering McGill University, Montreal, Canada

Feb 2015



A thesis submitted to the Faculty of Graduate and Postdoctoral Studies of McGill University in partial fulfillment of the degree of doctor of philosophy

#### **ABSTRACT**

Polar and charged amino acids (AAs) are the main components of non-collagenous proteins (NCPs), and are involved in hydroxyapatite (HA) mineralization in bone. These AAs are able to either promote HA mineralization by attracting Ca<sup>2+</sup> and PO<sub>4</sub><sup>3-</sup> ions in body fluids and increasing the local supersaturation or inhibit HA formation by binding to nuclei of calcium phosphate and preventing their further growth. The promoting AAs can be used to improve bone regeneration in damaged tissues, while the inhibitory AAs are potentially useful for treating pathological diseases caused by an excessive mineralization of HA in tissues like cartilage, blood vessels and cardiac valves.

Although AAs are promising candidates for controlling HA mineralization, the mechanism by which they interact with Ca<sup>2+</sup> and PO<sub>4</sub><sup>3-</sup> ions or with HA crystals to induce or inhibit mineralization is not well understood. Also, most of the studies on AAs and HA crystallization are conducted under experimental conditions different from the physiological ones, which has made it difficult to gain a real insight into the effects of AAs in the human body. In this work, we investigate the effect a positively (Arg) and a negatively (Glu) charged AA have on the morphology and crystalline structure of HA synthesized at room temperature and at a pH of 7.4. The AAs are either in an aqueous solution or bound to a graphene oxide (GO) surface. Graphene is a recently discovered carbon-based two-dimensional nanostructure, and it is used here as a substrate to bind the AAs on due to its many potential applications as a bone or dentin scaffold in tissue engineering. Our goal is to determine the inhibiting or promoting effect of AAs on HA mineralization, and to explore the mechanism by which AAs can control HA precipitation.

Our results showed that the positively charged AA, Arg, had a stronger inhibitory effect on HA nucleation, and was adsorbed in larger amount on HA particles, while the negatively charged AA, Glu, was more effective in inhibiting HA crystal growth along specific crystallographic directions. These results were interpreted in terms of the differences in stability constants between AAs and the ions in solution. We also showed that the inhibitory effect of the single AAs on HA nucleation was dampened if the two AAs were present together in solution, which we interpreted to be a consequence of the preferential interaction of the AAs with each other rather than with ions or nuclei in solution. However, the inhibitory effect of these AAs became stronger when the Ca- and P-precursor solutions were aged for 3 days. This was explained by the

formation of nano aggregates from the initial Ca/AAs and P/AAs complexes with aging of the precursor solutions. The AAs also affected the morphology and crystallinity of HA particles. In general, the presence of AAs resulted in the formation of well-organized micro-spherulitic particles, which had high degree of crystallinity. On the other hand, irregularly shaped micro aggregates with lower crystallinity were obtained in the absence of the AAs or when the AAs were mixed.

Contrary to when they were in solution, the AAs bound to a GO surface promoted HA precipitation by attracting Ca<sup>2+</sup> and PO<sub>4</sub><sup>3-</sup> ions and increasing the concentration of these ions on the GO substrate. However, similar to the effect of AAs dissolved in solution, the positively charged AA, Arg, bound to a GO surface showed a significantly stronger effect than the negatively charged AA, Glu. Also, more organized particles with Ca/P ratios closer to that of HA were obtained in the presence of Arg. These results were interpreted in terms of the differences in electrostatic interactions and the stability constants of complexes forming between the AAs and the Ca<sup>2+</sup> and PO<sub>4</sub><sup>3-</sup> ions. The strong effect of Arg on HA formation on a GO surface may provide a basis to design new graphene composite materials for bone regeneration applications.

### **RÉSUMÉ**

Les acides aminés (AAs) polaires et chargés sont les principaux composants des protéines non collagéniques, et sont impliqués dans la minéralisation d'hydroxyapatites (HA) dans les os. Bien que les AAs soit des candidats prometteurs pour contrôler la minéralisation d'HA, le mécanisme par lequel ils interagissent avec les ions Ca<sup>2+</sup> et PO<sub>4</sub><sup>3-</sup> ou avec les cristaux d'HA pour induire ou inhiber la minéralisation n'est pas encore bien compris. La plupart des études sur les AAs et sur la cristallisation d'HA sont menées dans des conditions expérimentales différentes des conditions physiologiques, ce qui a rendu difficile l'obtention d'un véritable aperçu des effets des AAs dans le corps humain. Dans ce travail, nous étudions l'effet d'un AA chargé positivement (Arg) et d'un AA chargé négativement (Glu) sur la morphologie et sur la structure cristalline d'HA synthétisés à température ambiante et à pH 7.4. Les AAs seront, soit en solution aqueuse, soit liés à une surface d'oxydes de graphène (GO). Le graphène est une nanostructure bidimensionnelle à base de carbone récemment découverte, et est utilisé ici en tant que substrat pour lier les AAs en raison de ses nombreuses applications potentielles comme support en ingénierie tissulaire de l'os ou de la dentine. Notre objectif est de déterminer l'effet inhibiteur ou promoteur des AAs sur la minéralisation d'HA, et d'explorer le mécanisme par lequel ils peuvent contrôler la précipitation d'HA.

Nos résultats ont montré que l'AA chargé positivement (Arg) a eu un effet inhibiteur plus important sur la nucléation d'HA et a été adsorbé en plus grande quantité sur les particules d'HA, tandis que l'AA chargé négativement (Glu), a été plus efficace sur l'inhibition de la croissance des cristaux d'HA selon des directions cristallographiques spécifiques. Ces résultats ont été interprétés en termes de différences dans les constantes de stabilité entre les AAs et les ions en solution. Nous avons également montré que l'effet inhibiteur des AAs seuls sur la nucléation d'HA a été atténué si les deux AAs étaient présents ensembles en solution. Ce que nous avons interprété comme une conséquence de l'interaction préférentielle des AAs entre eux plutôt que de leur intéraction avec les ions ou les noyaux en solution. Cependant, l'effet inhibiteur de ces AAs est devenu plus important lorsque les solutions de précurseurs de calcium et phosphore étaient âgés de trois jours. Ceci s'explique par la formation de nano-agrégats à partir des complexes initiaux Ca/AAs et P/AAs avec le vieillissement des solutions de précurseurs. Les AAs ont également affecté la morphologie et la cristallinité des particules d'HA. En général, la présence

des AAs a abouti à la formation de microparticules sphérulitiques bien organisées, qui ont un haut degré de cristallinité. D'autre part, les micro-agrégats de formes irrégulières avec des cristallinités inférieures ont été obtenus en l'absence d'AA ou lorsque les AAs été introduits ensemble.

Contrairement à quand ils étaient en solution, les AAs liés à la surface d'oxyde de graphène promeuvent la précipitation d'HA en attirant les ions Ca<sup>2+</sup> et PO<sub>4</sub><sup>3-</sup> et en augmentant la concentration de ces ions sur un substrat d'oxyde de graphène. Cependant, semblable à l'effet observé lorsque les AAs étaient en solution, l'AA chargé positivement (Arg) et lié à la surface d'oxyde de graphène a montré un effet beaucoup plus important que l'AA chargé négativement (Glu). En outre, les particules d'HA les plus organisées avec des rapports Ca/P plus proches de celui d'HA ont été obtenus en présence d'Arg. Ces résultats ont été interprétés en termes de différences dans les interactions électrostatiques et les constantes de stabilité des complexes formés entre les AAs et les ions Ca<sup>2+</sup> et PO<sub>4</sub><sup>3-</sup>. L'effet important de l'Arg sur la formation d'HA sur la surface d'oxyde de graphène peut fournir une ligne directive pour concevoir des matériaux composites Arg/graphène pour des applications de régénération osseuse.

#### **ACKNOWLEDGEMENTS**

First of all, I would like to express my deepest gratitude to my supervisor, Prof. Marta Cerruti for all her support, generous guidance, and continuous encouragement throughout my PhD. I've been honored to be her PhD student. Her vast experience and knowledge in the field of chemistry have helped me a lot during my PhD. Also, her motivation, enthusiasm, and positive attitude have been always inspiring to me. I would like to also thank her for the financial support and all materials and equipment she provided for my research. After all this research work together, I wanted to express her my heartfelt thanks for being so kind to share her nice moments and fun activities with us. I've always enjoyed her company.

I would like to thank the co-authors of the papers I published during my PhD, especially Prof. Raynald Gauvin and Dr. Nicolas Brochu for their assistance with SEM. Also, I would like to thank some members of our research group, Gul Zeb and Ghulam Jalani, for their help and nice company during my PhD. And, thanks to Ophelie Gourgas for her help with the French version of the thesis abstract. Also, thanks should be given to all staff and faculty at the Department of Materials Engineering especially Dr. Lihong Shang, Dr. Florence Paray, Monique Riendeau, Barbara Hanley, and Terry Zatylny for all their technical supports and kind assistance.

Also, I would like to acknowledge the funding sources of my PhD research project, McGill Engineering Doctoral Award (MEDA), the Canada Research Chair foundation (CRC), the Natural Science and Engineering Research Council of Canada (NSERC), and the Center for Self-Assembled Chemical Structures (CSACS), without their financial support this research was not possible.

I would like to take this opportunity to also express my gratitude to professors and faculties at Shiraz University, Department of Materials Engineering, where I did my Bachelor and learned the basics of Materials Science. The passion and honesty they put in their work, after all their knowledge, have been always inspiring to me.

Finally, from depth of my heart, I would like to thank my grandfather who passed away just a few days ago while I was working on the last pages of my thesis. His kind thoughts and prayers have been always with me and have guided me throughout my life. Also, thanks to my parents (my first and ever beloved ones!) who have constantly supported me and respected my decision for pursuing my study abroad.

## TABLE OF CONTENTS

ABSTRACT	i
RÉSUMÉ	iii
ACKNOWLEDGEMENTS	v
TABLE OF CONTENTS	vi
LIST OF FIGURES	xi
LIST OF TABLES	xviii
GLOSSARY OF ABBREVIATIONS AND SYMBOLS	<b>XX</b>
CONTRIBUTION OF AUTHORS	xxiii
CHAPTER 1: GENERAL INTRODUCTION	1
1.1. Introduction	1
1.1.1. Biomineralization	1
1.1.2. Precipitation from aqueous solution	2
1.2. Objectives	3
CHAPTER 2: LITERATURE REVIEW	6
2.1. Precipitation from aqueous solutions	6
2.1.1. Classical model	7
2.1.2. Non-classical precipitation	11
2.1.3. Precipitation inhibitors	12
2.2. HA precipitation from aqueous solution	13
2.2.1. Calcium phosphate phases and their transformation to HA	14
2.2.2. HA nucleation, growth, and morphology	17
2.3. HA biomineralization	19

2.3.1. Biomineralization in general	19
2.3.2. Bone (composition and structure)	21
2.3.3. HA nucleation and growth in bone	24
2.3.4. Role of collagen in bone mineralization	25
2.3.5. Role of NCPs in bone mineralization	26
2.3.6. Serum-associated proteins	29
2.3.7. HA inhibition in body by inorganic ions	30
2.4. HA precipitation in the presence of AAs	31
2.4.1. AAs dissolved in solution	33
2.4.2. AAs bound to surfaces	41
2.4.3. Poly amino acids and peptides	42
2.4.4. AA/HA interactions investigated by computational techniques	43
2.4.5. AA interaction with calcite vs hydroxyapatite	44
CHAPTER 3: STATEMENT OF THE PROBLEM	46
CHAPTER 4: HYDROXYAPATITE PRECIPITATION IN THE PRESENCE OF T	rhe
AMINO ACIDS, ARGININE AND GLUTAMIC ACID, DISSOLVED IN SOLUTION .	48
The importance of amino acid interactions in the crystallization of hydroxyapatite	49
4.1. Abstract	50
4.2. Introduction	50
4.3. Materials and methods	53
4.3.1. Synthesis of HA in the presence of AAs	53
4.3.2. Characterization techniques.	54
4.4. Results	56
4.4.1. Precipitation times and precipitate weights	56
4.4.2. Morphology	58

4.4.3. BET ssa of synthesized particles	59
4.4.4. Crystal structure and crystallite sizes measured by XRD	62
4.4.5. FT-IR analysis	64
4.4.6. Surface composition determined by XPS	66
4.4.7. Colorimetric technique to measure the adsorption of AAs to HA surfaces	68
4.4.8. ICP analysis on [Ca] and [P] in solution and on HA precipitates	68
4.5. Discussion	70
4.6. Conclusion	75
4.7. Acknowledgement	75
SI. 4. Supporting information	76
SI. 4.1. XRD pattern of precipitates synthesized after 2 days, in comparison with the reference pattern of OCP.	
SI. 4.2. Estimate of the stability constant of Glu/PO43- complex formation	77
CHAPTER 5: ROLE OF AMINO ACIDS DISSOLVED IN SOLUTION O	ON THE
PRENUCLEATION STAGE OF HYDROXYAPATITE PRECIPITATION	78
PRENUCLEATION STAGE OF HYDROXYAPATITE PRECIPITATION	<b>78</b>
PRENUCLEATION STAGE OF HYDROXYAPATITE PRECIPITATION	
PRENUCLEATION STAGE OF HYDROXYAPATITE PRECIPITATION  Amino acid/ion aggregate formation and their role in hydroxyapatite precipitation  5.1. Abstract	
PRENUCLEATION STAGE OF HYDROXYAPATITE PRECIPITATION  Amino acid/ion aggregate formation and their role in hydroxyapatite precipitation  5.1. Abstract	
5.2. Introduction	
PRENUCLEATION STAGE OF HYDROXYAPATITE PRECIPITATION	
PRENUCLEATION STAGE OF HYDROXYAPATITE PRECIPITATION  Amino acid/ion aggregate formation and their role in hydroxyapatite precipitation  5.1. Abstract	
PRENUCLEATION STAGE OF HYDROXYAPATITE PRECIPITATION	
PRENUCLEATION STAGE OF HYDROXYAPATITE PRECIPITATION	

5.7. Acknowledgement	97
SI. 5. Supporting information	97
SI. 5.1. FT-IR analysis of HA precipitates	98
SI. 5.2. Ca and P concentration in particles collected from the precursor solutio	ns aged for 1
month	100
SI. 5.3. Ca and P concentration in Ca- and P-precursor solutions at different agreement measured by ICP	
SI. 5.4. In-situ measurement of Ca concentration in Ca-precursor solutions at d	ifferent aging
times measured by Ca ion-selective electrode (ISE)	102
CHAPTER 6: EFFECT OF ARGININE AND GLUTAMIC ACID I	BOUND TO
GRAPHENE OXIDE SURFACES ON HYDROXYAPATITE PRECIPITATION	ON 103
Promoting effect of AAs bound to graphene oxide surface on HA precipitation	104
6.1. Abstract	105
6.2. Introduction	105
6.3. Materials and methods	108
6.3.1. Materials	108
6.3.2. Surface modification of GO flakes	108
6.3.3. Precipitation experiment	110
6.3.4. Characterization	110
6.4. Results	113
6.4.1. Characterization of GO surface modification	113
6.4.2. Mineralization assay	120
6.5. Discussion	129
6.5.1. Effect of Arg vs. Glu bound to CGO on HA precipitation	129
6.5.2. Arg-CGO as a strong nucleator of HA	130
6.6 Conclusion	131

6.7. Acknowledgement	132
SI. 6. Supporting information	133
SI. 6.1. EDC/NHS coupling reaction	133
SI. 6.2. XPS survey results for CGO-EDC and functionalized GO samples	134
SI. 6.3. TGA reference curves for Arg and Glu powders under N2 atmosphere	134
SI. 6.4. XPS survey results for GO and functionalized GO samples immersed in SBF	for 15
days	135
SI. 6.5. SEM pictures	135
SI. 6.6. Zeta potential measured on GO and functionalized GO samples	136
CHAPTER 7: CONCLUSIONS, SUMMARY OF CONTRIBUTIONS AND FU	JTURE
PERSPECTIVES	138
7.1. Conclusions: highlights	138
7.2. Original contributions to knowledge	139
7.3. Future perspective	140
REFERENCES	143

## LIST OF FIGURES

Chapter 1:
Fig. 1.1. Chemical structure of Glu (a) and Arg (b).
Chapter 2:
Fig. 2.1. Different factors that control precipitation from aqueous solution [22].
Fig. 2.2. Stages of precipitation and open questions in classical (a and c-k) and non-classical
precipitation (a-k) from aqueous solution [23].
Fig. 2.3. Dependence of homogeneous nucleation rate (J) on supersaturation (S). S <sub>cr, homo</sub> is S <sub>hom</sub>
at log J equal to zero. γ is the specific surface energy of nuclei [22].
Fig. 2.4. Free energy of precipitation as a function of nuclei size [62].
Fig. 2.5. Schematic showing mono-nuclear (a) vs. poly-nuclear (b) crystal growth
Fig. 2.6. (a) HA crystal structure and its electrical potential distribution: crystal form of HA
mineral; (b) experimental crystalline (P63/m) structure. P, O and Ca atoms not relevant for the
scheme were omitted for clarity of representation. Ca ions are at the vertices of triangles around
each hydroxyl group (red and gray spheres); (c and d) electrostatic potential view along the [010
direction of the HA (010) plane (c) and top/bottom view along [001] direction of HA (001) plane
(d). Atoms are color-coded: oxygen is red, calcium is cyan, phosphorous is yellow, and hydrogen
is grey. Positive/negative values of the electrostatic potential are shown as blue/red colour
[130]
Fig. 2.7. Solubility constant and stability of different phases of calcium phosphates at 37°C
[132]
Fig. 2.8. Phase and morphology evolution of calcium phosphate precipitate from ACP (a) to HA
(f) in SBF under physiological conditions at reaction times of 3 min (a), 67-73 min (b-d), 90 min
(e), and 7 h (f). Bar: (a-c) 100 nm; (d) 200 nm; (e-f) 1 mm [133].
Fig. 2.9. Phase transformation of OCP (a) to HA (d) in SBF under physiological conditions a
reaction times of 0 (a), 10 (b), 24 (c), and 100 h (d)
Fig. 2.10. Phase transformation of DCPD (a) to HA (c) in SBF under physiological conditions a
the reaction time of 0 h (a), 36 h (b), and 1 w (c) [145].

Fig. 2.11. Stable prenucleation cluster of calcium phosphate in SBF: a) High-resolution TEM
image of aggregated clusters in SBF kept at 37°C for 24 h; b) The diameter of prenucleation
clusters determined by extrapolation of the diameter measured in HR-cryo TEM images at
different defocusing values; c) computer representation of the Posner cluster with composition of
Ca <sub>9</sub> (PO <sub>4</sub> ) <sub>6</sub> [143]. The arrow indicates gold particles used as a fiducial marker for tomography.
Scale bar, 20 nm
Fig. 2.12. SEM images of HA crystals grown for 24 h in the SBF-based solution in the presence
of commercial HA nanoparticles seeds (a) at 37 (b-d) and 160° C (e and f) at the pH of 6.5 (b), 7
(c and e), and 7.5 (d and f) [156].
Fig. 2.13. The SEM images of HA particles, at different magnifications, synthesized from an
aqueous solution at physiological conditions [91]
Fig. 2.14. Effect of bis(2-ethylhexyl)sulfosuccinate sodium salt (AOT) on controlling the
morphology of calcium phosphate precipitate obtained from calcium chloride and potassium
dihydrogen phosphate under ambient conditions: a) control HA crystals; b) elongated plate-like
crystals of brushite, networks of amorphous nano particles, and octacalcium phosphate spheres
produced at low AOT concentration; c) bundles of aligned HA filaments with structural features
resembling mineral found in tooth enamel produced at high AOT concentration [157]
Fig. 2.15. Examples of biominerals with astonishing structures found in nature: a ) coccosphere,
which is a complex arrangement of individual plates of calcium carbonate produced by single-
celled algae known as coccolithophores;. b) intricately detailed silica cell walls, known as
frustules, produced by unicellular eukaryotic algae [4, 158]
Fig. 2.16. Sensory organs (otoliths in fish (a) and otoconia in higher vertebrates (b)) of inner ear
containing biomineralized structures that deflect the sensory hair bundles of these organs. Cross
sections show that these organs are composite materials consisting of organic matrices and
lighter zones of calcium carbonate microcrystals.
Fig. 2.17. The 9 levels of hierarchical structure in bone [164]
Fig. 2.18. Chemical structure of pyrophosphate.
Fig. 2.19. Schematic showing the factors that can regulate the uptake and release of AAs by
particular cells [245].
Fig. 2.20. Chemical structure of AAs.

Fig. 2.21. Different pathways for HA precipitation in a bricks (HA) and mortar (ACP)
configuration in presence of Glu and Gly [254].
Fig. 2.22. SEM images of the HA crystals synthesized without any AAs (a) or in the presence of
Gly (b), Ser (c), Asp (d), and Glu (d). Scale bar: 300 [37]
Fig. 2.23. Schematic showing the reduced interfacial energy barrier between DCPD and HA in
the presence of acidic AAs [32]
Fig. 2.24. Schematic showing the steps involved in the precipitation of HA in the presence of
Asp-capped gold nano particles [47]. 42
Chapter 4:
Fig. 4.1. Effect of AAs on the precipitation time (prec. time) of HA. The precipitation time was
considered to be the time at which the solution became visibly cloudy. Each data point is the
average of at least 3 samples. Asterisks (*) indicate the samples that were statically significantly
different ( $P < 0.003$ ) from the control sample.
Fig. 4.2. Effect of Glu, Arg, and combination of Glu and Arg on the weight of precipitates after 2
days of reaction. Each data point is the average of at least 3 samples. Asterisks (*) and plus sign
(+) indicate the samples that were statically significantly different from the control sample with
<i>P</i> <0.0005 and 0.02, respectively. 58
Fig. 4.3. SEM images of samples HA-Cont (a and b), HA-Glu (c and d), HA-Arg (e and f), and
HA-Combo (g and h) at precipitation time. Scale bars: $1\mu m$ (a, c, e, g) and 200 nm (b, d, f, h). $60$
Fig. 4.4. SEM images of samples HA-Cont (a and b), HA-Glu (c and d), HA-Arg (e and f), and
HA-Combo (g and h) after 2 days of reaction. Scale bars: $1\mu m$ (a, c, e, g) and 200 nm (b, d, f, h).
61
Fig. 4.5. Effect of Glu, Arg, and combination of Glu and Arg on the BET ssa of synthesized HA
powders after 2 days of reaction. Asterisks (*) indicate the samples that were statically
significantly different from the control sample with $P < 0.05$ .
Fig. 4.6. XRD patterns of HA-Cont, HA-Glu, HA-Arg, and HA-Combo collected at the
precipitation time (a), and after 2 days (b). The vertical lines are the reference pattern for HA
(PDF number: 00-009-0432)
Fig. 4.7. Average crystallite sizes along [002] and [310] measured by XRD for HA-Cont, HA-
Arg, HA-Glu, and HA-Combo at the precipitation time (a) and after 2 days (b). Asterisks (*)

indicate samples that were significantly different from HA-Cont ( $P < 0.05$ in a and $P < 0.08$ in b).
Fig. 4.8. IR spectra of control and AAs samples at precipitation time (a and b) and after 2 days (c
and d). All spectra are normalized with respect to the main phosphate peak of CHA at 1055 cm <sup>-1</sup> .
Spectra are then translated along the y axis for clarity. Sections (a and c): 4000-2400 cm <sup>-1</sup> region;
(b and d): 750-2000 cm <sup>-1</sup> region. Inset in section c: zoom-in of 3000 to 2800 cm <sup>-1</sup> region for
spectra HA-Cont (1), HA-Glu (2), HA-Arg (3), and HA-Combo (4)
Fig. 4.9. C and N atomic % relative to Ca atomic % for HA-Cont, HA-Glu, HA-Arg, and HA-
Combo at precipitation time and after 2 days of reaction, measured from XPS survey spectra.
Asterisks (*) indicate the samples that were statically significantly different from the control
sample with $P < 0.02$ .
Fig. 4.10. Surface Ca atomic % relative to P atomic % for HA-Cont, HA-Glu, HA-Arg, and HA-
Combo at precipitation time and after 2 days of reaction, measured from XPS survey spectra.
Asterisks (*) indicate samples that were significantly different from HA-Cont ( $P < 0.03$ ) 67
Fig. 4.11. [Ca] (a) and [P] (b) in the supernatant solution for HA-Cont, HA-Combo, HA-Glu,
and HA-Arg samples
Fig. 4.12. Bulk Ca/P atomic ratios as measured by ICP-AES on HA-Cont, HA-Glu, HA-Arg, and
HA-Combo at precipitation time and after 2 days of reaction. Asterisk (*) indicates the sample
that was significantly different from HA-Glu, HA-Arg, and HA-Combo samples synthesized
after 2 days (P<0.05).

#### Chapter 5:

**Fig. 5.1.** Effect of precursor solution aging on HA precipitation. (a and b), Precipitation time determined by visual observation (a) and precipitate weights after 2 days of reaction (b). Each data point is average of at least 3 samples. Asterisks (\*) and plus sign (+) indicate the difference between 3 day and not aged samples was significant with P=0.009 and 0.09. The weight of all precipitates is lower than expected if all Ca and P combined to form HA (0.081 g), thus confirming the inhibitory effect of tris and AAs on HA precipitation; (c), [Ca] in supernatant measured by ICP for HA-Cont and HA-Arg with not aged or aged precursors. [Ca] decreases in the supernatant of HA-Arg aged for 3 days earlier than when the visual precipitation occurs on this sample (a), thus indicating formation of Ca-containing nuclei even before visible

precipitation. (d-i), SEM images of HA-Cont (d and g), HA-Glu (e and h), and HA-Arg (f and i)
with not aged (d-f) or aged precursors (g-i); all samples are collected after 2 days of incubation.
Scale bars: 1µm. (j and k), XRD of HA-Cont, HA-Glu, and HA-Arg prepared with precursors
not aged (j) or aged (k). Vertical lines represent reference pattern for HA (PDF number: 00-009-
0432). Please note that Figs. g-k were also shown in our previous work [331]
Fig. 5.2. HA surface composition differs depending on precursor aging. Ca/P (a) and C/Ca (b)
atomic % for HA-Cont, HA-Glu, and HA-Arg collected after 2 days of reaction, measured from
XPS survey spectra. Asterisks (*) indicate that the difference between the samples prepared with
aged and not aged precursors was statically significant with $P < 0.04$ . C can originate from two
main sources: tris (present in all samples) and AAs (only present in the AA samples). HA-Arg
shows significantly higher C/Ca than HA-Glu when the precursors are aged. This indicates that
much more organic material is present in this sample, which suggests that Arg incorporates in
HA more than Glu. A quantitative estimate is hard to make, since Arg has a longer carbon chain
than Glu, and the tris/AA incorporation ratio is not known.
Fig. 5.3. Aging precursor solutions that contain AA drastically changes HA structure. TEM
images and SAED patterns of HA formed from 3 day old precursor solutions in the presence of
Glu (HA-Glu, a-d), Arg (HA-Arg, e-h), or in the absence of AAs (HA-Cont, m-p), and HA
formed from the not aged precursor solutions in the presence of Arg (HA-Arg, i-l). HA particles
were collected before visible precipitation, specifically after 1.5 (HA-Cont) and 6 h (HA-Glu and
HA-Arg)
Fig. 5.4. EDS spectra for HA samples shown in Fig. 5.3: (a) and (b), spot A and B in Fig. 5.3b,
respectively; (c), spot A in Fig. 5.3f; (d), spot A in Fig. 5.3j; (e), spot A in Fig. 5.3n. The Cl
observed on EDS spectra in a, b, d, and e could have originated from CaCl <sub>2</sub> or HCl
Fig. 5.5. Analyses of aggregates collected from the Ca- and P-precursor solutions aged for 1
month. (a) Weight of aggregates collected from precursor solutions by vacuum filtration using
filters with pore size of 200 nm. Asterisks (*) indicate the samples that were statically
significantly different with $P < 0.05$ . (b), C-N and C=O atomic % relative to C-C atomic %
measured from XPS C 1s high resolution spectra of aggregates collected from Ca-Glu-ps (c), P-
Glu-ps (d), Ca-Arg-ps (e) and P-Arg-ps (f). Asterisks (*) indicate the samples that were statically
significantly different from their correspondent samples containing Ca with $P < 0.05$ . (+)
indicates the sample that was different from its correspondent sample containing Glu with

P < 0.08. Peaks observed on C high resolution spectra (c-1) at 284.9, 286.3, and 288 correspond
C-C, C-N, and C=O, respectively. While C-C and C-N bonds are present in both AAs and tris,
the C=O component can only originate from the AAs
Fig. 5.6. TEM images and EDS spectra of aggregates collected from precursor solutions aged for
3 days. No aggregates are observed for Ca-Cont-ps (a) and P-Cont-ps (b) samples. Aggregates
with average dimensions of 16±4 nm, 34±8 nm, 158±67 nm, and 4±1 nm are observed for Ca-
Glu-ps (c), Ca-Arg-ps (e), P-Glu-ps (d), and P-Arg-ps (f) samples, respectively. Cl observed on
the EDS spectra of Ca-Glu-ps (c) and Ca-Arg-ps (e) must be derived from either $\text{CaCl}_2$ or $\text{HCl}.$
92
Fig. 5.7. Schematic representation of possible pathways for HA precipitation in the presence of
Ca- and P-aggregates. Ca (red sphere) and P (green triangle) precursor solutions containing AAs
(blue lines) are prepared separately. Complexes between AAs and ions form in the precursor
solutions (see left side of the figure). If the solutions are mixed right away (arrow "no aging"),
Ca/AA and P/AA aggregates do not have time to form, and HA crystals (cubes) only contain
$\text{Ca}^{2+}$ and $\text{PO}_4^{3-}$ ions. However, if Ca- and P-precursor solutions are aged for 3 days, Ca/AA (pink
sphere) and P/AA (green sphere) aggregates start forming (arrow "3 days"). The longer the aging
time, the larger the aggregates become (arrow "1 month"). If the precursor solutions are mixed
after 3 day aging, HA precipitates include not only $\mathrm{Ca}^{2^+}$ and $\mathrm{PO_4}^{3^-}$ ions, but also the aggregates
that had grown during the 3 day aging. The aggregates could be either occluded inside the HA
crystals, or at the interface between different crystals (A colored version of this figure can be
found online)
Chapter 6:
Fig. 6.1. XPS quantitative analysis: (a) O, C, S, and N atomic % on GO, CGO, CGO-Glu, and
CGO-Arg obtained from survey spectra; (b and c) percentages of the different components used
to fit high resolution XPS C 1s (b) and O 1s (c) spectra shown in Fig. 6.2
Fig. 6.2. XPS C 1s (a) and O 1s (b) high resolution spectra for GO, CGO, CGO-Glu, and CGO-
Arg samples
Fig. 6.3. FTIR spectra recorded on GO, CGO, CGO-Glu, and CGO-Arg

$\textbf{Fig. 6.4.} \   \text{TGA curves collected under} \   N_2 \   \text{atmosphere on GO, CGO, CGO-Glu, and CGO-Arg}$
samples. The empty circles correspond to the temperatures at which peaks were observed on the
δmass/δT derivative curves.
Fig. 6.5. [Ca] (a) and [P] (b) measured by ICP on negative control sample (SBF, grey bars) and
in SBF containing GO (solid black), CGO (striped black), CGO-Glu (solid red), CGO-Arg
(striped red) and positive control (HA powder, blue bars) after 0, 3, 8 and 15 days of immersion
in SBF. Asterisk (*) and plus (+) signs indicate values that are statically significantly different
from the correspondent values measured on GO and CGO samples, respectively, with P lower
than 0.05
Fig. 6.6. Analysis of precipitates formed on GO, CGO, CGO-Glu, and CGO-Arg after 15 day
immersion in SBF: (a) TGA curves collected in air. GO 0d is a GO sample not immersed in SBF.
The empty circles correspond to the temperatures at which peaks were observed on the $\delta mass/\delta T$
derivative curves. (b) P, Ca, and Mg atomic % measured from XPS survey spectra. Complete
survey results are shown in Table S6.2. Asterisk (*) and plus (+) signs indicate values that are
statically significantly different from the correspondent values measured on GO and CGO
samples, respectively, with P lower than 0.05. (c) FTIR spectra normalized with respect to the
C=C peak at approximately 1585-1597 cm <sup>-1</sup> . HA is a reference spectrum for HA powder 122
Fig. 6.7. BSE-SEM images of GO sample not immersed in SBF (a-c) and GO (d-f), CGO (g-i),
CGO-Glu (j-l), and CGO-Arg (m-q) sample immersed in SBF for 15 days
Fig. 6.8. TEM images (a and c), and corresponding SAED patterns (b and d), and EDS spectra
(insets) for CGO-Arg sample immersed in SBF for 15 days
Fig. 6.9. Schematic showing possible interactions of Glu and Arg with CGO surface and Ca <sup>2+</sup>
(circle) and PO <sub>4</sub> <sup>3-</sup> (triangle) ions. The ions are shown in red or blue if they are interacting with
the AAs by forming complexes or electrostatically, respectively

### LIST OF TABLES

Chapter 2:
Table 2.1. Calcium phosphate crystalline phases and their Ca/P ratios [84, 131].    14
Table 2.2. Bone composition of female Wistar rats [161].   20
Table 2.3. Mechanical properties of hard tissues in human body [92].    20
Table 2.4. Concentrations of ions in blood plasma [169].    24
Table 2.5. Review of HA syntheses in the presence of AAs in solution.    35
Table 2.6. Particle and crystal size of HA synthesized in the presence of AAs dissolved in
solution
<b>Table 2.7.</b> Affinity constants for various amino acid inhibitors of HA crystal growth [40] 37
Chapter 4:
<b>Table 4.1.</b> Summary of AA concentrations in different samples.    54
Table 4.2. Pore volume and pore size for HA samples synthesized in the presence of Glu, Arg,
and their combination after 2 days. 59
<b>Table 4.3.</b> AAs adsorbed to HA particle surfaces after 2 days of reaction.    68
Chapter 5:
<b>Table 5.1.</b> Concentrations of Ca, P and AAs in precursor solutions.    82
Chapter6:
<b>Table 6.1.</b> List of samples used in this work.   109
Table 6.2. Assignments of peaks found on FTIR spectra shown in Fig. 6.3 for GO, CGO, CGO-
Glu, and CGO-Arg. Note that only the main contributions for each peak are reported in this
table. Multiple species may contribute to each peak
Table 6.3. Weight loss temperature (°C) and corresponding weight loss (% WL) observed on the
TGA curves (Fig. 6.4) for GO, CGO, CGO-Glu, and CGO-Arg samples. Asterisk (*) and plus
(+) signs indicate values that are statically significantly different from the correspondent values
measured on GO and CGO samples, respectively, with P lower than 0.05
Table 6.4. Weight loss percentages and temperatures (°C) for GO not immersed in SBF (GO 0d),
and for GO, CGO, CGO-Glu, and CGO-Arg samples immersed in SBF for 15 days. Asterisk (*)

and plus (+) signs indicate values that are statically significantly different from the corresponde
values found on GO 15d and CGO 15d, respectively, with P-value lower than 0.05
Table 6.5. Assignments of the peaks related to HA measured by FTIR on GO, CGO, CGO-Gl
CGO-Arg and the control HA sample after immersion in SBF for 15 days (Fig. 6.6c). The other
peaks observed on these spectra are relative to GO, and have been already reported in Table 6.
Table 6.6. Mg/P and Ca/P ratio calculated from the SEM-EDS spectra on GO, CGO, CGO-Gl
and CGO-Arg after 15 day immersion in SBF.

#### GLOSSARY OF ABBREVIATIONS AND SYMBOLS

AA Amino acid

ACP Amorphpus calcium phosphate

Alanine
ANK
Ankylosis

AP Alkaline phosphatase

**Arg** Arginine

**ASARM** Acidic serine and aspartate-rich motif

AsnAsparagineAspAspartic acid

**BGP** Bone Gla protein

**BMPs** Bone morphogenic proteins

**BSE** Back-scattered electron

**BSP** Bone sialoprotein

**CFE-SEM** Cold-field emission scanning electron

microscope

**CGO** Carboxylated graphene oxide

CHA Carbonated hydroxyapatite

**CPP** Casein phosphopeptide

**CPP** Calciprotein particle

**Cys** Cysteine

**DCPA** Dicalcium phosphate anhydrate

**DFT** Density functional theory

**DI** Deionized

DMP 1 Dentin matrix protein 1DPP Dentin phosphophoryn

**DRIFT** Diffuse reflectance infrared fourier transform

**DTGS** Deuterated triglycine sulfate

**ECF** Extracellular fluid

**ECM** Extracellular matrix

**EDS** Energy dispersive spectrometer

FGF Fibroblast growth factor
FT-IR Fourier transform infrared
GFN Growth front nucleation

**Gla** γ-carboxylated glutamic acid

Glu Glutamic acid

**Gly** Glycine

**GFNs** Graphene family of nanomaterials

GO Graphene oxide
HA Hydroxyapatite
Hyp Hydroxyproline

**ICP-AES** Inductively coupled plasma atomic emission

Spectroscopy

**ISAB** Ionic strength adjustment buffer

**ISE** Ion-selective electrode

ITC Isothermal titration calorimetry

Lysine Lysine

MCT Mercury-cadmium-telluride

MD Molecular dynamic

MEPE Matrix extracellular phosphoglycoprotein

MGP Matrix Gla protein
MV Matrix vesicle

NCP Non-collagenous protein

NMR Nuclear magnetic resonance

**OCP** Octacalcium phosphate

**OPN** Osteopontin

PC Prenucleation cluster

**PDA** Polydopamine

PD-BSE Photo-diode backscattered electron detector

**Phe** Phenylalanine

**Pro** Proline

**PSer** Phospho Ser

**rGO** Reduced graphene oxide

SAED Selected area electron diffraction

SAMs Self-assembled monolayers

SBF Simulated body fluid

SEM Scanning electron microscope

Ser Serine

SIBLINGs Small integrin-binding ligand, N-linked

glycoproteins

SLRPs Small leucine-rich proteoglycans

ssa Specific surface area

Tau Taurine

**TEM** Transmission electron microscopy

**TGA** Thermogravimetric analysis

**TNAP** Tissue-nonspecific alkaline phosphatase

tris Tris(hydroxymethyl)aminomethane

**Tyr** Tyrosine

VSMC Vascular smooth muscle cell

**XPS** X-ray photoelectron spectroscopy

**XRD** X-ray diffraction

#### **CONTRIBUTION OF AUTHORS**

This thesis presents a collection of three published or submitted manuscripts written by the candidate under the supervision of Prof. Marta Cerruti. These articles form the basis of Chapters 4, 5 and 6 of this thesis.

As the first author of all manuscripts, I designed and conducted all the experiments. In addition, material preparation and testing, data collection and analysis, and writing the manuscripts have been my responsibility. The Candidate's supervisor, **Prof. Marta Cerruti**, guided me throughout the whole process and extensively reviewed the manuscripts.

Collaboration was necessary in order to cover all experiments and instruments required to fulfill the objectives of this research project. The role of each of the contributors and co-authors of the manuscripts is explained below:

**Dr. Raynald Gauvin** is a professor at McGill University. He collaborated on providing us with access to an advanced scanning electron microscopy (SEM) and advising us on the SEM analyses presented in manuscript 3 (Chapter 6).

**Dr. Nicolas Brodusch** is a research associate at McGill University and collaborated on taking and analyzing the SEM images shown in manuscript 3 (Chapter 6).

**Ms. Guanhan Yao** was an undergraduate student at McGill who worked in our lab for a summer project. She collaborated on material preparation, data collection and data analysis of the precipitation experiments presented in manuscript 1 (Chapter 4).

#### CHAPTER 1

#### **GENERAL INTRODUCTION**

#### 1.1. Introduction

#### 1.1.1. Biomineralization

Living organisms regulate the formation of a variety of inorganic minerals, ranging from apatite in bones, calcium carbonate in seashells, calcium sulphate in gypsum to iron oxide in magnetotactic bacteria. These biominerals are formed during a highly regulated process called biomineralization, and often they have exceptional mechanical properties, complex shapes, and intricate hierarchical structures, which distinguish them from their artificially synthesized counterparts [1-3]. These characteristic properties of biominerals are obtained under the direct influence of biomolecules, usually proteins and peptides, which remarkably control and regulate their nucleation and growth under conditions that are much milder than those used in conventional processing techniques [3-6].

The most well-known and maybe most complex example of biomineralization occurs during the formation of bone, an organic-inorganic hybrid material made of collagen, non-collagenous proteins (NCPs), and carbonated hydroxyapatite (CHA) ( $Ca_{10-x}(PO_4)_{6-x}(CO_3)_x(OH)_{2-x}$ ) crystals [7]. Collagen fibres provide a framework known as extracellular matrix (ECM), where CHA nucleates and grow. Even though the ECM determines the ultimate structure and orientation of hydroxyapatite (HA,  $Ca_5(PO_4)_3OH$ ) crystals, it does not have the capacity to initiate HA mineralization despite the fact that body fluids are supersaturated with respect to HA. HA nucleation is mainly initiated by a set of negatively charged phosphorylated NCPs associated with the ECM. These proteins attract  $Ca^{2+}$  and  $PO_4^{3-}$  ions and increase the local supersaturation to a level sufficient to form nuclei of a critical size, which can develop into HA crystals [7, 8]. Another set of NCPs have the ability to inhibit undesirable formation of HA in tissues such as

cartilage and arteries, continuously exposed to body fluids. These inhibitory proteins are either associated with the ECM of tissues or found in the plasma and limit the formation of HA by binding to the surface of nascent mineral nuclei, thus restricting their further growth [9].

While striving to understand the process of biomineralization, researchers have investigated the effect of smaller biomolecules like amino acids (AAs) and peptides (short polymers of AAs) on HA mineralization. AAs are the building block of proteins, and negatively charged AAs such as aspartic acid (Asp), glutamic acid (Glu) and phosphoserine (PSer) are highly abundant in the acidic domain of NCP (e.g. osteopontin (OPN), bone sialoprotein (BSP), dentin matrix protein 1 (DMP 1), and dentin phosphophoryn (DPP)) involved in HA mineralization in bone and dentine. Similar to proteins, charged AAs can either inhibit or induce HA mineralization [10-12]. AAs are also effective in modifying the morphology and crystalline structure of HA due to the electrostatic and stereochemical effects of their charged residues, especially carboxylate and phosphate groups [11, 13-15]. In comparison with proteins or peptides, AAs are much less expensive and more stable, which makes them cost-effective candidates for clinical applications. In-vitro studies show that promoting AAs are useful for improving bone regeneration in damaged tissues [14], while inhibitory AAs are potential candidates for treating pathological diseases caused by an excessive mineralization of HA in tissues like cartilages [16, 17], blood vessels and cardiac valves [17-19].

#### 1.1.2. Precipitation from aqueous solution

Biomineralization happens as a precipitation from aqueous solutions [53, 55]. According to classical models, precipitation involves two main stages: nucleation and growth. Nucleation happens in a supersaturated solution, when metastable nuclei of a critical size form by stochastic solute clustering [20]. These critical-sized nuclei would be the earliest precursors of crystalline materials: after they form, they grow and make larger and larger crystals [21, 22]. Recent studies however indicate that small clusters forming earlier than the critical sized nuclei play a dominant role in the precipitation of organic [23] and inorganic compounds [20], as well as in the presence of biomolecules [24]. The existence of these clusters, commonly known as prenucleation clusters (PCs), is reported by several researchers [24-31].

#### 1.2. Objectives

Although AAs are promising potential candidates for controlling HA mineralization, the mechanism by which they interact with HA crystals to induce or inhibit mineralization is hardly understood. In fact, the studies on AAs and HA crystallization are mostly conducted under experimental conditions different from the physiological ones (i.e. high supersaturation, high temperature or high pH) which have made it difficult to have a real insight into the effects of AAs inside the human body [32-35]. Moreover, most of the studies on the effect of AAs are conducted on the nucleation and growth stage of precipitation [10, 34, 36-47] while the prenucleation stage (stage before critical nuclei form) can play critical role in regulating HA precipitation.

Our objectives in this work are to:

# 1. Investigate the inhibitory effect of differently charged AAs (the positively charged Arg vs. the negatively charged Glu) dissolved in solution on HA precipitation at physiological conditions.

AAs dissolved in solution can inhibit HA precipitation by chelating Ca<sup>2+</sup> and PO<sub>4</sub><sup>3-</sup>ions. In general, it is believed that the negatively charged AAs containing carboxylate or phosphate groups are more effective in controlling HA precipitation due to their strong interaction with Ca<sup>2+</sup> ions [8, 48-51]. However, contradictory results reported by different authors make it difficult to draw a comprehensive conclusion about the effect of AAs dissolved in solution on HA crystallization. For example, Jack et al reported a significant inhibitory effect of alanine (Ala) and aspartic acid (Asp) on the growth of HA particles [52]. In contrast, Palazzo et al showed that Asp promoted HA particle growth while Ala had no effect on HA particle sizes [11]. According to Jack at al., a positively charged AA, lysine (Lys), had the strongest affinity to HA surfaces [52]; however, Koutsopoulos and Dalas showed that the negatively charged Asp had the largest affinity to HA among the AAs that they investigated [44, 53-56].

Here, we investigated the inhibitory effect of a positively charged (Arg) and a negatively charged (Glu) AA (Fig. 1.1) dissolved in solution on the morphology and crystallization (nucleation and growth) of HA synthesized at physiological temperature and pH. Negatively charged AAs, such as Asp and Glu are highly expressed in NCPs and play critical role in HA mineralization in the body [6]. NCPs also contain positively charged AAs, such as Arg and Lys.

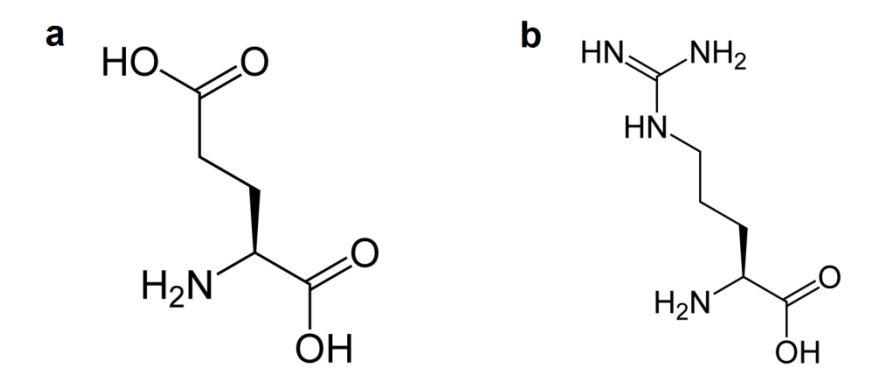


Fig. 1.1. Chemical structure of Glu (a) and Arg (b).

Here we focus on Glu and Arg because they are less investigated than their counterparts Asp and Lys [9, 22-27]. To achieve this objective, the AA-containing Ca- and P-precursor solutions were mixed after 3 days aging. The precipitation behavior of these AA-containing solutions was compared with the aged solution that didn't contain any AAs.

# 2. Investigate the formation of ion/AA clusters in AA-containing precursor solutions, and study the mechanism pathway through which these clusters can regulate HA precipitation.

While nanometer-sized PCs are formed in inorganic systems, larger clusters have been discussed as metastable precursors for the formation of crystals of many organic substances, including proteins and AAs [57]. Here, we investigated the formation of clusters made of precursor ions and AAs, and studied their role in HA precipitation before the nucleation stage. To do this, we ran two different sets of experiments. In the first set, the AA-containing Ca- and P-precursor solutions were mixed right away, and in the second set, these precursor solutions were mixed after 3 days of aging. The interaction between the AAs (Arg and Glu) and Ca<sup>2+</sup> and PO<sub>4</sub><sup>3-</sup> ions in the precursor solutions resulted in the formation of Ca/AAs and P/AAs complexes, and as the precursor solutions were aged, these complexes grew into larger and larger clusters. Once the aged Ca- and P-precursor solutions were mixed, the Ca/AAs and P/AAs clusters brought into contact and interacted with each other before HA nucleated. In this work, we investigated the clusters' interactions and their effect on HA precipitation.

# 3. Investigate the promoting effect of differently charged AAs bound to a graphene oxide (GO) surface on HA precipitation at physiological conditions, and develop a GO-based substrate with high mineralization ability for bone regeneration applications.

As discussed in the previous section, there have been many studies on the effect of AAs dissolved in solution on HA precipitation [10, 34, 36-46]; however the effect of AAs or other small biomolecules bound to surfaces has been the subject of just a few studies [47, 58, 59]. Since the AAs involved in HA precipitation in bone are associated with ECM and cannot move freely, studies concerning the AAs bound to surfaces can model the in-vivo precipitation of HA more closely than the AAs dissolved in solution. Similar to NCPs, AAs bound to surfaces can promote HA precipitation by attracting Ca<sup>2+</sup> and PO<sub>4</sub><sup>3-</sup> ions and increasing the local degree of supersaturation [12].

In this work, we used GO as a surface to bind the AAs on. There are just a few studies investigating the mineralization of graphene-based materials [58-61]. We study the promoting effect of a positively charged (Arg) and a negatively charged (Glu) AA bound to GO on the morphology and crystallization of HA synthesized at physiological conditions. To achieve this goal, we grafted the AAs onto GO flakes, and then immersed the AA-coated GO samples and a control GO sample without AA coating in simulated body fluid (SBF) to investigate the precipitation of HA on the GO flakes.

#### **CHAPTER 2**

#### LITERATURE REVIEW

Biomineralization is a process by which living organisms produce minerals. Biominerals usually have complex structures and excellent properties obtained under the influence of biomolecules that regulate the mineralization process. Bone, composed of 70% of HA, is one of the most studied examples of biomineralization.

Aqueous precipitation is the most common technique used to study HA biomineralization due to its similarity to biological systems. In this section, we first introduce concepts related to aqueous precipitation in general; then we review different studies on the synthesis of HA using this method, and finally we review the biomineralization of HA and describe the effect of various biomolecules, such as proteins, peptides, and their building blocks, AAs, on HA precipitation invitro.

#### 2.1. Precipitation from aqueous solutions

Precipitation is probably the most common operation in industries and laboratories [21, 22]. Aqueous precipitation is defined as the formation of a solid product via chemical reactions occurring in water. The properties of the solid product are determined by the following factors: (a) solid–liquid equilibria; (b) crystallization kinetics, i.e. supersaturation, nucleation, and growth; (c) colloid surface chemistry, i.e. the aggregation of particles and the adsorption of impurities/additives, and (d) the reactor design (**Fig.** 2.1) [22]. All these factors are important in directing the precipitation process. However, we will mainly focus on the crystallization kinetics (**Sections 2.1.1 and 2.1.2**), and will briefly discuss some effects of additives in **Section 2.1.3**.

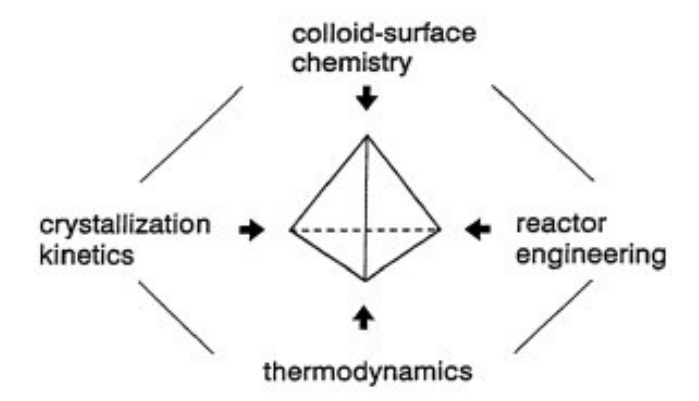


Fig. 2.1. Different factors that control precipitation from aqueous solution [22].

#### 2.1.1. Classical model

According to classical models, precipitation involves two main stages: nucleation and growth [21, 22]. Nucleation happens in a supersaturated solution, when metastable nuclei of a critical size form by stochastic solute clustering [20]. These critical sized nuclei would be the earliest precursors of crystalline materials: after they form, they grow and make larger and larger crystals [21, 22].

#### 2.1.1.1. Supersaturation

According to thermodynamics of classical precipitation, a solid phase forms when [22],

$$\Delta G = -RT \ln\left(\frac{\alpha}{\alpha_0}\right) < 0 \tag{2.1}$$

where  $\Delta G$ : molar Gibbs free energy; R: the universal gas constant; T: the absolute temperature;  $\alpha$ : activity of the solute in the initial solution; and  $\alpha o$ : activity of the solute in the final solution. We define the ratio  $\alpha/\alpha o$  as the saturation ratio, S. For crystallization reactions, i.e.  $A(aq)+B(aq) \rightarrow AB(s)$ , the saturation ratio can be defined as [22];

$$S = \frac{[A][B]}{K_{sp}} \tag{2.2}$$

where  $K_{sp} = [A]_{eq}[B]_{eq}$ . When S>1, we have  $\Delta$ G<0. This is the condition of supersaturation. Therefore, in classical models, supersaturation is considered to be the driving force for crystallization.

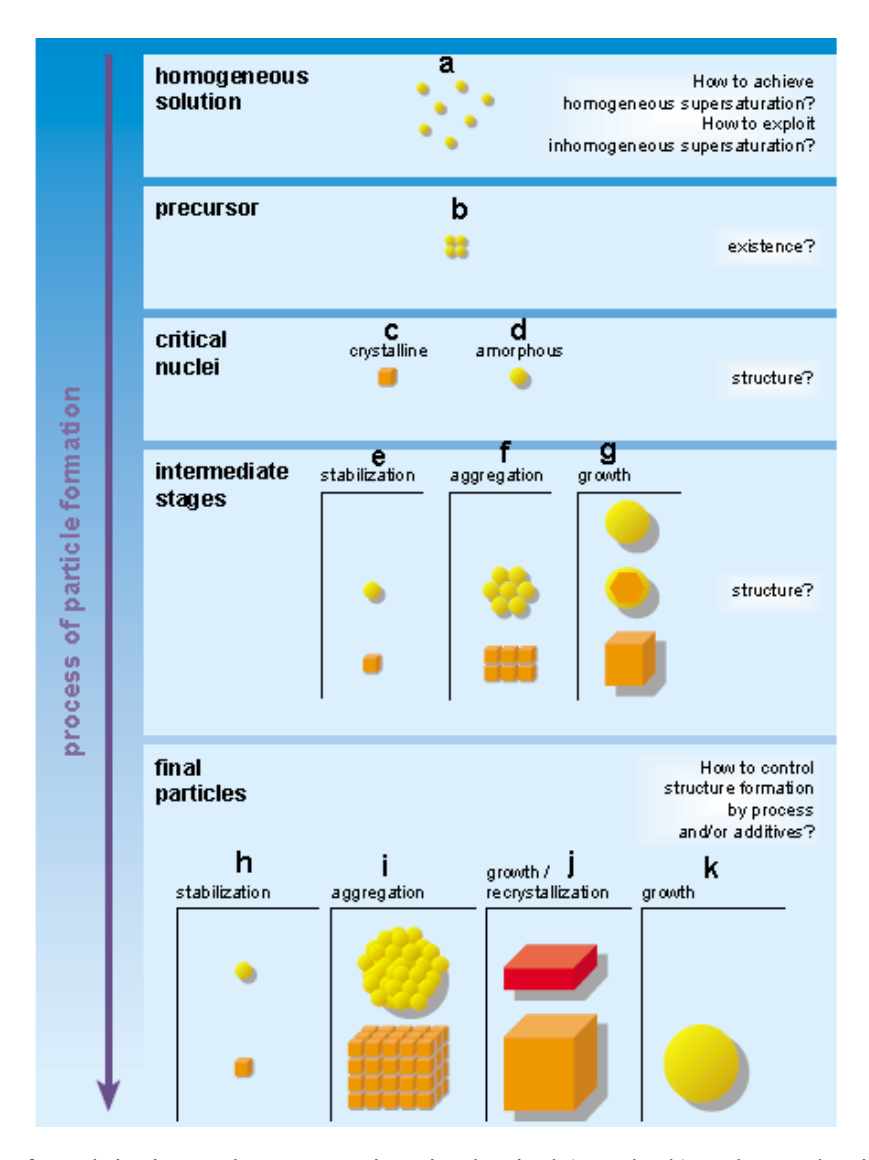


**Fig. 2.2.** Stages of precipitation and open questions in classical (a and c-k) and non-classical precipitation (a-k) from aqueous solution [23].

#### 2.1.1.2. *Nucleation*

Nucleation is the process in which molecules or precursor ions (**Fig. 2.2a**) combine together to form nuclei, which could be crystalline (**Fig. 2.2c**) or amorphous (**Fig. 2.2d**). The nuclei constantly form and disappear until they reach a critical size,  $r_c$  [22]. In fact, nucleation starts when a critical S value ( $S_{cr}$ ) is exceeded. Beyond this  $S_{cr}$  value the nucleation rate increases sharply and reaches its maximum quickly (**Fig. 2.3**) [22]. Nucleation rate (J) is an exponential or high power function of supersaturation as shown by the following equation; therefore, J has a strong dependency on supersaturation [62].

$$J = Aexp\left(-\frac{16\pi\gamma^3 v^2}{3(kT)^3 (Ln S)^2}\right)$$
 (2.3)

where A is a nucleation constant, k is the Boltzmann constant,  $\gamma$  is the interfacial tension between the developing surface of nuclei and the supersaturated solution, and v is the molecular volume of precipitate.

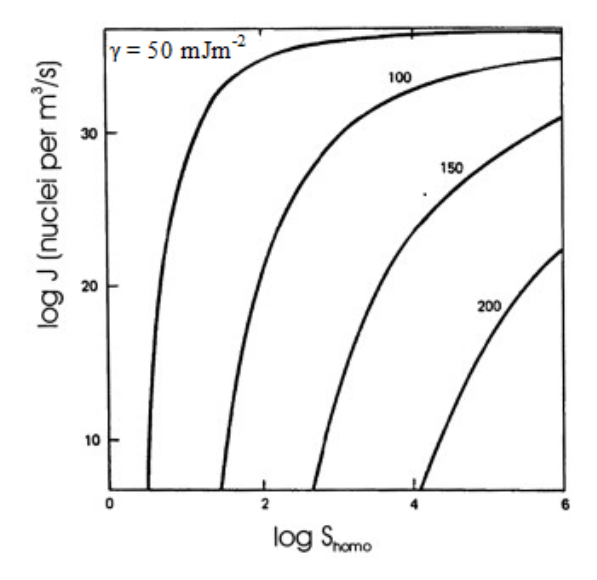
Depending on the nucleation site, we have three different nucleation mechanisms:

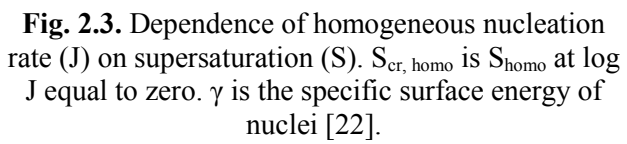
- i) Homogeneous nucleation: primary nuclei form in solution.
- ii) Heterogeneous nucleation: primary nuclei form on a foreign surface.
- iii) Surface nucleation: primary nuclei form on the surface of preformed precipitate.

The free energy change,  $\Delta G$  (r), associated with the formation of the nuclease is given by [22]:

$$\Delta G(r) = \Delta G_{vol} - \Delta G_{surf} \tag{2.4}$$

where the first term,  $\Delta G_{vol}$ , is the free energy change associated with the generation of volume and the second term,  $\Delta G_{surf}$ , is associated with the generation of new surface.  $\Delta G_{vol}$  is negative but the second term,  $\Delta G_{surf}$ , is positive; therefore, it is only after a certain size  $r_c$  that  $\Delta G(r)$  becomes negative. A plot of  $\Delta G(r)$  as a function of nuclei size (r) is shown in **Fig. 2.4**. The  $\Delta G_{max}$  represents an activation energy barrier [62].





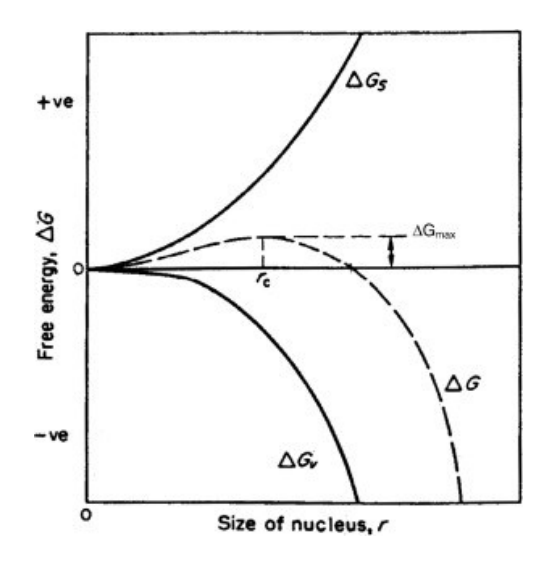


**Fig. 2.4.** Free energy of precipitation as a function of nuclei size [62].

Heterogeneous and surface nucleation are easier than homogeneous nucleation because the surface energy change, and as a result  $\Delta G_{max}$ , is lower than that required to create a new nucleus in solution [22]. Therefore, heterogeneous and surface nucleation are favored at lower supersaturations when the driving force for precipitation is lower while homogeneous nucleation happens at high supersaturation conditions. The critical supersaturation for nucleation decreases as follows for different mechanisms of nucleation:  $S_{cr,\ homo} > S_{cr,\ hetero} > S_{cr,\ surface} > 1$ .

#### 2.1.1.3. Growth

Crystal growth happens through a series of stages: a) transportation of solute in solution, b) solute adsorption on the particle surface, c) surface diffusion, and finally d) incorporation of solute into crystal [22].

While the nucleation rate is exponentially dependent on supersaturation (**Eq. 2.3**), the growth rate (G) of a spherical particle of radius r can be explained by a first order or more rarely second order equation in terms of supersaturation (**Eq. 2.5**) [22]; therefore, G shows less dependency to supersaturation than J.

$$G = \frac{dr}{dt} = k_g C_{eq}(S - 1)$$
 (2.5)

Where t is time,  $k_g$  is the growth constant, and  $C_{eq}$  is the solubility of the precipitating solute species.

There are two modes of particle growth depending on the relative magnitude of surface nucleation rate vs. crystal growth rate [22] (Fig. 2.5). The first mode is the layered or mononuclear growth. This occurs when the crystal growth is fast, but the surface nucleation is the rate limiting step. This results in crystal growth by addition of molecules to the initial nucleus formed instead of the formation of new nuclei (Fig. 2.5a). The second mode is the continuous or polynuclear growth, which occurs when growth is the rate-limiting step. In this case, the growth of the initial nucleus is not favored; therefore, the crystal grows by forming new nuclei on the favorable sites of its surface (Fig. 2.5b). The growth by either of these modes can result in crystalline (Fig. 2.3j) or amorphous particles (Fig. 2.3k).

There is also a third growth mode, which happens by aggregation of crystalline nuclei of 10 to 100 nm, which aggregate to form larger crystalline or amorphous particles (**Fig. 2.3i**). This mode of growth is favored when the colloid stability is suppressed or the population density of colloidal particles increases (**Fig. 2.3i**) [22].

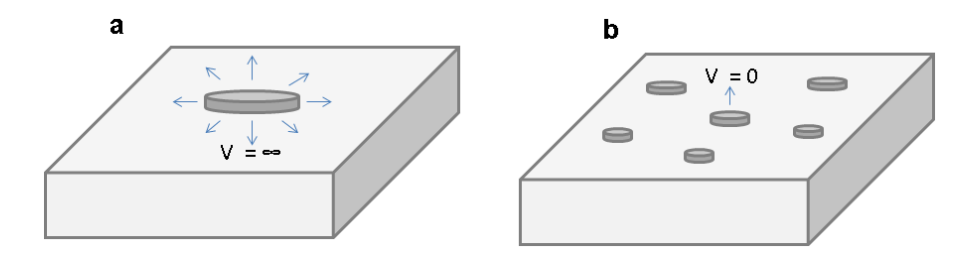


Fig. 2.5. Schematic showing mono-nuclear (a) vs. poly-nuclear (b) crystal growth.

#### 2.1.2. Non-classical precipitation

While classical models assume that the initial nuclei simply form by stochastic solute clustering, which results in an initial uphill in free energy to form a critical sized nucleus [24], recent studies indicate that small clusters (**Fig. 2.3b**) forming earlier than the critical nuclei play a dominant role in the precipitation of organic [23] and inorganic compounds [20], as well as in the presence of biomolecules [24].

According to recent studies [23, 24], nucleation and growth in complex systems involve i) the interaction of water, protons, hydroxyls, or biomolecules with the precursor ions, ii) the formation of PCs or biomolecule/ion aggregates, iii) the rupture or coalescence of aggregates to from critical nuclei, and finally iii) crystal growth. All these steps may involve activation energies different from the activation energy associated with the formation of critical nuclei in classical models. The interplay of all the factors described above will result in different crystallization behaviours, such as delayed or promoted precipitation, and will strongly affect the final properties of the precipitates in terms of crystalline structure, crystallite sizes, and morphology [23, 24]. The calcium carbonate system is one of the most studied at this regard [20, 63-66]. Several studies have shown the formation of stable ionic PCs as a prerequisite for the formation of calcium carbonate in a calcium and carbonate ion solution, even though the solution was not supersaturated with respect to calcium carbonate [20, 28]. Bewernitz et al also showed the formation of liquid-like calcium carbonate clusters as precursors for the formation of calcium carbonate [25]. These clusters seemed to be stabilized by organic additives, such as polyaspartate and acidic poly peptides [25, 26].

PCs have been observed in many other systems. Yang et al showed that an optically clear solution of dissolved silica contain a significant number of polymeric nano clusters acting as precursors for silica formation [67, 68]. Solutions containing aluminum (Al) ions at neutral pH include extensive amounts of clusters composed of a central AlO<sub>4</sub> tetrahedron bonded to 12 other

Al ions, with water and hydroxyl groups holding the cluster together [69, 70]. These clusters have many features characteristic of crystalline Al hydroxides. Large ions such as uranium, molybdenum, and tungsten also form complexes in aqueous solutions [71]. For example, carbonate groups are shown to play a major role in holding the uranium clusters together. The crystalline uranium is formed by the coalescence of such clusters rather than the nucleation of a crystalline phase [71, 72].

#### 2.1.3. Precipitation inhibitors

Precipitation inhibitors are important for applications as diverse as preventing scale formation in water treatment plants or inhibiting the formation of renal stones in the body. Inhibitors work mainly in two ways:

- i. The additive may form stable complexes with one of the precipitating ions. The effective concentration of free precursor ions would, therefore, be reduced. For this factor to be effective, the concentration of additives should be at least of the same order of magnitude as that of precipitating ions [73].
- ii. The additive may be adsorbed at particle or crystal growth sites, thus preventing their further growth [4]. If adsorption takes place preferentially only at certain cites, the morphology of the growing crystal may be significantly changed. For example, Mullin et al showed that the morphology of potassium dihydrogen phosphate crystals is significantly influenced not only by pH and supersaturation, but also by the presence of low concentration of foreign cations, such as  $Cr^{3+}$ ,  $Fe^{3+}$ , and  $Al^{3+}$  [74].

The absorbability of additives on crystal surfaces and the stability constants of complexes formed between the precipitating ions and additives are two important factors that determine the inhibitory effect of additives according to the mechanisms described in (i) and (ii) [38, 43-45, 73].

Ionic additives can also work according to a third, additional mechanism:

iii. They can influence the ionic strength of solution and change the solubility of the precipitating phase. If the solubility increases, the supersaturation with respect to the precipitating phase will decrease; therefore, precipitation will be inhibited. This mechanism could be active even at very low concentrations of inhibitors [73].

In general, organic phosphates are particularly at concentrations as low as  $5X10^{-8}$  M [73]. Pyrophosphate  $(P_2O_7^{4-})$  is an active inhibitor for the biomineralization of calcium oxalate [75],

calcium carbonate [76], and calcium phosphate [77, 78]. Researchers have also shown the inhibitory effect of many other ions, such as Fe<sup>3+</sup>, Cu<sup>2+</sup>, and Mg<sup>2+</sup> on the crystallization rate of different inorganic materials [79-83].

# 2.2. HA precipitation from aqueous solution

HA has a hexagonal structure (**Fig. 2.6**) belonging to the P6<sub>3</sub>/m space group, and cell dimensions of a=b=9.42 Å, and c=6.88 Å. HA has a stoichiometric Ca/P ratio of 1.67; however, the biological HA found in bone has lower Ca/P ratio due to the substitution of Ca<sup>2+</sup> ions with Na<sup>+</sup>, K<sup>+</sup>, and Mg<sup>2+</sup> ions [84]. HA can be synthesized by a variety of techniques including wet chemistry [85-100], solid state reaction [101, 102], and hydrothermal treatment [103-117]. However, HA precipitation from aqueous solutions containing Ca<sup>2+</sup> and PO<sub>4</sub><sup>3-</sup> ions best simulates the process of HA formation in the body [96, 98, 118-129].

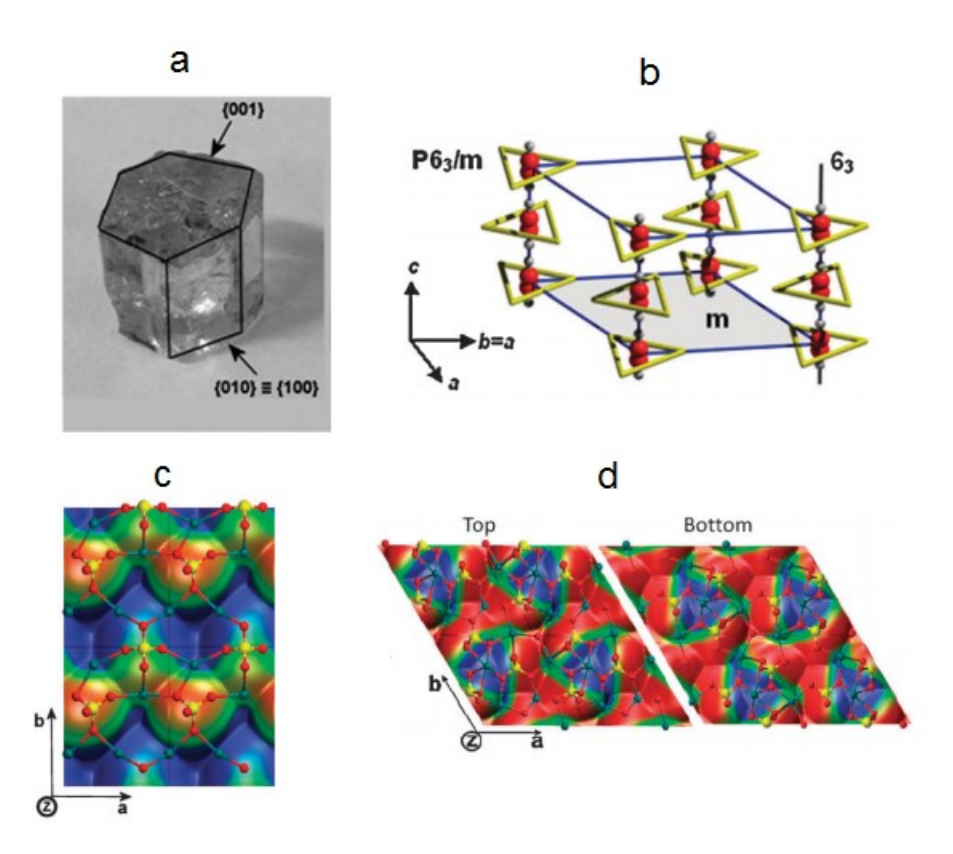


**Fig. 2.6.** (a) HA crystal structure and its electrical potential distribution: crystal form of HA mineral; (b) experimental crystalline (P63/m) structure. P, O and Ca atoms not relevant for the scheme were omitted for clarity of representation. Ca ions are at the vertices of triangles around each hydroxyl group (red and gray spheres); (c and d) electrostatic potential view along the [010] direction of the HA (010) plane (c) and top/bottom view along [001] direction of HA (001) plane (d). Atoms are color-coded: oxygen is red, calcium is cyan, phosphorous is yellow, and hydrogen is grey. Positive/negative values of the electrostatic potential are shown as blue/red colours [130].

**Table 2.1.** Calcium phosphate crystalline phases and their Ca/P ratios [84, 131].

Name	Symbol	Formula	Ca/P
Monocalcium Phosphate Monohydrate	MCPM	$Ca(H_2PO_4)_2.H_2O$	0.5
Monocalcium Phosphate Anhydrate	MCPA	$Ca(H_2PO_4)_2$	0.5
Dicalcium Phosphate Dihydrate	DCPD	CaHPO <sub>4</sub> .2H <sub>2</sub> O	1.0
Dicalcium Phosphate Anhydrate	DCPA	CaHPO <sub>4</sub>	1.0
Calcium Pyrophosphate	pyro	$Ca_2P_2O_7.2H_2O$	1.0
Octacalcium Phosphate	OCP	$Ca_8(HPO_4)_2(PO_4)_4.5H_2O$	1.33
Tricalcium Phosphate	TCP	$Ca_x(PO_4)_y.nH_2O$	1.2-2.2
Hydroxyapatite	HA	$Ca_{10}(PO_4)_6(OH)_2$	1.67
Tetracalcium Phosphate	TTCP	$Ca_4(PO_4)_2O$	2.0

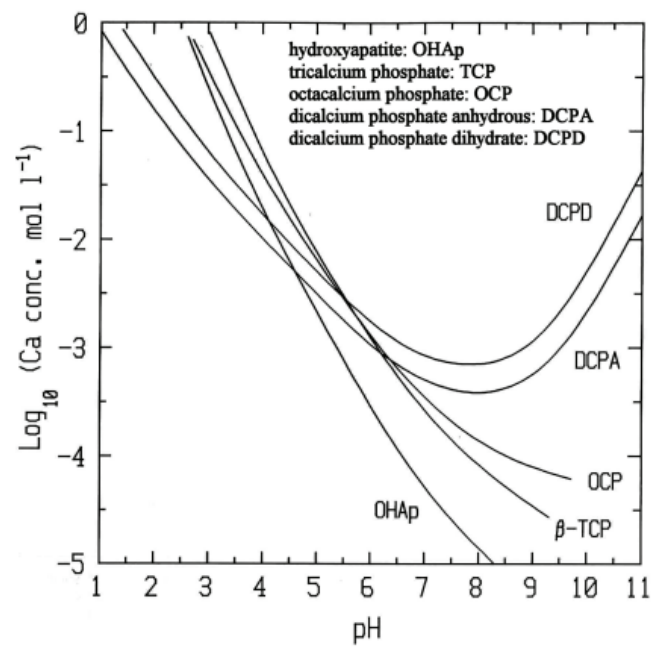


Fig. 2.7. Solubility constant and stability of different phases of calcium phosphates at 37°C [132].

## 2.2.1. Calcium phosphate phases and their transformation to HA

Calcium phosphates have many different crystalline forms as shown in **Table 2.1** [84, 131]. HA is the most stable form of calcium phosphate at physiological temperature and pH (**Fig. 2.7**); however, its crystallization from aqueous solutions does not occur right away. Amorphous calcium phosphate (ACP) is the first precursor forming in the reaction solution [21, 85, 133-135]; then, ACP transforms to HA either by the direct transformation of ACP to HA [21, 85, 133] (**Fig. 2.8**), or through the intermediate formation of octacalcium phosphate (OCP) (**Fig. 2.9**)

[134, 135]. There is some evidence that dicalcium phosphate dihydrate (DCPD) too can act as a precursor or an intermediate phase for HA crystallization (**Fig. 2.10**) [136]. However, the formation of HA (a basic calcium phosphate) from acidic phases such as DCPD is not strongly confirmed.

The ACP precursor itself consists of nano-building blocks, called Posner's clusters, containing both ionic and covalent bonds [137-143]. Posner's clusters with the formula of Ca<sub>9</sub>(PO<sub>4</sub>)<sub>6</sub> are likely to form the core of ACP [142], and are recently shown to form also the smallest (~1nm) unit of HA structure [139]. Posner's clusters can be the evidence of PCs for ACP and HA. Indeed, Dey et al showed that HA precipitation started from ACP nuclei previously formed through the aggregation of nano-sized PCs with the formula of Ca<sub>9</sub>(PO<sub>4</sub>)<sub>6</sub> (Fig. 2.11) [143]. However, Habraken et al [144] more recently showed that the very first PCs are in fact calcium triphosphate ion-association complexes, which can aggregate and take up an extra calcium ion to form Ca<sub>2</sub>(HPO<sub>4</sub>)<sub>3</sub><sup>2-</sup> cluster, which is a precursor for ACP. Continued calcium uptake can result in ACP converting into OCP and subsequently into HA, which both contain the calcium triphosphate complexes as their building blocks.

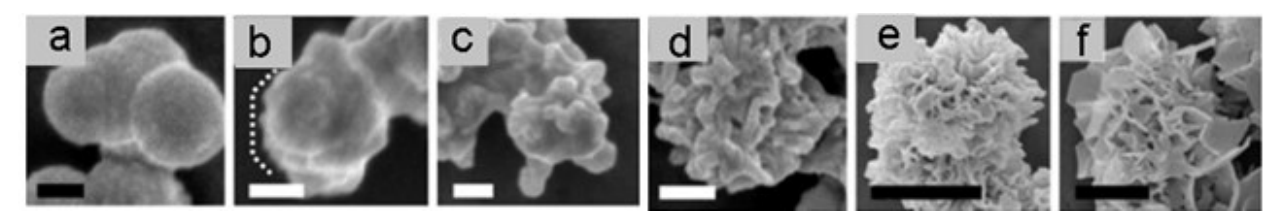


**Fig. 2.8.** Phase and morphology evolution of calcium phosphate precipitate from ACP (a) to HA (f) in SBF under physiological conditions at reaction times of 3 min (a), 67–73 min (b-d), 90 min (e), and 7 h (f). Bar: (a-c) 100 nm; (d) 200 nm; (e–f) 1 mm [133].

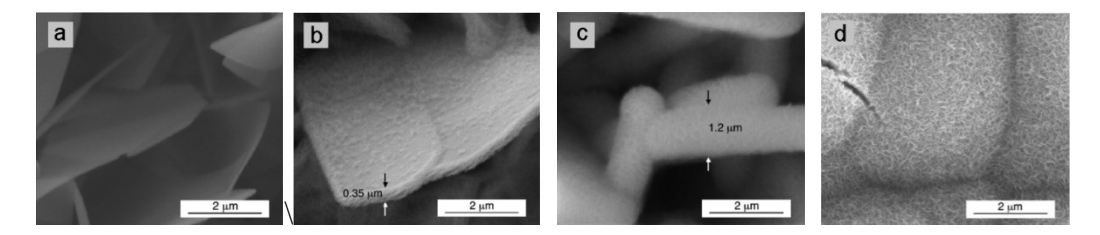


**Fig. 2.9.** Phase transformation of OCP (a) to HA (d) in SBF under physiological conditions at reaction times of 0 (a), 10 (b), 24 (c), and 100 h (d).



**Fig. 2.10.** Phase transformation of DCPD (a) to HA (c) in SBF under physiological conditions at the reaction time of 0 h (a), 36 h (b), and 1 w (c) [145].

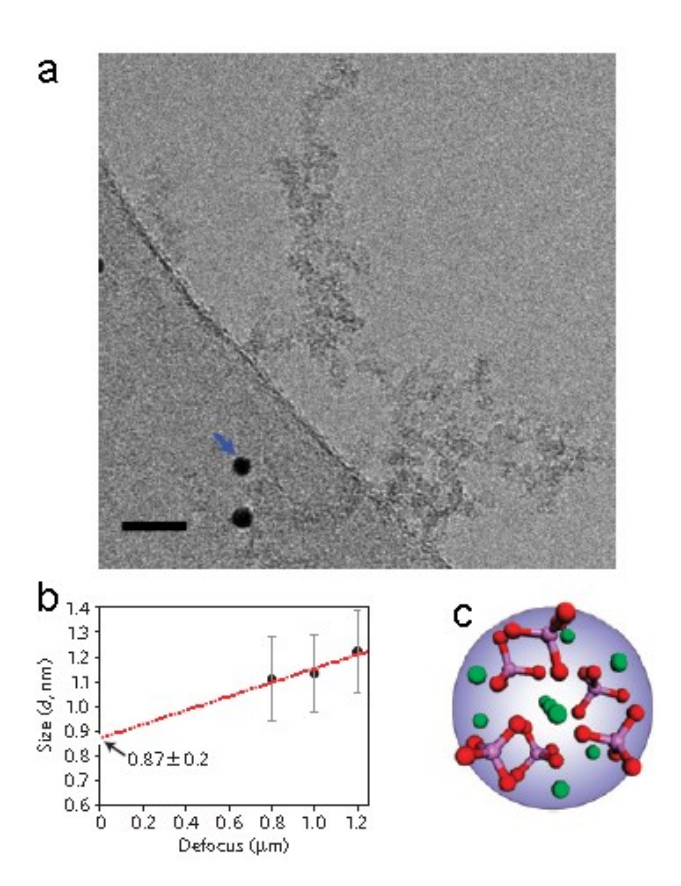


**Fig. 2.11.** Stable prenucleation cluster of calcium phosphate in SBF: a) High-resolution TEM image of aggregated clusters in SBF kept at 37°C for 24 h; b) The diameter of prenucleation clusters determined by extrapolation of the diameter measured in HR-cryo TEM images at different defocusing values; c) computer representation of the Posner cluster with composition of Ca<sub>9</sub>(PO<sub>4</sub>)<sub>6</sub>[143]. The arrow indicates gold particles used as a fiducial marker for tomography. Scale bar, 20 nm.

The presence of chemical additives, such as Mg<sup>2+</sup>, CO<sub>3</sub><sup>2-</sup>, and F<sup>-</sup> in the precipitation solution can strongly inhibit the conversion of ACP into HA [146-148]. This is explained by the incorporation of these additives in the ACP structure, which results in the formation of crystal defects, and delays ACP transformation into a crystalline phase. Also, any compounds with a phosphate group, such as pyrophosphate, tripolyphosphate, imidodiphospahte, phosphocitrate, or with an acidic group, such as citrate, polyacrylate, poly-glutamate, poly-lysine and casein can

potently inhibit the transformation of ACP to HA [146, 147]; however, the phosphate – containing molecules are more powerful inhibitors because they can substitute their phosphate groups for phosphates present in ACP structure [146, 147]. Also, ACP to HA transformation is slower at higher pH, ionic strength, and Ca/P ratio, and at lower initial supersaturation and temperature [147].

## 2.2.2. HA nucleation, growth, and morphology

Nucleation and growth of HA is faster at higher pH, temperature, ionic strength, Ca/P molar ratios, and initial supersaturation [90, 149-151]. On the other hand, both nucleation and growth are strongly inhibited in the presence of chemical additives, such as  $Mg^{2+}$ ,  $Zn^+$  and  $P_2O_7^{4-}$  [148, 152-155].

The crystallinity of HA increases with temperature, and higher degrees of crystallinity usually result in the formation of nano particles with regular shape and smooth surfaces. However, various morphologies can be obtained at different experimental conditions, such as pH and temperature (**Fig. 2.12**) [156]. The formation of spherulitic particles consisting of nanoplatelets is generally believed to be the result of synthesis of HA at physiological conditions [91, 118] (**Fig. 2.13**). In the presence of chemical additives, even other forms of calcium phosphates with different morphologies can be obtained (**Fig. 2.14**) [157].

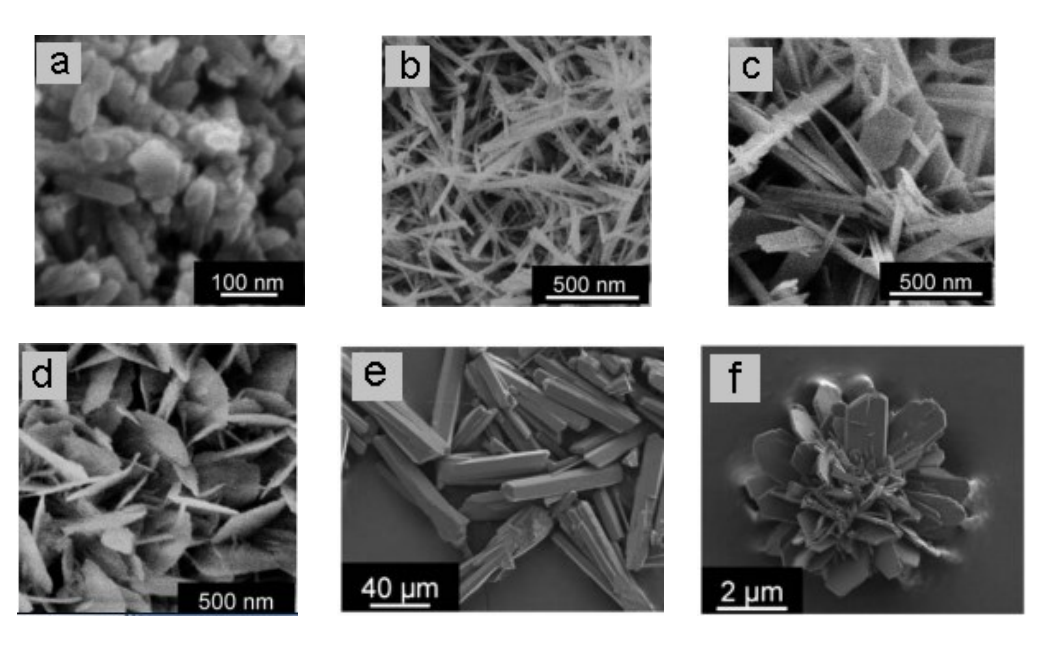


**Fig. 2.12.** SEM images of HA crystals grown for 24 h in the SBF-based solution in the presence of commercial HA nanoparticles seeds (a) at 37 (b-d) and 160° C (e and f) at the pH of 6.5 (b), 7 (c and e), and 7.5 (d and f) [156].

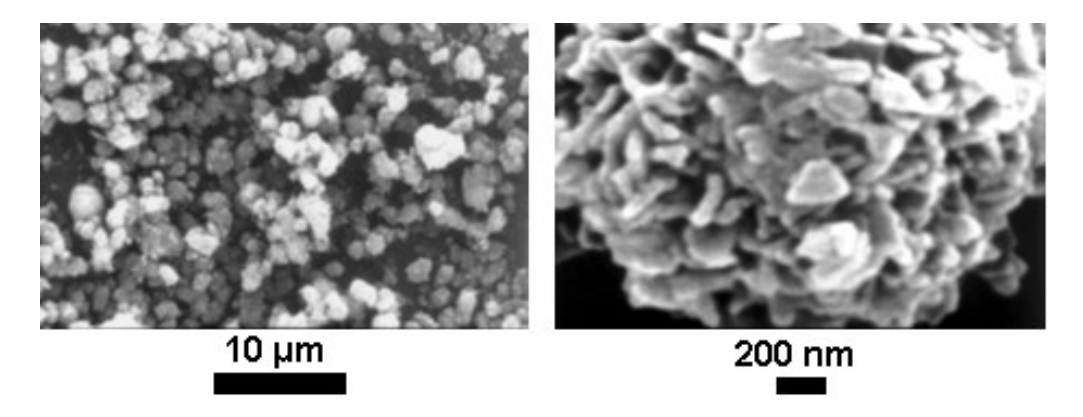


**Fig. 2.13.** The SEM images of HA particles, at different magnifications, synthesized from an aqueous solution at physiological conditions [91].

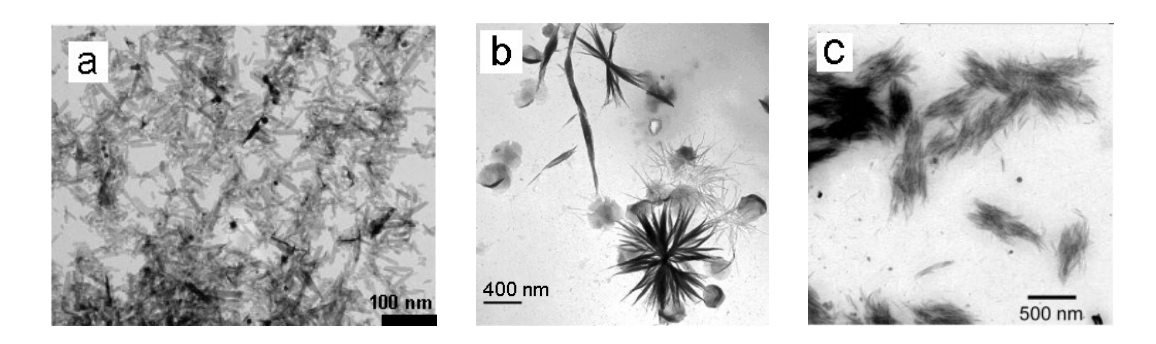


**Fig. 2.14**. Effect of bis(2-ethylhexyl)sulfosuccinate sodium salt (AOT) on controlling the morphology of calcium phosphate precipitate obtained from calcium chloride and potassium dihydrogen phosphate under ambient conditions: a) control HA crystals; b) elongated plate-like crystals of brushite, networks of amorphous nano particles, and octacalcium phosphate spheres produced at low AOT concentration; c) bundles of aligned HA filaments with structural features resembling mineral found in tooth enamel produced at high AOT concentration [157].

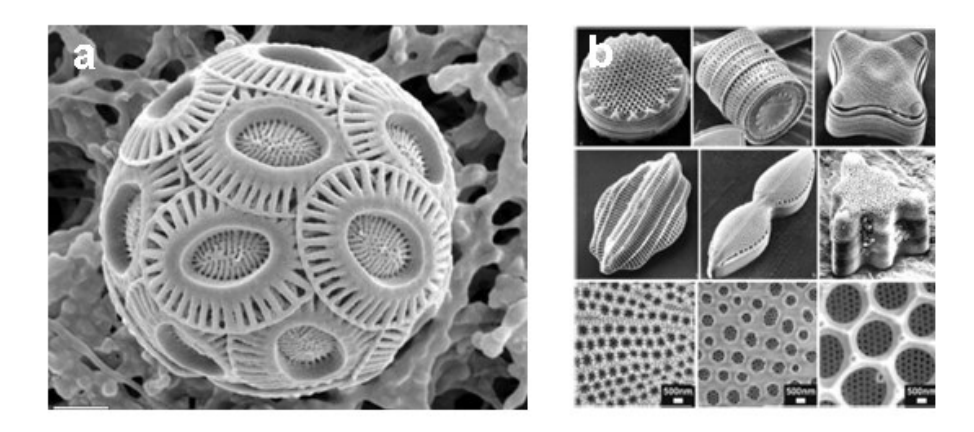


**Fig. 2.15.** Examples of biominerals with astonishing structures found in nature: a) coccosphere, which is a complex arrangement of individual plates of calcium carbonate produced by single-celled algae known as coccolithophores;. b) intricately detailed silica cell walls, known as frustules, produced by unicellular eukaryotic algae [4, 158].

## 2.3. HA biomineralization

## 2.3.1. Biomineralization in general

Biomineralization is a complex processes by which living organisms produce minerals including a variety of oxides and salts, the most well-known of which are calcium carbonate, calcium phosphate, calcium sulphate, and iron oxide. Biominerals are attractive due to their exceptional properties, complex shapes, and their intricate hierarchical structures (Fig. 2.15) which distinguish them from their inorganically produced counterparts [2-4, 158]. These unique characteristics of biominerals are obtained under the direct influence of biomolecules, which remarkably regulate their nucleation and growth [2, 3, 5, 6]. For example, fish can grow complex structures known as otoliths (Fig. 2.16a) within the inner ear. These structures assist the fish in sensing and balancing, and are composed of calcium carbonate crystallites surrounded by an organic matrix. An acidic protein called Starmaker regulates their mineralization and strongly influences their morphology and crystal structure [159, 160].

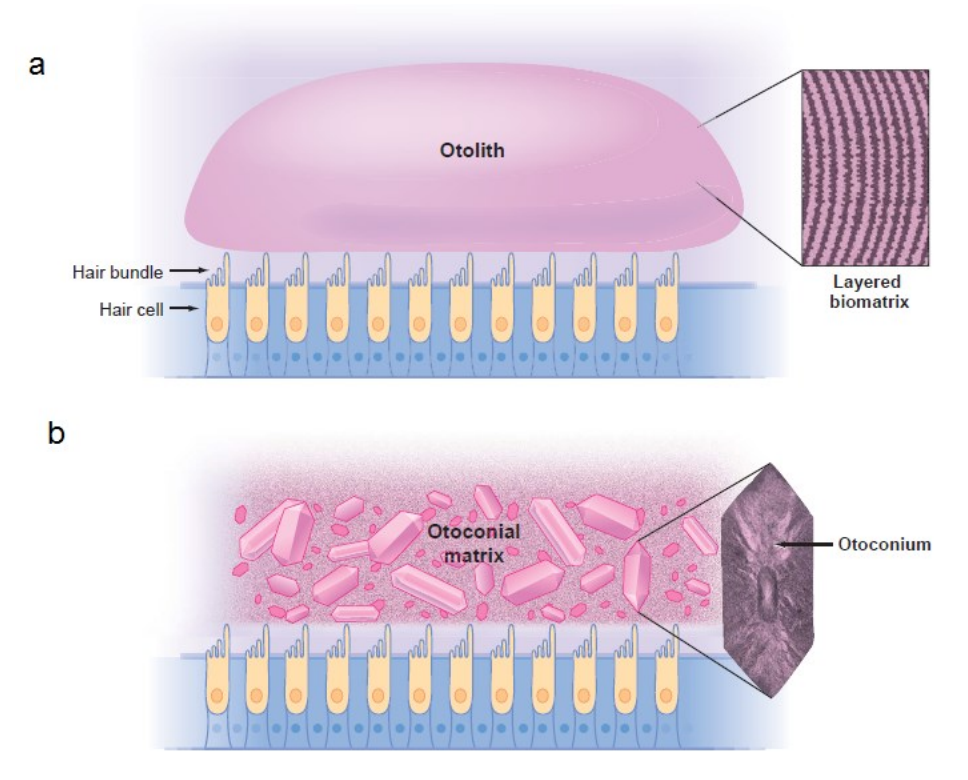


**Fig. 2.16.** Sensory organs (otoliths in fish (a) and otoconia in higher vertebrates (b)) of inner ear containing biomineralized structures that deflect the sensory hair bundles of these organs. Cross sections show that these organs are composite materials consisting of organic matrices and lighter zones of calcium carbonate microcrystals.

Similar to otolith in fish, otoconia (Fig. 2.16b) are small crystals of calcium carbonate in the human inner ear embedded in strongly acidic phosphorylated proteins. Due to their unique structure, otoconia are sensitive to gravity and linear acceleration and give information about vertical and horizontal movements [161]. As another example, nacre, also known as mother of pearl, is produced by molluscs. Nacre has a layered structure composed of aragonite (a form of calcium carbonate) and an organic matrix mainly consisting of silk-like proteins. This structure almost doubles the Young modulus of calcium carbonate (from 35-50 GPas to 70 GPas) [3], providing the shells with high mechanical strength.

**Table 2.2.** Bone composition of female Wistar rats [161].

Components	Percentage		
Total protein	15.99		
Raw fiber	3.86		
Raw fat	3.08		
Lysine	0.82		
Methionine with cystine	0.58		
Calcium	1.11		
Phosphorus	0.72		
Magnesium	0.19		
Zinc	$4.80 \times 10^{-3}$		
Copper	$0.85\times10^{-3}$		
Iron	$1.60\times10^{-2}$		
Vitamin D <sub>3</sub>	1 IU/g		
Cadmium	$1.15 \times 10^{-5}$		

**Table 2.3.** Mechanical properties of hard tissues in human body [92].

Tissue	Compressive Strength (MPa)	Tensile strength (MPa)	Modulus of normal elasticity (GPa)
Cortical tissue of bone	88-164	89-114	3.9-11.7
Dentin	295	52	18.2
Enamel	384	10	82.4

## 2.3.2. Bone (composition and structure)

Natural bone is an organic-inorganic hybrid material (**Table 2.2**) and has a complex hierarchical structure (**Fig. 2.17**) which gives rise to an ideal strength and elasticity (**Table 2.3**) for bone to undergo severe tensile and compressive stresses [162-164].

The molecular components of bone are water (9%), non-stoichiometric CHA (69%), collagen type I (20%), and other organic materials, such as proteins, polysaccharides, and lipids, which are present in small amounts based on weight. These components all together constitute the first level of bone hierarchical structure [162]. The CHA crystals in bone are plate-shaped and are among the smallest known biological crystals (30-50 nm long, 20-25 nm wide, and 1.5 to 4 nm thick). Collagen type I is the most abundant protein in the human body, and is mainly composed of the AAs, glycine (Gly), proline, and hydroxyproline, which all together constitute more than 50% of collagen AA composition. These are often expressed as Gly-X-Y repeats (where X and Y are either proline or hydroxyproline) [9]. The main role of collagen is to provide a matrix for bone mineralization, and to contribute to bone mechanical strength and toughness by providing flexible organic fibrils that are spread through the brittle inorganic phase of bone, CHA platelets [165, 166].

When analyzing the first level of bone organization, Reznikov et al recently found that two different materials can be distinguished [164]: a) an ordered material mainly made of aligned arrays of mineralized collagen fibrils arranged into different patterns, with minor amounts of non-collagenous organic materials, such as NCPs and proteoglycans, and b) a disordered material composed of a mineralized matrix with poorly oriented collagen type I fibrils and abundant non-collagenous organic materials. The disordered material is a continuous phase that mainly fills the spaces between the ordered fibril arrays. The ratio of the ordered to disordered material in humans is approximately 4 to 1 [164].

The second level of bone structure is given by collagen fibrils (80 to 120 nm in diameter) mineralized with CHA crystals. Mineralized collagen fibrils are the main component of the ordered material [164]. The disordered material also contains some mineralized collagen fibrils; however, they are only one of the components of this material, which also contains abundant organic materials such as NCPs and cells. In the disordered material, CHA was found both within and between the collagen fibrils [164]. The texture of the mineralized collagen fibrils reported in [164] was very similar to that reported by previous researchers, who usually call the

CHA crystals located within collagen fibrils "intrafibrillar" mineral, and those located between collagen fibrils "extrafibrillar" mineralization [167, 168]. However, the extrafibrillar mineralization reported in [164] was found only in the disordered components of bone.

The third level is given by mineralized collagen fibrils arrays associated as bundles or aligned along their long axis in the ordered material, and randomly oriented collagen fibrils in the disordered material [162]. The fourth level is given by the arrangement of mineralized collagen fibrils in specific patterns depending on the type of bone [162]. This can include unidirectional array pattern and fanning pattern in the ordered phase [164]. The disordered phase appears as thin layers of randomly orientated collagen fibrils located between the fibrillar patterns. The fifth level of hierarchy is given by the formation of superstructures [164]. In the ordered phase, this includes the cylindrical arrays of collagen bundles. In the disordered phase, the fifth level refers to the cells and lacunae and canaliculi networks that are embedded in the disordered component of bone, and they altogether form the disordered superstructure that fills the gap between the lamellae in the ordered phase [164].

The sixth level refers to the specific 3D patterns of the mineralized lamellae, which mainly includes lamellar bone, fibrolamellar bone, and woven bone [164]. Lamellar bone is composed of a series of lamellae, with the disordered material and embedded canaliculi network filling the gap between the lamellae. The fibrolamellar bone is composed of unidirectional bundles of mineralized collagen fibrils, which are separated by the thin layer of the disordered material. Woven bone is composed by mineralized collagen fiber bundles with no preferred 3D orientation. This type of bone is frequently found during bone development.

Lamellar bone is the most common structure in mammalian bone; the higher levels of bone hierarchy are relevant only to this type of bone. The seventh level refers to the formation of lamellar packets and osteons [164]. The lamellar packets are formed by the removal of some lamellar bone in trabecular or spongy bone. Osteons are cylindrical structures formed by osteoclast and osteoblast cellular activities in compact bone [162]: osteoclasts resorb bone and form tunnels, and osteoblasts subsequently lay down lamellae in stacked concentric layers until a small channel is left behind. The eight level of bone structure is the formation of osseous tissue, either as spongy (trabecular) or compact (cortical) bone [162]. The trabecular bone is extremely porous, providing space for marrow and blood vessels, while cortical bone is the dense outer

layer that allows for the supporting functions of bone [162]. Finally, the ninth level of hierarchy is the whole bone.

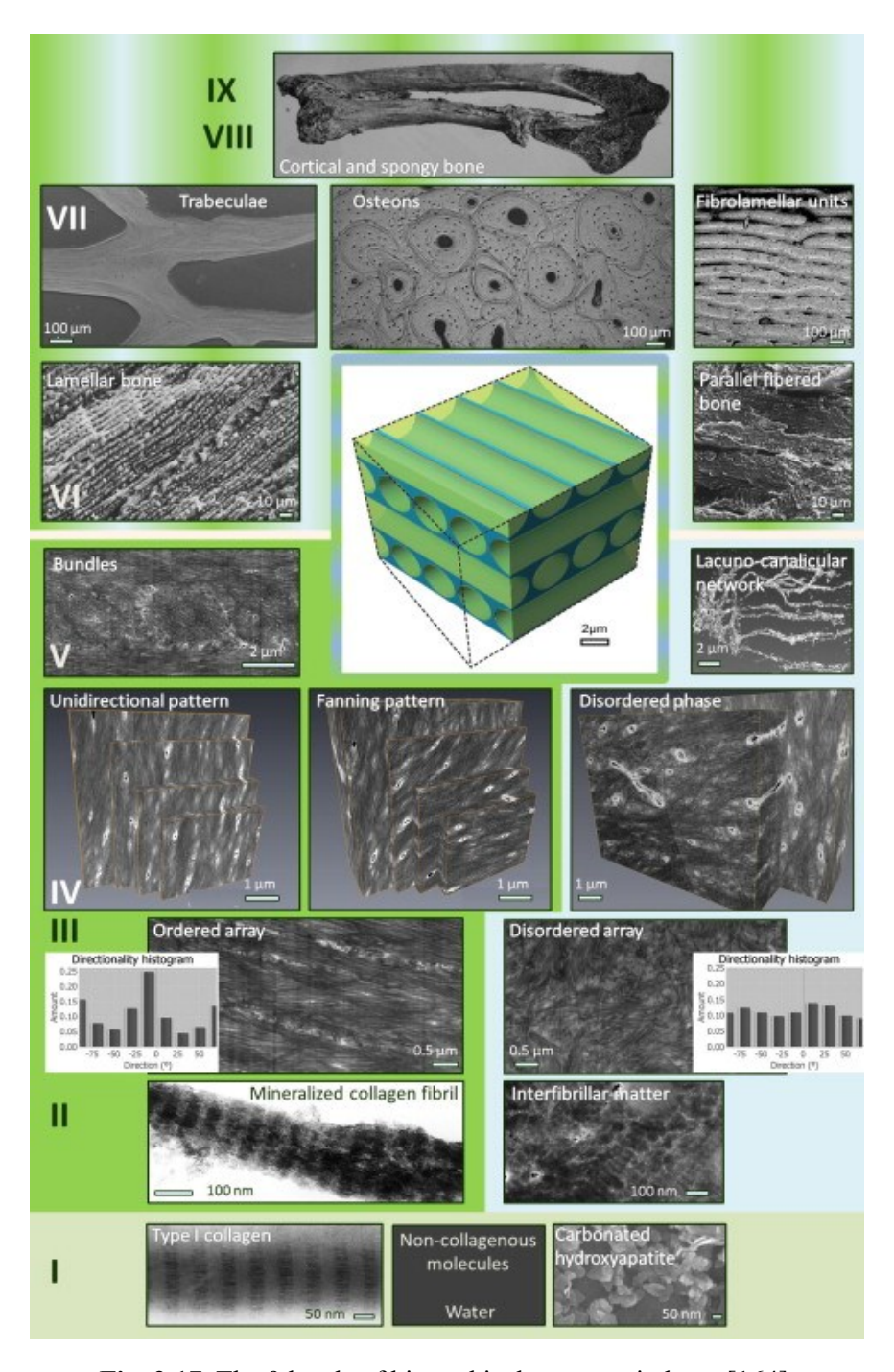


Fig. 2.17. The 9 levels of hierarchical structure in bone [164].

**Table 2.4.** Concentrations of ions in blood plasma [169].

	Na <sup>+</sup>	$\mathbf{K}^{+}$	$Mg^{2+}$	Ca <sup>2+</sup>	Cl	HCO <sub>3</sub>	HPO <sub>4</sub> <sup>2-</sup>	SO <sub>4</sub> <sup>2</sup> -
Blood plasma	142.0	3.6-5.5	1.0	2.1-2.6	95.0-107.0	27.0	0.65-1.45	1.0

## 2.3.3. HA nucleation and growth in bone

As previously discussed, HA crystals in bone are formed within and between collagen fibrils. This collagenous matrix, known as extracellular matrix (ECM), is thus the site where HA nucleates and grows. More specifically, it is generally believed that HA crystals start nucleating within the less dense hole zones (3-6 Å in width and 400 Å in) found within the collagen fibrils [170-174]. However, collagen itself is not able to initiate HA mineralization even though plasma (**Table 2.4**) is supersaturated with respect to HA, and many researchers have shown that a set of highly acidic, negatively charged non-collagenous proteins (NCPs), able to attract Ca<sup>2+</sup> and PO<sub>4</sub><sup>3-</sup> ions present in the body fluids, are required for the formation of HA on collagen [7, 8].

A relatively recent hypothesis is that collagen mineralization starts within matrix vesicles (MVs), round or oval-shaped entities with a diameter of approximately 100 nm or 30x300 nm, surrounded by a bilaminar membrane [175-177]. The MVs are released from the osteoblast cellular membranes, and migrate towards the ECM [178]. Although there is no general consensus [178, 179], it is believed the initial nucleation of minerals may first occur within the inner membrane of MV, where calcium would be attracted by the acidic phospholipids of the vesicle membrane and enters the membrane via an annexin channel. Phosphate can enter the vesicle membrane via a type III Na<sup>+</sup> dependent phosphate carrier [177, 179], and further increased in concentration by the action of alkaline phosphatase (AP) present within the MV membrane, which hydrolyzes pyrophosphate to inorganic phosphate [179]. Recent studies have shown that free phosphate in MVs can also be generated by the PHOSPHO1 enzyme, which can cleave phosphocholine and phosphoethanolamine. These molecules are the by-products of phospholipid degradation, which has been shown to occur extensively in MVs [178]. The initial HA crystals formed within the MV membrane grow until MVs rupture; after this, they are deposited on the collagenous ECM and exposed to extracellular body fluid, which contains sufficient Ca<sup>2+</sup> and PO<sub>4</sub><sup>3-</sup> ions to support further growth of HA [180]. Although the presence of MVs is now almost generally accepted, the extent of mineralization started by MVs is still unclear [179].

## 2.3.4. Role of collagen in bone mineralization

Although collagen cannot initiate mineralization, it certainly plays a role in this process. For example, the physical structure of collagen determines the size of the molecules that can penetrate into the water channels present within the fibrils, which contain the ionic precursors for HA nucleation [181]. Toroian et al showed that only molecules smaller than 6 kDa, such as osteocalcin, citrate, glucose, and etidronate, as well as calcium, phosphate, and pyrophosphate ions can move through the aqueous channels found within collagen type I fibrils, where HA forms. However, larger molecules such as fetuin, albumin, and dextran cannot penetrate into the collagen fibrils [181]. This finding can be extended to help our understanding of NCPs as important regulators of HA precipitation. Larger NCPs such as BSP would be able to induce extrafibrillar mineralization, while smaller NCPs such as osteonectin can actively induce mineralization within the hole zones, and start intrafibrillar mineralization [181]. Single AAs might therefore help intrafibrillar mineralization too, especially considering that some modeling studies have shown that AAs can fit within the hole zones of collagen matrixes [182].

In addition to its role as a framework for bone formation, some studies have also investigated the role of collagen in mineralization promotion. For example, using a combination of cryoTEM and modeling, Nudelman et al showed that charged AAs present both in the gap and overlap regions of collagen fibrils regulate collagen mineralization, including both the nucleation of ACP and its transformation to HA, and its orientation [182]. In addition, regions containing large concentrations of positively charged AAs were found to be crucial in determining the points where negatively charged ACP-poly Asp or ACP-fetuin complexes entered the collagen fibrils [182]. Landis and Silver investigated the molecular packing model of collagen fibrils and showed that the presence of charged AAs, such as Lys, Glu, and Arg in the vicinity of the hole zone of collagen fibrils creates a pocket that can accommodate and retain calcium and phosphate ions [183]. Overall, though, the specific domains of collagen involved in HA mineralization are not clear yet, and need further investigation [184].

### 2.3.5. Role of NCPs in bone mineralization

## 2.3.5.1. Glycoproteins

While many individual NCPs are involved in HA mineralization, a family of NCPs known as SIBLING (small integrin-binding ligand, N-linked glycoproteins) proteins are of particular importance. SIBLING proteins are a group of highly acidic proteins that play a key role in regulating HA precipitation in bone [8, 185-188]. A unique feature of SIBLING proteins is the presence of an acidic serine and aspartate-rich motif, known as ASARM motif. In addition to its acidic AAs, the ASARM motif contains several phosphorylated sites at serine residues, which play a critical role in HA nucleation and growth [189-191].

SIBLING family members include osteopontin (OPN), bone sialoprotein (BSP), matrix extracellular phosphoglycoprotein (MEPE), dentin matrix acidic phosphoprotein 1 (DMP1), and DPP (dentin phosphophoryn) [8]. These glycoproteins all contain an integrin binding tripeptide (Arg-Gly-Asp) and share similar phosphorylated and glycosylated sites [9]. SIBLING proteins are present ubiquitously in the bone matrix [9], but they are also present in non-mineralized tissues, such as salivary glands and kidneys [192]. This suggests many additional roles for these proteins; in fact, even in mineralized tissues their role is complex. This is attributed to the intrinsically disordered and flexible structure of these proteins, their extensive post-translational modifications, and their ability to interact with a variety of binding partners [193, 194].

MEPE is found in both bone and dentin and acts as a mineralization inhibitor [8]. MEPE is rich in serine phosphorylation sites and contains an RGD domain essential for integrin recognition. The ASARM peptide present at the C-terminal end is responsible for inhibiting mineralization by sequestering free calcium or binding to HA crystal surface through its phosphorylated residues [195-199]. PHEX (a phosphate-regulating gene with homologies to endopeptidases on the X chromosome), a proteolytic enzyme, can cleave the ASARM peptide and thus regulate MEPE activity. The loss of PHEX can lead to accumulation of ASARM peptides, which can bind to HA surfaces and prevent their further growth, thus resulting in defective bone mineralization (as found for example in osteomalacia) [195].

OPN is the most studied SIBLING due to its important role in HA mineralization and in other processes, such as immunology, inflammation, and cancer [9]. OPN is a potent mineralization inhibitor. This inhibitory action is achieved by the ASARM domains of OPN [8], which can bind to HA crystals and prevent the further precipitation of HA [200]. The high

flexibility of OPN structure may facilitate its adsorption to HA surface and promotes its inhibitory effect. While OPN is known for its inhibitory effect on HA mineralization [201, 202], it can also promote calcium phosphate precipitation in special circumstances, for example when it is crosslinked or bound to surfaces [203]. In these cases, HA nucleates on the aspartic acid-rich sequences of OPN, DDDDDDDDD in rats and DDEDDDD in humans [204]. The binary effect of OPN on HA mineralization is attributed to the fact that OPN is extensively post-translationally modified. Its phosphorylation and glycosylation state, its proteolytic processing by enzymes such as PHEX or thrombin, and whether it is crosslinked by enzymes such as transglutaminases affect its mineralization action [9].

BSP is the most abundant NCP in bone [8]. BSP has high affinity for calcium and it is a potent nucleator of HA owing to its polyglutamic acid regions, such as DSSEENGNGDSSEEEEEEETS located in the amino terminal half of the molecule [205-210]. Harris et al showed that the presence of at least eight consecutive glutamic acid residues is required for HA nucleation on BSP [211]. BSP also contain phosphorylated residues, but they are not as highly expressed as in OPN and they are fewer than thiol groups. Overall, the cooperative effect of phosphate, thiol, and carboxyl groups is responsible for the strong binding of BSP to HA [209, 210, 212, 213].

DMP1 and DPP are also highly acidic NCPs, and both are critical for the formation of normal teeth [9]. Two acidic domains at the C-terminal, ESQES and QESQSEQDS, play a critical role in HA mineralization by DMP1 [210]. These two peptides can form β-sheet structures in the presence of calcium ions, thus providing an ideal surface for the localized nucleation and growth of calcium phosphate. An important feature of DPP is the presence of DSS repeats throughout the molecule and of SD domains expressed at the C-terminal end [214]. Most of the serine groups in both DSS and SD domains are phosphorylated, thus strongly interacting with calcium ions and inducing calcium phosphate precipitation. However, in vitro studies show both DMP1 and DPP, when dissolved in solution, inhibit HA mineralization by sequestering calcium and phosphate ions [8].

In addition to SIBLINGs, there are also other individual glycoproteins that play important roles in body. For example, osteonectin is an acidic ECM glycoprotein that plays several roles in bone mineralization, cell-matrix adhesion, and collagen binding [215]. Osteonectin has four different domains: domain I is an acid domain rich in Glu. Domain II is rich in cysteine (Cys)

and contains N-Glycosylation sites. Domain III is a hydrophilic region with a high  $\alpha$ -helix content, and domain IV contains EF-hands (helix-loop-helix structural domains), which can bind Ca ions [216, 217]. The high affinity of osteonectin for Ca and HA surface is attributed to the Glu rich domains of osteonectin and the EF-hands [218], while the collagen binding and cell adhesion properties are assigned to domain III and IV, respectively [217].

Fibronectin is a high molecular weight ECM glycoprotein that binds to integrins and ECM components, such as collagen, fibrin, and heparin sulfate [9]. The main role of fibronectin is to improve cell adhesion, growth, migration, and differentiation, and it is important for processes such as wound healing [219]. However, studies demonstrate the ability of fibronectin to nucleate HA crystals even when dissolved in solution [220, 221]. The promoting effect of fibronectin on HA nucleation is attributed to the formation of fibronectin networks that can template HA nucleation and growth [220].

## 2.3.5.2. Proteoglycans

Proteoglycans are another major family of NCPs involved in bone mineralization [9, 222]. Proteoglycans are a heterogeneous group of proteins consisting of a core protein decorated by one or more covalently attached glycosaminoglycan chain. These side chains are long polysaccharides consisting of a repeating disaccharide unit. Common glycosaminoglycans include chondroitin sulfate, keratan sulfate, dermatan, heparin sulfate, and hyaluronan [9].

Proteoglycans can play different roles in mineralization depending on their molecular size [9]. Most studies show that small proteoglycans act as mineralization promoters. These proteoglycans usually carry chondroitin side chains. Mineralized matrixes, such as bone and dentin collagen, are often enriched in small leucine-rich proteoglycans (SLRPs), such as biglycan, decorin, fibromodulin, osteoadherin, and lumican. SLRPs promote bone mineralization by interacting with growth factors, such as fibroblast growth factor (FGF) and bone morphogenic proteins (BMPs), which play a key role in HA mineralization. Other small proteoglycans such as syndecan, serglycin, and glypican reside on the cell surface of many cells. They often contain heparan sulfate glycosaminoglycans and are involved in a variety of processes including, mineralization and cell adhesion [9].

On the other hand, large proteoglycans such as aggrecan are typically considered as mineralization inhibitors and they are usually found in high concentrations in matrixes that should remain unmineralized such as cartilage [9]. Large proteoglycans may inhibit

mineralization simply by covering the hole zones in collagen fibrils to prevent crystal nucleation [223], or by chelating calcium through their sulfate and carboxyl groups, thus reducing the available calcium necessary for calcium phosphate precipitation [9].

# 2.3.5.3. Gla-containing proteins

Osteocalcin is a small NCP involved in HA precipitation in bone and dentine, and is the only NCP whose crystallographic structure is known. The primary structure of osteocalcin is highly conserved among vertebrates, and it contains two or three residues of  $\gamma$ -carboxylated glutamic acid (Gla) responsible for its strong affinity for calcium ions [224]. Because of its Gla residues, osteocalcin has been also called bone Gla protein (BGP). Nuclear magnetic resonance (NMR) analysis has shown that osteocalcin has a  $\alpha$ -helical secondary structure in its folded state [225]. Hoang et al were able to find the X-ray crystallographic structure of this molecule; they showed that an extensively negatively charged surface of osteocalcin centered on helix  $\alpha$ 1 and containing three Gla residues together with an Asp residue coordinates five calcium ions in a spatial orientation that is complementary to calcium ions in the HA crystal lattice [226]. In addition, when osteocalcin is bound to HA surfaces, other regions including the carboxy terminus would be well oriented to interact with osteoclast [227] and osteoblast [228] cells, which are actively involved in bone resorption and deposition. Recent studies show that osteocalcin also plays a role in vascular calcification by stimulating the osteochondrogenic differentiation of vascular smooth muscle cells (VSMCs) [229, 230].

Matrix Gla protein (MGP) is another Gla-containing protein found in bone and cartilage ECM and in body plasma. Similar to osteocalcin, MGP has high affinity for calcium ions; however, MGP acts as an essential mineralization inhibitor in soft tissues, such as arteries and cartilage [231, 232]. The inhibitory action of MGP is associated with its Gla residues, which are located in the N-terminal half of the protein and can bind to HA surfaces [233]; however, the inhibitory mechanism of MGP is still unclear.

### 2.3.6. Serum-associated proteins

In addition to NCPs associated with ECM, many other NCPs are found in high concentration in blood plasma. Several of these proteins have been investigated for their interactions with HA. Albumin and fibrinogen are two abundant water-soluble proteins found in the plasma, both acting as inhibitors of HA precipitation. Albumin plays important roles, such as

regulating blood volume and acting as a carrier for lipophilic molecules. Unless it is immobilized, albumin can inhibit HA mineralization by complexing calcium ions [9]. Albumin can also stabilize the OCP phase thus preventing its conversion to HA [234]. Fibrinogen is a precursor for fibrin, a protein that is involved in blood clotting [9]. The presence of fibrinogen in solution delays ACP to HA transformation by adsorbing on ACP particles, thus overall inhibiting HA mineralization [235].

Statherin is a highly acidic protein in the saliva that strongly binds to HA surfaces and inhibits the formation of HA in mouth [149-152]. The acidic domain at the N-terminus of statherin interacts with HA surfaces [149-151] while the basic domains reduce protein-protein charge repulsion, thus increasing statherin packing density on HA surfaces [152]. Fetuin is another potent inhibitor of mineralization, found in blood plasma. Fetuin interacts with calcium and phosphate to form stable colloidal particles called calciprotein particles (CPPs), thus sequestering precursors for calcium phosphate precipitation [236, 237]. Price et al showed that due to its large size, fetuin cannot penetrate within the collagen fibrils; therefore, in the presence of fetuin, mineral growth is inhibited *outside* the collagen fibrils, and is restricted to interfibrillar zones where fetuin is absent [238]. The authors called this effect "mineralization by inhibitor exclusion", where selective mineralization of collagen matrix happens by excluding a macromolecular inhibitor from the hole zones within collagen fibrils.

## 2.3.7. HA inhibition in body by inorganic ions

There are many ions present in body fluids that can inhibit HA crystallization. The most prominent one is pyrophosphate (**Fig. 2.18**), produced by intracellular metabolic reactions. A transmembrane protein called ankylosis (ANK) regulates the intracellular to extracellular movement of pyrophosphate ions [239-241]. Extracellular pyrophosphates can be also produced by hydrolysis of extracellular nucleoside triphosphates [242]. Pyrophosphate is a potent mineral-binding ion and a strong inhibitor of both nucleation and growth of calcium phosphate [152-154, 243, 244]: pyrophosphate ions can bind to HA crystals and substitute for the phosphate ions in HA crystal structure, thus blocking the nucleation sites of calcium phosphate and inhibiting its further growth [244]. In addition to its direct binding to growing crystals, Addison et al showed that pyrophosphate can inhibit mineralization by at least two more mechanisms including the inhibition of tissue-nonspecific alkaline phosphatase (TNAP) activity and induction of OPN

expression [190]. In fact, if TNAP acts on pyrophosphate, it can cleave the ion into two phosphate ions, which in turn end up having a promoting effect on HA mineralization. [190].

Among metallic ions, Mg<sup>2+</sup> and Zn<sup>+</sup> are strong inhibitors of calcium phosphate nucleation and growth [148, 155]. This is explained by the role of these positively charged ions as substitutes for calcium ions in HA crystal structure and their interference with further growth of HA.

# 2.4. HA precipitation in the presence of AAs

AAs are organic molecules possessing an amine (-NH<sub>2</sub>) and a carboxylate (-COOH) functional group, along with a specific side-chain. Net uptake and release of AAs by cells is a complex process (Fig. 2.19), which depends on various factors, such as (a) the delivery (blood flow rate x AAs arterial concentration) of AAs to the tissue, (b) the activity of AA carriers in the cell membrane, which can transport the AAs into and outside of the cell, (c) the rate at which the substrate is synthesized and degraded within the cell, (d) the mass action gradients of the substrate across the plasma membrane [245].

Fig. 2.18. Chemical structure of pyrophosphate.

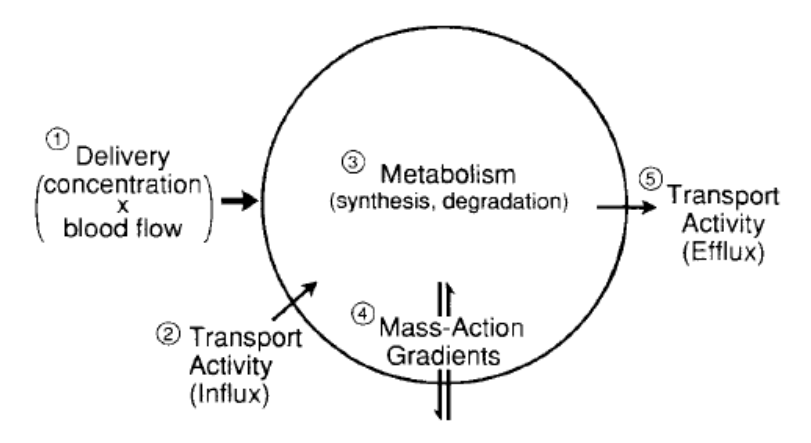


**Fig. 2.19.** Schematic showing the factors that can regulate the uptake and release of AAs by particular cells [245].

The transport of AAs into cells occurs via carrier-mediated processes that involve the binding of the AAs to a specific transporter protein that may contain several membrane spanning domains [245]. AAs can also diffuse into cells, but this mechanism of uptake is minor considering the low physiologic concentrations of AAs. Each carrier protein can transport a class of AAs (i.e., neutrals, positive, negative, or aromatics AAs) rather than one specific AA [245]. Many of these transporters require sodium for their maximal activity; initial binding of sodium ion increases the affinity of the transporter for AAs, thus forming a sodium/AA/transporter complex that can diffuse into cells. The high extracellular/intracellular sodium differential would improve the transport of AAs into cells. Efflux of AAs through sodium-dependent pathways cannot happen because of the inwardly directed sodium electrochemical gradient [245].

The transport of the majority of AAs across the cell membrane is clearly known to be a sodium dependent, carrier-mediated process [245]. There are still some AAs that can enter the cell by sodium-independent routes as well; however, this pathway is usually considerably slower than the sodium-dependent pathway. The transport of sodium-independent AA into or out of the cell depends on the relative concentrations of the AA inside and outside the cell. The direction of transport is usually determined by the AA gradient. For example, Arg is transported into the hepatocyte by a sodium-independent carrier; the movement is into the hepatocyte because the intracellular Arg concentration is very low compared to a circulating Arg concentration [245].

The average concentration of AAs in human blood in various vessels at fasting ranges between 6.3 and 7.4 mg/m³ [246]. However, body fluids passing though different organs contain various amounts of AAs depending on the activity of such organs. For example, Ishikawa et al reported that the overall concentration of AAs in chicken cartilage (18.3-55.3 mM) and muscle (44.3-114.7 mM) were generally higher than in serum (21.4 mM) and blood plasma (6.3 mM) [247]. More specifically, they showed that the concentrations of charged AAs, such as Arg, Asp, and Glu, which are strongly involved in mineralization, were 0.44, 3.76, and 15.37 mM in chicken hypertophic cartilage extracellular fluid (ECF) while it was 0.37, 0.06, and 0.16 mM, respectively, in blood plasma [247]. They reported that the pattern of AA uptake varied considerably among different cell types [247]. They also revealed that increasing the concentration of eight AAs (Asp, Glu, Tau, Ser, Asn, Gly, Ala, and Pro) in the culture medium to the level present in the native cartilage ECF remarkably stimulated the formation of AP and APrich MVs by chondrocytes [248]. Among these AAs Pro and Gly showed the weakest effect on

AP production while the combination of only two of the AAs, Ala and Glu, produced stimulatory effect on MV formation comparable to that seen in the presence of the eight AAs. Glu can form a-ketoglutarate, a tricarboxylic acid cycle intermediate by the action of the mitochondrial enzyme glutamate dehydrogenase, and Ala can be directly transminated to pyruvate, another important mitochondrial metabolite. Therefore, the effect of Ala and Glu on MV formation can be explained by the formation of mitochondrial metabolites than can interact with calcium ions, accumulate them, and finally release them. This is believed to be the key step in both MV formation and initiation of mineralization [249]. In summary, this study revealed that the level of specific AAs in the cartilage ECF is not only critical for the growth of the chondrocytes, but also it is important for the formation of MV [248]. However, the local environment of cells in-vivo varies significantly from cell to cell; therefore, this finding cannot be generalized to all cell types and further studies are required to determine the composition of media in which the response of various cell types can be achieved [248].

AAs are the building blocks of proteins, and negatively charged AAs such as Glu and PSer, and Asp are highly expressed in the acidic domains of NCPs involved in HA mineralization in bone and dentine. In vitro studies show that charged AAs have very different effects on HA crystallization if they are dissolved [10, 34, 36-46] or bound to a surface [47]. AAs dissolved in a solution can either chelate the Ca<sup>2+</sup> and PO<sub>4</sub><sup>3-</sup> ions in solution or cover the surface of nascent HA nuclei, thus inhibiting its further growth [10, 34, 36-46]. On the other hand, AAs bound to surfaces are able to promote HA crystallization by attracting Ca<sup>2+</sup> and PO<sub>4</sub><sup>3-</sup> ions, thus creating a local supersaturated environment that promotes heterogeneous nucleation of HA [47].

### 2.4.1. AAs dissolved in solution

### 2.4.1.1. HA nucleation and growth

**Tables 2.5 and 2.6** summarize studies on HA precipitation in the presence of AAs (see **Fig. 2.20** for their chemical structures) dissolved in solution. Most of these studies focus on the effect of AAs on HA growth rather than its nucleation. Also, these experiments are usually conducted under non-physiological conditions. As it is evident from **Table 2.6**, almost all AAs are able to inhibit both HA particle growth and crystal growth irrespective of their electrical charges. However, charged AAs, such as Glu, Asp, Arg, and Lys show a significantly stronger effect than non-charged ones [10, 11, 34]. This is related to the presence of stronger interactions

between charged AAs and  $Ca^{2+}$  and  $PO_4^{3-}$  ions, as well as with the surface of HA particles already formed in solution.

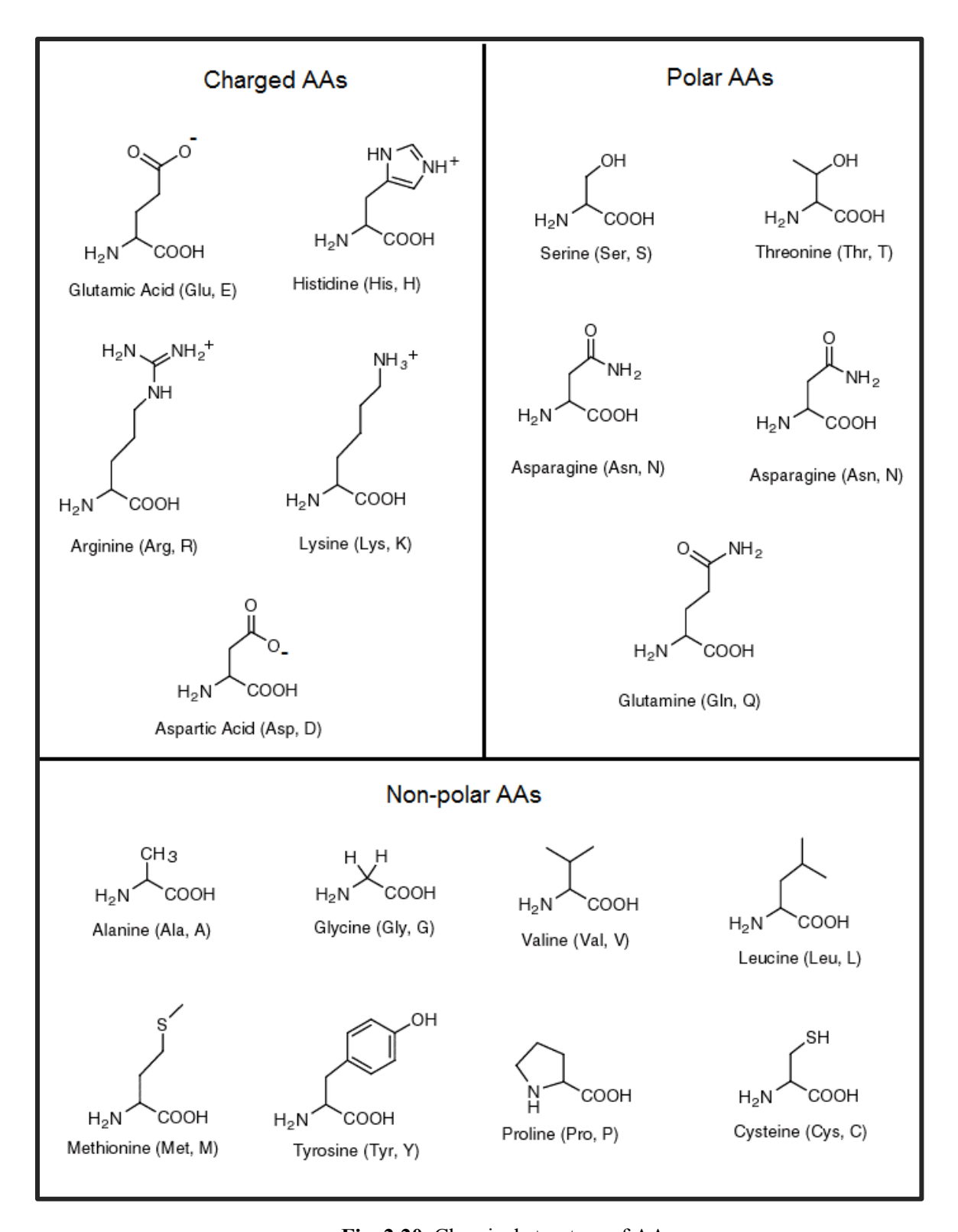


Fig. 2.20. Chemical structure of AAs.

 Table 2.5. Review of HA syntheses in the presence of AAs in solution.

Year	Ca Source (Conc. (mM))	P Source (Conc. (mM))	AAs (Conc. (mM))	Method	pН	Temp.	Time (h)	References
2011	CaCl <sub>2</sub> (0.5)	KH <sub>2</sub> PO <sub>4</sub> (0.3)	Asp, Glu (0.2)	const. comp.	8.45	25	48-96	Chu et al [32]
2009	(CH <sub>3</sub> COO) <sub>2</sub> Ca (75)	H <sub>3</sub> PO <sub>4</sub> (50)	Ala, Arg, Asp (150)	conventional	10 (cts)	RT	24	Palazzo et al [11]
2007	Ca(NO3) <sub>2</sub> .4H <sub>2</sub> O (-)	Orthophosphoric acid (-)	Gly, Ala, Ser, Lys, Asn (-)	conventional	9	80	18	Jack et al [10]
2007	CaCl <sub>2</sub> (0.25-0.5)	KH <sub>2</sub> PO <sub>4</sub> (0.17-0.33)	Leu (0-1.52)	const. comp.	7.4 (cts)	37	-	Dalas et al [40]
2007	CaCl <sub>2</sub> (3.2)	Na <sub>2</sub> HPO <sub>4</sub> (0.96)	Gly, Glu (40)	conventional	9.5 (cts)	37	720	Pan et al [250]
2007	CaCl <sub>2</sub> (2)	Na <sub>2</sub> HPO <sub>4</sub> (1.2)	Gly, Glu (11)	conventional	9 (cts)	37	24	Tao et al [251]
2006	Ca(NO <sub>3</sub> ) <sub>2</sub> (33.4-38)	(NH <sub>4</sub> )2HPO <sub>4</sub> (20)	Gly, Asp, Glu, Lys (4)	conventional	7.5	37	24	Rosseeva et al [252]
2004	Ca(NO3)2 (1000)	(NH <sub>4</sub> ) <sub>3</sub> PO <sub>4</sub> (333.33)	Gly, Ala, Val, Asn, Ser, Lys, Arg, Asp (166.67)	conventional	9 (cts)	80	16	Gonzalez et al [34]
2002	Ca(CH <sub>3</sub> COO) <sub>2</sub> (100)	(NH <sub>4</sub> ) <sub>2</sub> HPO <sub>4</sub> (60)	Gly, Ala, Pro, Hydroxy- Pro, Ser, Val, Thr, Met, Asp, Glu, Arg, His (500)	conventional	7.4	60	-	Matsumoto et al [37]
2001	CaCl2 (0.25-0.5)	KH <sub>2</sub> PO <sub>4</sub> (0.17-0.33)	Gly, Cys, Gln (0-0.66)	const. comp	7.4 (cts)	37	-	Koutsopoulos et al [45]
2000	CaCl <sub>2</sub> (0.25-0.5)	KH <sub>2</sub> PO <sub>4</sub> (0.17-0.33)	Ala, Phenyl-Ala, Pro, Met (0-2.25)	const. comp	7.4 (cts)	37	-	Koutsopolos et al [38]
2000	CaCl <sub>2</sub> (-)	KH <sub>2</sub> PO <sub>4</sub> (-)	Glu, Asp (-)	const. comp.	7.4 (cts)	37	-	Koutsopolos and Dalas [44]
2000	CaCl <sub>2</sub> (-)	KH <sub>2</sub> PO <sub>5</sub> (-)	Ser, Tyr, Hydroxy-Pro (-)	const. comp.	7.4 (cts)	37	0.5-12	Koutsopolos and Dalas [43]

Table 2.6. Particle and crystal size of HA synthesized in the presence of AAs dissolved in solution.

A	HA par	ticle size	HA crys	D.f	
Amino acids	Width (nm)	Length (nm)	D <sub>002</sub> (nm)	D <sub>310</sub> (nm)	References
	15±3	25±5	23±5	9±3	[11]
None	28±1	258±6	-	-	[10]
	20	80	36	8	[34]
Apolar	Width (nm)	Length (nm)	D <sub>002</sub> (nm)	D <sub>310</sub> (nm)	References
Clv	29±1	162±1	-	-	[10]
Gly	8	80	16	5.5	[34]
	15±3	25±5	18±2	6±2	[11]
Ala	30±1	96±2	-	-	[10]
	8	60	18.5	6.5	[34]
Val	5	50	-	-	[34]
Uncharged polar	Width (nm)	Length (nm)	D <sub>002</sub> (nm)	D <sub>310</sub> (nm)	References
	Width (nm)	Length (nm)	<b>D</b> <sub>002</sub> (nm)	<b>D</b> <sub>310</sub> (nm)	References [34]
polar Asn				` ′	
polar	8	50	15	5	[34]
polar Asn	8 29±1	50 118±3	15	5 -	[34]
polar Asn Ser Charged polar	8 29±1 5	50 118±3 25	15 - 14	5 - 4.5	[34] [10] [34]
Asn Ser Charged	8 29±1 5 Width (nm)	50 118±3 25 Length (nm)	15 - 14 <b>D</b> <sub>002</sub> (nm)	5 - 4.5 <b>D</b> <sub>310</sub> (nm)	[34] [10] [34] References
Asn Ser Charged polar	8 29±1 5 Width (nm) 6±2	50 118±3 25 Length (nm) 70±5	15 - 14 <b>D</b> <sub>002</sub> (nm) 19±2	5 - 4.5 <b>D</b> <sub>310</sub> (nm)	[34] [10] [34] References
polar Asn Ser Charged polar	8 29±1 5 Width (nm) 6±2 8	50 118±3 25 Length (nm) 70±5 80	15 - 14 <b>D</b> <sub>002</sub> (nm) 19±2 21	5 - 4.5 <b>D</b> <sub>310</sub> (nm) 6±2 7	[34] [10] [34]  References  [11] [34]
Asn Ser Charged polar Arg	8 29±1 5 Width (nm) 6±2 8 6±2	50 118±3 25 Length (nm) 70±5 80 70±5	15 - 14 <b>D</b> <sub>002</sub> (nm) 19±2 21	5 - 4.5 <b>D</b> <sub>310</sub> (nm) 6±2 7	[34] [10] [34]  References  [11] [34] [11]

AA/HA surface interactions have been extensively studied [10, 34, 38, 40, 43-45]. In general, AAs show an increase in adsorption to HA surfaces based on the charge of their side groups: apolar (Ala) < positively charged (Lys) < polar (Ser) < negatively charged (Asp) [34]. Koutsopoulos and Dalas conducted a number of studies on the affinity of various AAs to HA surfaces [38, 40, 43-45]. They showed that a negatively charged AA, Asp, has the highest affinity for HA (**Table 2.7**). However, Jack et al measured a stronger affinity to HA for a positively charged AA, Lys, and attributed this to the decrease in repulsion between the net negative charge of HA surface and any negatively charged segments on the AA side chains [10]. Despite their differences, both these sets of results imply a stronger effect of charged (positive or negative) AAs, such as Arg and Asp on inhibiting HA precipitation. Among the non-charged AAs, tyrosine (Tyr) and phenylalanine (Phe) show the largest affinity constant and strongest inhibiting effect on HA particle growth, respectively [38, 43]. This was attributed to the presence of an aromatic ring on Tyr and Phe side groups. This aromatic ring can lay down on the HA surface, possibly acting as an electron donor and creating a weak bond with the HA surface.

**Table 2.7.** Affinity constants for various amino acid inhibitors of HA crystal growth [40].

Inhibitor	K <sub>aff</sub> x 10 <sup>2</sup> L/mol
Alanine	2.86
phenylalanine	24.39
Proline	5.74
Methionine	6.21
Lysine	8.77
Aspartic acid	41.66
Glutamic acid	30.21
Serine	9.01
Tyrosine	30.30
4-Hydroxyproline	7.46
Cysteine	6.64
Glutamine	34.72
Glycine	17.14
Leucine	20.26

In addition to affinity constants, geometrical factors must be taken into account to determine the inhibitory effect of AAs on HA crystal growth. Adsorbed AAs can rotate freely around an axis perpendicular to the crystal surface and thus the effective volume of adsorption can be described by a cone. For example, for Asp and Glu, the projection of the cone onto HA surface is a circle of radius 3.32 and 5.23 Å, respectively [253]. This implies that the adsorbed Glu molecules cover a larger part of the HA crystal surface compared to Asp, and thus are more effective in inhibiting HA growth. Asp, on the other hand, has a higher affinity for the HA surface. So, it can be hypothesized that these two phenomena act simultaneously and result in a comparable inhibitory effect of the two acidic AAs against HA crystal growth.

In summary, AAs dissolved in solution are able to inhibit HA precipitation and growth. Polar AAs with negatively or positively charged groups generally show the strongest inhibitory effect on HA precipitation; however, the inhibitory effect of nonpolar AAs is not negligible either.

The inhibitory effect of AAs on HA nucleation and growth results from a few key factors:

- 1. The electrostatic interactions or the stability of complexes formed between the AAs and  $Ca^{2+}$  and  $PO_4^{3-}$  ions present in the precipitation solution [10, 38, 43-45].
- 2. The affinity of AAs to HA particle surfaces. This factor itself depends on:
  - a. Electrostatic interactions between AAs and HA particles. This includes both the electrostatic interaction between the net charges of AAs and HA surface as well as the interaction between specific segments of the AAs and HA particles. For example, although AAs usually interact through their COOH groups with calcium ions present on HA, a positively charged AA such as Lys shows a high affinity with the HA probably because overall it is less repelled by the negatively charged HA surface [10].
  - b. Possibility of forming chemical bonds between specific segments of AAs and HA surfaces. For example, among the polar AAs, Tyr shows the highest affinity to HA because it has an aromatic ring that can act as a  $\pi$ -electron donor and form a stronger bond with the HA surface [43].
  - c. Stereochemical and geometrical properties of AAs; for example, the presence of aromatic rings in Phe and Tyr increases their affinity to HA [38, 43].
- 3. Surface coverage ability of AAs. This mainly depends on geometrical factors; for example, Glu can cover a larger fraction of HA surface than Asp [253].

## 2.4.1.2. HA phase transformation and morphology

A few studies investigate the effect of AAs on HA morphology or transformation [32, 37, 254]. Tao et al showed that the addition of Gly in a solution where HA is nucleating can result in the formation of one-dimensional rod-like crystals, while two-dimensional plate-like crystals are obtained in the presence of Glu (**Fig. 2.21**). They suggested a brick and mortar model where an amorphous phase, ACP, acts as mortar and cements the bricks of rod-like or plate-like HA crystals to make enamel-like or bone like HA, respectively [254]. Matsumoto et al found flake-like particles consisting of nano-sized platelets for HA precipitation in the presence of AAs, such as Gly, Ser, Asp, and Glu (**Fig. 2.22**). The flake-like morphology was also observed on the control sample; however, the platelets on this sample were larger and thicker than those observed in the presence of AAs. These AAs reduced the degree of the crystallinity of the HA precipitate by stabilizing ACP [37].

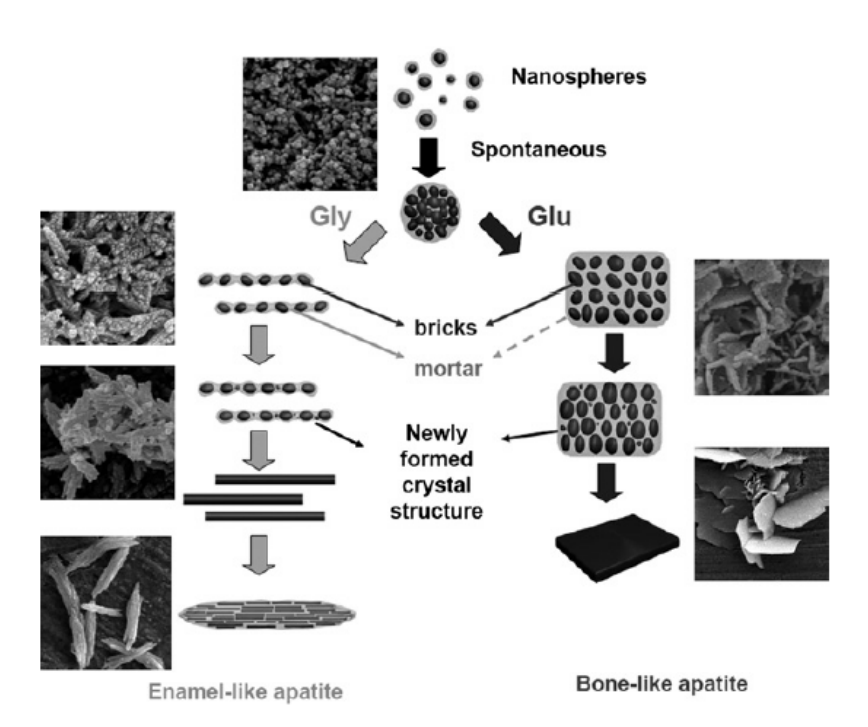


**Fig. 2.21.** Different pathways for HA precipitation in a bricks (HA) and mortar (ACP) configuration in presence of Glu and Gly [254].

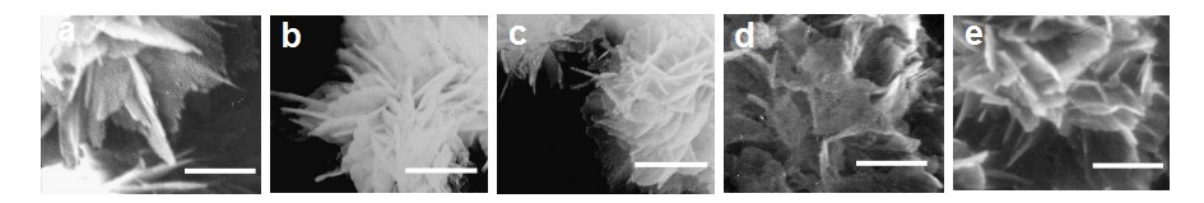


**Fig. 2.22.** SEM images of the HA crystals synthesized without any AAs (a) or in the presence of Gly (b), Ser (c), Asp (d), and Glu (d). Scale bar: 300 [37].

Chu et al showed that the acidic AAs, Asp and Glu, can improve brushite to HA phase transformation by reducing the interfacial energy barrier between brushite and HA (Fig. 2.23) [32]. Since HA is a basic calcium phosphate, its formation from acidic phases such as brushite is not usually favored. Chu et al attributed this to the higher solid/liquid interfacial energy of HA than brushite, which would make the brushite to HA transformation thermodynamically unfavorable. This was even more significant in Chu's study, since HA grew in the form of small crystallites with a high surface area, while the initial brushite seeds were much larger. However, Chu et al showed that Glu and Asp, if added to the reaction solution, adsorbed on the brushite surface and increased its interfacial energy to a value closer to that of HA, thus favoring HA nucleation on brushite surface.

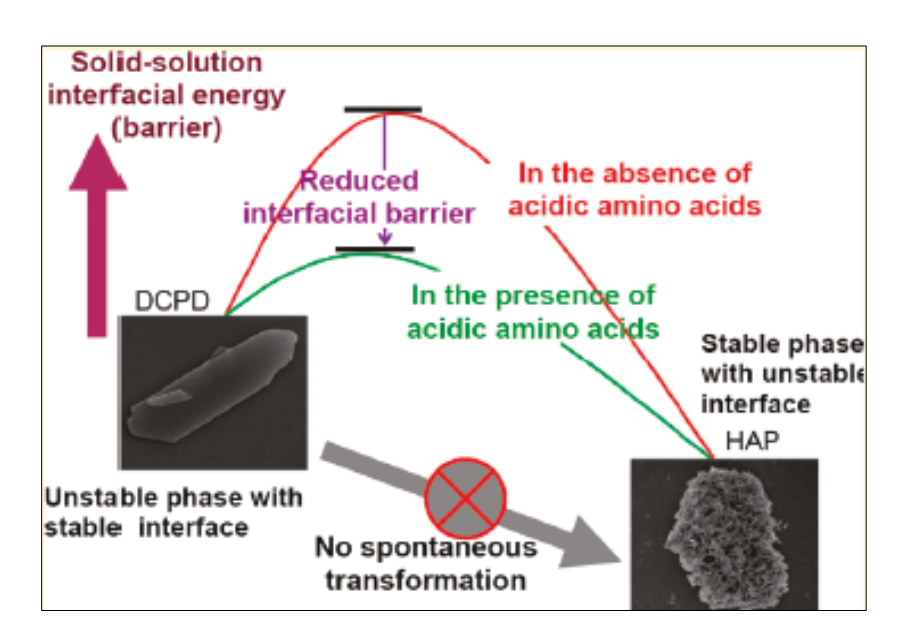


**Fig. 2.23**. Schematic showing the reduced interfacial energy barrier between DCPD and HA in the presence of acidic AAs [32].

## 2.4.2. AAs bound to surfaces

Template-directed precipitation is defined as precipitation in the presence of functionalized surfaces [255-258]. Functional groups with electrical charges are able to promote calcium phosphate precipitation [259-263]. This is attributed to the ability of these functional groups to attract Ca<sup>2+</sup> and PO<sub>4</sub><sup>3-</sup> ions, thus increasing the degree of local supersaturation with respect to calcium phosphate precipitation at regions close to the surfaces [259, 262].

While there have been many studies investigating the inhibitory effect of AAs dissolved in solution on HA mineralization [10, 34, 36-46], the effect of AAs or small molecules with similar functional groups bound to surfaces has been subject of just a few studies [47, 58, 59]. Rautaray et al investigated HA precipitation in the presence of Asp-capped gold nano particles [47] (Fig. 2.24). They showed that HA precipitation was promoted in the presence of Asp due to the interaction between COOH groups in Asp and the Ca2+ ions. Using isothermal titration calorimetry (ITC), they showed the interaction between Ca<sup>2+</sup> and Asp was favored thermodynamically. Other researchers have focused on the effect of surface functional groups with different electrical charges on HA precipitation. Zhu et al prepared self-assembled monolayers (SAMs) of silanes with NH<sub>2</sub> and OH functional groups on silicon to investigate the effect of positively vs. negatively charged surfaces on HA precipitation [259]. They showed that HA precipitation was faster in the presence of the negatively charged OH-SAM than the positively charged NH<sub>2</sub>-SAM. Similar results were obtained on gold substrates. Tanahashi et al investigated HA formation on gold modified with SAMs of alkanethiols terminated with neutral, negative and positive groups, such as CH<sub>3</sub>, PO<sub>4</sub>H<sub>2</sub>, COOH, CONH<sub>2</sub>, OH, and NH<sub>2</sub> [262]. They showed that negatively charged functional groups were the most potent enhancers of HA precipitation (PO<sub>4</sub>H<sub>2</sub> first and then COOH), while SAMs terminated with positively charged groups such as CONH2 and NH2 induced much less HA precipitation. Liu et al explored more in detail the effect of negatively charged groups, such as OH, PO<sub>4</sub>H<sub>2</sub>, and COOH bound to titanium foil [261], and showed that poorly crystalline calcium phosphate was precipitated in the presence of COOH and PO<sub>4</sub>H<sub>2</sub> functional groups. However, consistent with the study by Zhu et al [262], PO<sub>4</sub>H<sub>2</sub> exhibited a stronger nucleating ability than COOH. The control titanium sample and the OH modified sample showed less calcium phosphate deposition than the COOH and PO<sub>4</sub>H<sub>2</sub> modified samples [261].

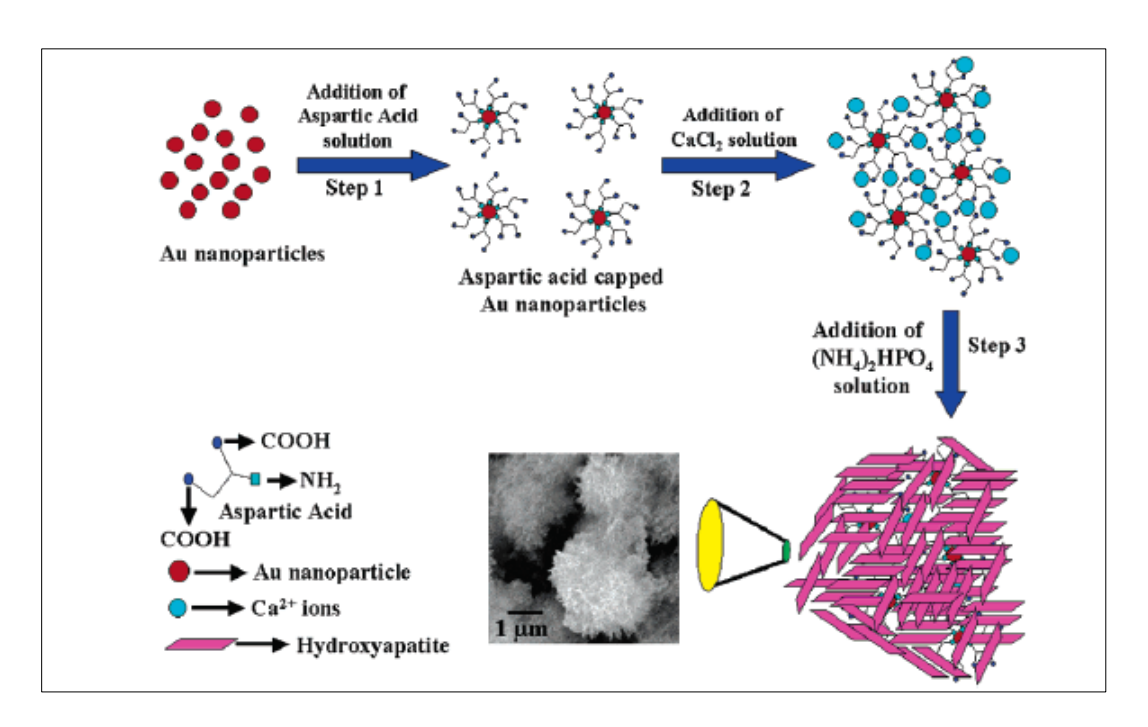


**Fig. 2.24.** Schematic showing the steps involved in the precipitation of HA in the presence of Asp-capped gold nano particles [47].

While most of the works done so far indicate that negatively charged functional groups are more effective than positive or neutral groups in inducing heterogeneous nucleation of HA [259, 262], there is at least one study showing different results: Zhang et al investigated HA precipitation in the presence of PO<sub>4</sub>, COOH, and NH<sub>2</sub> functional groups present on Langmuir monolayers made of dipalmitoylphosphatidylcholine, arachidic acid, and octadecylamine, respectively [264]. They showed that all PO<sub>4</sub>, COOH, and NH<sub>2</sub> functional groups promoted the nucleation of calcium phosphate to very similar extents [264]. However, the Ca/P ratio for the calcium phosphates formed in the presence of PO<sub>4</sub> was similar to that of HA (1.67) while COOH (1.49) and NH<sub>2</sub> (1.60) showed lower Ca/P ratios indicating the presence of amorphous calcium phosphate (ACP) precursor.

### 2.4.3. Poly amino acids and peptides

To better understand the role of the AAs present in the proteins involved in HA mineralization, a number of studies have been conducted on poly-AAs and peptides with residues that are abundant in body proteins [48, 187, 265-267]. Poly-Glu and poly-Asp are among the strongest inhibitors of HA growth when dissolved in solution, but they can act as HA

nucleators when adsorbed on a surface [39]. However, cross-linked poly-Glu can induce the heterogeneous nucleation of hydroxyapatite even when present in SBF. Phosphorylated residues are responsible for the inhibitory effect of statherin-like pentapeptides dissolved in solution [268]. This can explain the role of statherin as an inhibitory protein in the saliva. In general, all these studies elucidate the important role of negatively charged AAs, such as PSer, Glu, and Asp on regulating HA mineralization.

## 2.4.4. AA/HA interactions investigated by computational techniques

A molecular understanding of the interactions between AAs and HA is crucial to grasp the details of biomineralization. However, the molecular-level details of biomineralization are difficult to investigate by experimental techniques exclusively. In the last decades, sophisticated experimental techniques have been successfully coupled with computational techniques to model the mineralization of HA in the presence of AAs [41, 130, 250, 269].

Molecular dynamic (MD) simulations can investigate organic-inorganic interfaces at the atomic level; therefore, it can provide useful information relative to the adsorption energy and adsorption sites of AAs to HA. Zhang et al used MD simulations to investigate the adsorption of the different types of AAs on the (100) face of HA [41]. Their results indicate that the AAs occupy the vacant Ca and P sites of the growing HA (100) surfaces mainly through their amino and carboxylate groups, thus inhibiting HA growth along [100] direction. They showed that small and charged AAs, such as Gly, Glu, and Asp have a higher adsorption on HA, which was consistent with the experimental findings by Koutsapolous et al [43, 44, 270]. Pan et al. investigated the specific adsorption sites of Gly and Glu on the (100) and (001) faces of HA crystals at the atomic level using MD simulations [250]. Consistent with the results by Zhang et al, they showed that both Gly and Glu can bind to HA (001) and (100) faces through their amino groups. These groups occupy the vacant calcium sites, while carboxylate groups replace the phosphate or OH sites. However, they showed the adsorption of Glu was higher on the (001) face, while Gly did not have a preferential adsorption on a specific face.

Ab-initio density functional theory (DFT)-based calculations can model systems at the atomic level without needing to know force-fields such as MD. Almora-Barrios et al employed DFT to show that Gly, proline (Pro), and hydroxyproline (Hyp) (the main constituent AAs of the collagen matrix) showed a preferential adsorption to the (100) faces of HA rather than the (001) faces. This was due to the interaction between the AA carboxylate groups and the calcium ions

on HA; Hyp showed the strongest adsorption [269]. The preferential adsorption of AAs to (100) faces could explain why the HA crystals are elongated in the c-direction, as observed in bone.

Corno et al investigated in more detail the interaction of differently charged AAs, Gly, Glu, and Lys with HA surfaces again using DFT calculations [130]. They showed that Gly interacted with the (001) surface in its zwitterionic state, with the carboxylate group interacting electrostatically with the calcium ions and the amino group forming hydrogen bond with the oxygen atoms. However, Gly had a higher affinity for the (010) HA surface, where it was adsorbed as an anion as a result of spontaneous proton transfer towards the surface. Lys interacted very similarly with both the (001) and the (010) surfaces: the amino group of its side chain bound to the closest calcium ions. The behavior of Glu was more dependent on the surface: on the (001) surface, the carboxylate group of the side chain interacted with the closest calcium ions and formed H-bond with the surface P=O groups. On the (010) surface, however, the carboxylate groups of Glu could only form a relatively weak H-bond with the P-O moieties present on the (010) surface. In summary, the affinity of the studied AAs for the (001) surface followed the trend Gly < Lys < Glu, and for (010) surface, Gly < Glu < Lys.

Addison et al used RosettaSurface Monte-Carlo based simulations to simulate the adsorption of the VTKHLNQISQSY peptide to HA; the affinity of this peptide to apatite-based materials was previously discovered by phage display [271]. They showed that the peptide/apatite adsorption was primarily determined by the composition and net charge of the AAs rather than their order in the peptide sequence. In fact, the phosphorylated serine residues were mainly responsible for the adsorption of the peptide to HA.

Overall, consistent with experimental data, computational techniques discussed in this paragraph showed that charged AAs, such as Glu and phosphorylated Ser, have the highest affinity for HA surfaces.

### 2.4.5. AA interaction with calcite vs hydroxyapatite

Calcite is one of the most studied biominerals due to its abundance in marine organisms and its readily available large crystals (>10 cm) that allow researchers to investigate the specific interaction of biomolecules with them [272]. Similar to HA, calcite crystal surfaces have high affinity for AAs and larger biomolecules. However, differently from HA, calcite crystals possess a mirror symmetry and terraced growth features, which are potential for chiral selectivity, thus resulting in the D- or L-enantiomers of AAs showing selective adsorption on different surfaces

of the crystals. Hazen et al showed that the selective adsorption of AAs is greater on step-like features, resulting in the linear arrays of homochiral AAs forming on calcite surface [272]. Combining atomic force microscope observations and molecular modeling studies, Orme et al investigated the selective adsorption of a negatively charged AA, Asp, in more detail. They showed that the binding of Asp to the surface step-edges of calcite allows for the best geometric and chemical fit, thus minimizing the step free energy and modifying the crystal macroscopic shape [273]. Their results indicated that the binding of Asp to the (104) surface of calcite involves all charged groups of the molecule, and there is approximately no energy difference between the interactions of the D- or L-forms of Asp, because both adsorbates can rotate freely to maximize their binding energy. However, D- and L-Asp adsorb on opposite acute steps following their best geometrical fits, thus resulting in the symmetrical growth of calcite crystal. The glide plane symmetry can be broken if only one of the two Asp enantiomers is present during crystal growth stage.

Overall, similar to HA system, most of the studies on calcite biomineralization are focused on the negatively charged biomolecules due to their abundance in calcite biominerals. These studies indicate that the peptides or proteins bind to calcite surface through the intention between their negatively charged AA residues and calcium ions present on calcite surfaces [274-276]. However, there is at least on study highlighting the important role of positively charged sequences on calcite/peptide interactions. Masica et al showed that calcite interacted more strongly with the positively charged AA sequence of a chemically synthesized peptide than the negatively charged sequences [277].

# **CHAPTER 3**

# STATEMENT OF THE PROBLEM

Many researchers studied the effect of AAs on HA precipitation; however, most of the work was conducted on the growth stage of HA, while the effect of AAs on nucleation and prenucleation stage of HA precipitation is still quite unexplored. Moreover, these studies are usually conducted in non-physiological conditions, which make it difficult to have a real insight into the effects of these AAs on HA precipitation in body. Also, while it is generally accepted that negatively charged AAs such as Glu, Asp, and PSer are crucial components of the NCPs that regulate HA precipitation, different authors report contradictory results on the effect of differently charged AAs on HA precipitation. So, the effect of individual AAs and the dominant role of negatively charged ones are still strongly debated. Finally, most works are focused on the effect of AAs dissolved in solution, while the AAs which are involved in bone formation in body are either part of the ECM, a solid matrix secreted by the cells, or of the NCPs, which are strongly interacting with the ECM mineral.

The goal of this thesis is to clarify the effect of differently charged AAs on HA precipitation in physiological conditions, and to explore the mechanism under which these AAs regulate HA precipitation. The AAs were either dissolved in solution or bound to a surface. We used Arg as a model for a positive AA and Glu as a model of a negative AA, and graphene oxide as a model surface. Both Glu and Arg were present in NCPs and play an important role in HA mineralization in body. Graphene oxide is a highly oxidized form of graphene with various surface functional groups that make it easily modified. Also, GO has high a surface area, which favours the heterogeneous nucleation of HA.

Our results are reported in Chapters 4, 5 and 6 in the form of three papers, either published or submitted. Chapter 4 describes the effect of Arg and Glu dissolved in solution on HA

precipitation. In contrast to what is generally accepted, we showed a stronger effect for the positively charged AA, Arg, on inhibiting HA precipitation. We explained this in terms of the stability constants of complexes formed between the AAs and the precursor ions. The AAs also affected the morphology and crystallinity of the HA precipitate. More organized HA platelets with higher degree of crystallinity were obtained in the presence of AAs, especially Arg.

Chapter 5 describes the effect of Arg and Glu on HA nucleation and prenucleation. We observed aging of Ca- and P-precursor solutions for 3 days promoted the inhibitory effect of the AAs, and explained this by invoking the formation of Ca/AA and P/AA aggregates from initial Ca/AA and P/AA complexes. These aggregates, which form in the AA-containing Ca- and P-precursor solutions before they are mixed for HA precipitation, confirm the critical role of AAs on regulating HA precipitation even before the nucleation stage.

Chapter 6 investigates the promoting effect of AAs bound to GO. Here we show that Arg bound to GO promotes HA precipitation more than Glu, again showing a more important role for positively rather than negatively charged AAs on HA precipitation. We explained these results based on the electrostatic interactions and stability constants of complexes formed between the AAs and Ca<sup>2+</sup> and PO<sub>4</sub><sup>3-</sup> ions. At the end, we propose Arg/GO as a potential candidate for bone or dentin regeneration applications.

Overall, this work provides a basis to understand the effect of single AAs on HA mineralization in physiological conditions, and possibly informs a strategic rational approach for the design of oligopeptides or surface coatings with the purpose of inhibiting or promoting HA nucleation. These biomolecules could be used to treat pathological diseases caused by an excessive mineralization of HA in tissues like cartilage, blood vessels and cardiac valves, or, vice versa, to promote HA mineralization to repair in damaged bone or teeth.

# **CHAPTER 4**

# HYDROXYAPATITE PRECIPITATION IN THE PRESENCE OF THE AMINO ACIDS, ARGININE AND GLUTAMIC ACID, DISSOLVED IN SOLUTION

AAs are the building blocks of NCPs, which are proteins that (among other functions) inhibit undesirable precipitation of HA in body. Many studies investigate the effect of AAs dissolved in solution on HA precipitation; however, most of these studies are focused on the effect of AAs on HA growth rather than its nucleation, and are conducted in conditions that are far from the physiological ones. Moreover, these studies report contradictory results in terms of the inhibitory effect of differently charged AAs.

In this work we investigated the inhibitory effect of Arg (positive AA) and Glu (negative AA) on HA nucleation and growth in physiological conditions. While negatively charged AAs, such as Glu, are highly expressed in the NCPs, positively charged AAs are present in lower concentrations in NCPs, but may still be involved in NCP activity. Our goal was to explain the mechanism under which these AAs can inhibit HA precipitation in body. These inhibitory AAs can be potentially used for treating pathological diseases caused by the excessive mineralization of HA in body.

This work is reported in an article published in the "Journal of The Royal Society Interface".

## The importance of amino acid interactions in the crystallization of hydroxyapatite

<b>M</b> .	<b>Tavafoghi</b>	i Jahromi	G. Y:	ao, M.	Cerruti
-			,		

Materials Engineering, McGill University, Montreal, QC, Canada, H3A 2B2

Emails: maryam.tavafoghijahromi@mail.mcgill.ca; guanhan.yao@mail.mcgill.ca; marta.cerruti@mcgill.ca

Keywords: Hydroxyapatite, L-arginine, L-glutamic acid, inhibitory effect, precipitation, mechanism.

#### 4.1. Abstract

Non-collagenous proteins (NCPs) inhibit hydroxyapatite (HA, Ca<sub>5</sub>(PO<sub>4</sub>)<sub>3</sub>OH) formation in living organisms by binding to nascent nuclei of HA and preventing their further growth. Polar and charged amino acids (AAs) are highly expressed in NCPs, and the negatively charged ones, such as glutamic acid (Glu) and phosphoserine (PSer) seem to be mainly responsible for the inhibitory effect of NCPs. Despite the recognized importance of these AAs on the behaviour of NCPs, their specific effect on HA crystallization is still unclear, and controversial results have been reported concerning the efficacy of HA inhibition of positively vs. negatively charged AAs. We focused on a positively charged (Arginine, Arg) and a negatively charged (Glu) AA, and their combination in the same solution. We studied their inhibitory effect on HA nucleation and growth at physiological temperature and pH and we determined the mechanism by which they can affect HA crystallization. Our results showed a strong inhibitory effect of Arg on HA nucleation; however Glu was more effective in inhibiting HA crystal growth during the growth stage. The combination of Glu and Arg was less effective in controlling HA nucleation, but it inhibited HA crystal growth. We attributed these differences to the stability of complexes formed between AAs and Ca<sup>2+</sup> and PO<sub>4</sub><sup>3-</sup> ions at the nucleation stage, and in bonding strength of AAs to HA crystal faces during the growth stage. The AAs also influenced the morphology of synthesised HA. Presence of either Arg or Glu resulted in the formation of spherulites consisting of preferentially oriented nano-platelets orientation. This was attributed to the chelating effect of AAs, which resulted in a higher degree of supersaturation during the precipitation stage, thus favoring the formation of spherulitic particles.

#### 4.2. Introduction

Living organisms synthesize a variety of inorganic minerals, ranging from apatite in bones, calcium carbonate in seashells, to iron oxide in magnetotactic bacteria. These minerals form during a highly regulated process called biomineralization, and often have exceptional mechanical properties, complex shapes, and intricate hierarchical structures, which distinguish them from their artificially synthesized counterparts [1, 2, 278]. The unique characteristics of these minerals are obtained under the direct influence of biomolecules, usually proteins and peptides, which remarkably control and regulate their nucleation and

growth under conditions that are much milder than those used in conventional processing techniques [2, 5, 6, 278].

The most well-known and maybe most complex example of biomineralization is the formation of bone, an organic-inorganic hybrid material made of collagen, non-collagenous proteins (NCPs), and carbonated HA crystals. Collagen fibrils provide a framework known as extracellular matrix (ECM), where HA nucleates and grows. The ECM determines the ultimate structure and orientation of hydroxyapatite (HA, Ca<sub>5</sub>(PO<sub>4</sub>)<sub>3</sub>OH) crystals; however, HA nucleation is mainly initiated by a set of negatively charged phosphorylated NCPs associated with the ECM. These proteins attract Ca<sup>2+</sup> and PO<sub>4</sub><sup>3-</sup> ions and increase the local supersaturation to a level sufficient to form nuclei of a critical size, which can develop into HA crystals [8, 279]. Another set of NCPs has the ability to inhibit undesirable formation of HA in tissues such as cartilage, blood vessels and valves, which are continuously exposed to body fluids. These inhibitory proteins are dissolved in the plasma and limit the formation of HA by binding to the surface of nascent nuclei of minerals, thus restricting their further growth [11, 280].

While striving to understand the process of biomineralization, researchers have focused on the effect of smaller biomolecules like amino acids (AAs) and peptides on HA mineralization. Despite their minimal concentration as free biomolecules in human plasma [281], AAs are the building blocks of proteins, and negatively charged AAs such as Glu and PSer are highly expressed in the acidic domains of NCPs involved in HA mineralization in bone and dentine. Similar to proteins, charged AAs can either inhibit or induce HA mineralization depending if they are dissolved in solution or bound to a surface. AAs are also effective in modifying the morphology and crystalline structure of HA due to the electrostatic and stereochemical effects of their charged residues [11, 13, 14, 32, 282]. In comparison with proteins or peptides, AAs are much less expensive and more stable, which makes them attractive candidates for clinical applications. In-vitro studies show that promoting AAs are useful for improving bone regeneration in damaged tissues [13], while inhibitory AAs are potential candidates for treating pathological diseases caused by an excessive mineralization of HA in tissues like cartilages [15, 16], blood vessels and cardiac valves [16-18].

Despite the well-documented importance of these AAs in controlling HA mineralization, the mechanism by which they interact with HA crystals to induce or inhibit mineralization is still strongly debated. In general, it is believed that negatively charged AAs containing carboxylate and phosphorylated residues play a key role in controlling HA mineralization in bone [8, 48-51]. However, contradictory results reported by different authors make it difficult to draw a comprehensive conclusion about the effect of AAs on HA crystallization. For example, Jack et al reported a significant inhibitory effect of alanine (Ala) and aspartic acid (Asp) on the growth of HA particles [52]. In contrast, Palazzo et al showed that Asp promoted HA particle growth while Ala had no effect on HA particle sizes [11]. According to Jack at al., a positively charged AA, lysine, had the strongest affinity to HA surfaces [52]; however, Koutsopoulos and Dalas showed that the negatively charged Asp had the largest affinity to HA among the AAs that they investigated [44, 53-56]. In addition to these contradictory results, the studies on the effect of AAs are often focused on HA crystal growth rather than investigating HA formation at its very early stages (i.e. HA nucleation) [44, 53-56] and are mostly conducted under experimental conditions different from the physiological ones (i.e. high supersaturation, high temperature or high pH) [32, 34, 35, 52]. These factors have made it difficult to have a real insight into the effect of AAs on biomineralization in living organisms.

In this study, we investigate the inhibitory effect of a positively charged (Arg) and a negatively charged (Glu) AA dissolved in solution on the morphology and crystallization (nucleation and growth) of HA synthesized at physiological temperature and pH. Negatively charged AAs, such as Asp and Glu are highly expressed in the family of proteins called SIBLINGs (small-integrin-binding ligand, N-linked glycoprotein), known to play a key role in HA mineralization in the body [6]. SIBLINGs also contain positively charged AAs, such as Arg and Lys. Here we focus on Glu and Arg to understand the relative importance of negative and positive charges in HA mineralization, and we specifically select Glu and Arg because they have been less investigated than their counterparts Asp and Lys [9, 22-27]. We also study the effect of combination of Glu and Arg, with the goal of clarifying if different inhibiting or promoting mechanisms related to the two AAs could enhance or dampen each other. Our results show a key role of the positively charged AA on HA crystallization and shed some light on the mechanism under which these AAs influence HA nucleation and growth.

#### 4.3. Materials and methods

#### 4.3.1. Synthesis of HA in the presence of AAs

#### 4.3.1.1. Materials

Calcium (Ca) and phosphate (P) ion precursors were calcium chloride dehydrated (CaCl<sub>2</sub>, Sigma Aldrich, purity >97%) and sodium phosphate monobasic anhydrous (NaH<sub>2</sub>PO<sub>4</sub>, purity > 99%, Fisher Scientific). The amino acids used in the study (L-Arginine, purity  $\geq$  99.5%, and L-Glutamic acid, purity  $\geq$  99.5%) were purchased from Sigma Aldrich, as well as the buffer agent tris(hydroxymethyl)aminomethane (tris, purity  $\geq$  99.5%). Hydrochloric acid used to adjust pH was purchased from Fisher. The ninhydrin reagent from Sigma (N 7285) was used to measure the concentration of AAs in the supernatant solution.

#### 4.3.1.2. HA synthesis

Ca- and P-precursor solutions (130 ml) were prepared by mixing CaCl<sub>2</sub> (6.22 mM), tris (100 mM) and AAs (Arg and/or Glu, 10 mM), and NaH<sub>2</sub>PO<sub>4</sub> (3.74 mM), tris (100 mM) and AAs (Arg and/or Glu, 10 mM), respectively. Control solutions were prepared with identical CaCl<sub>2</sub>, NaH<sub>2</sub>PO<sub>4</sub> and tris concentration, in the absence of any AA. The pH of both Ca and P precursor solutions was adjusted at 7.4 using adequate amounts of concentrated HCl, and the temperature was adjusted at 37°C by placing the reaction vessels in water bath equipped with temperature controller (ColeParmer PolyStat Immersion Circulator). The same volume of Ca and P precursor solutions were added to the reaction vessel simultaneously, thus reaching final Ca and P concentrations of 3.11 and 1.87 mM, respectively. The ratio between these concentrations matches the physiological Ca to P ratio, but the absolute values are approximately 1.5 times higher than those found in human blood plasma, and they were chosen in order to decrease the required incubation time prior to precipitation. The supersaturation value for HA at these Ca and P concentrations is 122.96, calculated according to Eq. 4.1,

$$s = \left[\frac{IP}{K_s}\right]^{1/9} \tag{4.1}$$

where IP is the ionic activity product and  $K_s$  is the solubility constant equal to  $2.35 \times 10^{-59}$  for HA at 37°C [283]. The pH of the reaction solution was monitored, and remained constant at 7.4±0.05. The reaction solution was stirred at 100 rpm and the temperature was kept constant at 37°C. The samples were taken out at the precipitation time and after 2 days of reaction, and the

precipitates were filtered using 200 nm filters, and subsequently washed 3 times with DI water. The precipitates were finally dried using a VirTis freeze drier. The summary of the AAs present in different samples and their concentration is reported in **Table 4.1.** 

#### 4.3.2. Characterization techniques

#### 4.3.2.1. Bulk characterizations of dried precipitates

Fourier transform infrared (FT-IR) spectroscopy: IR spectra were recorded on a Bruker Tensor 27 FT-IR spectrometer using diffuse reflectance (DRIFT) mode. The reflected signals are converted and reported as absorbance in the figures shown in this paper. The powders were diluted with KBr to approximately 10% weight/weight ratio. Pure KBr powder was used to collect background spectra. The FT-IR spectra were recorded from 600 to 4000 cm<sup>-1</sup> using mercury-cadmium-telluride (MCT) detector. The spectra were collected by averaging 256 scans at 4 cm<sup>-1</sup> resolution.

*X-ray diffraction (XRD):* XRD spectra were collected using a Bruker AXS XRD instrument with Cu  $K_{\alpha}$  radiation generated at 40 kV and 40 mA. A quartz sample holder was used for these experiments. The range of diffraction angles collected (20) ranged from 5 to 100°, with step size of 0.05°. The crystallite sizes were measured using Debye Scherrer equation [284],

Crystallite size = 
$$\frac{k\lambda}{FWHM.Cos(\theta)}$$
 (4.2)

where k is shape factor (k = 0.9),  $\lambda$  is the wavelength of the X-rays ( $\lambda = 0.154056$  nm for Cu K<sub> $\alpha$ </sub> radiation),  $\theta$  is the diffraction angle, and *FWHM* is the full width half maximum of (001) and (310) peaks at 20 values of 25.88 and 39.82, respectively, referring to synthetic HA with hexagonal (P63/m) crystalline structure.

**Table 4.1.** Summary of AA concentrations in different samples.

Sample	Glu Conc. (mM)	Arg Conc. (mM)
HA-Cont	0	0
HA-Glu	10	0
HA-Arg	0	10
HA-Combo	5	5

#### 4.3.2.2. Surface characterization of dried precipitates

*X-ray photoelectron spectroscopy (XPS):* XPS measurements were performed using a monochromatic X-ray photoelectron spectrometer K Alpha (Thermo Scientific). The setup was equipped with an Al Kα X-Ray source (1486.6 eV, 0.834 nm), a micro-focused monochromator and an ultrahigh vacuum chamber ( $10^{-9}$  Torr). Survey scans were collected with energy steps of 1 eV and spot size of 50 μm. Scans were taken on at least 3 points on each sample and the quantitative results were averaged. A flood gun was used to neutralize electrical built-up charge generated on the non-conductive samples. The survey scans were analyzed using the software Thermo Avantage (version 4.60).

Surface area and porosity determination: the specific surface area (ssa) and porosity of the samples were determined at 77 K by the adsorption of N<sub>2</sub> using an automatic gas-volumetric apparatus (TriStar, Micromeritics). The BET model was adopted for ssa determination [285], [286], whereas the BJH model was used to analyze mesoporosity [33], [287].

*Morphology:* the particle morphology was analyzed with a scanning electron microscope (SEM) from Hitachi (S-4700 FE-SEM), using an acceleration voltage of 5 kV. The specimens were mounted on double sided conductive carbon tape and were coated with a thin layer of Au to increase their conductivity. The coating was done with a HUMMER VI sputtering system under vacuum of 70 millitorr and at the voltage of 10 V for 1 min.

#### 4.3.2.3. Characterization of supernatant solution

Inductively coupled plasma atomic emission spectroscopy (ICP-AES): Ca and P concentrations in solution were measured using an ICP-AES instrument (ICAP 6500 Duo). For this purpose aliquots were taken from the supernatant solution at the desired reaction times, filtered with a syringe filter with pore size of 100 nm to remove any trace of HA precipitates that were larger than 100 nm, and then diluted with 4% nitric acid. The Ca and P concentrations were measured at the wavelength of 3179 and 1782 nm, respectively. ICP-AES was performed also on the precipitates to measure the bulk Ca and P values in these samples. 1 mg of samples was dissolved in 10 ml of 4% nitric acid and the resulting Ca and P concentrations were measured using the same procedure described before.

AA concentration determination: The concentration of AAs in the supernatant solution was measured by a colorimetric technique based on the use of ninhydrin to transform free amino groups in a colored product [288]. For this purpose, aliquots were taken at desired times, and

then diluted with 10% glacial acetic acid to stop the reaction. An adequate amount of ninhydrin reagent was added to the samples, and the absorption of the solutions was measured at 570 nm using a UV-vis spectrometer (Perkin Elmer, Lambda 20). According to Duggan et al the free NH<sub>2</sub> groups from tris do not interfere with the colour generated at 570 nm by the interaction between the NH<sub>2</sub> group of AAs and ninhydrin [289]. Despite this, in our experiments we found a minor interference due to tris, and therefore we removed the tris contribution by comparing the results of the solutions containing both tris and AAs to those containing tris only. Calibration curves were constructed using 3.125, 6.25, 18.75, and 25 µM AAs solutions made by dissolving adequate amounts of AAs in 10% glacial acetic acid.

#### 4.4. Results

In order to understand the effect of Arg, Glu, and their combination on HA precipitation, we compared HA precipitation in the presence of these AAs with control samples which had no AAs. We characterized the synthesized powder with a range of different techniques, including FT-IR, XPS, XRD, SEM, ICP-AES, and UV-vis spectroscopy. The XRD results shown in **Fig. 4.6** and **Fig. 4.7** confirmed that all the precipitates were mainly composed of HA, as will be discussed in **Section 4.4.4**. From now on, we will refer to the samples prepared in the presence of the AAs and the control samples as HA-Glu, HA-Arg, HA-Combo, and HA-Cont (see **Table 4.1** for detail about their AA content).

#### 4.4.1. Precipitation times and precipitate weights

**Fig. 4.1** shows the effect of different AAs on the precipitation time of HA. Although both Glu and Arg inhibited the formation of HA precipitates, the effect of Arg was significantly stronger. In the presence of Arg, the precipitates took approximately 8 times longer to form compared to HA-Cont sample prepared in the presence of tris alone, while in the presence of Glu the precipitation time was increased by only approximately 5 folds. The combination of Arg and Glu had some inhibitory effect on the formation of HA particles, however to a lower extent than either of the AAs alone.

It is worth noting here that we specifically tested the inhibitory effect of tris alone as well. In fact, tris is known to have an inhibitory effect on calcium phosphate formation [290]. Samples prepared in the absence of both tris and AAs precipitated immediately after mixing (results not shown), while HA-Cont samples prepared in the presence of tris precipitated after approximately 2 hours (**Fig. 4.1**). This confirmed the inhibitory effect of tris reported by Kokubo et al [290]. However, the much longer delay in HA precipitation observed for the AA-containing samples despite the small concentration of the AAs (10 mM) relative to tris (100 mM) indicates a stronger inhibitory effect for the AAs compared to tris. This can be explained considering the electrical charges of these molecules. The pK<sub>a</sub> of tris at 25° C is 8 [291], while the pK<sub>a</sub> of the side chains of Arg and Glu are 12.5 and 4.25, respectively [292]. The larger electrical charges present on the AAs at pH 7.4 may contribute to making them more effective than tris in inhibiting HA formation."

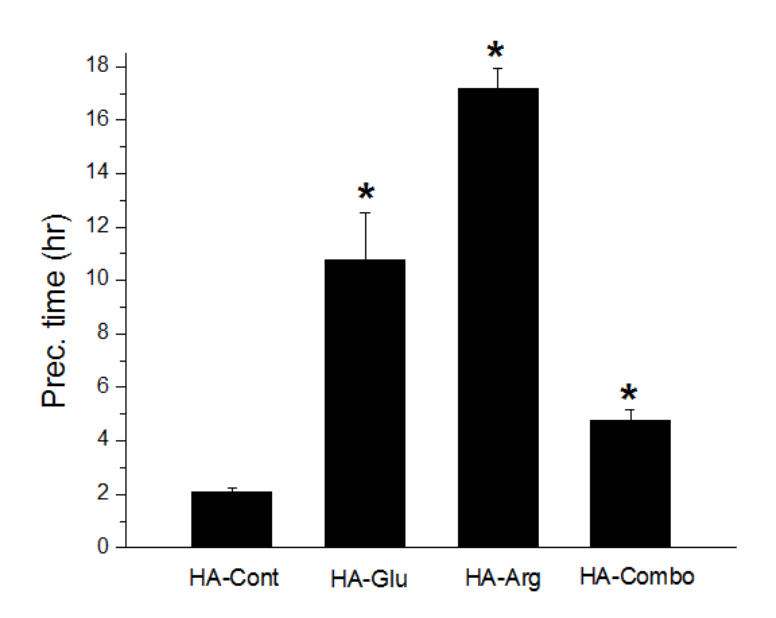


**Fig. 4.1.** Effect of AAs on the precipitation time (prec. time) of HA. The precipitation time was considered to be the time at which the solution became visibly cloudy. Each data point is the average of at least 3 samples. Asterisks (\*) indicate the samples that were statically significantly different (P < 0.003) from the control sample.

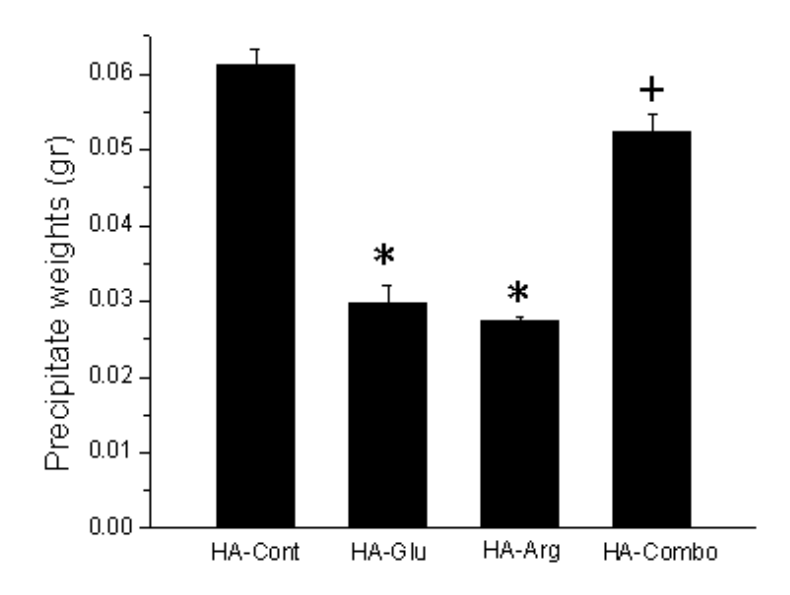


**Fig. 4.2.** Effect of Glu, Arg, and combination of Glu and Arg on the weight of precipitates after 2 days of reaction. Each data point is the average of at least 3 samples. Asterisks (\*) and plus sign (+) indicate the samples that were statically significantly different from the control sample with P < 0.0005 and 0.02, respectively.

**Fig. 4.2** shows the effect of the investigated AAs on the precipitate weights after 2 days of reaction. If we consider the initial moles of Ca and P present in solution, then we should expect a theoretical precipitate weight of 0.081 g if all of the Ca and P combined to form HA. This weight is higher than the weights observed for all precipitates, even after the reactions reached their stable state (**Fig. 4.11**). This confirms the inhibitory effect of organic molecules dissolved in the reaction solution. In line with the precipitation time results, both Glu and Arg strongly inhibited HA formation, resulting in smaller amounts of precipitate after two days in comparison with the control samples. The combination of Glu and Arg also inhibited the precipitation of HA, but not as strongly as the individual effect of Glu and Arg. This result was also consistent with the precipitation time result obtained for the HA-Combo samples.

#### 4.4.2. Morphology

**Fig. 4.3** shows the morphology of the HA samples obtained at precipitation time. Individual microspherulitic aggregates of 2 to 4 μm were found in both HA-Glu and HA-Arg samples (**Fig. 4.3c and e**), and were less evident for HA-Combo (**Fig. 4.3g**), while HA-Cont only showed aggregated particles without individual microspheres (**Fig. 4.3a**). The microspheres observed for HA-Glu and HA-Arg were composed of plate-like particles (**Fig. 4.3d and f**), more

densely packed on HA-Glu. High magnification SEM images for HA-Cont and HA-Combo (**Fig. 4.3b and h**) showed longer, curved strands that were not observed on HA-Glu and HA-Arg.

The spherulitic morphology observed for HA-Arg and HA-Glu became more evident after 2 days of reaction, while the size of the microspheres decreased (**Fig. 4.4c and e**), reaching approximately 2 µm for HA-Arg and 3 µm for HA-Glu. The microspheres at this point consisted of nanoplatelets preferentially oriented with their long axis pointing towards the center of the microsphere. The platelets were still curved, but they were less jagged at the borders in comparison to those seen at precipitation time. Similar nanoplatelets were observed in HA-Cont (**Fig. 4.4b**), however they lacked the orientation observed on HA-Arg and HA-Glu, and were agglomerated in random structures rather than organized in spherulitic particles. The morphology of Combo-HA after 2 days (**Fig. 4.4g and h**) was more similar to the samples synthesized in the presence of AAs than to the control sample. The microspheres in HA-Combo became more evident after 2 days. They were made of nanoplatelets similar to those observed on HA-Glu and HA-Arg.

#### 4.4.3. BET ssa of synthesized particles

**Fig. 4.5** shows the BET ssa results for HA particles synthesized in the presence of different AAs after 2 days of reaction. These results inversely correlated with the precipitation times reported in **Fig. 4.1**: the largest ssa  $(97 \pm 6 \text{ m}^2/\text{g})$  was observed for HA-Cont, which precipitated first; values of  $84 \pm 5$  and  $77 \pm 1$  m<sup>2</sup>/g were measured on HA-Combo and HA-Glu; and the lowest value of  $60 \pm 1$  m<sup>2</sup>/g was observed for HA-Arg, which showed the most delayed precipitation time. The overall high ssa values obtained were related to the presence of mesopores—in fact a similar trend was observed for mesopore volumes, and it was directly related to the pore size (**Table 4.2**).

**Table 4.2.** Pore volume and pore size for HA samples synthesized in the presence of Glu, Arg, and their combination after 2 days.

Sample	Mesopore volume (cm <sup>3</sup> /g)	Pore size (nm)
HA-Cont	$0.45 \pm 0.01$	12.92±0.33
HA-Glu	0.22±0.06	6.77±0.68
HA-Arg	0.17±0.03	7.99±0.65
HA-Combo	0.34±0.05	10.38±0.23

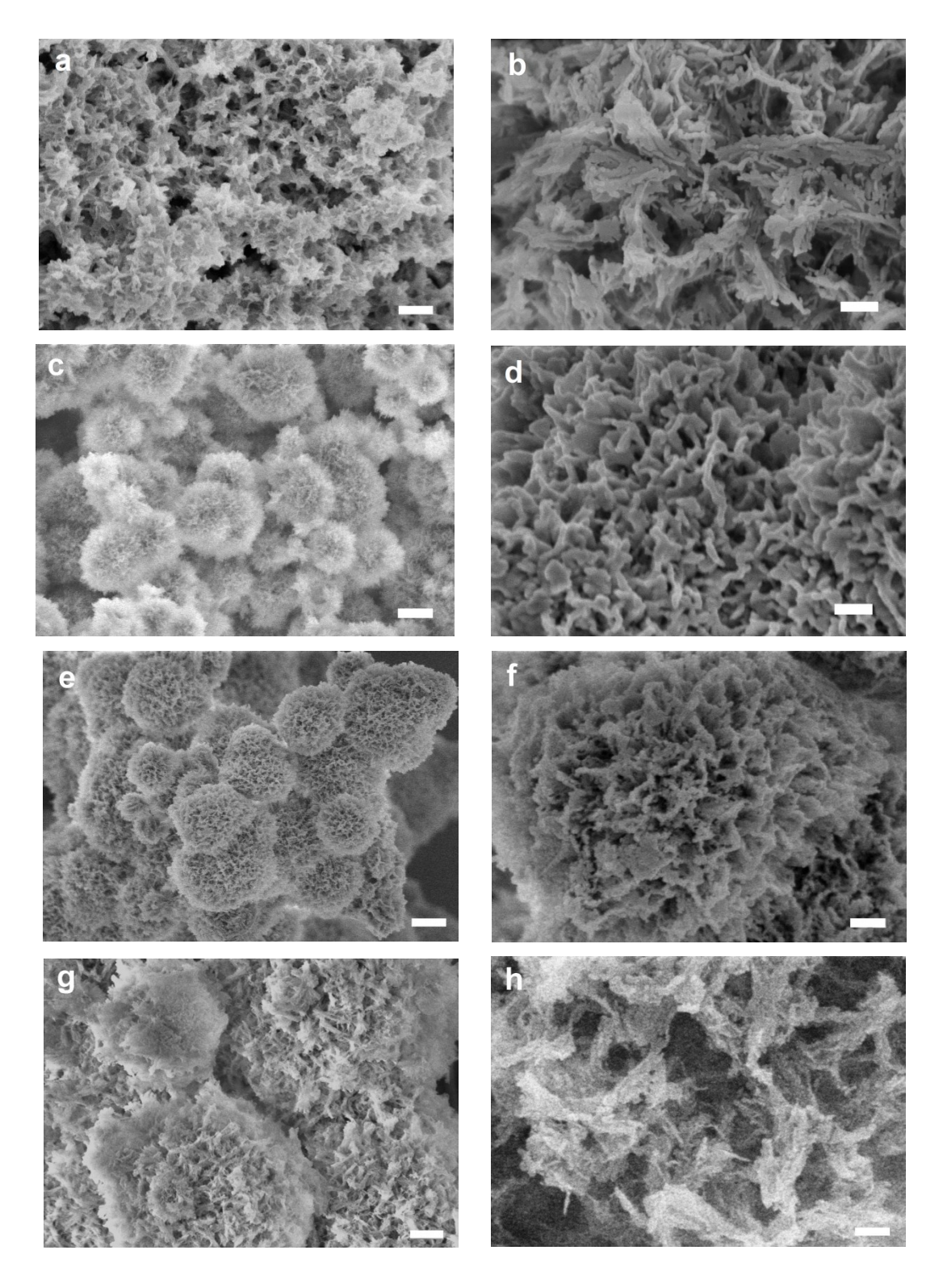
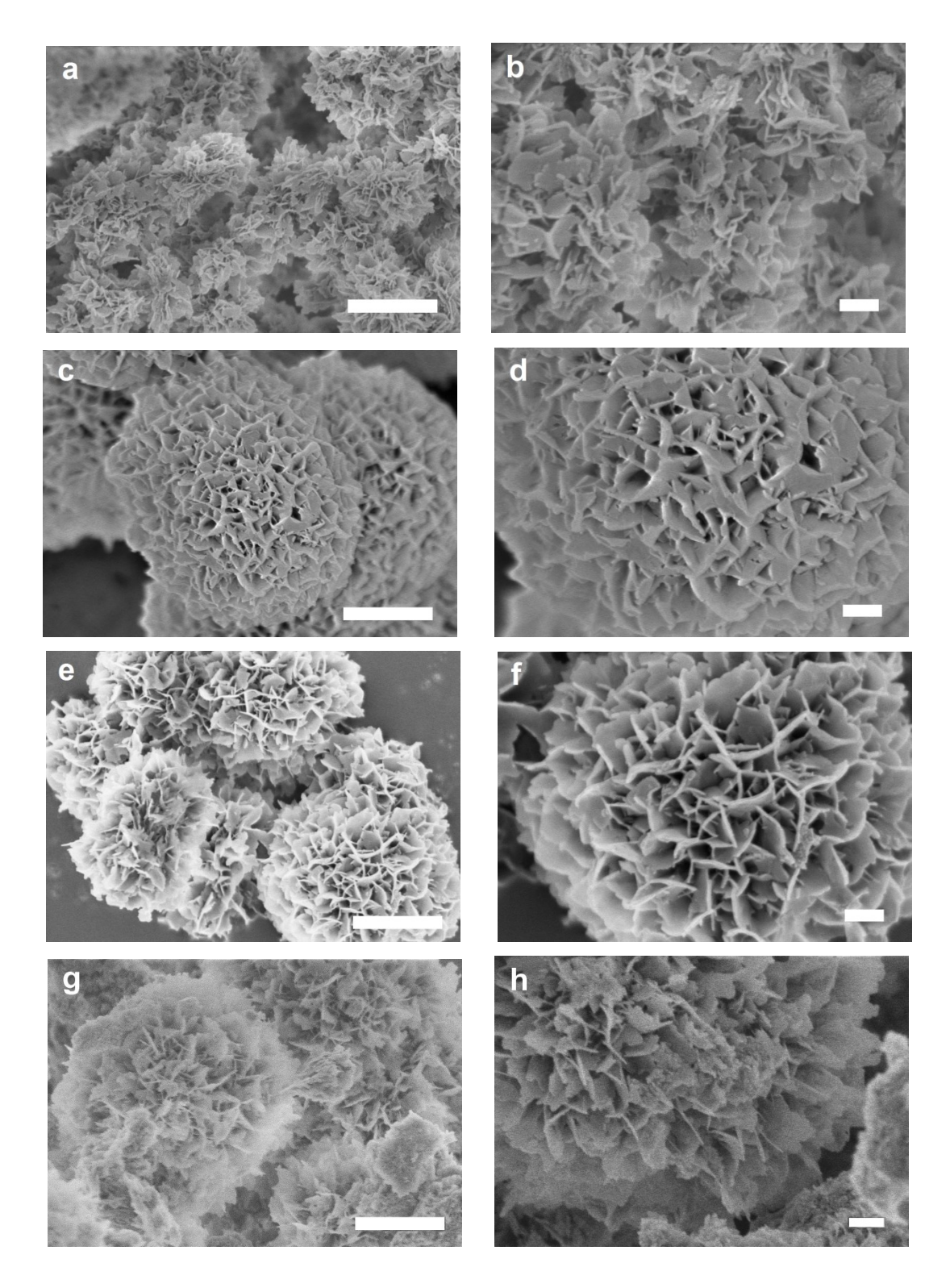
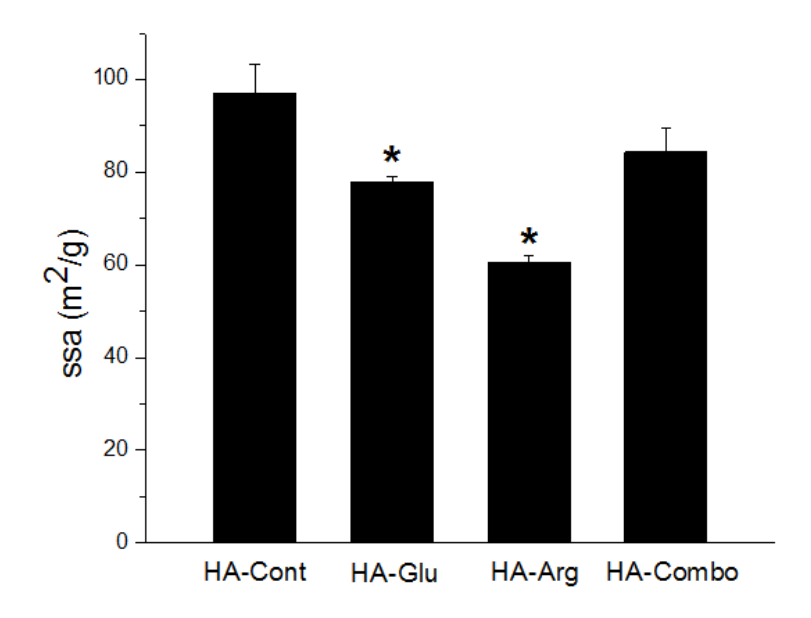


Fig. 4.3. SEM images of samples HA-Cont (a and b), HA-Glu (c and d), HA-Arg (e and f), and HA-Combo (g and h) at precipitation time. Scale bars: 1µm (a, c, e, g) and 200 nm (b, d, f, h).



 $\begin{tabular}{ll} \textbf{Fig. 4.4.} SEM images of samples HA-Cont (a and b), HA-Glu (c and d), HA-Arg (e and f), and HA-Combo (g and h) after 2 days of reaction. Scale bars: $1 \mu m$ (a, c, e, g) and $200 nm$ (b, d, f, h). \end{tabular}$ 



**Fig. 4.5**. Effect of Glu, Arg, and combination of Glu and Arg on the BET ssa of synthesized HA powders after 2 days of reaction. Asterisks (\*) indicate the samples that were statically significantly different from the control sample with P < 0.05.

#### 4.4.4. Crystal structure and crystallite sizes measured by XRD

**Fig. 4.6a and b** show the XRD patterns for samples measured at the precipitation time and after 2 days of reaction, respectively. All precipitates were HA, as confirmed by comparison with the standard HA pattern. The spectra collected on our samples were also compared with the reference pattern for octacalcium phosphate (OCP), which has a structure similar to HA. Neither the most intense peak of OCP at 20=4.7° nor the second most intense peaks at 20=9.308 and 9.703° matched the peaks observed in the spectra of our samples (see Supporting Information **Fig. S4.1 and S4.2**). The large backgrounds observed for all the powders at the precipitation time (**Fig. 4.6a**) indicated the presence of an amorphous calcium phosphate (ACP) component in these samples, which was partially retained even after two days of reaction in the presence of Glu and Arg (**Fig. 4.6b**). This result showed the ability of the AAs to stabilize ACP, possibly because they were trapped in the HA crystalline lattice, thus causing greater atomic disorder. This was consistent with the results obtained by Palazzo et al [11], who showed the formation of less crystalline HA in the presence of Arg, Asp and Ala. This lower degree of crystallinity makes HA synthesized in the presence of AAs resemble natural bone more closely than pure HA, since bone minerals are composed of poorly crystalline HA [254].

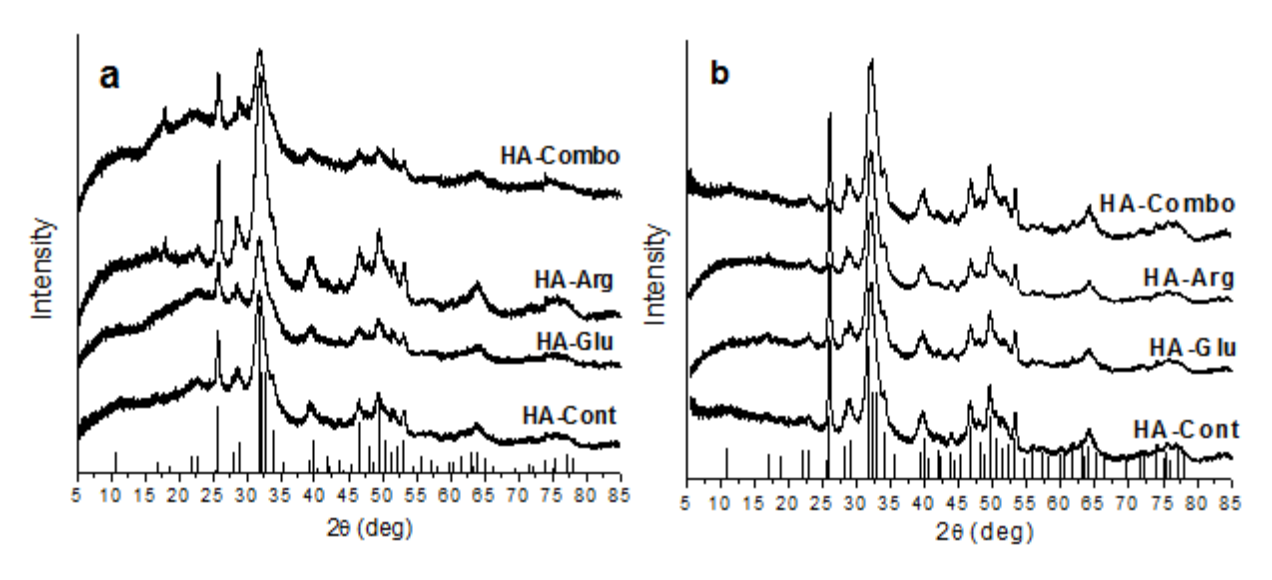


**Fig. 4.6.** XRD patterns of HA-Cont, HA-Glu, HA-Arg, and HA-Combo collected at the precipitation time (a), and after 2 days (b). The vertical lines are the reference pattern for HA (PDF number: 00-009-0432).

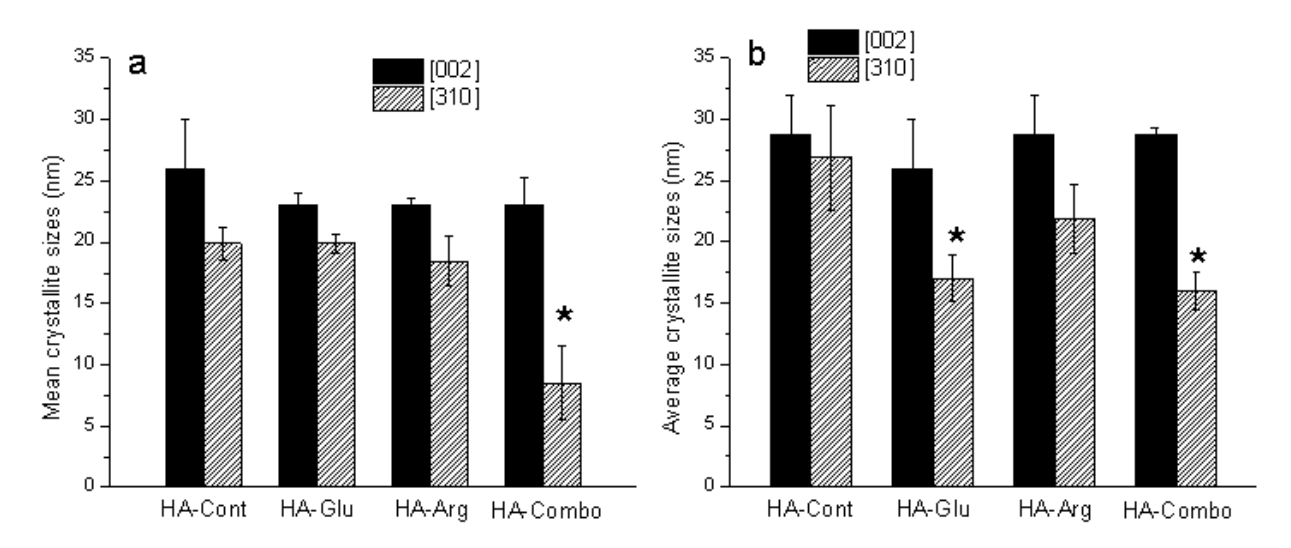


**Fig. 4.7.** Average crystallite sizes along [002] and [310] measured by XRD for HA-Cont, HA-Arg, HA-Glu, and HA-Combo at the precipitation time (a) and after 2 days (b). Asterisks (\*) indicate samples that were significantly different from HA-Cont (P < 0.05 in a and P < 0.08 in b).

The crystallite size along the [002] and [310] directions was estimated using the Debye-Scherrer equation and the FWHM of the corresponding peaks at  $2\theta = 25.88$  and  $39.82^{\circ}$ , respectively (**Eq. 4.1**) (**Fig. 4.7**). No statistically significant differences with HA-Cont were observed for AA-containing samples at precipitation time, except for HA-Combo along the [310] direction. After 2 days of reaction, statistically significant differences were observed for both HA-Glu and HA-Combo along [310]—in particular, a crystallite size along [310] of  $26 \pm 4$  nm

was measured for HA-Cont, while values of  $17 \pm 2$  nm and  $16 \pm 2$  nm were obtained for HA-Glu and HA-Combo, respectively.

#### 4.4.5. FT-IR analysis

In line with the XRD results, the FT-IR spectra for all samples recorded at the precipitation time and after 2 days of reaction matched the spectra recorded on carbonated HA (CHA) [293, 294] (**Fig. 4.8**), and were very different from those obtained for other crystalline phases of calcium phosphates like OCP [295]. However, the phosphate  $v_3$  peaks on HA-Cont and AA-containing HA samples were sharper than in CHA, most likely indicating that the HA samples were more crystalline than the reference CHA [296], which is very defective due to the incorporation of carbonate ions in its crystal lattice. Also, the HA samples did not show strong carbonate  $v_3$  peaks because the carbonates were not present in the bulk, but rather at the surface most likely due to reaction with atmospheric  $CO_2$  dissolved in the reaction solution—indeed, more carbonates were observed on the HA samples after 2 days of reaction. More water was adsorbed on the HA samples than on CHA, as shown by the stronger  $\delta_{HOH}$  peak at 1660 cm<sup>-1</sup> and more pronounced  $v_{OH}$  band in the 2600-3700 cm<sup>-1</sup> region. The peak at 3650 cm<sup>-1</sup> present on all samples is attributed to  $v_{OH}$  from structural OH groups in HA.

FT-IR spectroscopy can also provide information relative to the presence of organic components in the samples. Peaks at  $1200\text{-}1300~\text{cm}^{-1}$  were attributed to  $v_{\text{C-N}}$ ; these peaks were observed on HA-Arg more strongly at precipitation time, and were present after 2 days on both HA-Arg and HA-Glu, thus indicating the presence of AAs on these samples [11]. Confirming this, a small  $v_{\text{C=O}}$  peak, originating from the carboxylate groups in AAs, was observed for HA-Arg and HA-Glu samples after 2 days of reaction [11]. The  $v_{\text{C-H}}$  peaks observed in the 2800 to 3000 cm<sup>-1</sup> region showed that organic material, either tris or AAs, was present in all of the precipitates. The peaks at 2958 and 2873 cm<sup>-1</sup> correspond to  $v_{\text{CH2 asym}}$  and  $v_{\text{CH3 asym}}$ , respectively, and those at 2920 and 2852 cm<sup>-1</sup> to  $v_{\text{CH2 asym}}$  and  $v_{\text{CH2 sym}}$  (**Fig. 4.8 Inset**) [297]. While tris has only CH<sub>2</sub> groups, AAs contain both CH<sub>2</sub> and CH<sub>3</sub> groups; therefore, the CH<sub>3</sub> to CH<sub>2</sub> ratio can be considered as an indication of the presence of AAs in the samples. As shown in **Fig. 4.8 Inset**, the samples with higher CH<sub>3</sub> to CH<sub>2</sub> ratio were HA-Arg and HA-Glu, followed by HA-Combo and finally HA-Cont. This further confirmed the presence of AAs in HA-Arg and HA-Glu, and to a lower extent in HA-Combo.

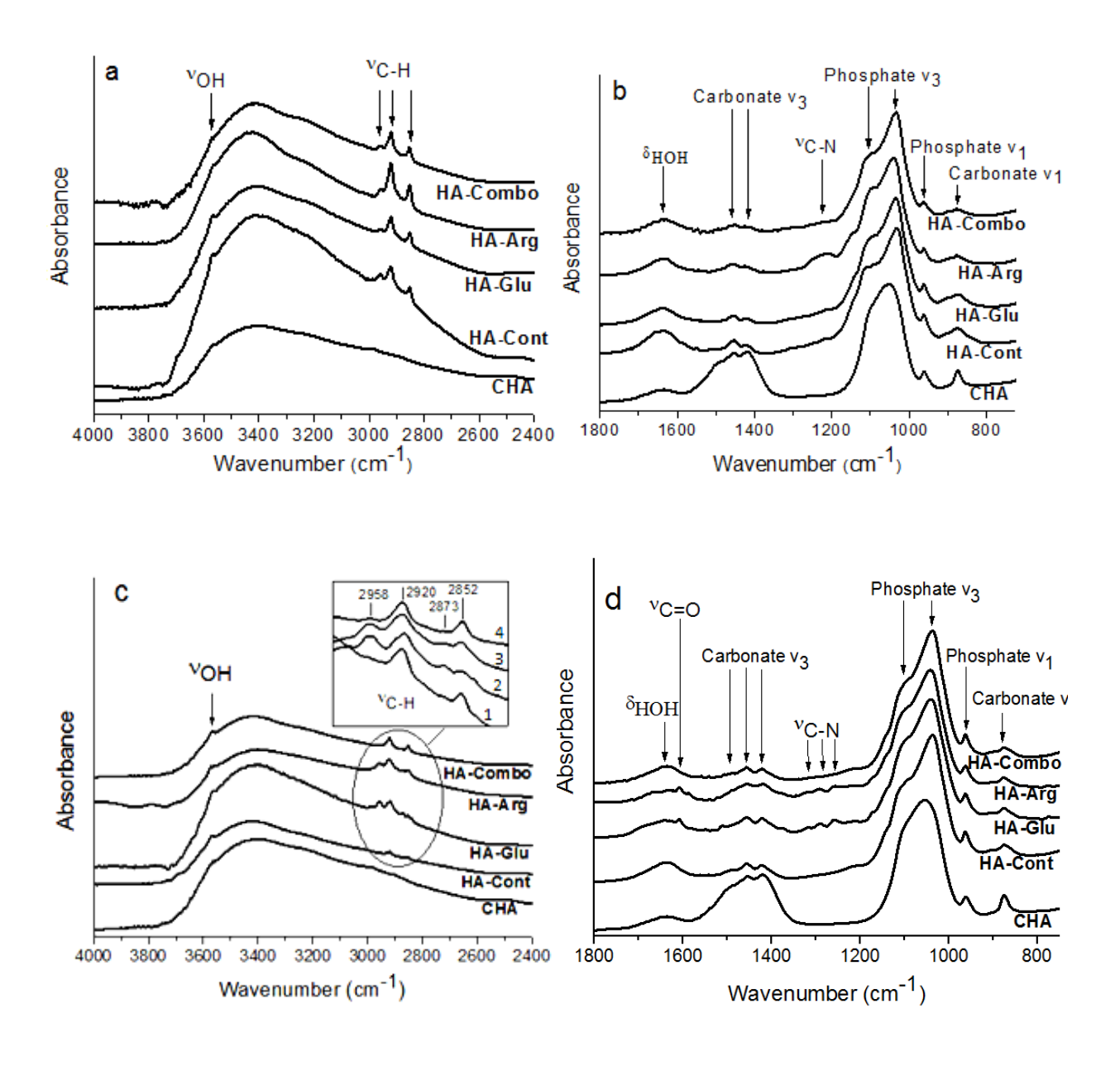


**Fig. 4.8.** IR spectra of control and AAs samples at precipitation time (a and b) and after 2 days (c and d). All spectra are normalized with respect to the main phosphate peak of CHA at 1055 cm<sup>-1</sup>. Spectra are then translated along the y axis for clarity. Sections (a and c): 4000-2400 cm<sup>-1</sup> region; (b and d): 750-2000 cm<sup>-1</sup> region. Inset in section c: zoom-in of 3000 to 2800 cm<sup>-1</sup> region for spectra HA-Cont (1), HA-Glu (2), HA-Arg (3), and HA-Combo (4).

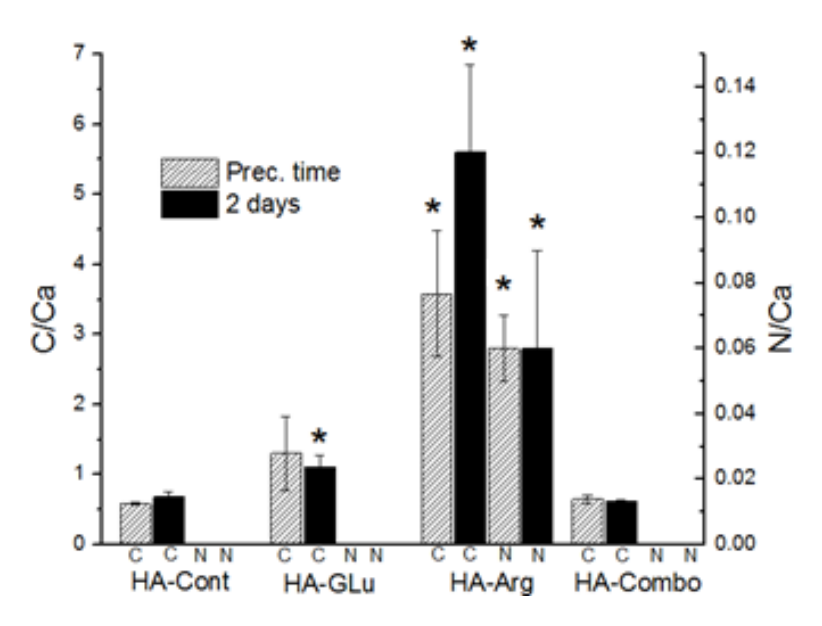


**Fig. 4.9**. C and N atomic % relative to Ca atomic % for HA-Cont, HA-Glu, HA-Arg, and HA-Combo at precipitation time and after 2 days of reaction, measured from XPS survey spectra. Asterisks (\*) indicate the samples that were statically significantly different from the control sample with P < 0.02.

#### 4.4.6. Surface composition determined by XPS

XPS allows identifying the elemental composition and chemical species present on the outmost few nm of the sample surface. Fig. 4.9 shows the C/Ca and N/Ca ratio for the control and AAs samples collected at different reaction times, calculated based on the areas of the C 1s, N 1s and Ca 2p peaks recorded in XPS survey spectra. The C measured on all the samples can originate from three sources: contamination, always present in some amount on any sample; carbonate ions; and organic material, including both tris and AAs. N too can originate from organic components including both tris and AAs. Therefore, it is possible to estimate the amounts of Arg and Glu in the AAs samples if the C/Ca and N/Ca ratios for the AAs samples are compared with those for the control samples at the same reaction times. While the C/Ca ratios measured on HA-Arg were approximately 6 and 8 times higher than those measured on HA-Cont at precipitation time and after 2 days, respectively, the same C/Ca ratios on HA-Glu were only approximately 2 and 1.6 times higher than those measured on HA-Cont. No significant differences between HA-Combo and HA-Cont were observed after 2 days of reaction and only minor differences were observed at precipitation time. These results thus indicate that HA-Arg samples synthesized both at the precipitation time and after 2 days of reaction contained significantly larger amounts of AAs in comparison with the HA-Glu and HA-Combo samples.

Small amounts of N detected in HA-Arg samples at the precipitation time and after 2 days of reaction further confirmed the presence of Arg in these samples (**Fig. 4.9**). The fact that no N is detected on HA-Glu while IR clearly shows the presence of AAs on this sample may be related to the fact that less N is present in the Glu structure than in Arg, and thus the small amount of N present on the HA-Glu sample is not detectable by XPS. Indeed, XPS is a more surface-sensitive technique than IR, and if small amounts of AAs are present all throughout the sample and are not concentrated on the surface, it might be harder to detect them using XPS rather than a bulk technique such as IR.

**Fig. 4.10** shows the surface Ca/P ratios measured from XPS survey spectra. All samples showed Ca/P ratios lower than the stoichiometric value for HA (1.67). This may be attributed to the presence of Ca vacancies and less crystallinity at the surface of HA particles [298]. No significant difference was observed in the Ca/P ratios for the HA samples collected at the precipitation time, and all of them showed lower ratios than the corresponding samples after 2 days of reaction, indicating more highly defective surfaces at the early stage of precipitation. After 2 days of reaction, HA-Glu and HA-Arg showed lower Ca/P ratio in comparison with the control samples. These results were consistent with the XRD results (**Fig. 4.6b**) showing ACP was still present in the HA-Glu and HA-Arg samples after 2 days of reaction.

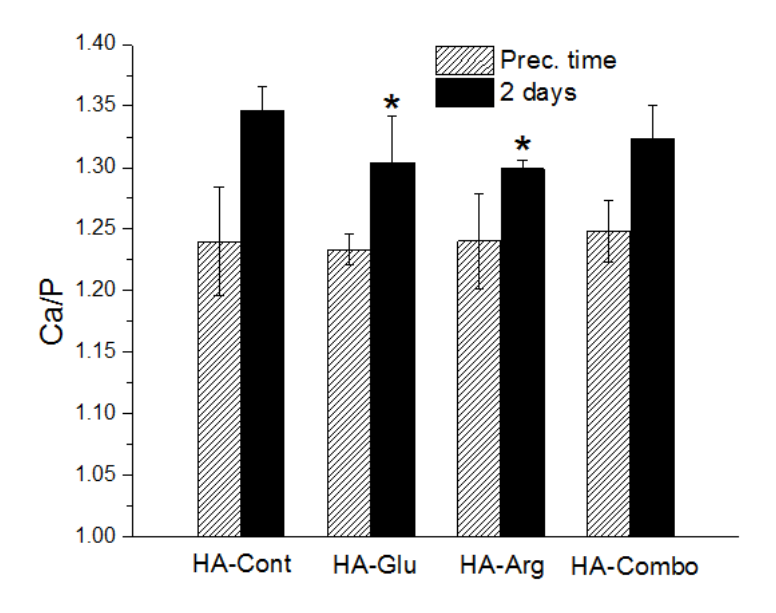


**Fig. 4.10.** Surface Ca atomic % relative to P atomic % for HA-Cont, HA-Glu, HA-Arg, and HA-Combo at precipitation time and after 2 days of reaction, measured from XPS survey spectra. Asterisks (\*) indicate samples that were significantly different from HA-Cont (*P*<0.03).

#### 4.4.7. Colorimetric technique to measure the adsorption of AAs to HA surfaces

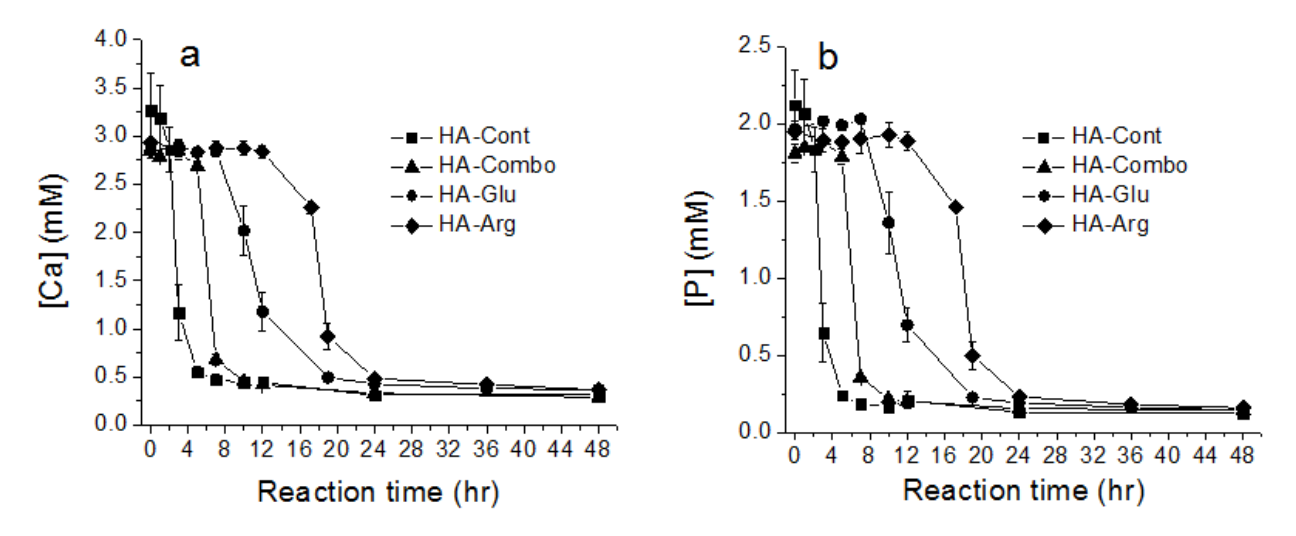
The amount of adsorbed AAs on HA surfaces was further evaluated by measuring the amount of AAs remaining in solution after 2 days of reaction. The AAs remaining in solution were converted to a colored derivative using ninhydrin, and the absorption of these compounds was evaluated with a UV-vis spectrometer according to a procedure widely reported in the literature [52]. Knowing the initial concentration of AAs in solution, it was then possible to estimate the amount of AAs adsorbed on HA particle surfaces. The amounts of adsorbed AAs were normalized with respect to the ssa of the particles reported in **Fig. 4.5**, and the final results are shown in **Table 4.3**. In accordance with XPS results (**Fig. 4.9**), the AA that adsorbed in larger amount on HA after 2 days was Arg, and lower amounts were observed when Glu or both Glu and Arg were present during HA synthesis.

#### 4.4.8. ICP analysis on [Ca] and [P] in solution and on HA precipitates

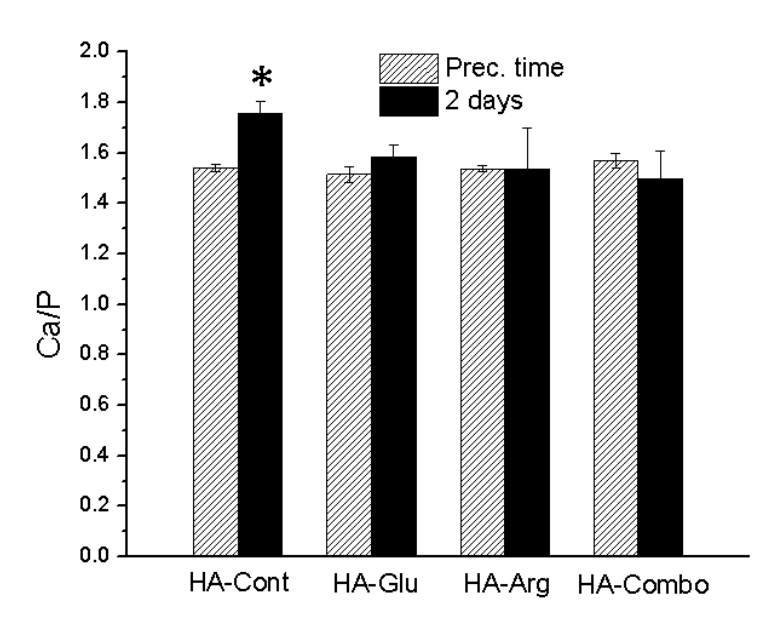
[Ca] and [P] in the supernatant solution were measured by ICP shown in Fig. 4.11. A sharp decrease in both [Ca] and [P] was observed after 1 and 5 h on HA–Cont and HA-Combo, respectively. This time corresponded very well to the time at which visible precipitation occurred on these samples. However, for HA-Glu and HA-Arg, the curves relative to [Ca] and [P] showed a much less sharp decrease at 8 and 12 h, respectively. This time was earlier than the time at which visible precipitation was observed for HA-Glu (11 h) and HA-Arg (17h). This indicated most likely the formation of smaller nuclei even before visible precipitation occurred for these samples. The longer delay observed before [Ca] and [P] decreased in HA-Arg and HA-Glu samples in comparison with HA-Cont and HA-Combo can be related to the inhibitory effect of Arg and Glu when they are present separately in the crystallization solution. This is consistent with the results obtained for precipitation times and precipitate weights shown in Fig. 4.1 and 4.2, respectively. Steady values of 0.4 mM for [Ca] and 0.2 mM for [P] were observed after 10 h for HA-Cont and HA-Combo, and after 24 hours for HA-Glu and HA-Arg.

Table 4.3. AAs adsorbed to HA particle surfaces after 2 days of reaction.

Sample	HA-Glu	HA-Arg	HA-Combo
Adsorption of AAs to particles (mmol/m <sup>2</sup> )	0.12±0.03	$0.39\pm0.07$	$0.19\pm0.02$



**Fig. 4.11.** [Ca] (a) and [P] (b) in the supernatant solution for HA-Cont, HA-Combo, HA-Glu, and HA-Arg samples.



**Fig. 4.12.** Bulk Ca/P atomic ratios as measured by ICP-AES on HA-Cont, HA-Glu, HA-Arg, and HA-Combo at precipitation time and after 2 days of reaction. Asterisk (\*) indicates the sample that was significantly different from HA-Glu, HA-Arg, and HA-Combo samples synthesized after 2 days (P < 0.05).

ICP-AES was also used to measure the amounts of Ca and P present in the precipitates. The resulting Ca/P atomic ratios are reported in **Fig. 4.12**. Values of ~1.55 were obtained for all samples except for HA-Cont after 2 days, which showed a significantly higher Ca/P ratio (1.76). Since the stoichiometric Ca/P value for HA is 1.67, these results confirm that the samples prepared in the presence of AAs never become fully crystalline HA, and are Ca-defective not

only at their surface, where much lower Ca/P ratios were measured by XPS (**Fig. 4.10**), but also in the bulk. The achievement of a higher Ca/P value after 2 days of reaction for HA-Cont may indicate that this sample was more crystalline than the others, as previously observed in the XRD spectra (**Fig. 4.6**), which showed a smaller background for HA-Cont synthesised after 2 days than for the AA-containing samples.

#### 4.5. Discussion

We investigated the effect of Arg, Glu, and their combination on HA crystallization with a number of techniques. From all the results obtained, we can outline three main discussion items.

1) The positively charged AA, Arg, showed the strongest inhibitory effect on HA precipitation and the largest adsorption on HA, while the negatively charged AA, Glu, had the strongest effect on HA crystallization. Specifically, all of our results pointed out that Arg had the largest ability to inhibit HA nucleation (Fig. 4.1), it was adsorbed in more massive amounts to HA while it nucleated, and it remained adsorbed on the HA particles during the growth stage (indeed, as evidenced by IR (Fig. 4.8), XPS (Fig. 4.9), and colorimetric techniques (Table 4.3), Arg was more abundant both at precipitation time and after 2 days of reaction). Despite this, the presence of Glu (alone or in combination with Arg) was more effective at inhibiting HA crystal growth (Fig. 4.7).

We can explain the stronger inhibitory effect of Arg on HA nucleation by considering what happens during crystal formation. At nucleation, the AAs present in solution can inhibit crystal formation by chelating the ions that form the crystals. We review here briefly what has been reported on complex formation between Arg and Glu and  $Ca^{2+}$  and  $PO_4^{3}$ .

• Interactions with  $Ca^{2+}$ . Clarke and Martell have investigated the formation of  $Arg/Ca^{2+}$  complexes at different pH, and they observed that at pH 7.4 complexes of the form  $HArgCa^{2+}$  are formed, whose stability constant (log K) is 2.21 [299]. To form such complexes, Arg (normally in the form  $H_2Arg^+$  at pH 7.4) loses the proton in the  $\alpha$ -amino position. Complexes between Glu and  $Ca^{2+}$  are more heavily investigated [300]. Lumb and Martell estimated a value for log K of 1.43 for the formation of such complexes [301], and more recently De Stefano et al estimated a value of 1.7 [302]. Both works hypothesize the formation of complexes of the type  $(CaHGlu)^+$ , where Glu is in the form  $HGlu^-$ . This is the chemical species we expect for Glu at pH 7.4, in which the  $\alpha$ -amino is neutral, and one of the carboxylate groups is deprotonated. Lumb and

Martell [301], who analyzed this complex in detail, concluded that the carboxylate group involved is the  $\alpha$ , and not the  $\gamma$ -carboxylate. In fact, Ca<sup>2+</sup> would be interacting both with the  $\alpha$ -carboxy and the  $\alpha$ -amino group. This hypothesis is in agreement with findings from older studies [303] focusing on interactions between Ca<sup>2+</sup> and compounds containing both amino and carboxylate groups. By comparing the log K values reported for Arg/Ca and Glu/Ca complexes, we can conclude that Arg can interact more strongly with Ca than Glu. This is confirmed by a recent mass spectroscopy study by Ho et al [304], who showed that among the 20 AAs, Arg is the one creating more stable homodymer complexes with Ca ions (Ca<sup>2+</sup>(Arg)(Arg)).

Interactions with PO<sub>4</sub><sup>3-</sup>. Arg is well known for its ability to interact with phosphate groups, and in fact this interaction is crucial in the stabilization of protein/nucleic acid complexes [305]. In these complexes, Arg is positively charged (H<sub>2</sub>Arg<sup>+</sup>), and phosphate groups interact with the guanidyl side chain of Arg [306]. A stability constant of 1.9 is reported by Lancelot et al for this complex [306]. Glu/phosphate interactions, on the other hand, are not heavily investigated, most likely because they are not very strong. In fact, we could not find reported stability constants for complexes involving Glu and phosphate or phosphonate groups. To estimate the value of this constant, we can consider a study by Luscombe et al [307]. In this work, the authors analyzed the interactions between the 20 AAs and the bases and backbone groups of DNA by modeling 129 protein-DNA structures. With respect to interactions with phosphate groups in all the structures analyzed, Arg was the AA that formed the largest number of H-bonds and water-mediated bonds, and was second only to Lys in the number of van der Waals bonds formed. Glu instead was among the AAs forming the least number of bonds with phosphate groups. If we just consider the difference in number of H-bonds observed in these 129 structures for Arg/phosphates and Glu/phosphates, we can roughly estimate the stability constant of Glu/PO<sub>4</sub><sup>3-</sup> to be 0. 34 (see SI. 4.2 for more detail). These values clearly show that Arg has a much stronger tendency than Glu to interact with both Ca<sup>2+</sup> and PO<sub>4</sub><sup>3-</sup>, thus indicating that these ions are less free to form calcium phosphate nuclei in the presence of Arg than of Glu. We hypothesize that this can explain why we observed a longer delay in HA precipitation in the presence of Arg than Glu (Fig. 4.1), and we found less precipitate after 2 days in the presence of Arg (Fig. 4.2). Also, the stronger tendency of Arg to interact with the ions in solution can explain why larger amounts of Arg than Glu were present in the HA-Arg sample at precipitation time (Fig. 4.9).

The effect of AAs on crystal growth is more complex than on nucleation, because during crystal growth AAs can both chelate the remaining ions and interact with the growing HA nuclei. HA particles at pH 7.4 are negatively charged, due to the presence of Ca vacancies and to the acidic pKa of HA surfaces [11, 52, 308, 309]. Therefore, a stronger electrostatic interaction should occur between HA growing nuclei and the positively charged AA, Arg. Indeed, our XPS (Fig. 4.9) and colorimetric results (Table 4.3) showed the highest adsorption of Arg on HA after 2 days of reaction. These results seem to confirm Jack et al's results, who measured greater affinity constants of positively charged AAs towards HA surfaces [52], while dispute Koutsopoulos and Dalas' results, who instead showed higher affinity of negatively charged AAs for HA surfaces [53]. However, more specific interactions need to be considered to explain the effect on crystal growth inhibition in specific directions. Several studies show that the chemical interactions between the zwitterionic alpha amino and carboxylate groups and Ca and O atoms at HA surfaces are more crucial in determining the interactions between HA and AAs than the electrostatic interactions of AA side residues [52, 310, 311]. Jack et al showed that the main interaction between AAs and HA surfaces is through the covalent bonding between -COO and calcium ions [52]. Therefore, the stronger chemical bonding between Glu and HA surfaces might have been responsible for the stronger inhibitory effect of Glu on HA crystal growth despite of its lower adsorption to HA surfaces.

Also, here we found that both Arg and Glu were more effective in inhibiting crystallite growth along the [310] than the [002] direction (**Fig. 4.7**). This can be explained by considering the higher surface free energy of the (100) plane (almost perpendicular to [310]) than the (001) plane (perpendicular to [002]), and also the higher polarity of the (100) plane, which make it more favourable to interact with dipolar molecules like AAs [312]. Also, there are 6 equivalent (100) surfaces in HA crystal while there are only 2 equivalent (001) surfaces. Therefore, the (100) surfaces are more prone to interact with the AAs, and the crystal growth is more influenced along their perpendicular [310] direction. Our results also showed that Glu was more effective than Arg in inhibiting crystallite growth along [310]. In line with the results reported in this paper, Palazzo et al showed that AAs had the ability to inhibit HA crystal growth [11]. However, they reported the equal inhibitory effect for the negatively, positively and non-charged AAs while in this work we showed that the negatively charged AA, Glu, was more effective in reducing crystal growth along [310] axis. This discrepancy may be attributed to the different

experimental conditions, such as lower pH and different precursors used in this experiment for HA precipitation.

The larger adsorption of Arg on HA compared to Glu might also be responsible for the lower ssa and porosity observed for HA-Arg particles (**Fig. 4.5 and Table 4.2**). In fact, both Arg and Glu caused a decrease in ssa when present separately during the synthesis of HA; this has to be related to the formation of compact spherulitic particles, which have lower ssa compared to the loser aggregates formed in the absence of AAs. The larger decrease observed for HA-Arg can be attributed to the higher adsorption of this AA on HA. The presence of Arg could screen the negative charge on HA nanoparticles, thus decreasing their electrostatic repulsion and allowing them to get in more intimate contact and form microsphares with lower overall ssa.

2) At precipitation time, both AAs induced the formation of spherulitic particles, while only random aggregates were found in the presence of tris alone (Figs. 4.3 and 4.4). The formation of HA spherulites under the influence of AAs and other organic additives is also reported by other authors [313, 314], but the mechanism by which these small molecules induce such a micron-scale ordering is still unclear. Granary et al showed that spherulitic particles form by growth front nucleation (GFN) in which new crystals nucleate at the surface with a different lattice orientation than the parent crystal [315]. Thermodynamically, GFN is favored at higher supersaturation since the nucleation driving force is higher relative to the orientational mobility of crystals [313, 314, 316, 317]. With increasing driving force, the branching frequency increases and the particles assume an overall spherulitic morphology. However GFN can also be favored by kinetic factors, in systems where new crystals nucleate on random sites on the growing crystals surfaces, rather than in continuous layer-by-layer structures on the parent crystal, as would be predicted by the classical growth mechanism [316]. In fact, spherulite formation strongly depends on the surface structure of the growing seed crystals [318]. The formation of complexes between the AAs and Ca<sup>2+</sup> and PO<sub>4</sub><sup>3-</sup> ions (see Section 4.5.1 and discussion relative to Fig. 4.11) indicates that the overall concentration of free Ca<sup>2+</sup> and PO<sub>4</sub><sup>3-</sup> ions should be lower in the AA-containing samples compared to the control sample. Thus, the effective supersaturation at which precipitation occurs in the AA-containing samples should be lower than in the control sample. This implies that the observation of more spherulitic particles for HA-Glu and HA-Arg than HA-Cont and HA-Combo cannot be explained based on thermodynamics. Instead, the presence of AAs interacting with the growing crystalline surfaces (confirmed by both IR (Fig.

**4.8**) and XPS (**Fig. 4.9**) results) may provide differently charged sites for the random nucleation and growth of HA, thus kinetically favouring spherulite formation. The XRD results shown in **Fig. 4.7** confirmed that the GFN mechanism was more favoured for the HA-Arg and HA-Glu than the HA-Cont and HA-Combo samples: the average crystallite size along [310] increased with time for HA-Cont and HA-Combo while the crystallite size along [310] decreased for H-Glu, and didn't significantly change for the HA-Arg. This is consistent with the GFN mechanism for HA-Arg and HA-Glu: on these samples, new crystals grow with different orientations relative to the parent crystals, thus resulting in smaller average crystallite sizes and no significant overall crystal growth, differently from the classical model in which the parent crystal grows continuously [61].

3) The combination of Arg and Glu in the same solution resulted in a much smaller effect on HA precipitation than when any of the AA was present alone. Specifically, we observed fewer AAs adsorbed on HA particles in HA-Combo than on HA-Arg or HA-Glu (Figs. 4.8 and 4.9), a more similar surface Ca/P ratio for this sample to HA-Cont (Fig. 4.10), weaker effect on precipitation time (Figs. 4.1 and 4.11) and precipitate weights (Fig. 4.2), and on the morphology of HA particles during the early stage of precipitation (Fig. 4.3g and h). These results can be explained by considering that when the two AAs are present in solution together, they have a higher tendency to interact with each other rather than with the ions in solution. Indeed, the interaction between Arg and carboxylate groups is known to be very strong, and crucial in the selective recognition of nucleic acid base sequences by proteins containing Arg in their structure [305]. This strong interaction is due to the formation of ion pairs between the positively charged guanidyl side groups of Arg and negatively charged γ-carboxylate groups of Glu [319]. The reported log K for this interaction is 2.3 [306], which is higher than any of those reported for Arg or Glu and Ca<sup>2+</sup> or PO<sub>4</sub><sup>3-</sup> [299, 301, 306]. This high constant can also help explain why some of the HA-Combo results were more similar to HA-Glu than to HA-Arg (see the results relative to crystal size (Fig. 4.7), surface area (Fig. 4.5) and affinity to HA surfaces (Table 4.3)). Indeed, Arg can interact with carboxylate groups from both Glu and from other Arg molecules. Hence, more Glu than Arg is free in solution to interact with growing HA nuclei.

These observations imply that if more than one type of AAs is present in solution, the effects of the single AAs do not simply add up. Rather, they can end up damping each other, because the AAs can form complexes among themselves rather than with the ions in solution.

This behaviour would be observed to a much lower extent if the AAs were bound together along protein or peptide chains, since their ability to combine with each other would be severely limited. Still, the affinity constant between Arg and carboxylate groups is almost as high as that measured for poly(Glu) and HA (199.5 [306] vs. 240 [39], respectively), which indicates that even in the presence of proteins or peptides, complexes formed between terminal AAs and side groups of AAs could be partially responsible for the overall effect observed on HA formation.

#### 4.6. Conclusion

Polar and charged AAs are the main components of NCPs, and are involved in HA mineralization in bone. These AAs are able to inhibit HA mineralization by binding to the nuclei of HA and preventing their further growth. Here we investigated the effect of a positively charged AA, Arg, and a negatively charged one, Glu, as well as their combination, at physiological pH and temperature. Our results showed that the positively charged AA, Arg, had a stronger inhibitory effect on HA formation, and was adsorbed in larger amount on HA particles, while the negatively charged AA, Glu, was more effective in inhibiting HA crystal growth along specific crystallographic directions. These results were interpreted in terms of the differences in stability constants between AAs and the ions in solution. The formation of AA/ion complexes was also deemed responsible for the observed formation of spherulitic particles in the presence of either Arg or Glu. We also showed that the inhibitory effect of the single AAs on HA nucleation was dampened if the two AAs were present together in solution, which we interpreted to be a consequence of the preferential interaction of the AAs with each other rather than with ions or nuclei in solution.

Overall this work gives a basis for the understanding of the effect of single AAs on HA mineralization in physiological conditions, and may provide a guideline to rationally design oligopeptides with the purpose of inhibiting HA nucleation. These could be used for treating pathological diseases caused by an excessive mineralization of HA in tissues like cartilage, blood vessels and cardiac valves.

#### 4.7. Acknowledgement

This research project is funded by McGill Engineering Doctoral Award (MEDA) and by the Canada Research Chair foundation.

#### SI. 4. Supporting information

This document contains a comparison between the XRD patterns measured on our samples and the reference octacalcium phosphate (OCP) pattern (SI. 4.1), as well as the estimation of the stability constant for the  $Glu/PO_4^{3-}$  complex based on the results shown in reference 1, corresponding to reference 56 in the main paper (SI. 4.2).

### SI. 4.1. XRD pattern of precipitates synthesized after 2 days, in comparison with the XRD reference pattern of OCP.

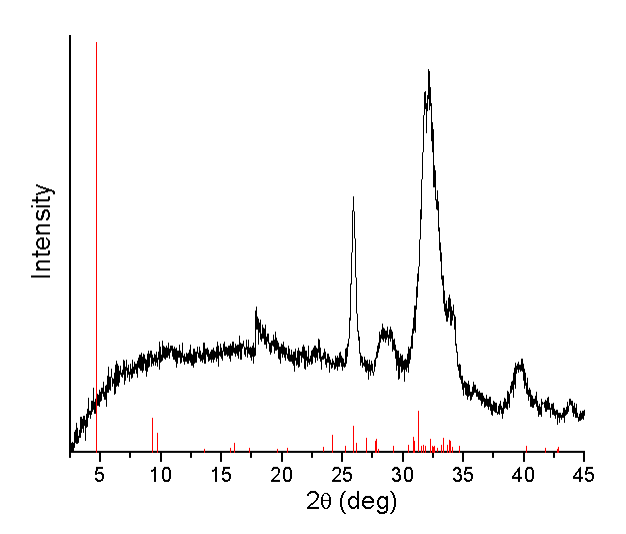


**Fig. S4.1.** XRD patterns of HA-Glu collected after 2 days, measured for 2θ ranging from 2.5 to 45°. The red lines represent the reference spectrum of OCP (PDF card n. 01-074-1301).

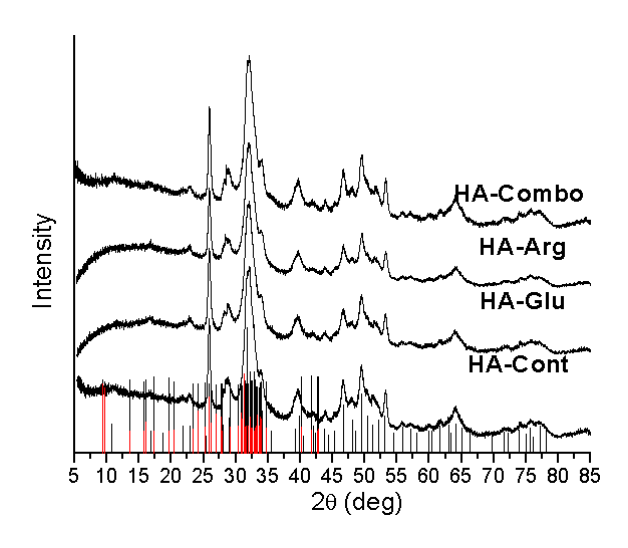


**Fig. S4.2**. XRD patterns of HA-Cont, HA-Glu, HA-Arg, and HA-Combo collected after 2 days (2θ range between 5 and 85°), compared with reference spectra for HA (black lines, PDF card n. 00-009-0432) and for OCP (red lines, PDF card n. 01-074-1301).

#### SI. 4.2. Estimate of the stability constant of Glu/PO43- complex formation

Luscombe et al [307] studied the interactions between AAs and DNA bases and backbone groups, based on the modeling of 129 different protein-DNA complexes. In the 129 structures studied:

- a) Arg was found to interact with phosphate groups extensively: H-bonds were observed 218 times, Van der Waals bonds 238 times, and water-mediated interactions were observed 113 times.
- b) Glu was found to interact to a very low extent with phosphate groups. H-bonds were observed only 6 times, Van der Waals bonds 61 times, and water-mediated bonds 29 times.

Among these interactions, H-bonds are the strongest ones. So if we just consider the number of H-bonds observed in these structures we can have *a very rough* estimate of how much stronger the Arg/PO<sub>4</sub><sup>3-</sup> interaction is compared with Glu/PO<sub>4</sub><sup>3-</sup>. Within these structures, the number of H-bonds observed between Arg and PO<sub>4</sub><sup>3-</sup> groups was 36 fold larger than between Glu and PO<sub>4</sub><sup>3-</sup>. This would indicate that Arg/PO<sub>4</sub><sup>3-</sup> complexes are approximately 36 times more likely to occur than Glu/PO<sub>4</sub><sup>3-</sup> complexes, which could mean that (very roughly) the stability constant of Glu/PO<sub>4</sub><sup>3-</sup> complexes would be 36 fold smaller than that of Arg/PO<sub>4</sub><sup>3-</sup> complexes. Based on this estimate and on the value of 1.9 reported for log K Arg/PO<sub>4</sub><sup>3-</sup> complexes [320], we can estimate that the stability constant of Glu/PO<sub>4</sub><sup>3-</sup> complexes would be approximately 0.34:

This is of course just an estimate. We are in the process of performing some calorimetric measures in order to find an experimental value for this constant. A paper describing the results of these measures will be published soon.

#### **CHAPTER 5**

# ROLE OF AMINO ACIDS DISSOLVED IN SOLUTION ON THE PRENUCLEATION STAGE OF HYDROXYAPATITE PRECIPITATION

In the previous chapter, we investigated the effect of Arg and Glu on HA precipitation, with a focus on what happens at the nucleation stage. In this chapter, we study the effect of these AAs on the prenucleation stage. To achieve this goal, we aged the precursor solutions containing Ca<sup>2+</sup> and PO<sub>4</sub><sup>3-</sup> ions and the AAs (Arg or Glu) for 3 days before mixing them to achieve HA precipitation. Aging provides a sufficient time for ions/AA aggregates to form and grow before HA nucleates. The formation of these aggregates delayed HA precipitation much more than when the AAs interacted with the ions in the form of small complexes.

The findings of this work are reported in an article published in the journal "Crystal Growth and Design".

# Amino acid/ion aggregate formation and their role in hydroxyapatite precipitation

M. Tavafoghi Jahromi, M. Cerruti

Materials Engineering, McGill University, Montreal, QC, Canada, H3A 2B2

Emails: maryam.tavafoghijahromi@mail.mcgill.ca; marta.cerruti@mcgill.ca

#### 5.1. Abstract

Hydroxyapatite (HA, Ca<sub>5</sub>(PO<sub>4</sub>)<sub>3</sub>OH) constitutes the inorganic component of bone. Its formation is regulated by non-collagenous proteins, and especially negatively charged amino acids present in their structure. Here we show that Ca<sup>2+</sup> and PO<sub>4</sub><sup>3-</sup> ions can interact with both a negative (Glu) and a positive (Arg) amino acid, and form aggregates that grow if left undisturbed. Depending on how long these aggregates are allowed to grow for, once they come into contact they give rise to HA crystals that form at different times and that differ in content and properties. This finding points out that the aging time of precursor solutions is an important variable that needs to be taken into account in all biomineralization experiments, and that not only proteins but also small molecules like amino acids can form aggregates that alter biomineral formation. The formation of biomolecular aggregates in the aged precursor solutions may also mirror what happens in-vivo, where biominerals are formed upon compartmentalization of precursor ions and mineralization inhibitors or promoters.

#### 5.2. Introduction

Precipitation from solution is one of the most frequent operations in industries and laboratories, and is crucial in natural processes such as biomineralization [21, 22]. Precipitation involves two stages: nucleation and growth [21, 22]. Nucleation happens in a supersaturated solution, when metastable nuclei of a critical size form by stochastic solute clustering [20]. Recent studies [24-31, 57, 321] have attempted to probe the organization of solute clusters even before the formation of critical size nuclei; these clusters, often referred to as prenucleation clusters (PCs) [28, 29, 57], have been found to play a dominant role in the precipitation of organic [23] and inorganic compounds [20], and when crystals are formed within living organisms (biomineralization) [24]. For example, several studies have shown that ionic PCs are a prerequisite for the formation of calcium carbonate [20, 28, 322]. Liquid-like calcium carbonate clusters stabilized by organic additives, such as polyaspartate and acidic poly peptides have also been found as precursors for calcium carbonate [25, 26]. PCs have been studied for hydroxyapatite (HA) too [139, 142, 323].

While nanometer-sized PCs are formed in inorganic systems, larger clusters with liquidlike properties have been discussed as metastable precursors for the formation of crystals of many organic substances, including proteins and amino acids [57]. These large aggregates may exist in equilibrium with smaller clusters. For example, nanodroplets of  $\sim 250$  nm diameters were found as solid glycine dissolved in water, in equilibrium with smaller molecular clusters; however glycine crystallization seemed to occur preferentially within larger nanodroplets of  $\sim 750$  nm diameter [324].

HA precipitation within a collagen matrix is probably the most well-known example of biomineralization [325-329]. HA nucleation and growth is directed by a set of non-collagenous proteins (NCP), which can either promote or inhibit its nucleation and growth [330]. The mechanism by which NCPs act is still under discussion: negatively charged amino acids (AAs) are highly expressed in their structure; however positively charged and polar AAs can inhibit HA formation too, and can influence HA particle size and crystallinity [10, 11, 43, 45, 50, 185, 188, 331]. In fact, contradictory results have been published on the role of AAs dissolved in reaction solutions with concentrations ranging from 0.2 to 160 mM on HA nucleation. We have previously shown that a positive AA (arginine, Arg) inhibited HA precipitation more than a negative AA (glutamic acid, Glu), and attributed this to the stronger complexes formed between Ca<sup>2+</sup> and PO<sub>4</sub><sup>3-</sup> and Arg vs. Glu [331]. Here we show that AA/precursor ion complexes can grow into larger aggregates, which contain AAs and traces of inorganic ions; they differ in size depending on which ion/AA pair they contain. Most importantly, it is these aggregates rather than just the small molecular-ion complexes that determine HA precipitation time and its composition and properties. This study thus links the formation of AA/ion aggregates with HA nucleation and growth. We show that such complexes should be treated as chemical entities reacting with each other and with other molecules present in the system, following different reaction pathways and giving rise to different reaction products according to the environment.

#### **5.3.** Materials and methods

#### 5.3.1. Materials

Calcium (Ca) and phosphate (P) precursors were calcium chloride dehydrated (CaCl<sub>2</sub>, Sigma Aldrich, purity >97%) and sodium phosphate monobasic anhydrous (NaH<sub>2</sub>PO<sub>4</sub>, purity > 99%, Fisher Scientific). The amino acids used in the study (L-Arginine, purity  $\geq$  99.5%, and L-Glutamic acid, purity  $\geq$  99.5%) were purchased from Sigma Aldrich, as well as the buffer agent tris(hydroxymethyl)aminomethane (tris, purity  $\geq$  99.5%). Hydrochloric acid used to adjust pH was purchased from Fisher.

#### 5.3.2. HA synthesis

Ca- and P-precursor solutions were prepared by mixing CaCl<sub>2</sub> (6.22 mM) or NaH<sub>2</sub>PO<sub>4</sub> (3.74 mM) with AAs (Arg and/or Glu, 10 mM) and tris (100 mM) as a buffer agent. These precursor solutions are called Ca-Arg-ps and Ca-Glu-ps in the manuscript. Control solutions (Ca-Cont-ps) were prepared with identical CaCl<sub>2</sub>, NaH<sub>2</sub>PO<sub>4</sub> and tris concentration, in the absence of any AA (see **Table 5.1**). The pH of both Ca- and P-precursor solutions was adjusted to 7.4 using adequate amounts of concentrated HCl, and the temperature was adjusted to 37°C by placing the reaction vessels in a water bath equipped with a temperature controller (ColeParmer PolyStat Immersion Circulator). The supersaturation of reaction solution was 123 with respect to HA precipitation.

The Ca- and P-precursor solutions were either mixed right after making the solutions (0 day aging) or mixed after allowing them to age for 3 days. For the precipitation experiments, the same volume of Ca- and P-precursor solutions were added to the reaction vessel simultaneously, thus reaching final Ca and P concentrations of 3.11 and 1.87 mM, respectively. The ratio between these concentrations matches the physiological Ca to P ratio, but the absolute values are approximately 1.5 times higher than those found in human blood plasma, and they were chosen in order to decrease the required incubation time prior to precipitation.

**Table 5.1**. Concentrations of Ca, P and AAs in precursor solutions.

Sample	Ca Conc. (mM)	P Conc. (mM)	Glu Conc. (mM)	Arg Conc. (mM)
Ca-Cont-ps	6.22	0	0	0
Ca-Glu-ps	6.22	0	10	0
Ca-Arg-ps	6.22	0	0	10
P-Cont-ps	0	3.74	0	0
P-Glu-ps	0	3.74	10	0
P-Arg-ps	0	3.74	0	10

The pH of the reaction solution was monitored, and kept constant at 7.40±0.05 using tris as a buffer agent. The reaction solution was stirred at 100 rpm and the temperature was kept constant at 37°C. The reaction solutions became visibly cloudy after certain time periods. These times were considered as the precipitation time of samples. The samples were removed from the bath after 2 days of reaction, and the precipitates were filtered using vacuum filtration with filters with pore size of 200 nm, and subsequently washed with DI water for 3 times. The precipitates were finally dried using a VirTis freeze drier. Throughout the paper, we have referred to the samples prepared in the presence of the AAs and the control samples as HA-Glu, HA-Arg, and HA-Cont.

#### 5.3.3. Aggregates collection

Aggregates were collected from the precursor solutions after 30 days of aging using vacuum filtration with filters with pore size of 200 nm. They were then washed with DI water for 3 times and dried using a VirTis freeze drier. Although washing with DI water might remove some of the AAs adsorbed on the aggregates, this is necessary in order to perform further analyses.

#### 5.3.4. Characterization techniques

*X-ray diffraction (XRD):* XRD spectra were collected using a Bruker AXS XRD instrument with Cu  $K_{\alpha}$  radiation generated at 40 kV and 40 mA. A quartz sample holder was used. Diffraction angles collected (20) ranged from 5 to 100°, with step size of 0.05°.

X-ray photoelectron spectroscopy (XPS): XPS measurements were performed using a monochromatic X-ray photoelectron spectrometer K Alpha (Thermo Scientific). The setup was equipped with an Al Kα X-Ray source (1486.6 eV, 0.834 nm), a micro-focused monochromator and an ultrahigh vacuum chamber (10<sup>-9</sup> Torr). The survey scans were collected with energy steps of 1 eV and spot size of 50 μm. Scans were taken on at least 3 points on each sample and the quantitative results were averaged. The high resolution scans were collected with energy steps of 0.1 eV and a spot size of 400 μm on at least 3 points. The spectral energies were calibrated by setting the binding energy of the C1s component corresponding to C=C-C bonds at 284.4 eV. A flood gun was used to neutralize electrical built-up charge generated on the non-conductive samples. Peak-fitting procedures and the quantitative analyses of survey spectra were performed using the software Thermo Avantage (version 4.60).

Inductively coupled plasma atomic emission spectroscopy (ICP-AES): Ca and P concentration in the precipitation (Fig. 5.1c) and precursor solutions (Fig. S5.3) were measured using an ICP-AES instrument (ICAP 6500 Duo). The aliquots were taken from the solutions at desired times, filtered with centrifugation filters (Amicon Ultra-4 Centrifugal Filter Unit with Ultracel-3memberane, Millipore) with pore size of 4 nm for 3 h at 4000 rpm to remove any trace of aggregates or precipitate, and then immediately diluted with 4% nitric acid. The dilution with 4% nitric acid ensured that no more precipitate formed in the solutions after filtration. The Ca and P concentrations were measured at the wavelength of 317.9 and 178.3 nm, respectively.

Scanning electron microscopy (SEM): The particle morphology was analyzed with a scanning electron microscope (SEM) from Hitachi (S-4700 FE-SEM), using an acceleration voltage of 5 kV. The specimens were mounted on double sided conductive carbon tape and were coated with a thin layer of Au to increase their conductivity. The coating was done with a HUMMER VI sputtering system under vacuum of 70 millitorr and at the voltage of 10 V for 1 min.

Transmission electron microscopy (TEM): we used a high resolution TEM (Philips CM200) with line resolution of 0.17 nm and operating voltage of up to 200 kV. The TEM was fitted with LaB6-cathode thermoionic gun and genesis EDAX detector. Images were digitized using a high-resolution Gatan 2kX2k CCD camera. To prepare the TEM samples, 4 ml of Ca-and P-precursor solutions aged for 0 and 3 days were poured in centrifugation filtering tubes and centrifuged for 3 h at 4000 rpm. The solution remaining on the top of the filter (50 μl) was washed 3 times with 2 ml of deionized water, and then a drop of this solution (5 μl) was placed on a TEM grid (200-mesh carbon-coated Cu TEM grids, SPI Supplies). The same procedure was followed to collect the samples obtained after mixing the precursor solutions. Finally, the grids were dried overnight in air and were analyzed under TEM.

#### 5.4. Results

We prepare HA precursor solutions containing tris buffer, Ca<sup>2+</sup> and PO<sub>4</sub><sup>3-</sup>, both with and without AAs, and perform two sets of precipitation experiments. In the first set, we mix the precursor solutions right after preparing them; in the second set we age these solutions for three days prior to mixing. All evidence showing the effect of Ca- and P-precursor solution aging on HA precipitation is summarized in Figs. 5.1, 5.2, 5.3, and 5.4. Aging delays HA precipitation in both Glu- and Arg-containing solutions (the latter to a higher extent), while no delay is observed in the absence of AAs (Fig. 5.1a). Aging in the presence of AAs also decreases the amount of precipitate collected (Fig. 5.1b). HA precipitation inhibition caused by aging the AA-containing precursor solutions is also shown by the delay in [Ca] decrease in the supernatant solution (Fig. **5.1c**). The slower precipitation induced by aging the AA-containing precursor solutions is mirrored by the morphology of the aggregates collected after two days of incubation (Fig. 5.1di). Spherulitic aggregates formed by organized individual platelets are observed only when aged precursors containing AAs are used (Fig. 5.1h and i). This is to be attributed to the slower precipitation achieved for these samples (Fig. 5.1a), which provides enough time for the platelet formation and arrangement [331]. XRD spectra show that all samples are HA (Fig. 5.1j and k). However an amorphous background signal especially evident at low values of  $2\theta$  is present on the spectra of the HA recovered from the AA-containing aged solutions, while it is not present in the spectra collected in the absence of AAs or with non-aged precursors (Fig. 5.1j and k). A lower surface Ca/P ratio is measured on the samples prepared with AA-containing aged solutions (Fig. 5.2a), indicative of a surface structure further from HA for these samples. A larger C/Ca ratio is observed on these samples (Fig. 5.2b), indicating the presence of larger amounts of AAs. This is also confirmed by IR spectroscopy (Fig. S5.1).

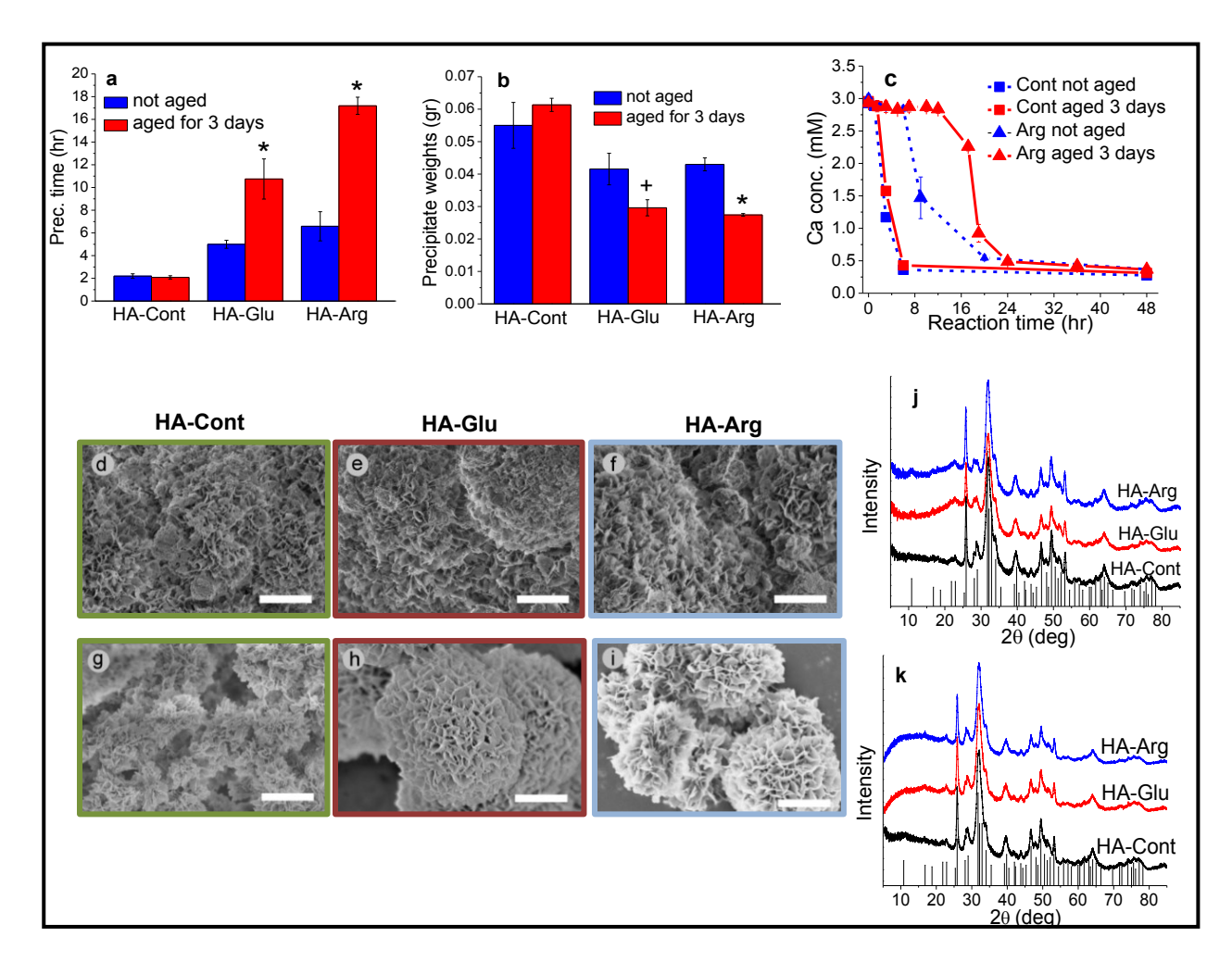


**Fig. 5.1. Effect of precursor solution aging on HA precipitation.** (a and b), Precipitation time determined by visual observation (a) and precipitate weights after 2 days of reaction (b). Each data point is average of at least 3 samples. Asterisks (\*) and plus sign (+) indicate the difference between 3 day and not aged samples was significant with *P*=0.009 and 0.09. The weight of all precipitates is lower than expected if all Ca and P combined to form HA (0.081 g), thus confirming the inhibitory effect of tris and AAs on HA precipitation; (c), [Ca] in supernatant measured by ICP for HA-Cont and HA-Arg with not aged or aged precursors. [Ca] decreases in the supernatant of HA-Arg aged for 3 days earlier than when the visual precipitation occurs on this sample (a), thus indicating formation of Ca-containing nuclei even before visible precipitation. (d-i), SEM images of HA-Cont (d and g), HA-Glu (e and h), and HA-Arg (f and i) with not aged (d-f) or aged precursors (g-i); all samples are collected after 2 days of incubation. Scale bars: 1μm. (j and k), XRD of HA-Cont, HA-Glu, and HA-Arg prepared with precursors not aged (j) or aged (k). Vertical lines represent reference pattern for HA (PDF number: 00-009-0432). Please note that Figs. g-k were also shown in our previous work [331].

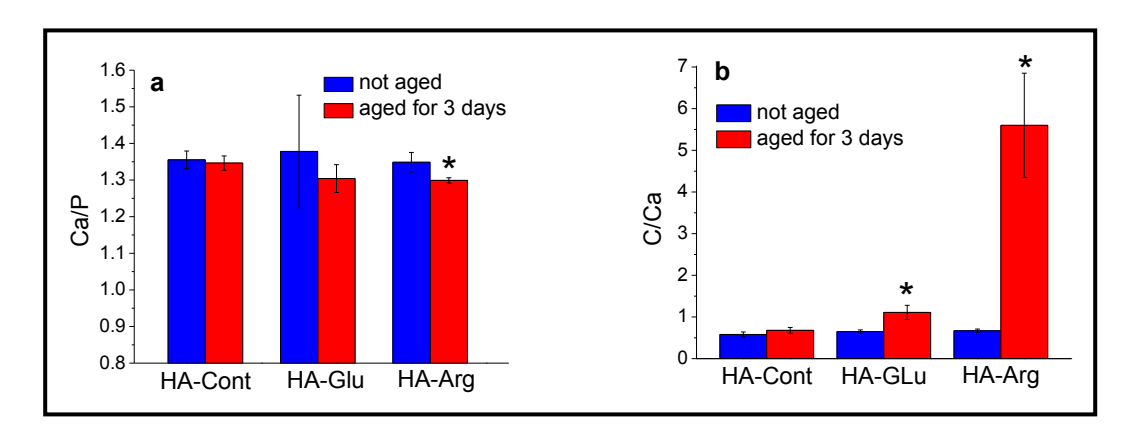


**Fig. 5.2. HA surface composition differs depending on precursor aging.** Ca/P (a) and C/Ca (b) atomic % for HA-Cont, HA-Glu, and HA-Arg collected after 2 days of reaction, measured from XPS survey spectra. Asterisks (\*) indicate that the difference between the samples prepared with aged and not aged precursors was statically significant with P < 0.04. C can originate from two main sources: tris (present in all samples) and AAs (only present in the AA samples). HA-Arg shows significantly higher C/Ca than HA-Glu when the precursors are aged. This indicates that much more organic material is present in this sample, which suggests that Arg incorporates in HA more than Glu. A quantitative estimate is hard to make, since Arg has a longer carbon chain than Glu, and the tris/AA incorporation ratio is not known.

Fig. 5.3 shows TEM images of HA particles collected just before precipitation (see caption for details). The particles formed from aged precursor solutions in the presence of AAs (Fig. **5.3b** and f) are larger than those formed in the not-aged precursor solutions in the presence of AAs (Fig. 5.3j), or with aged precursors without AAs (Fig. 5.3n): HA particles have a diameter of 100±15 (HA-Glu, 3 day aged), 110±23 nm (HA-Arg, 3 day aged), 95±20 nm (HA-Arg, not aged), and 70±20 (HA-Cont). Additionally, the particles formed from aged precursor solutions with AAs are unstable under the TEM beam. This is clearly shown by the formation of round structures at high magnification in these samples (see bright circles in Fig. 5.3c and g), which are indicative of voids. Such examples of beam damage are sometimes seen in HA using high voltage [332]; however a lower voltage is required to damage HA that contains some amorphous component [333]; and biological apatites are more prone to beam damage than synthetic apatites [334]. Very recently Meldrum et al reported the formation of very similar voids on calcite containing organic inclusions [335], using a TEM at a voltage similar to ours. The presence of beam damage on the HA formed in the presence of AAs from aged solutions but not on any of the other samples imaged in the same conditions (Figs. 5.3j-k, and 5.3n-o) is thus a clear indication that the HA-Arg and HA-Glu prepared from aged precursors contain some organic

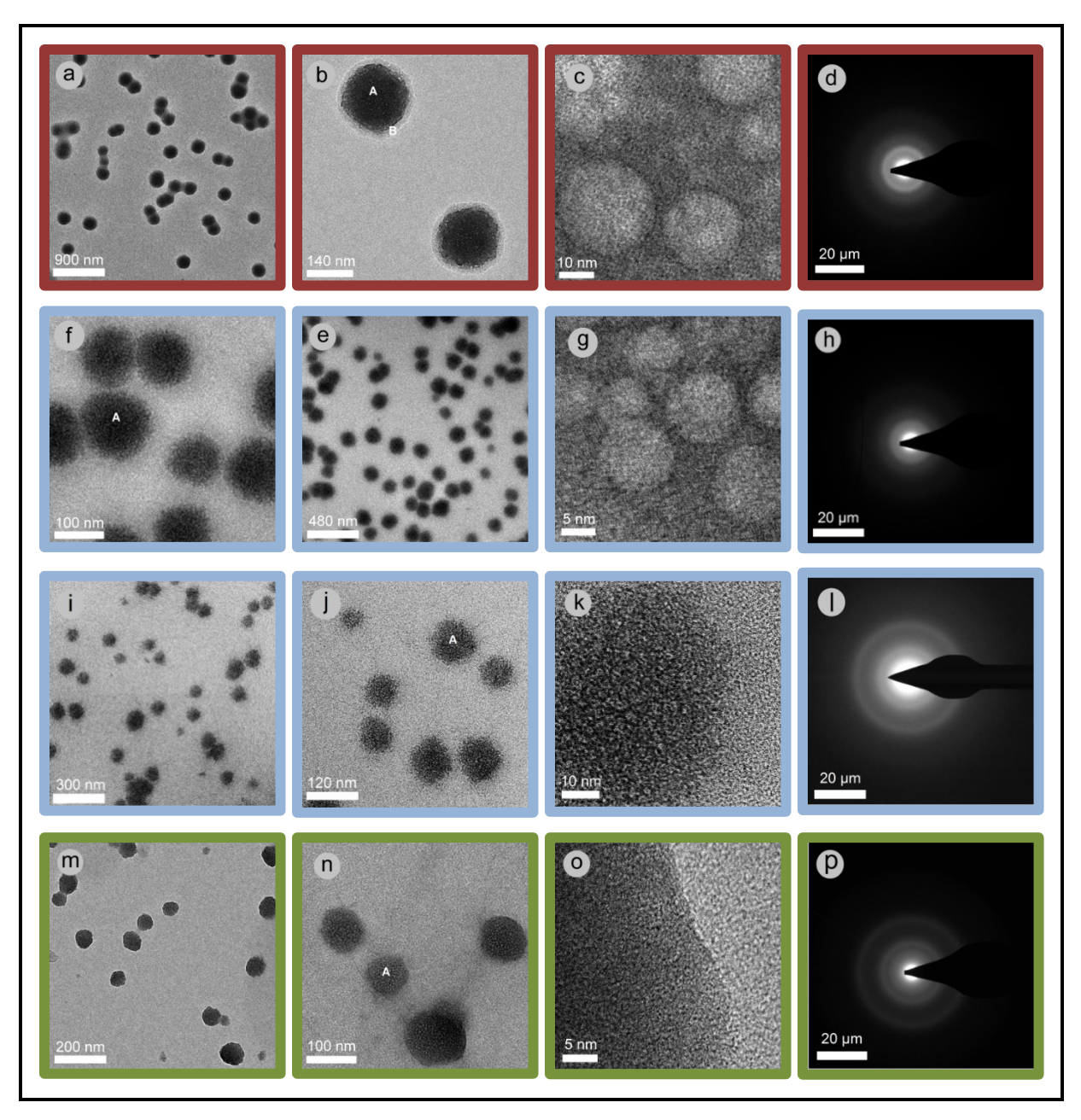


**Fig. 5.3. Aging precursor solutions that contain AA drastically changes HA structure.** TEM images and SAED patterns of HA formed from 3 day old precursor solutions in the presence of Glu (HA-Glu, a-d), Arg (HA-Arg, e-h), or in the absence of AAs (HA-Cont, m-p), and HA formed from the not aged precursor solutions in the presence of Arg (HA-Arg, i-l). HA particles were collected before visible precipitation, specifically after 1.5 (HA-Cont) and 6 h (HA-Glu and HA-Arg).

material. Indeed, EDS analysis shows that, aside from the omnipresent carbon and some Si and Cl contamination, HA-Arg (**Fig. 5.4c**) and HA-Glu (**Fig. 5.4b**) both contain N, whereas the other samples do not (**Fig. 5.4d and e**). Also, HA-Glu prepared from aged precursors shows the formation of a brighter ring around the particles (**Fig. 5.3b**); this brighter ring contains N (**Fig.** 

**4b**), whereas the interior of the particles does not (**Fig. 5.4a**). The formation of this ring may have occurred under the TEM beam, since organic materials are known to be able to diffuse under the TEM beam [336]. This can be also attributed to drying artifacts that may have occurred during TEM sample preparation. A more in-depth TEM analysis using a cryogenic stage may be able to clarify this point, and is left for future work. The selected area electron diffraction (SAED) patterns indicate that all samples at this stage, i.e. prior to visible precipitation (see caption of **Fig. 5.3** for detail), are almost completely amorphous (**Fig. 5.3d, h, l, and p**); however some rings are more evident in the SAED of HA-Cont aged for 3 days (**Fig. 5.3p**) and HA-Arg not aged (**Fig. 5.3l**), thus indicating a less amorphous structure for these samples. This confirms what observed by XRD on the samples collected after two days (**Fig. 5.1j and k**).

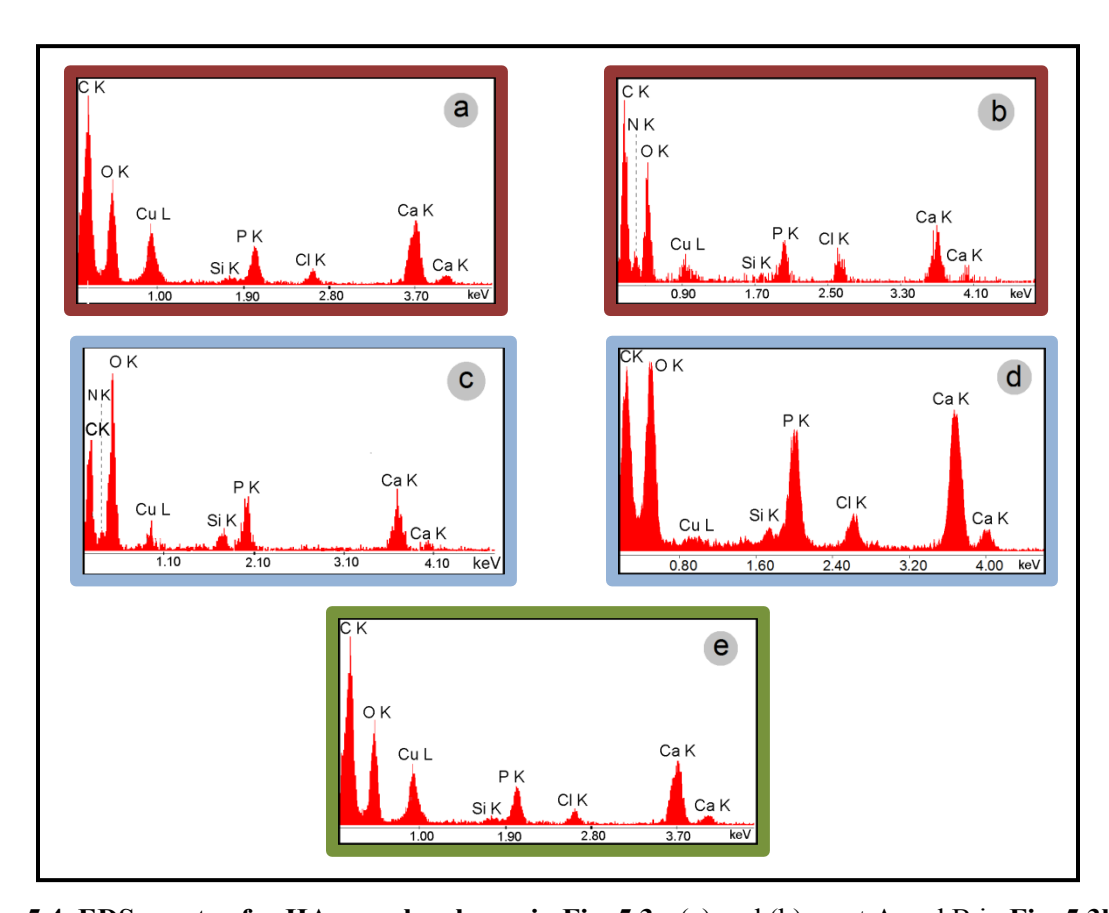


**Fig. 5.4**. **EDS** spectra for HA samples shown in Fig. 5.3: (a) and (b), spot A and B in Fig. 5.3b, respectively; (c), spot A in Fig. 5.3f; (d), spot A in Fig. 5.3j; (e), spot A in Fig. 5.3n. The Cl observed on EDS spectra in a, b, d, and e could have originated from CaCl<sub>2</sub> or HCl.

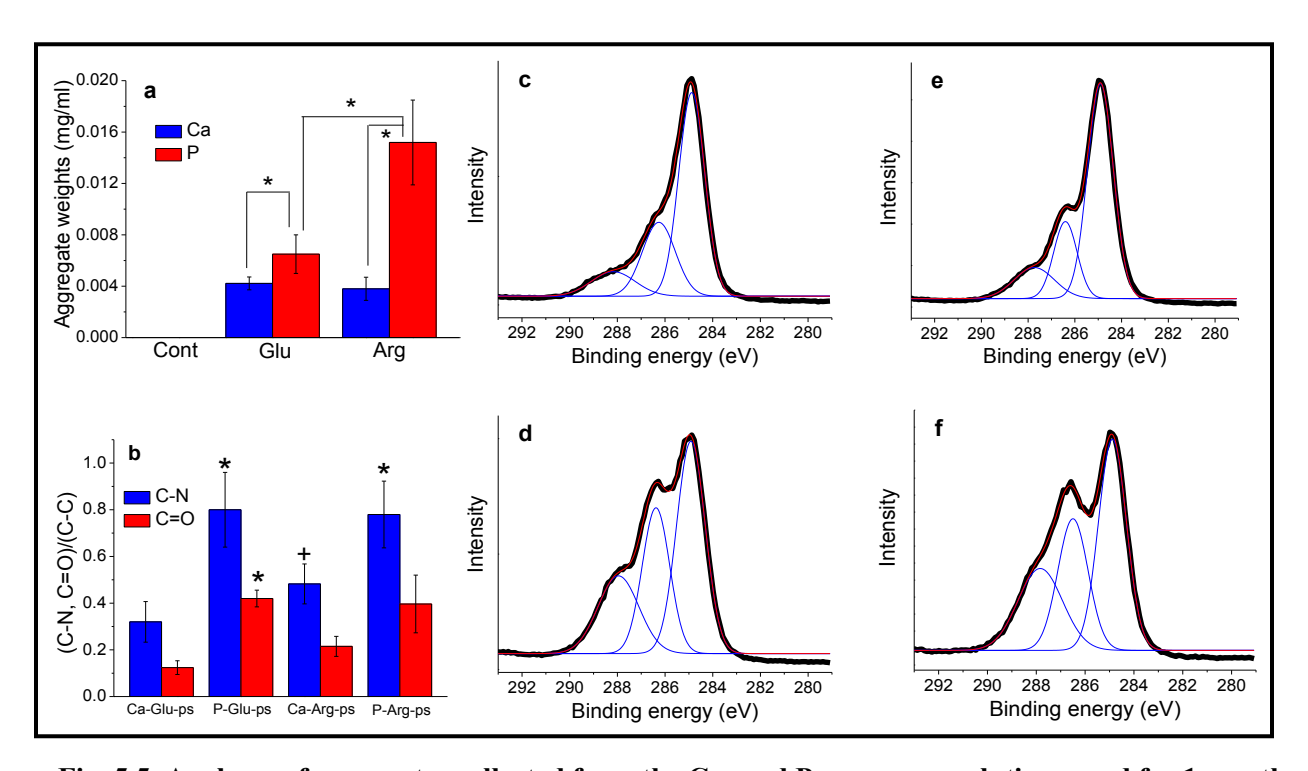


**Fig. 5.5.** Analyses of aggregates collected from the Ca- and P-precursor solutions aged for 1 month. (a) Weight of aggregates collected from precursor solutions by vacuum filtration using filters with pore size of 200 nm. Asterisks (\*) indicate the samples that were statically significantly different with P < 0.05. (b), C-N and C=O atomic % relative to C-C atomic % measured from XPS C 1s high resolution spectra of aggregates collected from Ca-Glu-ps (c), P-Glu-ps (d), Ca-Arg-ps (e) and P-Arg-ps (f). Asterisks (\*) indicate the samples that were statically significantly different from their correspondent samples containing Ca with P < 0.05. (+) indicates the sample that was different from its correspondent sample containing Glu with P < 0.08. Peaks observed on C high resolution spectra (c-f) at 284.9, 286.3, and 288 correspond C-C, C-N, and C=O, respectively. While C-C and C-N bonds are present in both AAs and tris, the C=O component can only originate from the AAs.

All results shown in Figs. 5.1 and 5.2 indicate that aging the AA-containing precursor solutions strongly affects HA precipitation. We hypothesize that this is due to the formation of aggregates containing AAs and Ca<sup>2+</sup> and PO<sub>4</sub><sup>3-</sup> ions (Ca/AA and P/AA aggregates, respectively), growing in the precursor solutions. We will prove this at first by analyzing what is formed in the precursor solutions left to age for 1 month. After this time, some aggregates can be collected from all AA-containing precursor solutions, but none in the absence of AAs (**Fig. 5.5a**). About the same amount of aggregates can be collected from Ca-Arg-ps and Ca-Glu-ps; however, more is obtained from P-Glu-ps than P-Arg-ps, and from P-AA-ps than Ca-AA-ps. The aggregates collected from the aged Ca-AA-ps and P-AA-ps are mostly organic, and contains only trace amounts (<1%) of Ca and P, respectively (**Fig. S5.2**). A larger amount of Ca than P is present in

these aggregates, and specifically more in those formed in the Ca-Arg-ps, as evidenced by the fact that a decrease in [Ca] in the supernatant is detectable only for this sample (**Fig. S5.3**). High resolution C 1s XPS spectra (**Fig. 5.5c-f**) show C-C, C-N, and C=O components in all samples; however, the intensity of the C-N and C=O peak is higher in the spectra of the aggregates collected from the P-AA-ps (**Fig. 5.5b**). This indicates that a larger AA/tris ratio is present in the aggregates collected from the P-AA-ps than the Ca-AA-ps. Similarly, a higher AA/tris ratio is present in the aggregates collected from the Ca-Arg-ps than the Ca-Glu-ps.

The results obtained on precursor solutions aged for one month prove that the complexes formed between AAs, tris, Ca and P grow into larger and larger structures during this time. We can use TEM to analyse these structures after only 3 days of aging, i.e. right before they were mixed to study their effect on HA precipitation. While nothing is observed in the absence of AAs (Fig. 5.6a and b), aggregates of sizes ranging from 4 to 160 nm are found in the AA-containing precursor solutions (Fig. 5.6c-f, see caption for detail on sizes). EDS spectra confirm that these aggregates contain traces of Ca or P, depending if they derive from Ca- or P-precursor solutions. A higher Ca/organic ratio is found in the aggregates formed in Ca-Arg-ps than Ca-Glu-ps (compare EDS spectra from Fig. 5.6c and e), while a comparable P/organic ratio is observed for P-Glu-ps and P-Arg-ps (Fig. 5.6d and f). This result is consistent with the larger decrease in [Ca] observed at later times in the Ca-Arg-ps (Fig. S5.3).

To better understand the composition of the aggregates, we measured [Ca] in situ in the precursor solutions using an ion-sensitive Ca-meter over the course of 3 days. The results (**Fig. S5.4**) show that both AA-containing precursor solutions contain lower amounts of free Ca than the precursor solutions prepared in the absence of AAs. This is consistent with the formation of AA-ion complexes, previously hypothesized to be the cause of the differences in delay of HA precipitation [331]. Still, there are no significant differences between [Ca] measured in the Arg or Glu-containing solution over the course of 3 days. This shows that the amount of complexes between Ca<sup>2+</sup> and PO<sub>4</sub><sup>3-</sup> ions and AAs remain virtually unchanged during the three days, and further confirms that the aggregates are mostly composed by AAs and contain only minor traces of ions. However, since the aggregate size is different for the same AA in the presence of Ca<sup>2+</sup> and PO<sub>4</sub><sup>3-</sup> ions, we conclude that inorganic ions must be part of these structures, and the differences in [Ca] present in the aggregates must be below the sensitivity limit of the Ca meter used in this work.

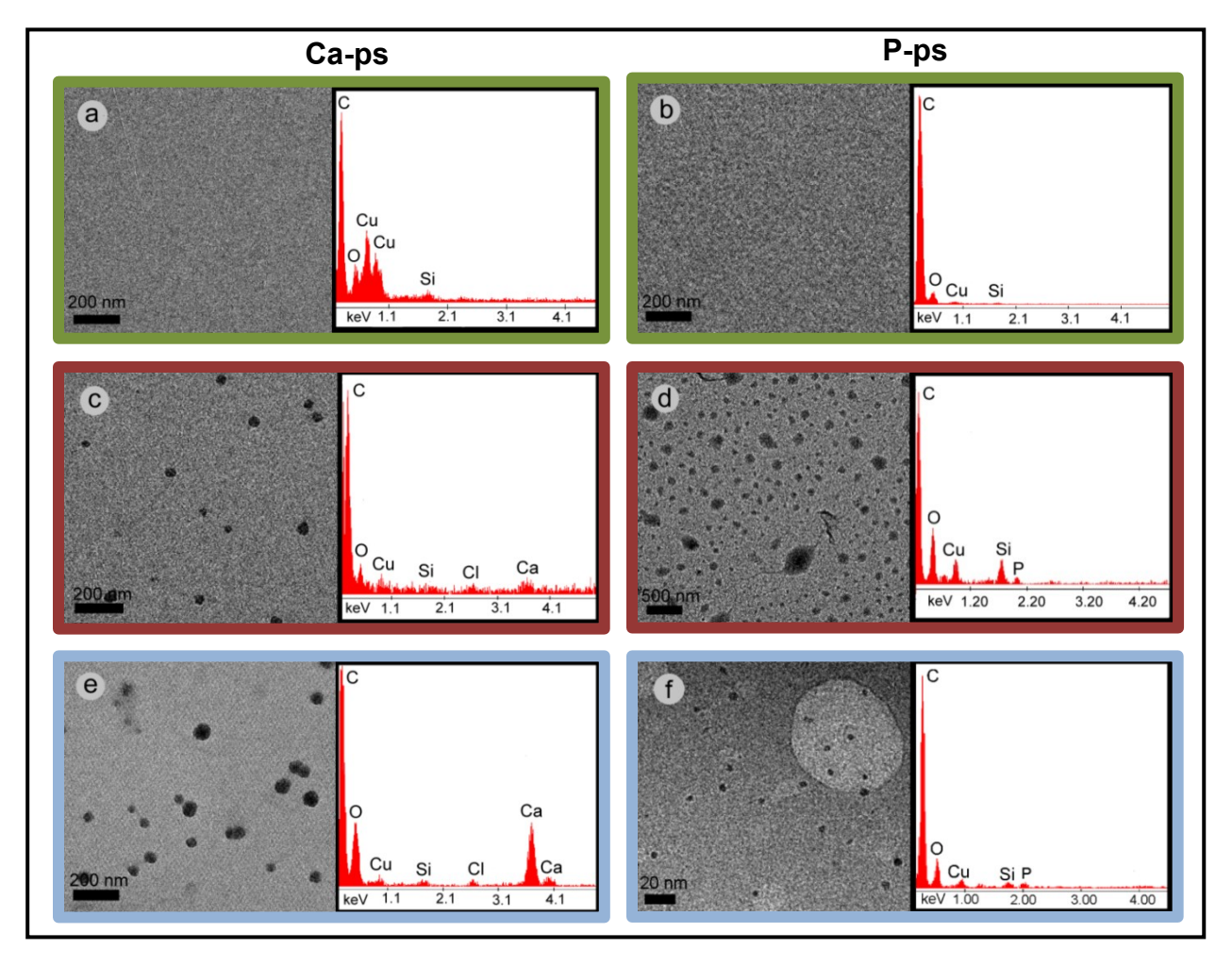


Fig. 5.6. TEM images and EDS spectra of aggregates collected from precursor solutions aged for 3 days. No aggregates are observed for Ca-Cont-ps (a) and P-Cont-ps (b) samples. Aggregates with average dimensions of 16±4 nm, 34±8 nm, 158±67 nm, and 4±1 nm are observed for Ca-Glu-ps (c), Ca-Arg-ps (e), P-Glu-ps (d), and P-Arg-ps (f) samples, respectively. Cl observed on the EDS spectra of Ca-Glu-ps (c) and Ca-Arg-ps (e) must be derived from either CaCl<sub>2</sub> or HCl.

#### 5.5. Discussion

It is known that AAs can inhibit HA precipitation and change its morphology and crystallinity [10, 36, 43, 331]. The results presented here show that this effect is much stronger if the AAs are allowed to interact with Ca<sup>2+</sup> and PO<sub>4</sub><sup>3-</sup> ions for some time (3 days in this example) before mixing the AA/ion solutions, due to the formation of nano-sized aggregates composed of organic material and traces of Ca<sup>2+</sup> or PO<sub>4</sub><sup>3-</sup>. In this section we will try to answer two main questions: i) what is the structure of the aggregates formed by interaction between AAs and Ca<sup>2+</sup> and PO<sub>4</sub><sup>3-</sup> ions?; and, ii) what is the role of these aggregates in HA nucleation and growth?

#### i) Structure of aggregates in the precursor solutions

While the inhibition of HA by Arg and Glu can be well explained in terms of the different constants of interaction between Arg, Glu and Ca<sup>2+</sup> and PO<sub>4</sub><sup>3-</sup> [331], our results indicate that not only do the inorganic ions and the AAs form complexes, but that these complexes are able to organize themselves into larger and larger structures as time goes by. The formation of large AA aggregates was recently shown for glycine [324] and a few other AAs [337]. Differently from what reported in [324] and [337], though, the aggregates found here contain also traces of Ca and P, and their structure is strongly influenced by the presence of these inorganic ions.

Aggregates of about 4 to 160 nm in diameter containing Ca, P and organic material can be separated out of AA-containing precursor solutions aged for 3 days (**Fig. 5.6c-f, left**). These aggregates may contain tris as well; however, although tris too is able to delay HA formation [290], no aggregates are observed in the aged precursor solutions that do not contain AAs (**Fig. 5.6a and b**), which indicates that the complexes formed by tris alone are not stable enough to form detectable aggregates after 3 days, or even after one month (**Fig. 5.5a**).

The amount of aggregates collected after aging AA-containing solutions for one month is large enough to perform several analyses and understand more in detail the structure of these aggregates. Although more P than Ca-containing aggregates are collected (Fig. 5.5a), more Ca is removed from the Ca-precursor solutions than P from the P-precursor solutions aged for 30 days (Fig. S5.3). This implies that a larger fraction of the Ca-aggregates is made by inorganic ions than the P-aggregates. Also, a larger amount of Ca is present in the Arg-aggregates than in the Glu-aggregates (Figs. 5.6e and c (right), and S5.3). These results can be interpreted considering the stabilities of the complexes formed between Ca<sup>2+</sup> and PO<sub>4</sub><sup>3-</sup> ions and Glu and Arg [10]: larger stability constants are observed for Ca<sup>2+</sup>/Glu (1.7) [239] and Ca<sup>2+</sup>/Arg (2.21) [299] complexes in comparison with the  $PO_4^{3-}/Glu$  (0.34) [307, 331] and  $PO_4^{3-}/Arg$  (1.9) [306] complexes. The larger constants reported for the Ca<sup>2+</sup>/AA complexes compared with the PO<sub>4</sub><sup>3-</sup> /AA complexes can explain the higher concentration of Ca than P in the aggregates collected from the aged precursor solutions. Also, more AAs may be required to stabilize P/AA aggregates because of the fewer interaction sites available between PO<sub>4</sub><sup>3</sup>-ions and AAs. This can explain the higher amount of AAs in the P-containing aggregates than in the Ca-containing aggregates (Fig. **5.5b**). Overall, our results seem to imply that the aggregates form by growing larger and larger

complexes between the AAs and the inorganic ions. The slow rate of this process, though, seems to indicate a kinetically activated mechanism, which deserves further investigation.

#### ii) Formation of HA in the presence of AA/ion aggregates

Our results allow us to propose a reaction pathway describing the formation of Ca/AA and P/AA aggregates and their interaction to form HA (**Fig. 5.7**). Ca/AA and P/AA complexes form as soon as they are mixed in the HA precursor solutions. Their structure, and the relative amounts of AA to Ca<sup>2+</sup> and PO<sub>4</sub><sup>3-</sup> ions, is dictated by the strength of the interactions between the AAs and the ions [331]. These complexes grow into larger and larger aggregates as time goes by, by addition of many AAs and few ions; tris molecules are integrated too, although not shown in **Fig. 5.7** for simplicity. The aggregates become quite large if left undisturbed for one month (**Fig. 5.7**, **arrow "1 month"**). If the solutions containing Ca or P and AAs are mixed right after the complexes start forming, i.e. without aging, the Ca<sup>2+</sup> and PO<sub>4</sub><sup>3-</sup> ions can interact easily; HA is formed with little delay; the crystals are made of HA, as shown both by XRD (**Fig. 5.1j**) and XPS (**Fig. 5.2a**) (**Fig. 5.7**, **arrow "no aging"**). If the solutions are mixed after some time, for example three days, Ca/AA and P/AA aggregates have formed (**Fig. 5.7**, **arrow "3 days"**). When the solutions are mixed, the aggregates become part of the HA precipitates. Their presence likely hinders the reaction kinetics, thus explaining the longer delay in precipitation observed when aged AA-containing precursors are used.

Our results do not allow us to determine the exact structure of the HA containing AA/ion aggregates. We know that the HA crystals are quite small (~ 30 nm) [331]; further studies, possibly using solid-state NMR [338], will be required to understand if the aggregates are introduced as occlusions, or at the interfaces between crystals. However the presence of aggregates only in the samples prepared with AA-containing aged precursors is clearly evidenced by all our results: XRD patterns of the HA formed from aged precursor solutions containing AAs (Fig. 5.1k) show some amorphous material in these samples; the presence of an AA-rich phase is confirmed by EDS (Fig. 5.4), XPS (Fig. 5.2) and IR (Fig. S5.1), and explains the instability under the TEM beam observed on the HA formed in this condition (Fig. 5.3b, c, and g). Such instability, typically observed for biominerals containing organic material [334, 335], is not observed in the absence of AAs (Fig. 5.3o) or in the presence of AAs, but without aging the precursor solutions (Fig. 5.3k).

#### **5.6.** Conclusion

Charged AAs are able to inhibit HA mineralization by complexing the Ca<sup>2+</sup> and PO<sub>4</sub><sup>3-</sup> ions necessary to form HA crystals. We have shown here that the complexes formed between Arg and Glu and Ca<sup>2+</sup> and PO<sub>4</sub><sup>3-</sup> ions can grow into large aggregates; once formed, these aggregates are involved in the HA precipitation process. Indeed, striking differences in precipitation time, HA morphology, composition and stability can be observed if HA grows from AA-containing solutions that have been aged for three days, compared to freshly prepared solutions. No differences are found in aged precursor solutions that do not contain any AA. These results show that complexes formed between charged AAs and Ca<sup>2+</sup> and PO<sub>4</sub><sup>3-</sup> ions can evolve in time and react differently following pathways that depend on their level of organization and structure. Larger biomineralization inhibitors are known to form aggregates that influence biomineral formation [339, 340]. For example, osteopontin aggregates seem to be responsible of the delay in HA precipitation by stabilizing Ca/P aggregates [341], while amelogenin aggregates have been linked to the spacing and organization of HA in enamel [342]. Here we have shown that a similar effect can be observed for much smaller biomolecules, i.e. AAs. Based on our results, we suggest that the waiting time between precursor solution preparation and their mixing should be taken in consideration as an important variable in any biomineralization experiment. This concept may actually mirror the effect of compartmentalization in biological systems, where vesicles that separate ions and biological molecules are involved in the formation of a variety of biominerals [343, 344].

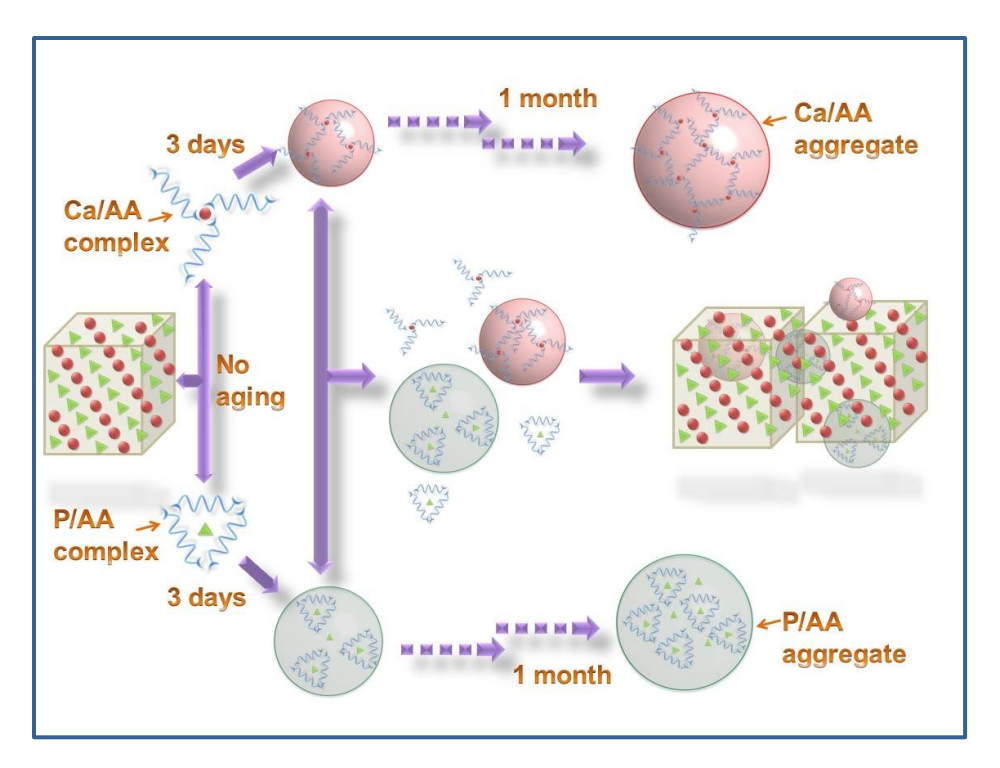


**Fig. 5.7.** Schematic representation of possible pathways for HA precipitation in the presence of Caand P-aggregates. Ca (red sphere) and P (green triangle) precursor solutions containing AAs (blue lines) are prepared separately. Complexes between AAs and ions form in the precursor solutions (see left side of the figure). If the solutions are mixed right away (arrow "no aging"), Ca/AA and P/AA aggregates do not have time to form, and HA crystals (cubes) only contain Ca<sup>2+</sup> and PO<sub>4</sub><sup>3-</sup> ions. However, if Ca- and P-precursor solutions are aged for 3 days, Ca/AA (pink sphere) and P/AA (green sphere) aggregates start forming (arrow "3 days"). The longer the aging time, the larger the aggregates become (arrow "1 month"). If the precursor solutions are mixed after 3 day aging, HA precipitates include not only Ca<sup>2+</sup> and PO<sub>4</sub><sup>3-</sup> ions, but also the aggregates that had grown during the 3 day aging. The aggregates could be either occluded inside the HA crystals, or at the interface between different crystals (A colored version of this figure can be found online).

#### 5.7. Acknowledgement

This research project is supported by the McGill Engineering Doctoral Award, the Canada Research Chair foundation, the Natural Science and Engineering Research Council of Canada, the Canada Foundation for Innovation, the Center for Self-Assembled Chemical Structures, and the Fonds Quebecois de la Recherche sur la Nature et les Technologies. Also, we would like to thank Dr. David Liu for his help with TEM, Prof. Raynald Gauvin and Dr. Nicolas Brochu for SEM assistance, and Prof. Fiorenzo Vetrone and Dr. Rafik Naccache for their help with drawing the schematic in **Fig. 5.7.** 

#### SI. 5. Supporting information

This document shows Fourier transform infrared (FT-IR) analysis of HA precipitates (**Fig. S5.1**), X-ray photoelectron spectroscopy (XPS) analysis of particles collected from Ca- and P-precursor solutions aged for 1 month (**Fig. S5.2**), [Ca] and [P] measured by inductively coupled plasma atomic emission spectroscopy (ICP-AES) in Ca- and P- precursor solutions, respectively, aged up to 1 month (**Fig. S5.3**), and [Ca] measured by Ca ion-selective electrode (ISE) in Ca-precursor solution aged up to 3 days (**Fig. S5.4**).

#### SI. 5.1. FT-IR analysis of HA precipitates

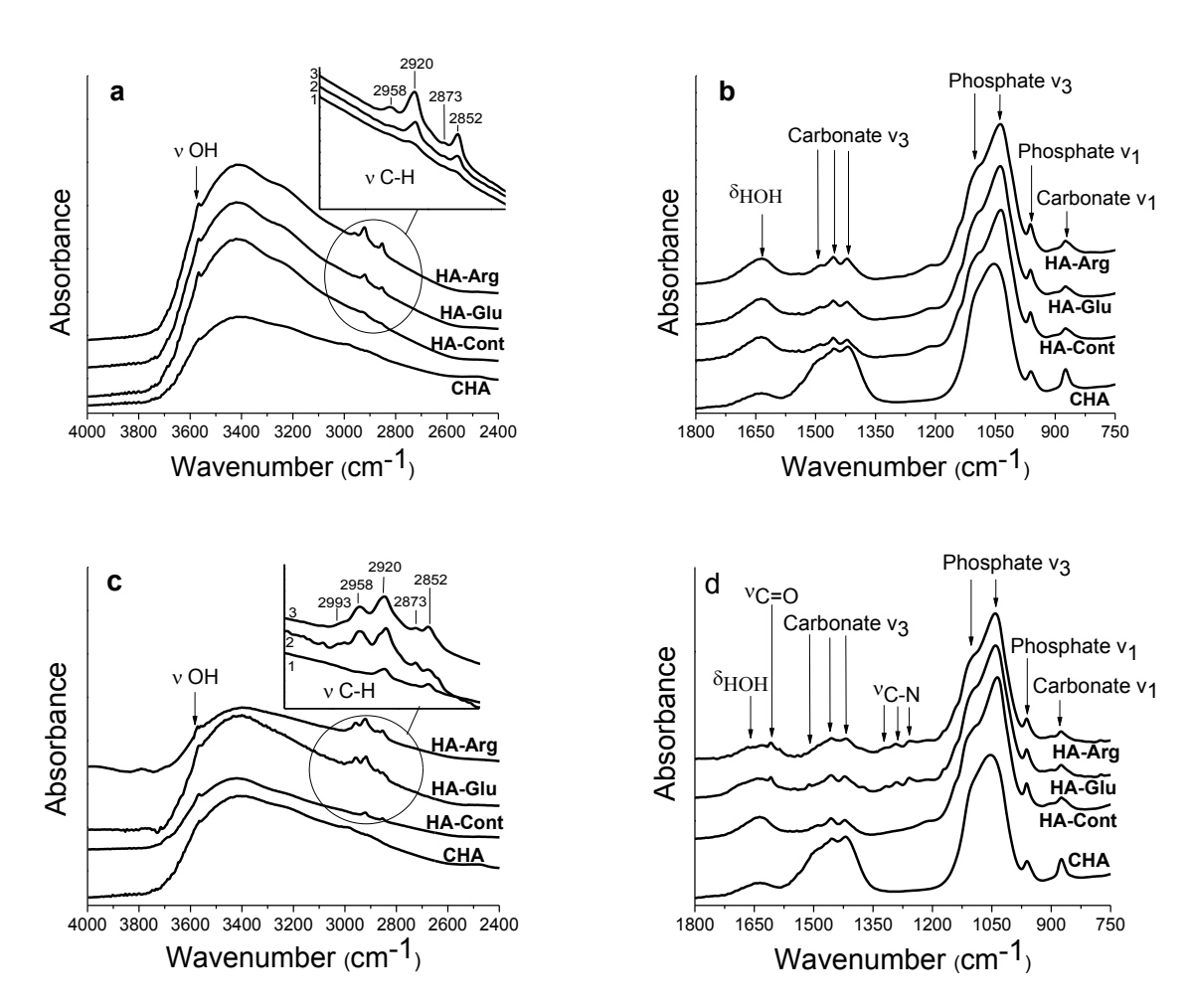


**Fig. S5.1.** IR spectra of HA-Cont, HA-Glu, and HA-Arg samples prepared with precursor solutions that were not aged (a and b) or aged for 3 days (c and d). All spectra are normalized with respect to the main phosphate peak of HA at 1055 cm<sup>-1</sup>. Spectra are then translated along the y axis for clarity. Sections (a and c): 4000-2400 cm<sup>-1</sup> region; (b and d): 750-1800 cm<sup>-1</sup> region. Inset in section a and c: zoom-in of 3000 to 2800 cm<sup>-1</sup> region for spectra HA-Cont (1), HA-Glu (2), HA-Arg (3).

The FT-IR spectra for all samples match the spectra recorded on carbonated HA (CHA) [293, 294], and are very different from those obtained for other crystalline phases of calcium phosphates like OCP [295]. However, the phosphate  $v_3$  peaks are sharper than in CHA, most likely indicating that the HA samples are more crystalline than the reference CHA [296], which is very defective due to the incorporation of carbonate ions in its crystal lattice. In fact, none of the HA samples show strong carbonate  $v_3$  peaks. On these samples, carbonates are not present in the bulk, but rather at the surface due to reaction with atmospheric CO<sub>2</sub> dissolved in the reaction

solution. More water is adsorbed on the HA samples than on CHA, as shown by the stronger  $\delta_{HOH}$  peak at 1660 cm<sup>-1</sup> and more pronounced  $\nu_{OH}$  band in the 2600-3700 cm<sup>-1</sup> region. The peak at 3650 cm<sup>-1</sup> present on all samples is attributed to  $\nu_{OH}$  from structural OH groups in HA.

FT-IR spectroscopy can provide information relative to the presence of organic components in the samples. Peaks at 1200-1300 cm<sup>-1</sup> are attributed to  $v_{C-N}$  [11], which can originate from tris and AAs. These peaks are observed on the HA samples prepared from aged precursors containing AAs, but they are not visible on the samples prepared in the absence of AAs or from non-aged precursor solutions (**Fig. S5.1b and d**). This indicates the presence of AAs on the HA samples prepared with aged precursors in the presence of AAs [11]. Confirming this, a small  $v_{C=O}$  peak, originating from the carboxylate groups in AAs, is observed on these samples (**Fig. S5.1d**) [11, 345, 346].

The  $v_{C-H}$  band observed in the 2800 to 3000 cm<sup>-1</sup> region shows that organic materials, either tris or AAs, are present in all of the precipitates (**Fig. S5.1a and c**). The peaks at 2920 and 2852 cm<sup>-1</sup>, which are present in the AA samples as well as the control sample, can be attributed to  $v_{CH2}$  originating from tris [347]. The intensity of these peaks is lower on the HA-Cont spectrum than on those of HA-Arg or HA-Glu, which indicates that less tris is present in the HA formed in the absence of AAs. Also, these peaks are more intense for the AA-containing HA prepared with aged precursors than the HA prepared with fresh precursors (**Fig. S5.1a and c, Inset**), which indicates that more tris is present in the samples aged for 3 days. Additional peaks at 2993, 2958, and 2873 cm<sup>-1</sup> are observed in the spectra of the HA prepared in the presence of AAs, and are broader and more intense when the precursor solutions are aged for 3 days. These peaks can be attributed to the AAs, Arg or Glu [348], thus confirming the presence of AAs in the HA-Arg and HA-Glu samples, and confirms the increase in AA content with the aging time of precursor solutions.

## SI. 5.2. Ca and P concentration in particles collected from the precursor solutions aged for 1 month

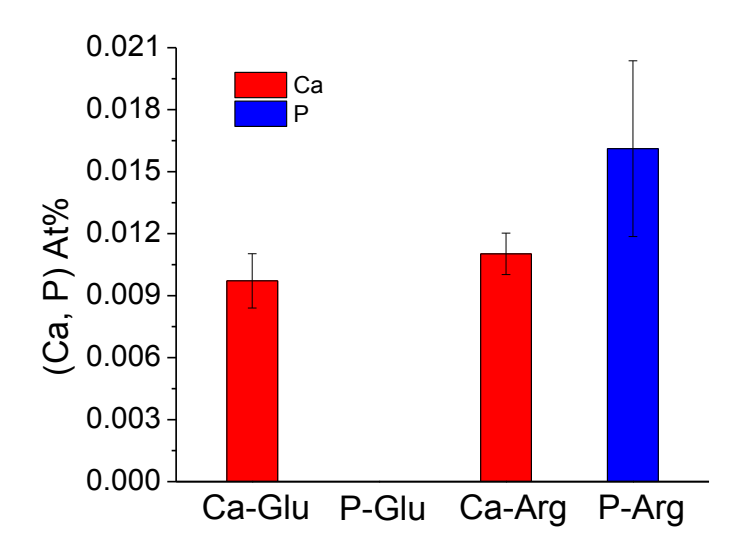


**Fig. S5.2.** Ca (red) and P (blue) atomic % measured from XPS survey spectra for the particles collected from Ca-Glu-ps, P-Glu-ps, Ca-Arg-ps, and P-Arg-ps solutions aged for 1 month.

**Fig. S5.2** shows the Ca and P atomic % recorded in XPS survey spectra for the particles collected from the Ca and P precursor solutions aged for 1 month. No particles are formed in the control Ca and P solutions without AAs, hence no XPS results are shown. Very low concentrations of Ca and P are found, close to the detection limit of XPS, thus indicating that all samples are mainly composed of organic materials, tris or amino acids. The particles collected from P-Arg-ps and Ca-Arg-ps contain larger amounts of P and Ca in comparison with those collected from the P-Glu-ps and Ca-Glu-ps, respectively. This shows the stronger interaction of Arg than Glu with both Ca and P in the precursor solutions. The concentration of P in the particles collected from P-Glu-ps most likely is below XPS detection limit.

## SI. 5.3. Ca and P concentration in Ca- and P-precursor solutions at different aging times measured by ICP

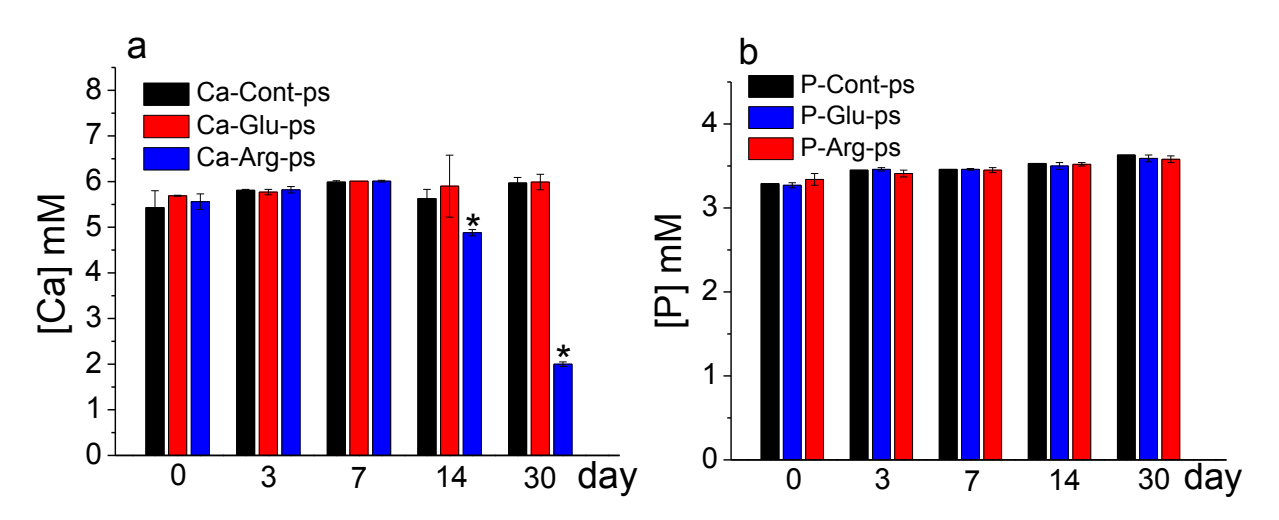


**Fig. S5.3.** (a) [Ca] and (b) [P] measured by ICP in Ca- and P-precursor solutions, respectively, aged for 0 to 30 days. Asterisks (\*) indicate the samples that were statically significantly different from their correspondent samples aged for 0 day with P<0.05.

Fig. S5.3 shows the [Ca] and [P] measured by ICP in the Ca and P precursor solutions, respectively, at different aging times. The aliquots are taken from the solutions, filtered with a filter with 5 nm pore size, and then the [Ca] and [P] are measured by ICP. The minor increase in both [Ca] and [P] observed overall for all samples between 0 and 1 month aging is to be related to evaporation occurring in the solutions. No significant change in [Ca] is detectable in the Caprecursor solutions (Fig. S5.3a), either with or without AAs, until 7 days. However after 14 days of aging, [Ca] significantly decreases in the Ca-Arg-ps. No significant decrease in [Ca] is found in Ca-Glu-ps and Ca-Cont-ps, and no change in [P] in any of the P-containing precursor solutions (Fig. S5.3b). These results indicate that a large amount of particles forms in the presence of Arg and Ca after 14 days, so that after their filtration [Ca] decreases noticeably in the Ca-Arg-ps. In all the other solutions, instead, the amounts of Ca and P that are consumed to form Ca/AA and P/AA clusters are probably lower than the detection limit of ICP. This is noteworthy, since as shown in Fig. 5, a significant amount of clusters is formed in the P-precursor solutions after 1 month of aging, and yet ICP does not show any change in [P]. Indeed, XPS showed that these clusters contain very little P (less than 1%, Fig. S5.2), and their removal from solution is not detected by ICP.

## SI. 5.4. In-situ measurement of Ca concentration in Ca-precursor solutions at different aging times measured by Ca ion-selective electrode (ISE)

**Fig. S5.4** shows [Ca] measured in situ by ISE in Ca-precursor solutions at different aging times. To eliminate the effect of ionic strength on ISE readings, an adequate amount of ionic strength adjustment buffer (ISAB) solution is added to the Ca solutions. [Ca] is calculated based on calibration curves obtained on the same days as the measurement was done.

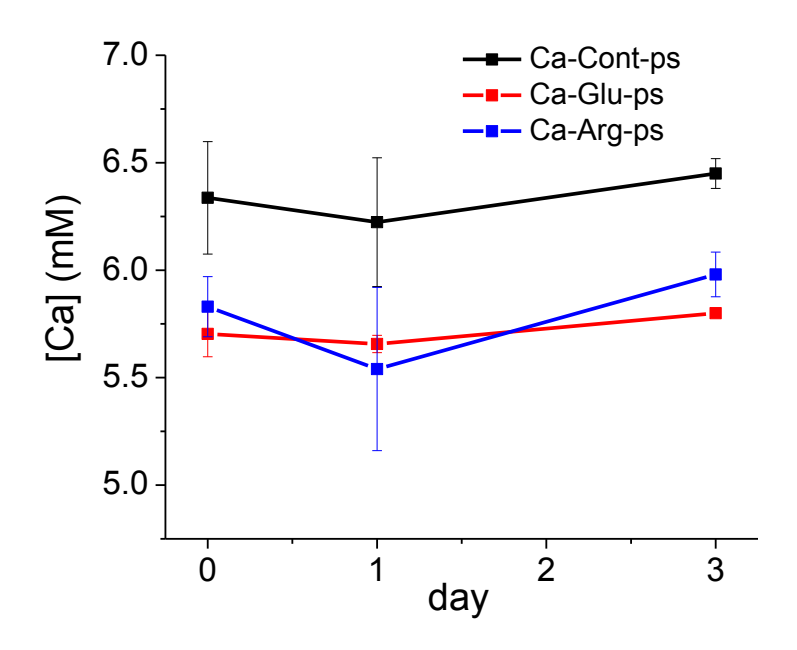


**Fig. S5.4.** [Ca] measured by ISE in Ca-precursor solutions aged for 0 to 3 days.

#### **CHAPTER 6**

# EFFECT OF ARGININE AND GLUTAMIC ACID BOUND TO GRAPHENE OXIDE SURFACES ON HYDROXYAPATITE PRECIPITATION

In chapter 4 and 5, we investigated the inhibitory effect of Arg and Glu dissolved in solution on HA precipitation. In this chapter we will focus on the effect of these AAs bound to GO surface. Both Arg and Glu promoted HA precipitation by attracting Ca<sup>2+</sup> and PO<sub>4</sub><sup>3-</sup> ions toward GO surface, but Arg had a stronger promoting effect. This GO/Arg composite material can be potentially used in tissue engineering to promote HA precipitation in damaged tissues.

The findings of this paper are reported in a manuscript submitted to "Nanoscale".

## Promoting effect of AAs bound to graphene oxide surface on HA precipitation

M.	Tavafoghi,	N.	Brodusch,	R.	Gauvin,	and M.	Cerruti*
----	------------	----	-----------	----	---------	--------	----------

Materials Engineering, McGill University, Montreal, QC, Canada, H3A 2B2

Emails: maryam.tavafoghijahromi@mail.mcgill.ca; marta.cerruti@mcgill.ca

Keywords: Hydroxyapatite, precipitation, arginine, glutamic acid, graphene oxide.

#### 6.1. Abstract

Hydroxyapatite (HA, Ca<sub>5</sub>(PO<sub>4</sub>)<sub>3</sub>OH) is the main inorganic component of hard tissues, such as bone and dentine. HA nucleation involves a set of negatively charged phosphorylated proteins known as non-collagenous proteins (NCPs). These proteins attract Ca<sup>2+</sup> and PO<sub>4</sub><sup>3-</sup> ions and increase the local supersaturation to a level required for HA precipitation. Polar and charged amino acids (AAs) are highly expressed in NCPs, and seem to be responsible for the mineralizing effect of NCPs; however, the individual effect of these AAs on HA mineralization is still unclear.

In this work, we investigate the effect of a negatively charged (Glu) and positively charged (Arg) AA bound to carboxylated graphene oxide (CGO) on HA mineralization in simulated body fluids (SBF). Our results show that Arg induces HA precipitation faster and in larger amount than Glu. We attribute this to the higher stability of the complexes formed between Arg and Ca<sup>2+</sup> and PO<sub>4</sub><sup>3-</sup> ions, and also to the fact that Arg exposes both carboxyl and amino groups on the surface. These can electrostatically attract both Ca<sup>2+</sup> and PO<sub>4</sub><sup>3-</sup> ions, thus increasing local supersaturation more than Glu, which exposes carboxyl groups only. The morphology and crystal structure of the precipitates are also affected by the type of AAs used. After 15 days of immersion in SBF, well-organized micro spherulites are found on the sample modified with Arg, while Glu mainly induce the formation of irregularly shaped aggregates with larger Ca/P ratios than that expected for HA.

#### 6.2. Introduction

Biomineralization is the process by which living organisms produce minerals. Biominerals have complex hierarchical structures, often coupled with exceptional properties, such as high mechanical, electrical, or magnetic properties, which are achieved under the direct control of biomolecules [2, 3, 5, 6, 158]. The formation of human bone is one of the most well-known examples of biomineralization. Bone is an organic-inorganic hybrid material made of collagen, non-collagenous proteins (NCPs), and carbonated hydroxyapatite (HA, Ca<sub>5</sub>(PO<sub>4</sub>)<sub>3</sub>OH) crystals. Collagen fibrils provide a framework known as extracellular matrix (ECM) for HA nucleation and growth.

HA nucleation is mainly initiated by a set of negatively charged phosphorylated NCPs associated with the ECM. These proteins can attract Ca<sup>2+</sup> and PO<sub>4</sub><sup>3-</sup> ions and increase the local

supersaturation to a level required for HA precipitation [8, 279]. Another set of NCPs inhibits undesirable formation of HA in tissues such as cartilage and blood vessels by chelating Ca<sup>2+</sup> and PO<sub>4</sub><sup>3-</sup> ions or binding to the surface of nascent nuclei of minerals, thus restricting their further growth [201, 202]. NCPs that inhibit HA nucleation can become HA promoters when bound to a surface, since they lose their ability to adhere to the surface of mineral nuclei [8, 9].

To answer fundamental questions about biomineralization, researchers have investigated the effect of smaller biomolecules, such as amino acids (AAs) and peptides. AAs are the building blocks of proteins, and negatively charged AAs such as glutamic acid (Glu) and phosphoserine (PSer) are highly expressed in NCPs. Similar to proteins, charged AAs can either inhibit or induce HA mineralization if they are dissolved in solution or bound to a surface.

While several researchers have analyzed the inhibitory effect of AAs dissolved in solution on HA mineralization [10, 34, 36-46], the effect of AAs bound to surfaces has been the subject of just a few studies [47, 58, 59, 259, 261, 262, 264]; in most papers, researchers analyzed the effect of molecules with functionalities simulating those found in protein [259, 261, 262, 264]. Rautaray et al investigated HA precipitation in the presence of aspartic acid (Asp)-capped gold nanoparticles [47]. They showed that HA precipitation was promoted in the presence of Asp due to the interaction between the COOH groups from Asp and the Ca<sup>2+</sup> ions. Using isothermal titration calorimetry (ITC), they showed that the interaction between Ca2+ and Asp was thermodynamically favored. Other researchers have focused on the effect of surface functional groups with different electrical charges on HA precipitation. Zhu et al prepared self-assembled monolayers (SAMs) of silanes on silicon, with NH<sub>2</sub> and OH end-groups, to investigate the effect of positively vs. negatively charged surfaces on HA precipitation [259]. They showed that HA precipitation was faster on the negatively charged OH-SAMs than on the positively charged NH<sub>2</sub>-SAM. Similar results are reported for functionalized gold substrates. Tanahashi et al looked at HA formation on gold modified with SAMs of alkanethiols terminated with neutral, negative and positive groups, such as CH3, PO4H2, COOH, CONH2, OH, and NH2 [262]. They showed the most potent inducers of HA precipitation were negatively charged (PO<sub>4</sub>H<sub>2</sub> first and then COOH), while the SAMs terminated with positively charged groups, such as CONH<sub>2</sub> and NH<sub>2</sub>, induced much less HA precipitation. Liu et al explored more in detail the effect of negatively charged groups, such as OH, PO<sub>4</sub>H<sub>2</sub>, and COOH bound to titanium foil [261]; they showed that poorly crystalline calcium phosphate was precipitated in the presence of COOH and PO<sub>4</sub>H<sub>2</sub>.

Consistent with the study by Zhu et al [262], PO<sub>4</sub>H<sub>2</sub> exhibited a stronger nucleating ability than COOH. The control titanium foil sample and the OH-modified sample showed the least calcium phosphate deposition [261].

While most of these works indicate that negatively charged functional groups are more effective than positive or neutral groups in inducing heterogeneous nucleation of HA [259, 262], there is at least one study showing different results: Zhang et al investigated HA precipitation in the presence of PO<sub>4</sub>, COOH, and NH<sub>2</sub> functional groups present on Langmuir monolayers made of dipalmitoylphosphatidylcholine, arachidic acid, and octadecylamine, respectively [264]. They showed that PO<sub>4</sub>, COOH, and NH<sub>2</sub> functional groups promoted the nucleation of calcium phosphate to a very similar extent [264]. However, the Ca/P ratio for the calcium phosphate formed in the presence of PO<sub>4</sub> was similar to that of HA (1.67) while lower Ca/P ratios were found for COOH (1.49) and NH<sub>2</sub> (1.60), indicating the presence of some amorphous calcium phosphate (ACP) on these samples.

In this work, we use graphene oxide (GO) as a substrate onto which we bind both positively and negatively charged AAs, and we study their role in HA precipitation. GO surface contains many different functional groups, making it easily modified [349]. Its high surface area is ideal to speed up HA precipitation [349]. In addition, both GO and other members of the graphene family of nanomaterials (GFNs) have been recently considered in bio-related applications [350], especially bone tissue engineering, due to their ability to promote osteogenic differentiation in mesenchymal stem cells [60, 351-356].

A few researchers have explored the modification of GFNs with biomolecules, and investigated the effect of such modifications on in-vitro HA mineralization [58, 59, 61, 353, 355, 357]. All these studies showed that HA precipitation was improved in the presence of biomolecules, mainly due to the interaction between negatively charged groups (phosphonic, carboxyl, and hydroxyl groups) and Ca<sup>2+</sup> ions. Here we want to extend these studies and use GO as a substrate to further our fundamental understanding of the effect of positively and negatively charged AAs on HA mineralization, while providing an example of a highly promising GO-based substrate for bone tissue engineering.

#### 6.4.1.4 Summary of characterization results

#### 6.3. Materials and methods

#### 6.3.1. Materials

The AAs used in the study (L-Arginine, purity  $\geq$  99.5% and L-Glutamic acid, purity  $\geq$  99.5%), chloroacetic acid (purity $\geq$ 98%), NHS (N-Hydroxysuccinimide, purity $\geq$ 98%), sodium bicarbonate (purity $\geq$ 99.7%), MES (2-(N-Morpholino)ethanesulfonic acid, purity  $\geq$ 99%), and 2-Mercapto ethanol were all purchased from Sigma Aldrich. Highly concentrated graphene oxide aqueous solution (6 mg/ml) was purchased from Graphene Supermarket. The graphene oxide flake size was 0.5 to 5  $\mu$ m, and a surface area of 1200 m²/g was estimated based on this. HA powder used as a reference was synthesized with a homogeneous precipitation technique explained in detail in our previous paper [331]. The HA particle size and surface area was ~3  $\mu$ m and ~100 m²/g, respectively. EDC (1-(3-Dimethylaminopropyl)-3-ethylcarbodiimide hydrochloride,  $\geq$ 98%) was from Alfa Aesar. Sodium chloride (purity $\geq$ 99%), sodium hydroxide (purity $\geq$ 97%), and nitric acid (69 - 70% w/w) were purchased from Fisher Scientific.

#### 6.3.2. Surface modification of GO flakes

The AAs can be grafted onto the GO surface by coupling the NH<sub>2</sub> group from the AAs with the carboxyl groups that are naturally present on the surface of GO flakes. However, to improve this process, more carboxyl groups were introduced on GO surface using a previously described technique [358] with a few modifications, as described in 6.3.2.1. The AAs were then grafted onto carboxylated GO (CGO) using the well-known EDC coupling technique (6.3.2.2).

#### 6.3.2.1. GO surface modification with carboxyl groups (preparation of CGO)

To make CGO, 20 ml of as-purchased GO solution (6 mg/ml) was diluted 3 times by deionized (DI) water to reach the final concentration of 2 mg/ml. This was then stirred for 10 min under sonication. The GO solution after dilution had a light brown color. 7.4 g of sodium hydroxide (3 M) and 6.2 g (1 M) of chloroacetic acid were added to the GO solution, and were left to react while being stirred at room temperature for 7 h. This led to the conversion of the epoxy and hydroxyl groups on GO to carboxyl via conjugation of acetic acid moieties [358]. The color of GO solution turned to black at the end of reaction due to the higher absorbance of CGO than GO in the visible and near-infrared range at 500, 808, and 1200 nm [358]. CGO solution,

which was strongly basic and contained a significant amount of sodium hydroxide, was centrifuged at 15000 rpm for 30 min. The supernatant was discarded, and the CGO pellet was redispersed in DI water and sonicated for 10 min. This procedure was repeated at least 15 times until the pH of the supernatant solution reached 7. The centrifugation time was increased to 1 h for the last few washing cycles because the purer the CGO became, the more stable it became in water. The final precipitate was dispersed in DI water, and freeze-dried using a VirTis freeze-drier.

#### 6.3.2.2. CGO modification with AAs

EDC coupling (see Fig. S6.1 for a schematic of the reaction) was used to bind the AAs, Arg or Glu, on CGO. 20 mg of CGO were dispersed in 20 ml of a buffer composed by 100 mM MES and 500 mM NaCl, with final pH=6. 38 mg of EDC (10 mM) and 12 mg of NHS (5 mM) were added to this solution and allowed to react at room temperature for 15 min. After this, 28 µl of mercaptoethanol were added to the solution in order to deactivate the remaining EDC, and the pH was raised to 7-8 using adequate amounts of sodium bicarbonate. Finally, 100 mg of the AAs (final concentration in solution: 5 mg/ml) (Glu or Arg) were added to the solution, and allowed to react overnight at room temperature. At the end of reaction no significant change in CGO solution color was observed. To wash the AA-modified CGO flakes, the reaction solution was centrifuged at the rate of 4000 rpm for 15 min, and the supernatant solution was discarded. The CGO pellet was re-suspended in DI water. This cycle was repeated at least 3 times, until the pH of supernatant solution reached 7. The collected pellet was re-suspended in DI water and freezedried using a VirTis freeze-drier. The summary of all samples prepared in this work is shown in Table 6.1.

**Table 6.1.** List of samples used in this work.

Sample names	Surface modification		
GO	None		
CGO	Carboxylated GO		
CGO-Glu	CGO modified with Glu via EDC/NHS coupling		
CGO-Arg	CGO modified with Arg via EDC/NHS coupling		

#### 6.3.3. Precipitation experiment

Simulated body fluid (SBF) was prepared according to a well-known recipe provided by Kokubo et al [359]. 1.9 mg of GO, CGO, CGO-Glu, or CGO-Arg were dispersed in 40 ml of SBF in centrifugation tubes, to achieve the recommended surface area/SBF volume suggested by Kokubo. The tubes were placed in an incubator at 37° C for 15 days. The samples were then removed from the incubator, washed 3 times with DI water (3 cycles of centrifugation at 4000 rpm for 15 min and re-suspension in DI water), and finally dried using a VirTis freeze-drier.

#### **6.3.4.** Characterization

#### 6.3.4.1. X-ray photoelectron spectroscopy (XPS)

XPS measurements were performed using a monochromatic X-ray photoelectron spectrometer K Alpha (Thermo Scientific). The setup was equipped with an Al Kα X-Ray source (1486.6 eV, 0.834 nm), a micro-focused monochromator and an ultrahigh vacuum chamber (10<sup>-9</sup> Torr). The survey scans were collected with energy steps of 1 eV and spot size of 400 μm. Scans were taken on at least 3 points on each sample and the quantitative results were averaged. The high resolution scans were collected with energy steps of 0.1 eV and a spot size of 400 μm on at least 3 points. The spectral energies were calibrated by setting the binding energy of the C 1s component corresponding to C-C bonds at 285.0 eV. A flood gun was used to neutralize electrical built-up charge generated. Peak fitting and quantitative analysis of survey spectra were performed using the software Thermo Avantage (version 4.60).

#### 6.3.4.2. Fourier transform infrared (FT-IR) spectroscopy

IR spectra were recorded on a Bruker Tensor 27 FT-IR spectrometer using diffuse reflectance (DRIFT) mode. The reflected signals are converted and reported as absorbance in the figures shown in this paper. The samples were diluted with KBr to approximately 10% wt/wt. Pure KBr powder was used as background. The FT-IR spectra were recorded from 600 to 4000 cm<sup>-1</sup> using a deuterated triglycine sulfate (DTGS) detector. The spectra were collected by averaging 256 scans at 4 cm<sup>-1</sup> resolution.

#### 6.3.4.3. Thermogravimetric analysis (TGA)

Thermogravimetric analysis (TGA) data were recorded on a Q500 TG analyzer from TA Instruments from ambient temperature to 800 or 1000° C at a heating rate of 20° C min<sup>-1</sup> under nitrogen atmosphere.

#### 6.3.4.4. Inductively coupled plasma atomic emission spectroscopy (ICP-AES)

Ca and P concentration in the SBF solutions containing GO, CGO, CGO-Glu, or CGO-Arg sample were measured using an ICP-AES instrument (ICAP 6500 Duo). 1 ml aliquots were taken from the SBF solutions at the desired incubation times, filtered with a syringe filter with a pore size of 100 nm to remove any trace of precipitates or GO flakes, and then immediately diluted 5 times with 4% nitric acid. The dilution with 4% nitric acid ensured that no more precipitate formed in the solutions after filtration. The Ca and P concentrations were measured at the wavelength of 317.9 and 178.3 nm, respectively.

#### 6.3.4.5. SEM

The particle morphology was analyzed with a Hitachi SU-8000 cold-field emission scanning electron microscope (CFE-SEM), using an acceleration voltage of 5 kV. Images were collected using a solid-state photo-diode backscattered electron detector (PD-BSE). The SEM was equipped with an Oxford Instrument XMax 80mm² silicon drift detector as the energy dispersive spectrometer (EDS). Acquisition of EDS spectra as well as standardless quantitative analysis were performed using the INCA software. The specimens were mounted on double sided conductive carbon tape and were not metal coated. Before SEM analysis, samples were cleaned using a Hitachi ZoneSEM ozone cleaner to remove adsorbed organic species.

#### 6.3.4.6. TEM

A high resolution TEM, Philips CM200, was used with line resolution of 0.17 nm and operating voltage of 200 kV. The TEM was equipped with a LaB6-cathode thermoionic gun and genesis EDAX detector. Images were digitized using a high-resolution Gatan 2kX2k CCD camera. The TEM analysis was performed only on the CGO-Arg sample immersed in SBF for 15 days. To prepare the TEM sample, a small amount of CGO-Arg sample was dispersed in 2 ml of ethanol, sonicated for 5 m, and then a drop of this solution (5 μl) was placed on a TEM grid (200-mesh carbon-coated Cu TEM grids, SPI Supplies). The grids were dried overnight in air before analysis.

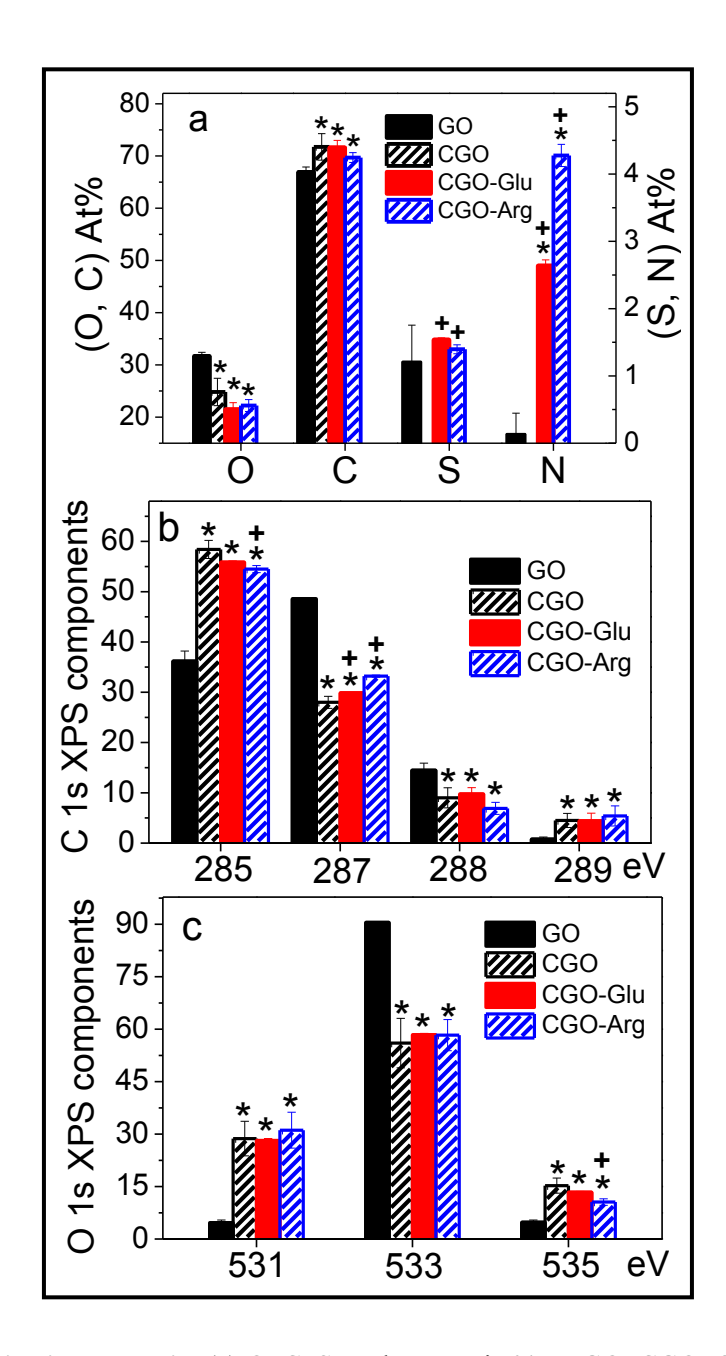


**Fig. 6.1. XPS quantitative analysis:** (a) O, C, S, and N atomic % on GO, CGO, CGO-Glu, and CGO-Arg obtained from survey spectra; (b and c) percentages of the different components used to fit high resolution XPS C 1s (b) and O 1s (c) spectra shown in **Fig. 6.2**.

#### 6.4. Results

To study the effect of positively and negatively charged AAs bound to GO, we first transformed GO in carboxylated GO (CGO), thus increasing the number of carboxylated groups on its surface. Then, we bound a positive (Arg) and a negative (Glu) AA on it via an amidation process achieved with the aid of EDC and NHS. We then immersed the AA-modified CGO in SBF, to study how AAs influence heterogenous nucleation of HA on CGO.

#### 6.4.1. Characterization of GO surface modification

#### 6.4.1.1. XPS analysis

Fig. 6.1a shows O, C, S, and N at% on GO, CGO, and CGO-AA samples obtained from XPS survey spectra. C and O mainly originate from GO on all samples; however, all CGO samples show a significant decrease in O and increase in C compared to GO. This suggests that the amount of O in the O-containing groups that are removed from GO (hydroxyl, epoxy, and carbonyl groups) is larger than the amount of O that is introduced by carboxylation. No significant differences in C and O are observed between CGO samples before and after AA coupling. However, while CGO does not show any N and S, as expected, CGO-AA samples show the presence of some N and S. S can originate from the physisorbed coupling components, NHS and MES, and N can originate from both the physisorbed coupling components, EDC, NHS, and MES, or from the AAs. The unexpected S and N observed on the GO sample may be attributed to the precursors used in Hummer's method for GO production [360], which seem to have been removed after the extensive washing performed during the carboxylation stage (see Section 6.3.2.1) since no S and N are observed on the CGO sample. A control sample prepared by immersion of CGO in EDC/NHS solution without further AA coupling showed a similar amount of S as the CGO-AA samples, but much less N (see Table S6.1), thus confirming that while the presence of S on CGO-AA samples is due to physisorbed components from the coupling solution, the N is mainly related to the presence of AAs on the surface of the CGO-AA samples. While Arg has 3 times more N atoms than Glu in its molecular structure, CGO-Arg shows only 2 times more N than CGO-Glu. This may indicate that less Arg was able to react with CGO than Glu. However, XPS data is affected by the orientation of the AAs in the coating, and by the coating thickness, and thus this interpretation needs to be corroborated by results obtained with other techniques.

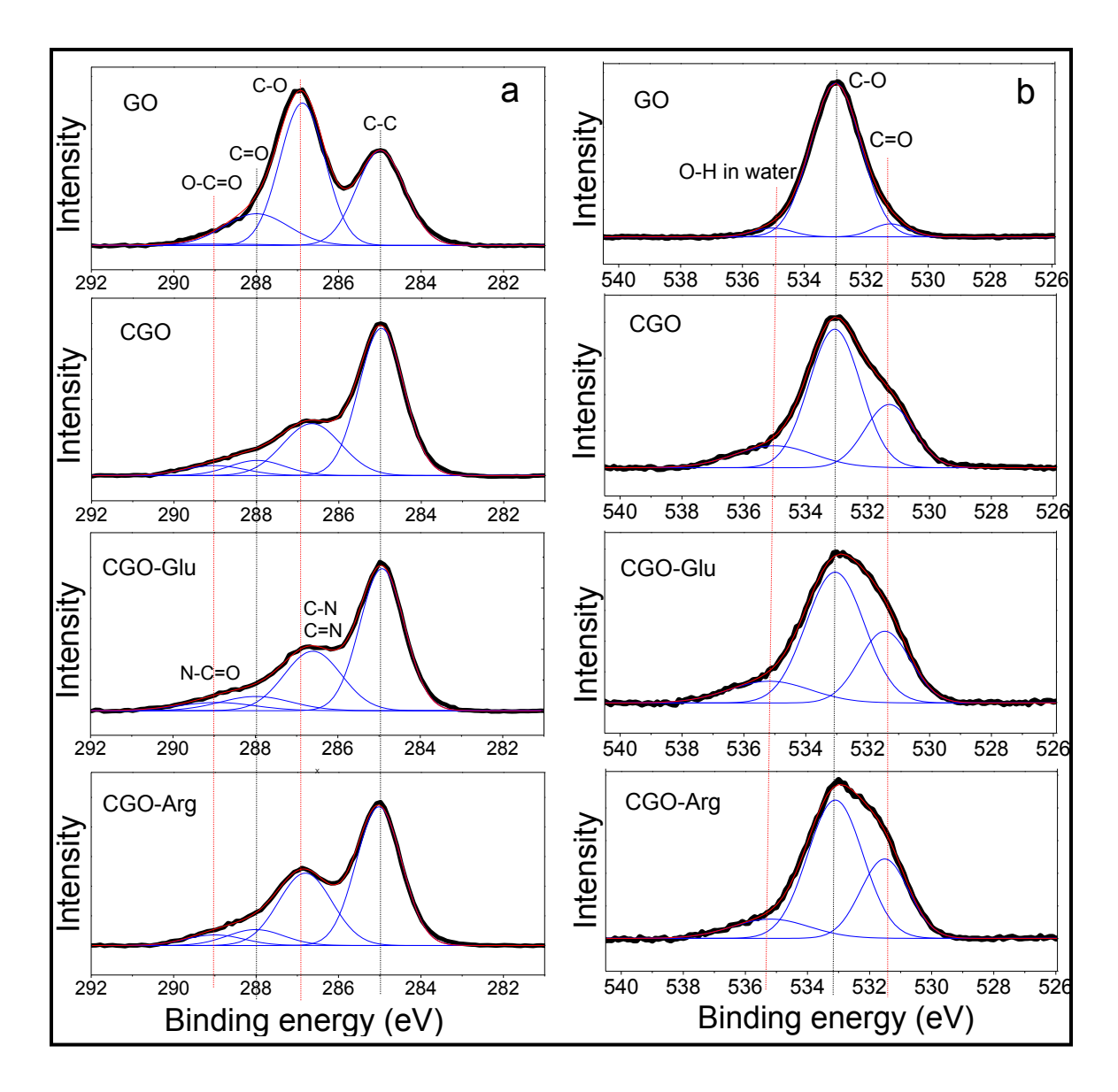


**Fig. 6.2.** XPS C 1s (a) and O 1s (b) high resolution spectra for GO, CGO, CGO-Glu, and CGO-Arg samples.

Further confirmation of the presence of AAs can be obtained by analyzing the high resolution C1s and O1s spectra (**Fig. 6.1b and c**, and **Fig. 6.2**). The C 1s spectra can be deconvoluted into four components, centered at 284.9, 286.9±0.2, 288.00±0.05, and 289.00±0.05 eV (**Fig. 6.2a**). On all samples, the 284.9 eV component originates from C-C/C=C bonds from the benzene rings in GO [361, 362]. The components at 287, 288 and 289 eV originate from the oxygenated functional groups, namely epoxy/hydroxyl (C-O), carbonyl (C=O) and carboxyl (O-C=O) groups, respectively [361, 362]. **Fig. 6.1b** shows a drastic decrease in C-O and C=O bonds and a significant increase in O-C=O bonds on CGO compared to GO. This confirms the

replacement of epoxy, hydroxyl and carbonyl groups on GO by carboxyl groups during the carboxylation stage.

Both CGO-Arg and CGO-Glu show a similarly drastic decrease in the 285 eV and 287 eV components, and an increase in the 289 eV component compared to GO (**Fig. 6.1b**), due to the replacement of epoxy, hydroxyl and carbonyl groups in the carboxylation stage. However, on these samples, the 287 eV component is significantly more intense than on CGO; this is to be related to the fact that on these samples, this component can also correspond to C-N [363] and C=N [364] bonds, which can originate from the AAs present on their surface. The higher intensity of the 285 eV component on CGO-Arg compared to CGO-Glu can be explained by the fact that Arg has more C-N/C=N bonds than Glu. The peak at ~289 eV (**Fig. 6.2a**) on these samples can be also assigned to amide groups (N-C=O) originating from the coupling between AAs and carboxyl groups during EDC coupling [365]. The CGO-AA samples do not show significant changes in this component intensity compared with CGO (**Fig. 6.1b**); this is to be expected, since the amide bond formed by EDC coupling substitute for carboxylate groups already present on CGO.

The changes in C=O and C-O bonds are also evident from the high resolution O 1s spectra shown in Fig. 6.2b (components centered at 531.4±0.2 and 533.1±0.1 eV, respectively) [366]. Consistent with the C 1s results, the C-O component of O 1s, originating from hydroxyl or epoxy groups, is significantly lower for the CGO and CGO-AA samples in comparison with the GO sample, while their C=O component, relative to carbonyls or carboxylates, is significantly higher (Fig. 6.1c). This further confirms the replacement of oxygen-containing functional groups on GO by carboxyl groups during the carboxylation stage. The small component at 535.0±0.1 eV observed on all samples (Fig. 6.2b) can be attributed to water molecules [367]. Its higher intensity (Fig. 6.1c) on CGO and CGO-AA samples compared to GO nicely confirms the presence of more charged functional groups on these samples, making them more hydrophilic.

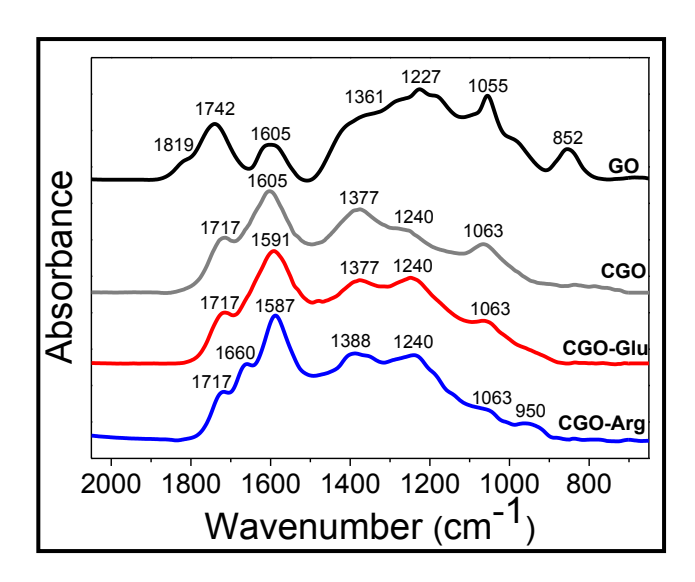


Fig. 6.3. FTIR spectra recorded on GO, CGO, CGO-Glu, and CGO-Arg.

**Table 6.2.** Assignments of peaks found on FTIR spectra shown in **Fig. 6.3** for GO, CGO, CGO-Glu, and CGO-Arg. Note that only the main contributions for each peak are reported in this table. Multiple species may contribute to each peak.

Dooles	Wavenumbers (cm <sup>-1</sup> )					
Peaks	GO	CGO	CGO-Glu	CGO-Arg		
v C-O-C	852	-	-	-		
ν С-ОН	1055	1063	1063	1063		
v C-O-C	1227	1240	1240	1240		
δОН	1361	1377	1377	1388		
v C-C	1605	overlapping with carboxyls at 1605	overlapping with carboxyls at1591	overlapping with carboxyls at 1587		
ν C=O from amide I band	-	-	-	1660		
$\nu$ C=O from carboxyl $\delta_{NH}$ from amide II band	Overlapping with carbonyl at 1742	1717, 1605	1717, 1591	1717, 1587		
ν C=O from carbonyl	1819, 1742	overlapping with carboxyls at 1717	overlapping with carboxyls at 1717	overlapping with carboxyls at 1717		

#### 6.4.1.2. FTIR analysis

FTIR analysis confirms the presence of AAs on the surface of CGO-AA samples. **Fig. 6.3** shows the FTIR spectra recorded on GO, CGO, CGO-Glu, and CGO-Arg sample from 650 to 2050 cm<sup>-1</sup> (see **Table 6.2** for more detail). Many of the features between 700 and 1400 cm<sup>-1</sup> decrease in intensity when going from GO to all other samples. Vibrations in this region include mainly  $\nu_{\text{C-O-C}}$  (~852 and 1227 cm<sup>-1</sup>),  $\delta_{\text{OH}}$  (~1361 cm<sup>-1</sup>), and  $\nu_{\text{C-OH}}$  (~1055 cm<sup>-1</sup>), i.e. epoxy and alcohol groups from GO [368, 369]. Their disappearance in CGO and CGO-derived samples confirms the elimination of these groups upon carboxylation. The peak at 1361 shifts to 1377-1388 cm<sup>-1</sup> on functionalized samples, as it becomes superimposed and substituted with  $\nu_{\text{OH}}$  from carboxylic groups [370].

Similarly, the peaks at ~1819 cm<sup>-1</sup> and 1742 cm<sup>-1</sup> are observed only on GO. These peaks are related to  $v_{C=O}$  from carbonyl groups [368]; possibly the presence of two different peaks is related to the fact that some of them are isolated (absorbing at 1819 cm<sup>-1</sup>) and some H-bonded to closeby OH groups or water molecules (peak at 1742 cm<sup>-1</sup>). The peak at 1742 cm<sup>-1</sup> may include contributions from carboxylic groups, too [371]. The peak relative to isolated carbonyls completely disappears on all functionalized samples, while the one at 1742 cm<sup>-1</sup> shifts or becomes superimposed with other peaks, as discussed below. This confirms the elimination of most carbonyl groups upon GO carboxylation.

The peak roughly centered at ~1605 cm<sup>-1</sup> is attributed to  $v_{CC \text{ aromatic}}$  on GO [368]. This peak is superimposed with  $v_{CO}$  from carboxylic acids on CGO and CGO-AA;  $v_{CO}$  in fact involves two peaks, at 1605 cm<sup>-1</sup> and at 1717 cm<sup>-1</sup> [372]. The 1717 cm<sup>-1</sup> peak may be superimposed with  $v_{CO}$  from residual carbonyls, too. After EDC coupling, these carboxylic groups are converted to amides. On CGO-Glu, carboxylic functionalities are added again, due to the binding of Glu on the surface, and therefore not many differences are observed between the CGO and CGO-Glu spectra; only, the  $v_{CO}$  peak shifts from 1605 cm<sup>-1</sup> on CGO to 1591 cm<sup>-1</sup> on CGO-Glu, likely because it is superimposed with the amide II band ( $\delta_{NH}$ ) that is expected in this same frequency region [371]. On CGO-Arg, a similar shift, although more prominent, is observed (from 1605 to 1587 cm<sup>-1</sup>); the presence of amides on this sample is more clearly visible thanks to a clear peak due to amide I band at 1660 cm<sup>-1</sup>. This difference between the spectra of CGO-Glu and CGO-Arg indicates the presence of more amide bonds on CGO-Arg than CGO-Glu. This could be interpreted as indicating that more Arg molecules are bonded to CGO-Arg than Glu on CGO-

Glu, which would be in disagreement with what previously discussed by XPS. However, Arg can form more than one amide bond per Arg molecule, since it has three NH<sub>2</sub> groups per molecule while Glu only one. Thus this result alone is not sufficient to determine the relative amount of Arg and Glu present on the CGO-AA samples.

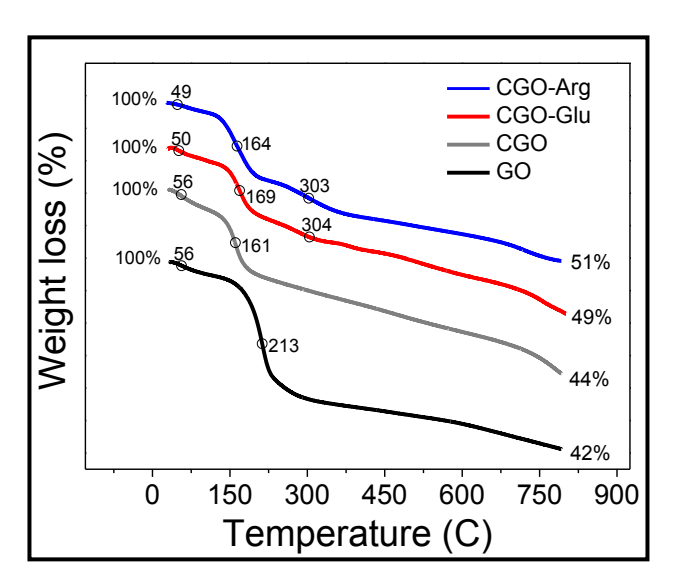


**Fig. 6.4.** TGA curves collected under N<sub>2</sub> atmosphere on GO, CGO, CGO-Glu, and CGO-Arg samples. The empty circles correspond to the temperatures at which peaks were observed on the δmass/δT derivative curves.

**Table 6.3.** Weight loss temperature (°C) and corresponding weight loss (% WL) observed on the TGA curves (**Fig. 6.4**) for GO, CGO, CGO-Glu, and CGO-Arg samples. Asterisk (\*) and plus (+) signs indicate values that are statically significantly different from the correspondent values measured on GO and CGO samples, respectively, with P lower than 0.05.

Samples	GO	CGO	CGO-Glu	CGO-Arg
WL (T1)	5±1 (57±1)	6±1 (57±2)	4±1 (53±3)	3±0*+ (53±6)
WL (T2)	38±1 (206±9)	20±1* (163±3)	19±1* (167±2)	21±0* (165±1)
WL (T3)	$0\pm0~(N/A)$	0±0 (N/A)	$11\pm1*^{+}(340\pm15)$	$11\pm1*^{+}(302\pm1)$

#### 6.4.1.3. TGA

We attempted to quantify the amount of functional groups on our samples by TGA (Fig. 6.4). Two main decomposition temperatures are observed for GO and CGO, and three for CGO-AA samples. These temperatures are summarized in **Table 6.3**, along with the corresponding weight loss at each temperature. The weight loss observed at T1 (~55° C) can be attributed to the evaporation of water molecules [373]. These are mainly trapped inside the GO structure, and there are no significant differences in WL% at this temperature among all samples. The weight loss at T2 observed on all samples can be ascribed to the pyrolysis of oxygen-containing functional groups, such as carboxyl, epoxy, carbonyl, and hydroxyl groups into CO, CO<sub>2</sub>, and steam [373, 374]. T2 is lower for CGO (163±3 °C), CGO-Glu (167±2 °C), and CGO-Arg samples (165±1 °C) than for GO (206±9 °C). This can be attributed to the higher concentration of carboxyl groups on CGO and CGO-derived samples, since carboxyls are more labile and have lower decomposition temperatures than carbonyl, epoxy or hydroxyl groups [369, 375]. The weight loss at this temperature is significantly higher for GO (38±1 %) than on CGO (20±1), CGO-Glu (19±1), and CGO-Arg (21±0). This once again confirms that there are more hydroxyls/epoxy/carbonyl groups on GO than carboxylic groups on CGO and CGO-derived samples.

The weight loss observed at T3 only on CGO-AA samples can be attributed to the decomposition of CN bonds, either formed during EDC coupling [376], or present in the AAs, as shown by the presence of similar temperatures on the TGA graphs of Arg and Glu powders (**Fig. S6.2**). Since the weight loss observed at T3 is about the same on both samples (~11%), we can conclude that there are probably fewer Arg molecules on CGO-Arg than Glu molecules on CGO-Glu because Arg (i) has more CN than Glu; (ii) can form more amide bonds than Glu; and (iii) has a higher MW than Glu (174.2 g/mol and 147.1 g/mol, respectively) [376]. This is in agreement with XPS survey data discussed before (**Fig. 6.1a**).

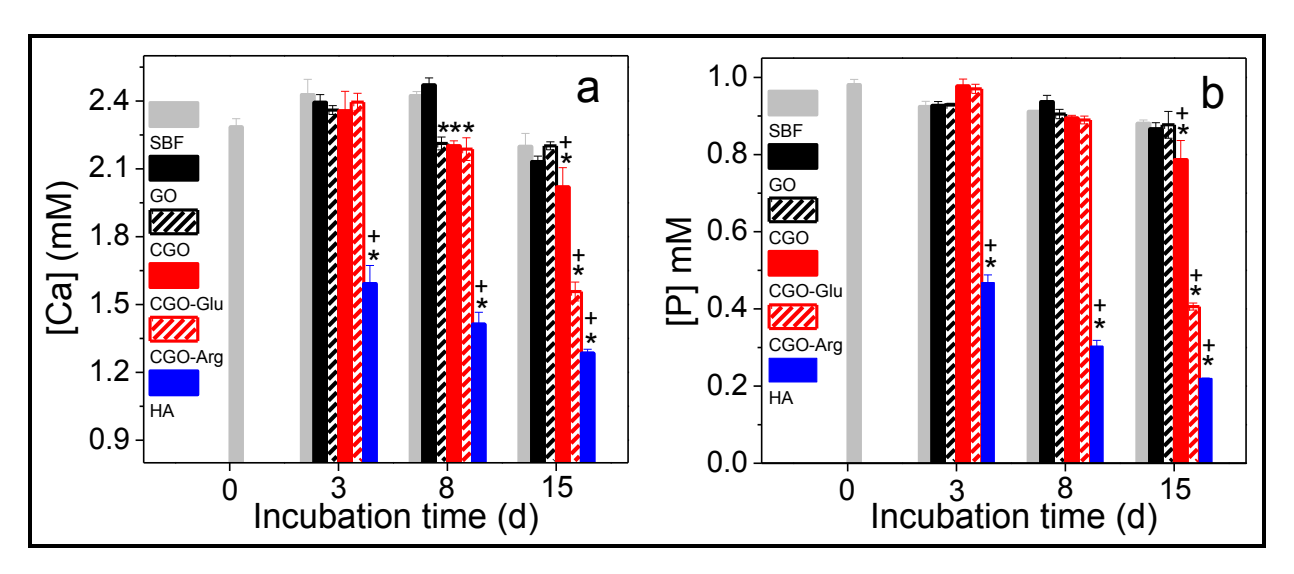


**Fig. 6.5.** [Ca] (a) and [P] (b) measured by ICP on negative control sample (SBF, grey bars) and in SBF containing GO (solid black), CGO (striped black), CGO-Glu (solid red), CGO-Arg (striped red) and positive control (HA powder, blue bars) after 0, 3, 8 and 15 days of immersion in SBF. Asterisk (\*) and plus (+) signs indicate values that are statically significantly different from the correspondent values measured on GO and CGO samples, respectively, with P lower than 0.05.

We have analyzed the functionalization of GO using XPS, FTIR and TGA. All techniques clearly show that carboxylation and further AA coupling was successful; although we were not able to quantify how many Glu and Arg molecules were bound on CGO-Arg and CGO-Glu, both XPS and TGA results indicate that fewer Arg molecules were present on CGO-Arg than Glu on CGO-Glu. FTIR results could not be interpreted quantitatively, since the main difference observed between the spectra of CGO-AA samples was related to the amide peaks, and Arg can form more amide bonds than Glu.

#### 6.4.2. Mineralization assay

After characterizing the surface of all samples, we immersed them in SBF to evaluate the mineralization potential of the modifications introduced on GO. We used ICP to measure the changes in [Ca] and [P] (**Fig. 6.5a and b**) in SBF over a period of 15 days. The sample "SBF" reported in **Fig. 6.5** in grey is a negative control, i.e. SBF without any sample immersed in it, to control for SBF stability. The sample "HA" in **Fig. 6.5** is, instead, a positive control sample, i.e. HA particles that act as nucleation seeds to promote HA precipitation (see materials and methods). No significant decrease in [Ca] (**Fig. 6.5a**) and [P] (**Fig. 6.5b**) is observed for GO, CGO and CGO-AA samples after 3 days of incubation in SBF, as well as for the negative control, while the positive control shows significantly lower [Ca] and [P] values. Significantly lower [Ca] values are observed after 8 days for both CGO and CGO-AA samples, while no

differences are found between GO and the negative control. [P] is also lower for CGO-based samples; however, this is not statically significant, thus indicating a lower decrease in PO<sub>4</sub><sup>3-</sup> than Ca<sup>2+</sup> ions. The effect of AAs on calcium phosphate precipitation becomes evident only after 15 days of incubation, when all CGO-AA samples show significantly lower [Ca] and [P] than both GO and CGO. CGO-Arg shows the strongest decrease, thus indicating that more Ca- and P-containing minerals are formed on this sample than on CGO-Glu; the decrease observed on this sample is lower than that observed on the positive control HA powder, despite the much lower surface area of the latter.

**Table 6.4.** Weight loss percentages and temperatures (°C) for GO not immersed in SBF (GO 0d), and for GO, CGO, CGO-Glu, and CGO-Arg samples immersed in SBF for 15 days. Asterisk (\*) and plus (+) signs indicate values that are statically significantly different from the correspondent values found on GO 15d and CGO 15d, respectively, with P-value lower than 0.05.

Samples	GO 0d	GO 15d	CGO 15d	CGO-Glu 15d	CGO-Arg 15d
WL % (T1)	3.0±0.3 (45)	2.0±0.2 (53)	2.0±0.2 (61)	2.0±0.2 (60)	2.0±0.2 (60)
WL % (T2)	40±4 (202)	27±3 (190)	18±2* (184)	19±2* (182)	$13\pm1*^{+}(170)$
WL % (T3)	48±5 (516)	55.0±5.5 (455)	66±7 (491)	57±6 (525)	41±4*+ (482)
Residue	9±1	16±2	14±1	21±2*+	44±4* <sup>+</sup>

**Table 6.5.** Assignments of the peaks related to HA measured by FTIR on GO, CGO, CGO-Glu, CGO-Arg and the control HA sample after immersion in SBF for 15 days (**Fig. 6.6c**). The other peaks observed on these spectra are relative to GO, and have been already reported in **Table 6.2**.

Peaks	Wavenumbers (cm <sup>-1</sup> )					
	GO (0d)	GO (15d)	CGO (15d)	CGO-Glu (15d)	CGO-Arg (15d)	НА
$v_4 PO_4$	-	-	578	578	567,604	567, 607
$\nu_1CO_3$	-	-	-	-	876	876
$\nu_1PO_4$	-	-	-	-	960	960
$\nu_3PO_4$	-	-	-	-	1040, 1105	1053, 1105
$v_3  CO_3$	-	-	-	-	-	1417, 1450, 1635

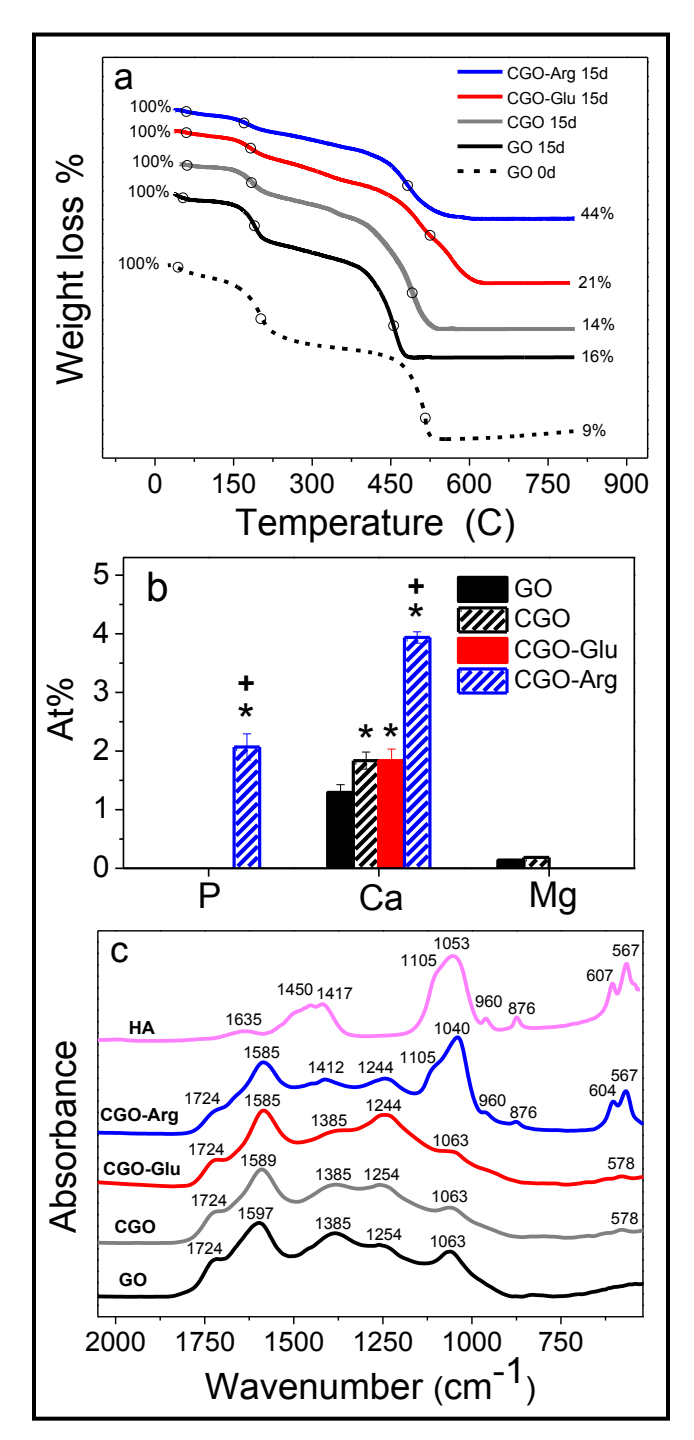


Fig. 6.6. Analysis of precipitates formed on GO, CGO, CGO-Glu, and CGO-Arg after 15 day immersion in SBF: (a) TGA curves collected in air. GO 0d is a GO sample not immersed in SBF. The empty circles correspond to the temperatures at which peaks were observed on the δmass/δT derivative curves. (b) P, Ca, and Mg atomic % measured from XPS survey spectra. Complete survey results are shown in Table S6.2. Asterisk (\*) and plus (+) signs indicate values that are statically significantly different from the correspondent values measured on GO and CGO samples, respectively, with P lower than 0.05. (c) FTIR spectra normalized with respect to the C=C peak at approximately 1585-1597 cm<sup>-1</sup>. HA is a reference spectrum for HA powder.

The amount of precipitates formed on the samples after 15 days of immersion in SBF was measured by TGA (**Fig. 6.6a** and **Table 6.4**). These TGAs are performed in air to fully burn the organic components and leave only the inorganic component as residues at the end of experiment. The weight loss at T1, T2 and T3 correspond to the removal of water molecules, C/O bonds destruction, and carbon combustion to CO and CO<sub>2</sub>, respectively [374]. The amounts of residues in **Table 6.4** indicate that CGO-Arg (44±4%) contained the highest amount of precipitate, followed by CGO-Glu (21±2%). The GO (16±2%) and CGO (14±1%) samples showed comparable amounts of inorganic component as residual mass. The residual mass (9±1%) found on GO not soaked in SBF (GO-0d) is attributed to contamination.

We analyzed the nature of the precipitates by XPS (**Fig. 6.6b** and **Table S6.2**) and FTIR (**Fig. 6.6c and Table 6.5**) spectroscopy. CGO-Arg is the only sample where both Ca and P can be detected (**Fig. 6.6b**); the Ca/P ratio is 1.9±0.2, i.e. not significantly different from what expected for HA (1.67). Ca is also present on GO, CGO, and CGO-Glu; however, its amount is significantly lower than on CGO-Arg sample, and no P can be detected, likely because it is below the XPS detection limit. This confirms what previously observed by ICP (**Fig. 6.5**), i.e. a larger amount of calcium phosphate precipitates on CGO-Arg.

The amount of Ca detected on CGO and CGO-Glu is comparable and significantly higher than on GO, which again is in line with the observed depletion of Ca in solution measured by ICP. Some Mg is observed on GO and CGO; this indicates the formation of a precipitate including Mg on these samples. Other researchers noticed the presence of Mg in HA precipitating from SBF on titanium [377]. Some N is found on GO and CGO after immersion in SBF (between approximately 1.4 and 1.7%, **Table S6.2**). Since almost no N was present on these samples before SBF immersion (**Fig. 6.1a**), this may indicate the incorporation of tris, used as a buffer in SBF, in the precipitates formed on these samples.

FTIR spectra recorded on GO, CGO, and the CGO-AA samples after 15 days of immersion in SBF are shown in **Fig. 6.6c**, along with a reference spectrum of HA. Similar to XPS, FTIR spectra for CGO-Arg show the most differences compared with the spectra recorded before SBF immersion (compare **Fig. 6.6c** and **Fig. 6.3**). New peaks related to phosphate (567, 607, 960, 1040 and 1105 cm<sup>-1</sup>) and carbonate (876 cm<sup>-1</sup>) groups appear, which indicate the formation of carbonated HA on this sample [331, 378], as clearly shown by comparing with the HA reference spectrum shown in the same graph. The peaks due to graphene that are not superimposed with

HA peaks do not change in relative intensity or position after immersion in SBF. Spectra of GO, CGO, and CGO-Glu do not show significant changes after immersion in SBF; the only visible difference is the appearance of a low intensity peak centered at ~578 cm<sup>-1</sup>, which may be related to the formation of amorphous calcium phosphate [379]. If this was the case, a corresponding peak centered at around 950 cm<sup>-1</sup> should be expected [380]; on these samples, though, this peak would be masked by the tail of the peak centered at 1063 cm<sup>-1</sup> due to the graphene substrate.

The precipitates formed on all samples are visualized using back-scattered electron (BSE) images obtained by SEM, along with images of GO flakes before immersion in SBF for comparison (Fig. 6.7). The difference in brightness observed in these images can be related to the presence of different materials on the samples. Before immersion in SBF, randomly oriented GO flakes are observed (Fig. 6.7a), with no impurities or particles on their surface (Fig. 6.7b) and c). Similar images were collected on functionalized GO samples before immersion in SBF (Fig. S6.3). After immersion in SBF for 15 days, some particles are observed on all samples (Fig. 6.7d-q). The largest amount of precipitation on CGO-Arg is clearly confirmed by the low magnification SEM images shown in Fig. 6.7a, d, g, j, and m. On GO, CGO and CGO-Glu irregularly shaped aggregates are found (average size of 1.5±1, 1.0±0.5, and 2.0±1 μm, respectively). The aggregates consist of spherical particles with average diameter of ~100±20 nm on GO and CGO (Fig. 6.7f and i), and of a more wide variety of particles on CGO-Glu (Fig. 6.71). On CGO-Arg, instead, two different sets of particles are observed (Fig. 6.7n-q): many micron-sized spherulites of 3.5±0.5 µm diameter made of nano-sized platelets (20±3 nm) (Fig. **6.6n and o)**, and a few spherical particles of 60±5 nm diameter (Fig. 6.7p and q). We discuss this in more detail below when we analyze the TEM results for this sample.

**Table 6.6**. Mg/P and Ca/P ratio calculated from the SEM-EDS spectra on GO, CGO, CGO-Glu, and CGO-Arg after 15 day immersion in SBF.

Samples	Ca/P	Mg/P
GO	10.1±3.1	$0.64 \pm 0.1$
CGO	9.8±1.2	9.13±3.18
CGO-Glu	$4.0 \pm 1.8$	$0.64 \pm 0.45$
CGO-Arg (spherulite)	$1.8 \pm 0.3$	$0.04 \pm 0.02$
CGO-Arg (sphere)	1.7±1.2	$0.14 \pm 0.17$

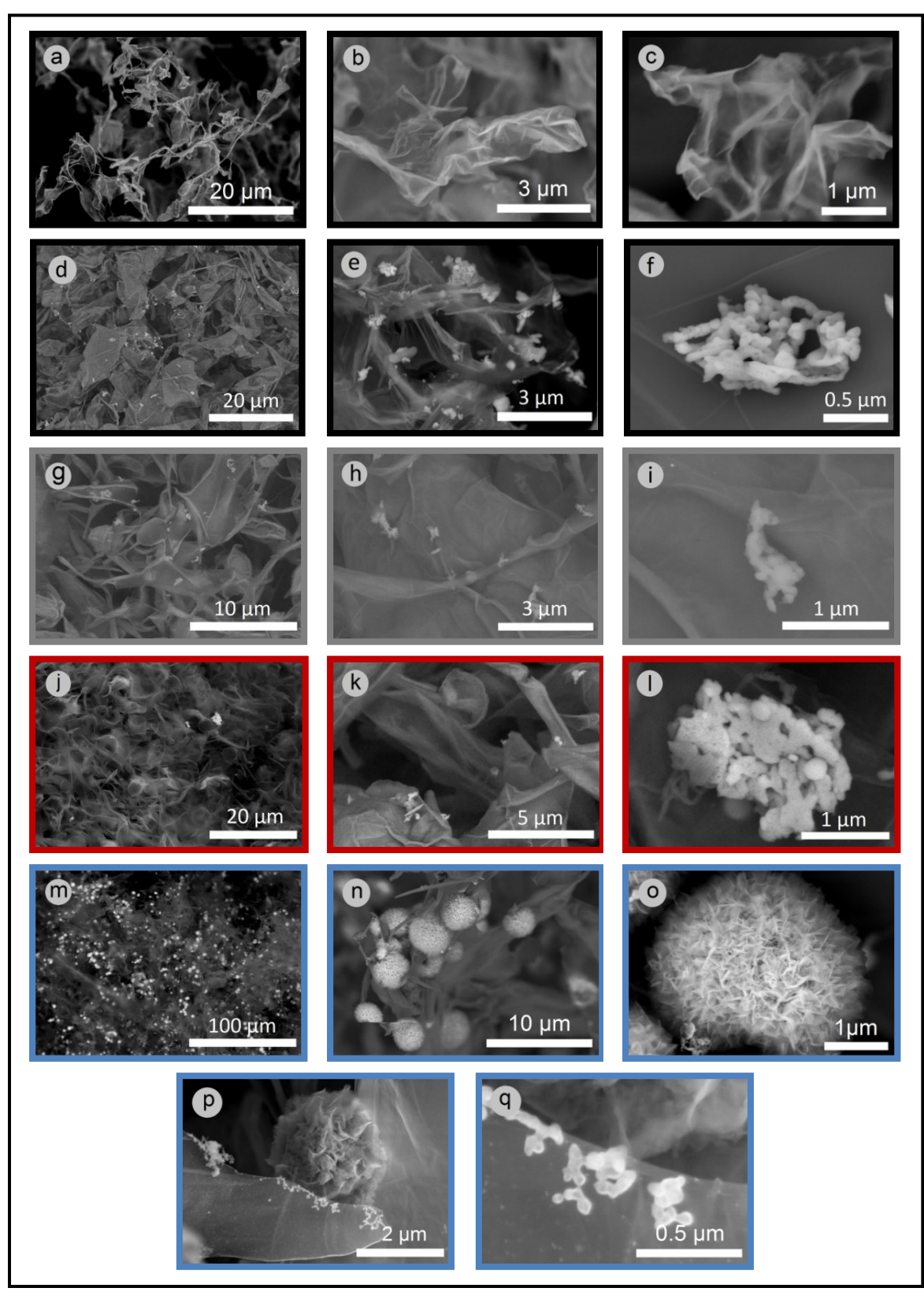


**Fig. 6.7**. BSE-SEM images of GO sample not immersed in SBF (a-c) and GO (d-f), CGO (g-i), CGO-Glu (j-l), and CGO-Arg (m-q) sample immersed in SBF for 15 days.

EDS analysis showed the presence of C, N, O, P, Ca, and Mg on all samples. A small amount of S was also present on the smaller particles obseved on CGO-AA samples, possibly due to the S originally present on these samples (Fig. 6.1a). The Ca and Mg content in each sample is normalized to P and shown in **Table 6.6.** The Ca/P ratio measured on the micron-sized particles on CGO-Arg (Fig. 6.70) is 1.8±0.3, which is very close to that of HA (1.67). This confirms that these particles are HA, as hypothesized before based on both IR and XPS (Fig. **6.6b** and c). Both we and other researchers previously reported the formation of micron-sized HA spherulites in the presence of AAs with morphology very similar to that shown in Fig. 6.7 [37, 290, 331]. The Ca/P ratios measured on the small spherical particles observed on CGO-Arg (Fig. 6.7q) have large variability  $(1.7\pm1.2)$ , likely due to the fact that it was difficult to isolate them during the analysis. More definite results on these particles are provided by TEM, discussed below. Much higher Ca/P ratios are found on GO and CGO (10.1±3.3 and 9.8±1.2, respectively). These values indicate that on these samples there is no significant amount of HA, and the high amount of Ca may be related to physisorbed Ca ions or Ca(OH)<sub>2</sub> derivatives [381]. A Ca/P ratio closer to HA is found on CGO-Glu (4.0±1.8). Similarly to what found by XPS, EDS shows the presence of significant amounts of Mg only on GO and CGO (error bars on the Mg/P found on the other samples make them not statistically significant). Finding Mg only on the samples that show the highest Ca/P ratios and lowest amounts of HA may be related to the role of Mg as an inhibitor of HA crystallization [382].

CGO-Arg immersed in SBF for 15 days was further analyzed by TEM (**Fig. 6.8**). Again, we observed both spherulitic particles with diameters of ~3±1μm (**Fig. 6.8a**) and much smaller nanoparticles with diameters of ~50±5 nm (**Fig. 6.8d**). Both types of particles contained mainly Ca and P (see EDS spectra shown in the insets). Traces of Mg are detected on the larger particles only, although its absence on the nanoparticle spectrum may be due its overall lower intensity. The selected area electron diffraction (SAED) pattern shown in **Fig. 6.8b** shows that the spherulitic particles are crystalline, consistent with IR results and previous SEM discussion based on Ca/P ratios. SAED on the nanoparticles, instead, show only amorphous material. Most likely, then, these smaller particles are amorphous calcium phosphate precursors not yet transformed into HA. The presence of these particles on CGO-Arg may be interpreted in two different ways. Nucleation may be continuously occurring on this sample. The ACP nanoparticles are formed first, and with time they conglomerate and reorganize into the micron-

size spherulitic crystalline HA particles observed in **Figs. 6.70 and 6.8a**. Throughout SBF immersion, ACP nanoparticles keep nucleating, and thus after 15 days some of them are still visible. Alternatively, it is possible that some precipitates remain in the form of ACP nanoparticles and never transform into HA. A study performed at different time points will be the subject of a forthcoming publication, to help elucidate which of these mechanisms is correct, and to attempt explaining the similar shape but different composition observed for the nanoparticles found on CGO-Arg and all other samples.

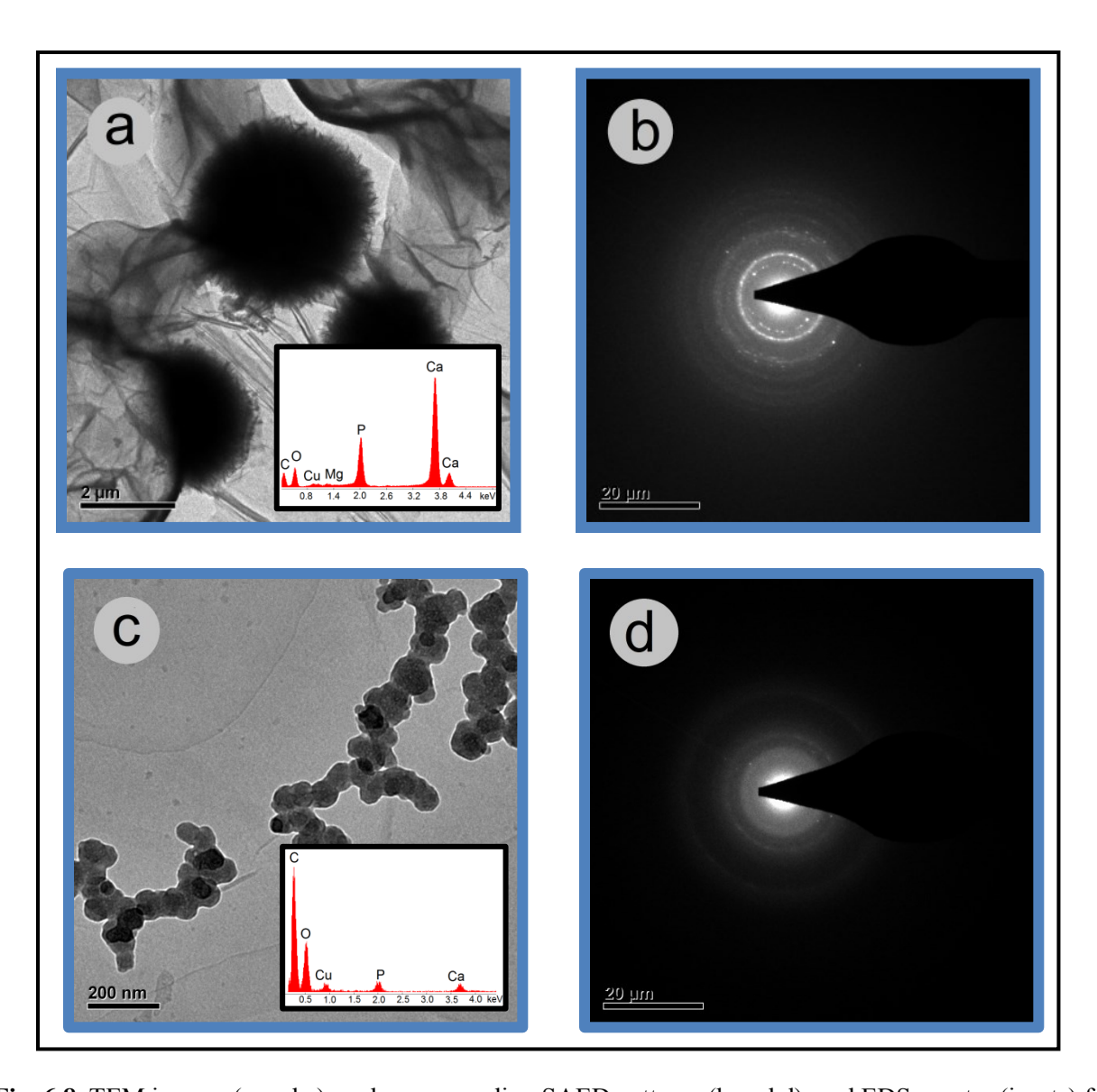


**Fig. 6.8.** TEM images (a and c), and corresponding SAED patterns (b and d), and EDS spectra (insets) for CGO-Arg sample immersed in SBF for 15 days.

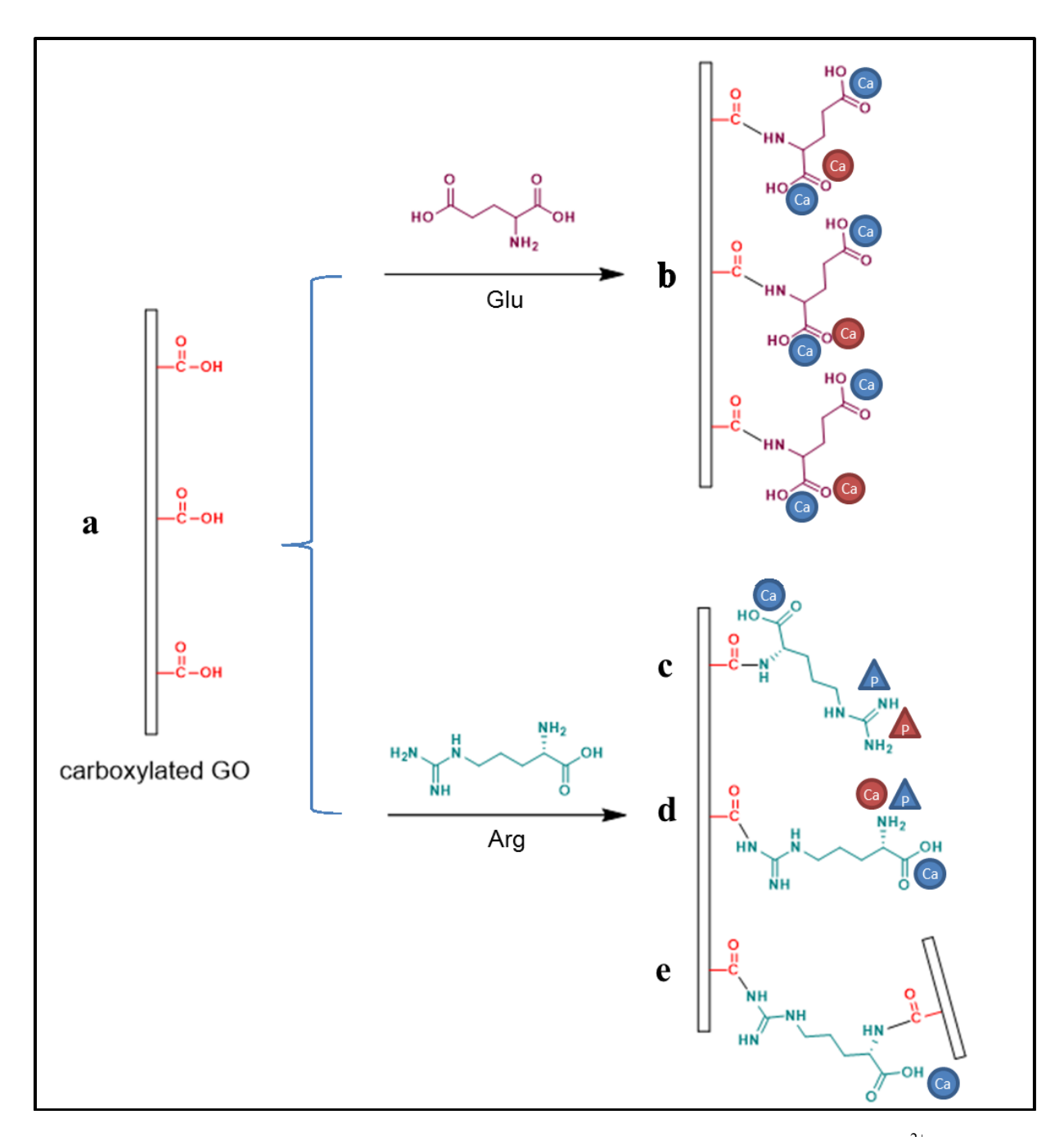


**Fig. 6.9**. Schematic showing possible interactions of Glu and Arg with CGO surface and Ca<sup>2+</sup> (circle) and PO<sub>4</sub><sup>3-</sup> (triangle) ions. The ions are shown in red or blue if they are interacting with the AAs by forming complexes or electrostatically, respectively.

### 6.5. Discussion

The results presented before overall show that both a positive (Arg) and a negative (Glu) AA increase HA precipitation rate compared to CGO and GO; however, despite the fact that we probably had fewer Arg molecules bound on CGO-Arg than Glu on CGO-Glu, Arg increased HA precipitation rate much more than Glu, and much more HA was found on CGO-Arg than CGO-Glu after 15 days of immersion in SBF. This result contradicts many previous studies, which showed that the interaction between Ca<sup>2+</sup> and negatively charged residues of biomolecules, such as carboxylate and phosphorylated groups play a key role in HA precipitation [58, 61, 259, 261, 262, 355]. In this section, we first attempt to provide an explanation for this result, and then we compare the effectiveness of CGO-Arg on HA precipitation with previously reported GFN substrates.

### 6.5.1. Effect of Arg vs. Glu bound to CGO on HA precipitation

Precipitation happens when the concentration of precursor ions in solution increases above a critical level. This can be achieved locally on a surface, if there are some functionalities that can strongly interact with the ions. Our results show that both Arg and Glu are able to locally increase Ca<sup>2+</sup> and PO<sub>4</sub><sup>3-</sup> surface concentration, and induce early nucleation of HA compared to what observed on both GO and CGO. Since we had somewhat fewer Arg molecules on CGO-Arg than Glu on CGO-Glu, Arg must be able to interact with the ions more strongly than Glu. **Fig. 6.9** shows a few possible ways in which Arg and Glu may bind to CGO, and the subsequent interactions between the remaining functional groups exposed by the AAs and Ca<sup>2+</sup> and PO<sub>4</sub><sup>3-</sup> ions in solution. With the help of this schematic, we discuss here two reasons why Arg is a more effective HA nucleator than Glu.

As shown in **Fig. 6.9b**, after binding to CGO, Glu exposes two carboxylate groups, one alpha and one gamma, which can interact with the ions present in solution. While Ca<sup>2+</sup> ions can interact with these groups (stability constants of log K=1.4 [301] and 1.7 [301] are reported for Glu/Ca<sup>2+</sup> complexes at pH 7.4), PO<sub>4</sub><sup>3-</sup> ions do not have strong interactions with carboxylate groups [331]. Therefore, Glu/PO<sub>4</sub><sup>3-</sup> complexes are not shown in **Fig. 6.9**. Arg can bind to CGO through both its  $\alpha$ -amino (**Fig. 6.9c**) and guanidyl group (**Fig. 6.9d**), which implies that it exposes to the solution its  $\alpha$ -carboxyl group and either its guanidyl group (**Fig. 6.9c**) or  $\alpha$ -amino (**Fig. 6.9d**). Arg can also form more than one amide bond to CGO (**Fig. 6.9e** shows an example

of this). At pH 7.4, Arg can interact with  $Ca^{2+}$  ions through its  $\alpha$ -amino group, forming complexes whose stability constant (log K) is 2.21 [299]. Arg can interact with  $PO_4^{3-}$  ions through its guanidyl side chain , forming a complex with reported stability constant of log K=1.9 [306]. The stability constants of complexes formed between Arg and both  $Ca^{2+}$  and  $PO_4^{3-}$  are higher than between Glu and  $Ca^{2+}$ . Thus, the faster precipitation of HA on CGO-Arg than on CGO-Glu may be partially explained by the stronger  $Arg/Ca^{2+}$  and  $Arg/PO_4^{3-}$  interactions leading to more stable complexes formed on CGO-Arg, which result in higher concentration of  $Ca^{2+}$  and  $PO_4^{3-}$  ions on the CGO-Arg surface.

In addition to complex formation, electrostatic interactions between surface functional groups and Ca<sup>2+</sup> and PO<sub>4</sub><sup>3-</sup> ions could play a role in HA precipitation. As shown by zeta potential measures (**Fig. S6.4**), all surfaces are overall negatively charged. However, locally, CGO-Arg exposes both positive and negative charges (**Fig. 6.9c and d**) while CGO-Glu exposes only negative charges (**Fig. 6.9b**). This implies that locally, CGO-Arg is more likely to attract both Ca<sup>2+</sup> and PO<sub>4</sub><sup>3-</sup> ions than CGO-Glu, which is likely to attract only Ca<sup>2+</sup> ions. This factor may contribute to a higher increase in local supersaturation with respect to HA for CGO-Arg than CGO-Glu sample, and thus a faster precipitation of HA on CGO-Arg. This hypothesis is confirmed by the EDS (**Table 6.6**) and XPS (**Fig. 6.6b**) results, which showed higher Ca/P ratios on CGO-Glu than on CGO-Arg, thus confirming the larger tendency for CGO-Glu to attract positively charged ions than CGO-Arg. Thus, the presence of both positively and negatively charged groups close to each other on CGO-Arg may be another justification for the stronger HA-nucleating effect of this sample compared to CGO-Glu.

### 6.5.2. Arg-CGO as a strong nucleator of HA

In this section we compare our precipitation results with the few previous studies on invitro precipitation of HA on GFNs [58, 61, 355], despite the difficulties related to different SBF concentrations used and sometimes lack of quantitative data like TGA. In general, GFNs are good HA nucleators due to their high surface area, and the presence of biomolecules always increase the amount and rate of HA precipitation [58, 59, 61, 355, 357].

Liu et al showed the formation of HA on reduced GO (rGO) modified with a layer of insitu polymerized dopamine (polydopamine, PDA) after 1 week and gelatin-modified GO after 2 weeks of immersion in 1.5 X SBF [58, 355]. On rGO-PDA, a layer of HA nanoparticles was formed, in an amount corresponding to ~50% in weight of the composite, as evaluated by TGA

[58]. This result is comparable with what we observed after 2 weeks of immersion in SBF (**Fig. 6.6a**); however, we used 1.5 less concentrated SBF than Liu et al. Thus, we conclude that Arg and PDA are similarly effective in promoting HA nucleation, despite their large differences in size. On rGO-gelatin, Liu et al show spherulitic particles similar to what we found on CGO-Arg [355]. Although no quantitative TGA results are reported, SEM images show a more extensive coverage on this sample after 2 weeks of immersion in 1.5 X SBF than what we observed. However, since no images at earlier times are shown on this sample, it is hard to compare the effects of the two substrates, given the larger SBF concentration used in Liu's work.

Fan et al showed that the surface of casein phosphopeptide (CPP)-modified CGO was partially covered with HA nanoparticles after only 1 day incubation in 1.5 X SBF and was completely covered with HA after 3 days, corresponding to a HA content of ~80 wt% by TGA [61]. This amount of precipitation achieved in such a short time is significantly larger than what we observed after 15 days (**Fig. 6.6a**), and thus cannot be just related to the higher concentration of SBF used in [61]. Evidently, the high concentration of phosphonate groups on CPP makes these peptides much stronger HA nucleators than Arg.

Overall, this comparison shows that although a small, positively charged molecule like Arg cannot compete with highly phosphonated biomolecules, its effectiveness at promoting HA nucleation once bound to GO or CGO is not drastically different from that of large, negatively charged biomolecules such as PDA or gelatin. This confirms the importance of the large local supersaturation achieved in the presence of Arg, due to both complex formation and electrostatic reasons, as discussed in the previous section.

### 6.6. Conclusion

We studied the effect of a positively (Arg) and a negatively (Glu) charged AA bound to GO flakes on the precipitation of HA at physiological conditions. Both AAs were bound to GO after transforming oxygenated GO functionalities in carboxyl groups (CGO). We showed that while both AAs increased HA precipitation rate on CGO compared to GO and CGO, Arg increased GO mineralization rate much more than Glu, giving rise to larger amounts of HA precipitates, including both micron-sized spherulitic aggregates and smaller nanoparticles. We explained these results based on two factors: Arg can form more stable complexes with Ca<sup>2+</sup> and PO<sub>4</sub><sup>3-</sup> ions than Glu; and, the presence of both carboxyl and amino groups exposed to the

solution on CGO-Arg may favor local supersaturation with respect to HA by electrostatically attracting both Ca<sup>2+</sup> and PO<sub>4</sub><sup>3-</sup> ions. This result may not be generalized to *all* positive and negative functionalities; for example, groups able to form even stronger complexes with either ion, such as phosphonate groups, which can attract Ca<sup>2+</sup> ions very strongly, may change this balance. Indeed, when comparing our results with previous work studying mineralization of surface-modified rGO, we showed that the amount of HA deposited on CGO-Arg was much lower than that observed in the presence of heavily phosphonated peptides like CPP.

Overall, this report provides new insights on the effect of single AAs bound to surfaces on HA mineralization in physiological conditions, and some guidelines on how to improve the mineralization of GO for bone regeneration applications. If our insight on the importance of both complex formation and presence of positive and negative groups to increase local supersaturation is correct, future attempts to modify material surfaces to improve HA mineralization should include similar amounts of phosphonates and amino groups.

# 6.7. Acknowledgement

This research project is supported by the McGill Engineering Doctoral Award, the Canada Research Chair foundation, the Natural Science and Engineering Research Council of Canada, the Canada Foundation for Innovation, the Center for Self-Assembled Chemical Structures, and the Fonds Quebecois de la Recherche sur la Nature et les Technologies. Also, we would like to thank Mr. Gul Zeb for his help with drawing the schematic in **Fig. 6.8**.

# SI. 6. Supporting information

This document shows a schematic representation of EDC/NHS coupling reaction (SI.6.1), X-ray photoelectron spectroscopy (XPS) survey results for GO and functionalized GO samples before immersing in SBF (SI.6.2), thermogravimetric analysis (TGA) analysis of Arg and Glu powder as reference samples (SI.6.3), XPS survey results for GO and fictionalized GO samples immersed in SBF for 15 days (SI.6.4), scanning electron microscopy (SEM) pictures of CGO and CGO-Arg samples (SI.6.5), and zeta potential measured on GO and fictionalized GO samples (SI.6.6).

### SI. 6.1. EDC/NHS coupling reaction

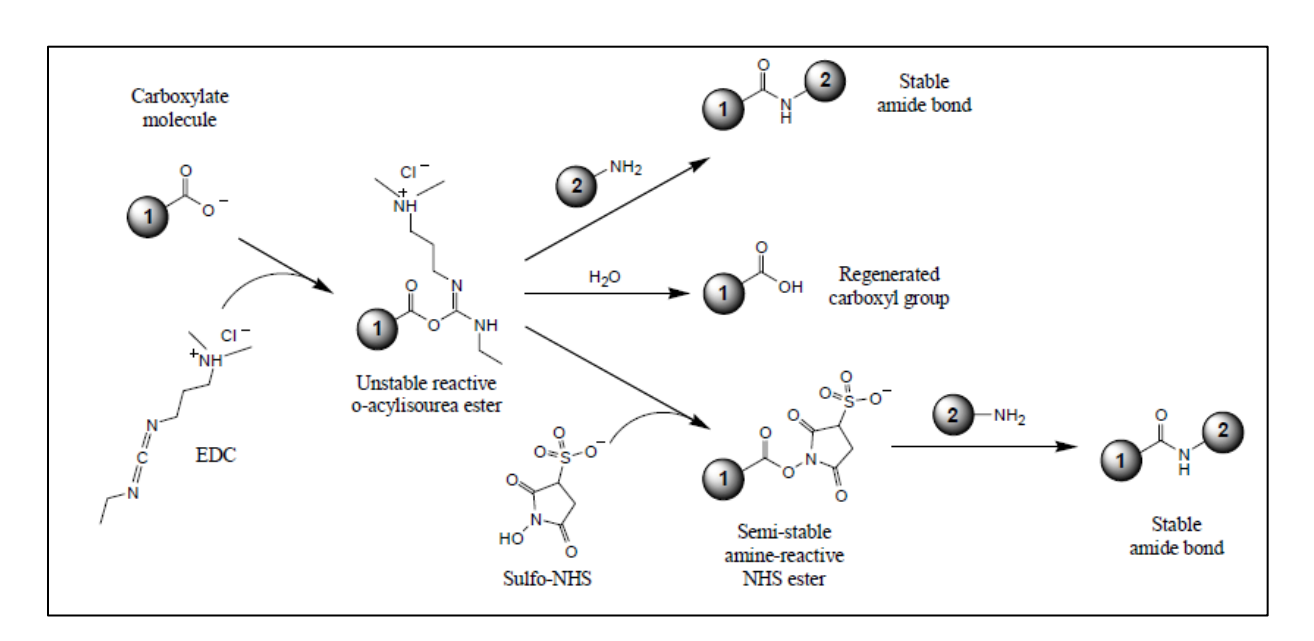


**Fig. S6.1.** Schematic showing general EDC/NHS coupling reactions (reproduced from http://www.piercenet.com/instructions/2160650.pdf).

#### SI. 6.2. XPS survey results for CGO-EDC and functionalized GO samples

CGO-EDC is a CGO sample that has been immersed in the EDC/NHS coupling solution and treated as the CGO-AA samples, with the difference that no AAs were added on its surface.

**Table S6.1.** O, C, S, and N atomic % on GO, CGO, CGO-EDC, CGO-Glu, and CGO-Arg sample obtained from XPS survey spectra. Asterisk (\*), plus (+), and cross (x) signs indicate values that are statically significantly different from the correspondent values measured on GO, CGO and CGO-EDC samples, respectively, with P lower than 0.05.

Samples	GO	CGO	CGO-EDC	CGO-Glu	CGO-Arg
О	32±1	25±3*	23.7±0.2*	21±1*	22±1*
C	67±1	72±3*	72±1*	72±1*	70±1*
S	1.2±0.5	$0\pm0$	$1.1\pm0.1^{+}$	$1.54\pm0.03^{+x}$	$1.4\pm0.1^{+x}$
N	$0.1 \pm 0.3$	$0\pm0$	$1.4\pm0.5^{*+}$	$2.6\pm0.1*^{+x}$	$4.3\pm0.2^{*+x}$

### SI.6.3. TGA reference curves for Arg and Glu powders under N2 atmosphere

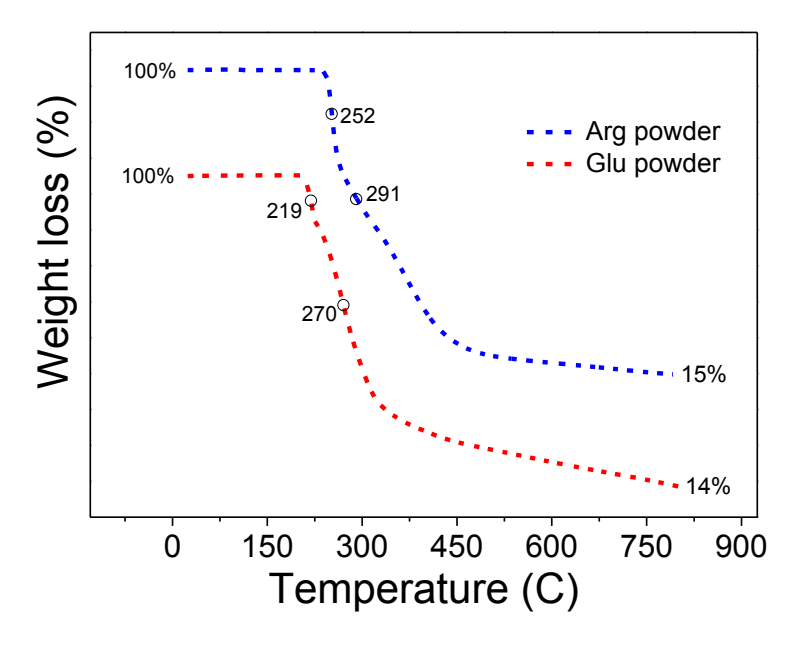


Fig. S6.2. TGA curves collected under  $N_2$  atmosphere on the AA powders as reference samples. The empty circles correspond to the temperatures at which  $\delta$ mass/ $\delta$ T peaks, indicating weight loss, were observed on the derivative curves.

# SI. 6.4. XPS survey results for GO and functionalized GO samples immersed in SBF for 15 days

**Table S6.2**. C, O, S, N, P, Ca, and Mg at% measured from XPS survey spectra on GO, CGO, CGO-Glu, and CGO-Arg samples immersed in SBF for 15 days. Asterisk (\*) and plus (+) signs indicate values that are statically significantly different from the correspondent values measured on GO and CGO samples, respectively, with P lower than 0.05.

Samples	GO	CGO	CGO-Glu	CGO-Arg
С	$68.4 \pm 0.8$	70.5±0.4*	$72.0\pm0.3*^+$	63.8±0.5*+
O	$28.3 \pm 0.8$	26.1±0.3*	$22.7 \pm 0.4^{*+}$	26.2±0.3*
S	$0.0 \pm 0.0$	$0.0 \pm 0.0$	$1.0\pm0.1*^{+}$	$0.8 \pm 0.2^{*+}$
N	1.7±0.1	1.4±0.1*	2.6±0.3*+	3.2±0.3*+
P	$0.0 \pm 0.0$	$0.0 \pm 0.0$	$0.0 \pm 0.0$	$2.1 \pm 0.2^{*+}$
Ca	1.3±0.1	1.8±0.1*	1.8±0.2*	3.9±0.1*+
Mg	$0.1 \pm 0.0$	$0.2 \pm 0.0 *$	$0.0 \pm 0.0 *$	$0.0 \pm 0.0 *^+$

## SI. 6.5. SEM pictures

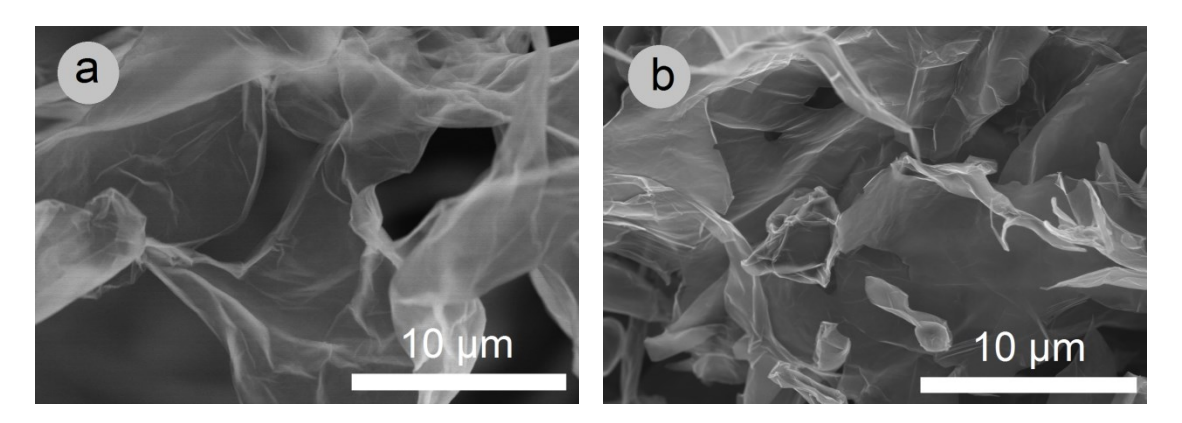
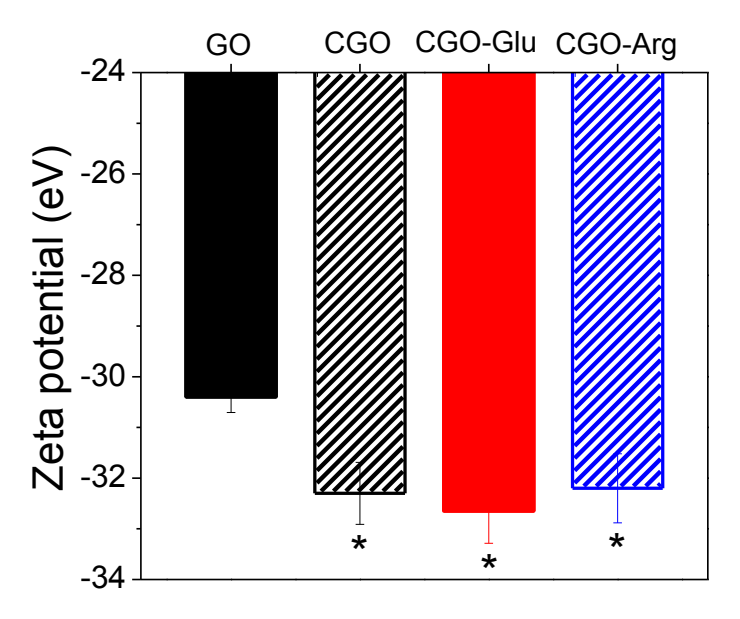


Fig. S6.3. SEM images of CGO (a) and CGO-Arg (b) sample not immersed in SBF.

### SI. 6.6. Zeta potential measured on GO and functionalized GO samples



**Fig. S6.4.** Zeta potential measured on GO, CGO, CGO-Glu, and CGO-Arg samples. Asterisk (\*) signs indicate values that are statically significantly different from the correspondent values measured on GO with P lower than 0.05.

Sample surface charge was measured using a Zetasizer Nano ZS (Malvern Instruments, UK). The samples were dispersed in DI water to make a suspension with a concentration of  $\sim$  0.02 mg/ml. Each measurement was performed three times using disposable capillary cells with an electrical field (E) between 5 and  $10 \pm 0.1$  V/m as automatically setup by the instrument.

Zeta potential measurements at pH 7 on GO, CGO, and the CGO-AA samples show that all samples have negatively charged surfaces ranging from -30 to -36 eV. The value measured for GO is in agreement with previous reports [383], and has to be attributed to the presence of negatively charged oxygen-containing species on its surface. CGO shows a more negative charge than GO; this once again confirms the transformation of surface oxygenated groups into carboxylates, which are more negatively charged than alcohols or epoxy groups. No significant differences in surface charge are observed between CGO-AA and CGO. However, one would expect a more negatively charged surface on CGO-Glu than on CGO, if all carboxylate groups from CGO had reacted and been covalently bound to Glu molecules, since each carboxylate from CGO would be replaced with two carboxylate groups from Glu, exposed towards the surface (see Fig. 9b). Vice versa, if all carboxylate groups from CGO had reacted with Arg, one would

expect a more positive potential on CGO-Arg, since each of them would have been substituted with a carboxylate and an amino group exposed at the surface (see **Fig. 9c and d**). Although there is a somewhat lower potential on CGO-Glu than on CGO and a somewhat higher potential on CGO-Arg than CGO, the fact that we do not see significant differences among these samples may imply that the overall surface potential is still dominated by unreacted carboxylated groups.

### CHAPTER 7

# CONCLUSIONS, SUMMARY OF CONTRIBUTIONS AND FUTURE PERSPECTIVES

# 7.1. Conclusions: highlights

- Arg and Glu inhibit HA precipitation when dissolved in solution. However, the positively charged AA, Arg, has a stronger inhibitory effect on HA nucleation while the negatively charged AA, Glu, is more effective in inhibiting HA crystal growth along specific crystallographic directions. This was attributed to the differences in stability constants between AAs and the ions in solution and the adsorption of AAs on HA crystal surfaces.
- The presence of AAs, either Arg or Glu, dissolved in solution results in the formation
  of spherulitic HA particles while randomly shaped aggregates are obtained when the
  AAs are absent.
- The inhibitory effect of the single AAs on HA nucleation is dampened if the two AAs are present together in solution. This is explained by the preferential interaction of the AAs with each other rather than with ions or HA nuclei in solution.
- If the Glu- and Arg-containing Ca- and P-precursor solutions are aged, the Ca/AA and P/AA complexes initially formed in the solution can grow into large aggregates. These aggregates can interact with each other once the precursor solutions are mixed and regulate HA precipitation under a different pathway than in the non-aged solutions.

This results in striking differences in precipitation time, HA morphology and composition.

- Aged precursor solutions have a stronger effect on HA precipitation if they contain
  Arg rather than Glu. This is attributed to the stronger interactions of Ca<sup>2+</sup> and PO<sub>4</sub><sup>3-</sup>
  ions with Arg than Glu.
- Both Arg and Glu increased HA precipitation rate on CGO compared to GO and CGO; however, Arg increased GO mineralization rate much more than Glu, giving rise to larger amounts of HA precipitates. We explained these results based on two factors: Arg can form more stable complexes with Ca<sup>2+</sup> and PO<sub>4</sub><sup>3-</sup> ions than Glu; and, the presence of both carboxyl and amino groups exposed to the solution on CGO-Arg may favor local supersaturation with respect to HA by electrostatically attracting both Ca<sup>2+</sup> and PO<sub>4</sub><sup>3-</sup> ions.

### 7.2. Original contributions to knowledge

- We described the mechanism of HA precipitation at prenucleation, nucleation, and growth stages in the presence of Arg and Glu dissolved in solution. We found that both of these AAs inhibit HA precipitation, but the positively charged AA, Arg, shows a stronger effect. These AAs are useful for inhibiting excessive mineralization of HA in tissues, such as blood vessels and valves.
- We showed the formation of Ca/AA and P/AA aggregates in the prenucleation stage of
  HA precipitation. Such aggregates strongly regulate the precipitation behavior of HA
  in the nucleation and growth stages, and show the important role of organic/inorganic
  aggregates in the formation of a variety of biominerals.

- We showed that Arg and Glu bound to GO improved the precipitation of HA, with Arg showing a significantly stronger effect. We proposed Arg/GO as a potential substrate to include in bone tissue engineering scaffolds.
- We also suggested a mechanism for the improved HA precipitation in the presence of Arg- and Glu-modified GO surfaces. Based on this, we suggested that the next generation of surface modifiers used to improve HA mineralization should be rich in both negatively (e.g. carboxyl and phosphonate groups) and positively (e.g. amino groups) charged groups.
  - Overall, this work sheds some light on the existing controversy on the importance of charge when discussing the effect of AAs on HA precipitation. Despite the recognized importance of the negatively charged domains of NCPs in regulating HA precipitation in body, here we showed a positively charged AA, Arg, had both stronger inhibitory and promoting effect than a negatively charged one, Glu, depending if it was dissolved in solution or bound to a surface. This can underline the importance of other mechanisms, such as strength of complex formation rather than the AA charges only.

# 7.3. Future perspective

The results reported in this work can serve as a basis for future studies on regulating HA mineralization in the body. We suggest the following studies to further expand this research:

• In this work, we focused on the effect of small biomolecules, AAs, to better understand the role of different segments of large biomolecules, such as NCPs on HA mineralization. However, the AAs studied in this work can be bonded together to form oligopeptides with stronger effects on mineralization. Also the multivalency introduced by joining differently charged AAs to a protein can provide several sites at which attachment to calcium and phosphate ions can occur. The synthesis of such oligopeptides and proteins and the study of HA precipitation in their presence can be the subject of future work.

- We showed that the formation of Ca/AA and P/AA aggregates in the aged precursor solutions strongly affected the precipitation behavior of HA. However, the details of the formation of such aggregates in the precursor solutions should be clarified in future studies. These aggregates were very stable and were difficult to dissolve in any kinds of organic/inorganic solvent including strong acids and bases, and pure alcohol and ketones. It is possible that the Ca<sup>2+</sup> and PO<sub>4</sub><sup>3-</sup> ions are covalently bonded to the AAs, and a new material is formed upon the ions/AAs interactions. However, further characterization is required to determine the nature of these aggregates. This could help better understand the mechanism of HA precipitation in the presence of such aggregates and AAs in general.
- Although our TEM results showed the presence of some organic materials originating from the Ca/AA and P/AA aggregates in the HA structure, it is not still clear if these aggregates are incorporated within HA crystal structure or they just surround the crystals. More detailed high resolution TEM studies can determine the structure of these Ca/AA and P/AA aggregates and explain their relation with HA crystals.
- In this work, we studied the effect of AAs dissolved in solution on the prenucleation and nucleation stage of HA precipitation; however, there is no report on the effect of AAs bound to surfaces on HA precipitation at its early stages. Cryo TEM or high resolution SEM combined with EDS would enable the detection of nano-sized particles at very early nucleation stages and investigating their morphology, composition, and their evolution to HA crystals with time. Also, using GO as a substrate would allow having a thin and conductive layer ideal for TEM analyses. These studies should be performed to elucidate the effect of AAs on the transformation of HA from nuclei to crystals.
- There are several studies on the interaction of Ca<sup>2+</sup> and PO<sub>4</sub><sup>3-</sup> ions with the AAs dissolved in solution, and the stability constants of some of the Ca/AA and P/AA complexes forming by these interactions have been already reported. However, the interaction of these ions with the AAs bound to surfaces is almost completely neglected. We suggest

that the interaction of the Ca<sup>2+</sup> and PO<sub>4</sub><sup>3-</sup> ions with the AAs bound to surfaces be studied by isothermal titration calorimetry (ITC). With this technique it is possible to measure the heat of interaction between ions and solid surfaces, and one could quantify which of the bound AAs have a stronger interaction with Ca<sup>2+</sup> and PO<sub>4</sub><sup>3-</sup> ions. These findings would allow to better understand the role of different domains of larger biomolecules such as NCPs in regulating HA precipitation in the body.

Although our experiments were performed in physiological conditions, they were still far from in-vivo conditions, where many other agents, such as collagen, mineralization inhibitors, inorganic ions, etc. are involved in HA precipitation. This resulted in the formation HA with relatively different properties from the biological HA. For example, the spherulitic particles we observed in this study are different from biological HA, which consists of network-like aggregates of nano-platelets; this can be attributed to the absence of the collagen mineralization matrix. Also, the lack of carbonate ions in our precipitation solution resulted in the formation HA instead of CHA, which is found in bone. If the carbonate ion was introduced in the solution, it could interact with the positively charged AAs, and dampen their effect. At the same time, a larger amount of carbonate ions may be incorporated in HA grown in the presence of positively charged AAs than of negatively charged ones. Overall, the interaction of the mineralization inhibitors present in-vivo with the AAs is likely to be complex and worth being studied. Experiments performed in the presence of AAs in conditions closer to the biological ones could be the subject of future work.

# REFERENCES

- [1] S. Weiner and P. M. Dove, "An overview of biomineralization processes and the problem of the vital effect," *Biomineralization*, vol. 54, pp. 1-29, 2003.
- [2] J. J. De Yoreo, A. Wierzbicki, and P. M. Dove, "New insights into mechanisms of biomolecular control on growth of inorganic crystals," *CrystEngComm*, vol. 9, pp. 1144-1152, 2007.
- [3] M. B. Dickerson, K. H. Sandhage, and R. R. Naik, "Protein- and peptide-directed syntheses of inorganic materials," *Chem Rev*, vol. 108, pp. 4935-78, 2008.
- [4] J. J. De Yoreo and P. G. Vekilov, "Principles of Crystal Nucleation and Growth," *Reviews in Mineralogy and Geochemistry*, vol. 54, pp. 57-93, January 3, 2003.
- [5] E. Dujardin and S. Mann, "Bio-inspired Materials Chemistry," *Advanced Materials*, vol. 14, pp. 775-788, 2002.
- [6] S. V. Patwardhan, G. Patwardhan, and C. C. Perry, "Interactions of biomolecules with inorganic materials: principles, applications and future prospects," *Journal of Materials Chemistry*, vol. 17, pp. 2875-2884, 2007.
- [7] J. Song, V. Malathong, and C. R. Bertozzi, "Mineralization of Synthetic Polymer Scaffolds: A Bottom-Up Approach for the Development of Artificial Bone," *Journal of the American Chemical Society*, vol. 127, pp. 3366-3372, 2005.
- [8] A. George and A. Veis, "Phosphorylated Proteins and Control over Apatite Nucleation, Crystal Growth, and Inhibition," *Chemical Reviews*, vol. 108, pp. 4670-4693, 2008.
- [9] A. K. Rosenthal, "The role of noncollagenous proteins in mineralization," *Current Opinion in Orthopaedics*, vol. 18, pp. 449-453, 2007.
- [10] K. S. Jack, T. G. Vizcarra, and M. Trau, "Characterization and Surface Properties of Amino-Acid-Modified Carbonate-Containing Hydroxyapatite Particles," *Langmuir*, vol. 23, pp. 12233-12242, 2007.
- [11] B. Palazzo, D. Walsh, M. Iafisco, E. Foresti, L. Bertinetti, G. Martra, *et al.*, "Amino acid synergetic effect on structure, morphology and surface properties of biomimetic apatite nanocrystals," *Acta Biomaterialia*, vol. 5, pp. 1241-1252, 2009.
- [12] D. Rautaray, S. Mandal, and M. Sastry, "Synthesis of Hydroxyapatite Crystals Using Amino Acid-Capped Gold Nanoparticles as a Scaffold," *Langmuir*, vol. 21, pp. 5185-5191, 2005.
- [13] N. Almora-Barrios and N. H. de Leeuw, "A Density Functional Theory Study of the Interaction of Collagen Peptides with Hydroxyapatite Surfaces," *Langmuir : the ACS journal of surfaces and colloids*, vol. 26, pp. 14535-14542, 2010.
- [14] A. Sugino, T. Miyazaki, and C. Ohtsuki, "Apatite-forming ability of polyglutamic acid hydrogels in a body-simulating environment," *Journal of Materials Science: Materials in Medicine*, vol. 19, pp. 2269-2274, 2008.
- [15] H. Pan, J. Tao, X. Xu, and R. Tang, "Adsorption Processes of Gly and Glu Amino Acids on Hydroxyapatite Surfaces at the Atomic Level," *Langmuir: the ACS journal of surfaces and colloids*, vol. 23, pp. 8972-8981, 2007.
- [16] A. L. Boskey, "Pathogenesis of cartilage calcification: mechanisms of crystal deposition in cartilage," *Curr Rheumatol Rep*, vol. 4, pp. 245-51, 2002.

- [17] G. V. Gordon, T. Villanueva, H. R. Schumacher, and V. Gohel, "Autopsy study correlating degree of osteoarthritis, synovitis and evidence of articular calcification," *J Rheumatol*, vol. 11, pp. 681-6, 1984.
- [18] S. Koutsopoulos, A. Kontogeorgou, E. Dalas, and J. Petroheilos, "Calcification of porcine and human cardiac valves: testing of various inhibitors for antimineralization," *Journal of Materials Science: Materials in Medicine*, vol. 9, pp. 421-424, 1998.
- [19] J. W. Tsao, F. J. Schoen, R. Shankar, J. D. Sallis, and R. J. Levy, "Retardation of calcification of bovine pericardium used in bioprosthetic heart valves by phosphocitrate and a synthetic analogue," *Biomaterials*, vol. 9, pp. 393-7, 1988.
- [20] D. Gebauer, A. Völkel, and H. Cölfen, "Stable Prenucleation Calcium Carbonate Clusters," *Science*, vol. 322, pp. 1819-1822, 2008.
- [21] G. H. Nancollas, "The growth of crystals in solution," *Advances in Colloid and Interface Science*, vol. 10, pp. 215-252, 1979.
- [22] G. P. Demopoulos, "Aqueous precipitation and crystallization for the production of particulate solids with desired properties," *Hydrometallurgy*, vol. 96, pp. 199-214, 2009.
- [23] D. Horn and J. Rieger, "Organic Nanoparticles in the Aqueous Phase—Theory, Experiment, and Use," *Angewandte Chemie International Edition*, vol. 40, pp. 4330-4361, 2001.
- [24] A. Navrotsky, "Energetic clues to pathways to biomineralization: precursors, clusters, and nanoparticles," *Proc Natl Acad Sci U S A*, vol. 101, pp. 12096-101, 2004.
- [25] M. A. Bewernitz, D. Gebauer, J. Long, H. Colfen, and L. B. Gower, "A metastable liquid precursor phase of calcium carbonate and its interactions with polyaspartate," *Faraday Discussions*, vol. 159, pp. 291-312, 2012.
- [26] A. S. Schenk, H. Zope, Y.-Y. Kim, A. Kros, N. A. J. M. Sommerdijk, and F. C. Meldrum, "Polymer-induced liquid precursor (PILP) phases of calcium carbonate formed in the presence of synthetic acidic polypeptides-relevance to biomineralization," *Faraday Discussions*, vol. 159, pp. 327-344, 2012.
- [27] T. Kovacs and H. K. Christenson, "A two-step mechanism for crystal nucleation without supersaturation," *Faraday Discussions*, vol. 159, pp. 123-138, 2012.
- [28] A. R. Finney and P. M. Rodger, "Probing the structure and stability of calcium carbonate pre-nucleation clusters," *Faraday Discussions*, vol. 159, pp. 47-60, 2012.
- [29] M. Kellermeier, R. Rosenberg, A. Moise, U. Anders, M. Przybylski, and H. Colfen, "Amino acids form prenucleation clusters: ESI-MS as a fast detection method in comparison to analytical ultracentrifugation," *Faraday Discussions*, vol. 159, pp. 23-45, 2012.
- [30] P. Raiteri, R. Demichelis, J. D. Gale, M. Kellermeier, D. Gebauer, D. Quigley, *et al.*, "Exploring the influence of organic species on pre- and post-nucleation calcium carbonate," *Faraday Discussions*, vol. 159, pp. 61-85, 2012.
- [31] C. G. Sinn, R. Dimova, and M. Antonietti, "Isothermal Titration Calorimetry of the Polyelectrolyte/Water Interaction and Binding of Ca2+: Effects Determining the Quality of Polymeric Scale Inhibitors," *Macromolecules*, vol. 37, pp. 3444-3450, 2004.
- [32] X. Chu, W. Jiang, Z. Zhang, Y. Yan, H. Pan, X. Xu, et al., "Unique Roles of Acidic Amino Acids in Phase Transformation of Calcium Phosphates," *The Journal of Physical Chemistry B*, vol. 115, pp. 1151-1157, 2010.

- [33] K. S. Jack, T. G. Vizcarra, and M. Trau, "Characterization and Surface Properties of Amino-Acid-Modified Carbonate-Containing Hydroxyapatite Particles," *Langmuir : the ACS journal of surfaces and colloids*, vol. 23, pp. 12233-12242, 2007.
- [34] R. Gonzalez-McQuire, J.-Y. Chane-Ching, E. Vignaud, A. Lebugle, and S. Mann, "Synthesis and characterization of amino acid-functionalized hydroxyapatite nanorods," *Journal of Materials Chemistry*, vol. 14, pp. 2277-2281, 2004.
- [35] T. Matsumoto, M. Okazaki, M. Inoue, Y. Hamada, M. Taira, and J. Takahashi, "Crystallinity and solubility characteristics of hydroxyapatite adsorbed amino acid," *Biomaterials*, vol. 23, pp. 2241-7, 2002.
- [36] B. Palazzo, D. Walsh, M. Iafisco, E. Foresti, L. Bertinetti, G. Martra, *et al.*, "Amino acid synergetic effect on structure, morphology and surface properties of biomimetic apatite nanocrystals," *Acta Biomater*, vol. 5, pp. 1241-52, 2009.
- [37] T. Matsumoto, M. Okazaki, M. Inoue, Y. Hamada, M. Taira, and J. Takahashi, "Crystallinity and solubility characteristics of hydroxyapatite adsorbed amino acid," *Biomaterials*, vol. 23, pp. 2241-2247, 2002.
- [38] S. Koutsopoulos and E. Dalas, "Inhibition of Hydroxyapatite Formation in Aqueous Solutions by Amino Acids with Hydrophobic Side Groups," *Langmuir*, vol. 16, pp. 6739-6744, 2000.
- [39] A. Tsortos and G. H. Nancollas, "The Role of Polycarboxylic Acids in Calcium Phosphate Mineralization," *Journal of Colloid and Interface Science*, vol. 250, pp. 159-167, 2002.
- [40] E. Dalas, P. Malkaj, Z. Vasileiou, and D. G. Kanellopoulou, "The effect of Leucine on the crystal growth of calcium phosphate," *J Mater Sci Mater Med*, vol. 19, pp. 277-82, 2008.
- [41] Z.-s. Zhang, H.-h. Pan, and R.-k. Tang, "Molecular dynamics simulations of the adsorption of amino acids on the hydroxyapatite {100}-water interface," *Frontiers of Materials Science in China*, vol. 2, pp. 239-245, 2008.
- [42] S.-p. Huang, K.-c. Zhou, and Z.-y. Li, "Inhibition mechanism of aspartic acid on crystal growth of hydroxyapatite," *Transactions of Nonferrous Metals Society of China*, vol. 17, pp. 612-616, 2007.
- [43] S. Koutsopoulos and E. Dalas, "Hydroxyapatite crystallization in the presence of serine, tyrosine and hydroxyproline amino acids with polar side groups," *Journal of Crystal Growth*, vol. 216, pp. 443-449, 2000.
- [44] S. Koutsopoulos and E. Dalas, "The effect of acidic amino acids on hydroxyapatite crystallization," *Journal of Crystal Growth*, vol. 217, pp. 410-415, 2000.
- [45] S. Koutsopoulos and E. Dalas, "Hydroxyapatite Crystallization in the Presence of Amino Acids with Uncharged Polar Side Groups: Glycine, Cysteine, Cystine, and Glutamine," *Langmuir*, vol. 17, pp. 1074-1079, 2001.
- [46] A. T. C. Wong and J. T. Czernuszka, "Transformation behaviour of calcium phosphate 2. Effects of various phosphorylated amino acids," *Colloids and Surfaces A: Physicochemical and Engineering Aspects*, vol. 103, pp. 23-36, 1995.
- [47] D. Rautaray, S. Mandal, and M. Sastry, "Synthesis of hydroxyapatite crystals using amino acid-capped gold nanoparticles as a scaffold," *Langmuir*, vol. 21, pp. 5185-91, 2005.
- [48] J. D. Hartgerink, E. Beniash, and S. I. Stupp, "Self-Assembly and Mineralization of Peptide-Amphiphile Nanofibers," *Science*, vol. 294, pp. 1684-1688, November 23, 2001.

- [49] G. He, T. Dahl, A. Veis, and A. George, "Nucleation of apatite crystals in vitro by self-assembled dentin matrix protein 1," *Nat Mater*, vol. 2, pp. 552-558, 2003.
- [50] S. Ito, T. Saito, and K. Amano, "In vitro apatite induction by osteopontin: Interfacial energy for hydroxyapatite nucleation on osteopontin," *Journal of Biomedical Materials Research Part A*, vol. 69A, pp. 11-16, 2004.
- [51] T. Saito, M. Yamauchi, Y. Abiko, K. Matsuda, and M. A. Crenshaw, "In Vitro Apatite Induction by Phosphophoryn Immobilized on Modified Collagen Fibrils," *Journal of Bone and Mineral Research*, vol. 15, pp. 1615-1619, 2000.
- [52] K. S. Jack, T. G. Vizcarra, and M. Trau, "Characterization and surface properties of amino-acid-modified carbonate-containing hydroxyapatite particles," *Langmuir : the ACS journal of surfaces and colloids*, vol. 23, pp. 12233-42, 2007.
- [53] E. Dalas, P. Malkaj, Z. Vasileiou, and D. Kanellopoulou, "The effect of Leucine on the crystal growth of calcium phosphate," *Journal of Materials Science: Materials in Medicine*, vol. 19, pp. 277-282, 2008.
- [54] S. Koutsopoulos and E. Dalas, "Inhibition of Hydroxyapatite Formation in Aqueous Solutions by Amino Acids with Hydrophobic Side Groups," *Langmuir : the ACS journal of surfaces and colloids*, vol. 16, pp. 6739-6744, 2000.
- [55] S. Koutsopoulos and E. Dalas, "Hydroxyapatite crystallization in the presence of serine, tyrosine and hydroxyproline amino acids with polar side groups," *Journal of Crystal Growth*, vol. 216, pp. 443-449, 2000.
- [56] S. Koutsopoulos and E. Dalas, "Hydroxyapatite Crystallization in the Presence of Amino Acids with Uncharged Polar Side Groups: Glycine, Cysteine, Cystine, and Glutamine," *Langmuir: the ACS journal of surfaces and colloids*, vol. 17, pp. 1074-1079, 2001.
- [57] D. Gebauer, M. Kellermeier, J. D. Gale, L. Bergstrom, and H. Colfen, "Pre-nucleation clusters as solute precursors in crystallisation," *Chemical Society Reviews*, vol. 43, pp. 2348-2371, 2014.
- [58] H. Liu, P. Xi, G. Xie, Y. Shi, F. Hou, L. Huang, *et al.*, "Simultaneous Reduction and Surface Functionalization of Graphene Oxide for Hydroxyapatite Mineralization," *The Journal of Physical Chemistry C*, vol. 116, pp. 3334-3341, 2012.
- [59] J. Zhao, Z. Zhang, Z. Yu, Z. He, S. Yang, and H. Jiang, "Nucleation and characterization of hydroxyapatite on thioglycolic acid-capped reduced graphene oxide/silver nanoparticles in simplified simulated body fluid," *Applied Surface Science*, vol. 289, pp. 89-96, 2014.
- [60] J. Lu, Y.-S. He, C. Cheng, Y. Wang, L. Qiu, D. Li, *et al.*, "Self-Supporting Graphene Hydrogel Film as an Experimental Platform to Evaluate the Potential of Graphene for Bone Regeneration," *Advanced Functional Materials*, vol. 23, pp. 3494-3502, 2013.
- [61] Z. Fan, J. Wang, Z. Wang, Z. Li, Y. Qiu, H. Wang, et al., "Casein Phosphopeptide-Biofunctionalized Graphene Biocomposite for Hydroxyapatite Biomimetic Mineralization," *The Journal of Physical Chemistry C*, vol. 117, pp. 10375-10382, 2013.
- [62] J. W. Mullin, "5 Nucleation," in *Crystallization (Fourth Edition)*, J. W. Mullin, Ed., ed Oxford: Butterworth-Heinemann, 2001, pp. 181-215.
- [63] M. A. Bewernitz, D. Gebauer, J. Long, H. Colfen, and L. B. Gower, "A metastable liquid precursor phase of calcium carbonate and its interactions with polyaspartate," *Faraday Discussions*, vol. 159, pp. 291-312, 2012.
- [64] A. R. Finney and P. M. Rodger, "Probing the structure and stability of calcium carbonate pre-nucleation clusters," *Faraday Discussions*, vol. 159, pp. 47-60, 2012.

- [65] P. Raiteri, R. Demichelis, J. D. Gale, M. Kellermeier, D. Gebauer, D. Quigley, *et al.*, "Exploring the influence of organic species on pre- and post-nucleation calcium carbonate," vol. 159, pp. 61-85, 2012.
- [66] A. S. Schenk, H. Zope, Y.-Y. Kim, A. Kros, N. A. J. M. Sommerdijk, and F. C. Meldrum, "Polymer-induced liquid precursor (PILP) phases of calcium carbonate formed in the presence of synthetic acidic polypeptides-relevance to biomineralization," *Faraday Discussions*, vol. 159, pp. 327-344, 2012.
- [67] S. Yang and A. Navrotsky, "In Situ Calorimetric Study of the Growth of Silica TPA-MFI Crystals from an Initially Clear Solution," *Chemistry of Materials*, vol. 14, pp. 2803-2811, 2002.
- [68] S. Yang, A. Navrotsky, and B. L. Phillips, "In Situ Calorimetric, Structural, and Compositional Study of Zeolite Synthesis in the System 5.15Na2O-1.00Al2O3-3.28SiO2-165H2O," *The Journal of Physical Chemistry B*, vol. 104, pp. 6071-6080, 2000.
- [69] W. H. Casey, M. Karlsson, and B. L. Phillips, "Bonding and reactivity at oxide mineral surfaces from model aqueous complexes," *Nature*, vol. 404, p. 379+, 2000/03/23/ 2000.
- [70] G. Furrer, B. L. Phillips, K.-U. Ulrich, R. Pöthig, and W. H. Casey, "The Origin of Aluminum Flocs in Polluted Streams," *Science*, vol. 297, pp. 2245-2247, 2002.
- [71] W. H. Casey and T. W. Swaddle, "Why small? The use of small inorganic clusters to understand mineral surface and dissolution reactions in geochemistry," *Rev. Geophys.*, vol. 41, p. 1008, 2003.
- [72] A. Abdelouas, W. Lutze, and H. E. Nuttall, "Uranium contamination in the subsurface; characterization and remediation," *Reviews in Mineralogy and Geochemistry*, vol. 38, pp. 433-473, 1999.
- [73] O. J. Vetter, "An Evaluation of Scale Inhibitors," *Journal of Petroleum Technology*, vol. 24, pp. 997 1006, 1972.
- [74] J. W. Mullin, A. Amatavivadhana, and M. Chakraborty, "Crystal habit modification studies with ammonium and potassium dihydrogen phosphate," *Journal of Applied Chemistry*, vol. 20, pp. 153-158, 1970.
- [75] F. Grases and P. March, "A study about some phosphate derivatives as inhibitors of calcium oxalate crystal growth," *Journal of Crystal Growth*, vol. 96, pp. 993-995, 1989.
- [76] Y.-P. Lin and P. C. Singer, "Inhibition of calcite crystal growth by polyphosphates," *Water Research*, vol. 39, pp. 4835-4843, 2005.
- [77] R. W. Marshall and G. H. Nancollas, "Kinetics of crystal growth of dicalcium phosphate dihydrate," *The Journal of Physical Chemistry*, vol. 73, pp. 3838-3844, 1969.
- [78] N. Eidelman, W. E. Brown, and J. L. Meyer, "Selective inhibition of crystal growth on octacalcium phosphate and nonstoichiometric hydroxyapatite by pyrophosphate at physiological concentration," *Journal of Crystal Growth*, vol. 113, pp. 643-652, 1991.
- [79] S. Takasaki, K. I. Parsiegla, and J. L. Katz, "Calcite growth and the inhibiting effect of iron(III)," *Journal of Crystal Growth*, vol. 143, pp. 261-268, 1994.
- [80] K. I. Parsiegla and J. L. Katz, "Calcite growth inhibition by copper(II): I. Effect of supersaturation," *Journal of Crystal Growth*, vol. 200, pp. 213-226, 1999.
- [81] Y.-P. Lin and P. C. Singer, "Effect of Mg2+ on the kinetics of calcite crystal growth," *Journal of Crystal Growth*, vol. 312, pp. 136-140, 2009.
- [82] J. L. Bischoff, "Kinetics of calcite nucleation: Magnesium ion inhibition and ionic strength catalysis," *Journal of Geophysical Research*, vol. 73, pp. 3315-3322, 1968.

- [83] W. J. Benton, I. R. Collins, I. M. Grimsey, G. M. Parkinson, and S. A. Rodger, "Nucleation, growth and inhibition of barium sulfate-controlled modification with organic and inorganic additives," *Faraday Discussions*, vol. 95, pp. 281-297, 1993.
- [84] S. J. Kalita, A. Bhardwaj, and H. A. Bhatt, "Nanocrystalline calcium phosphate ceramics in biomedical engineering," *Materials Science and Engineering: C*, vol. 27, pp. 441-449, 2007.
- [85] E. D. Eanes, J. D. Termine, and M. U. Nylen, "An electron microscopic study of the formation of amorphous calcium phosphate and its transformation to crystalline apatite," *Calcified Tissue Research*, vol. 12, pp. 143-158, 1973.
- [86] S. Zhang and K. E. Gonsalves, "Preparation and characterization of thermally stable nanohydroxyapatite," *Journal of Materials Science: Materials in Medicine*, vol. 8, pp. 25-28, 1997.
- [87] M. Jarcho, C. H. Bolen, M. B. Thomas, J. Bobick, J. F. Kay, and R. H. Doremus, "Hydroxylapatite synthesis and characterization in dense polycrystalline form," *Journal of Materials Science*, vol. 11, pp. 2027-2035, 1976.
- [88] T. V. Safronova, "Phase composition of ceramic based on calcium hydroxyapatite powders containing byproducts of the synthesis reaction," *Glass and Ceramics*, vol. 66, pp. 136-139, 2009.
- [89] T. V. Safronova, M. A. Shiryaev, V. I. Putlyaev, V. A. Murashov, and P. V. Protsenko, "Ceramics based on hydroxyapatite synthesized from calcium chloride and potassium hydrophosphate," *Glass and Ceramics*, vol. 66, pp. 66-69, 2009.
- [90] Y. X. Pang and X. Bao, "Influence of temperature, ripening time and calcination on the morphology and crystallinity of hydroxyapatite nanoparticles," *Journal of the European Ceramic Society*, vol. 23, pp. 1697-1704, 2003.
- [91] S. Sarig and F. Kahana, "Rapid formation of nanocrystalline apatite," *Journal of Crystal Growth*, vol. 237–239, Part 1, pp. 55-59, 2002.
- [92] V. P. Orlovskii, V. S. Komlev, and S. M. Barinov, "Hydroxyapatite and Hydroxyapatite-Based Ceramics," *Inorganic Materials*, vol. 38, pp. 973-984, 2002.
- [93] P. W. Brown and M. Fulmer, "The effects of electrolytes on the rates of hydroxyapatite formation at 25 and 38 degrees C," *J Biomed Mater Res*, vol. 31, pp. 395-400, 1996.
- [94] N. Y. Mostafa, "Characterization, thermal stability and sintering of hydroxyapatite powders prepared by different routes," *Materials Chemistry and Physics*, vol. 94, pp. 333-341, 2005.
- [95] A. Oyane, K. Onuma, T. Kokubo, and A. Ito, "Clustering of Calcium Phosphate in the System CaCl2–H3PO4–KCl–H2O," *The Journal of Physical Chemistry B*, vol. 103, pp. 8230-8235, 1999.
- [96] A. R. Chughtai, R. Marshall, and G. H. Nancollas, "Complexes in calcium phosphate solutions," *The Journal of Physical Chemistry*, vol. 72, pp. 208-211, 1968.
- [97] J. Zhang, M. Maeda, N. Kotobuki, M. Hirose, H. Ohgushi, D. Jiang, *et al.*, "Aqueous processing of hydroxyapatite," *Materials Chemistry and Physics*, vol. 99, pp. 398-404, 2006.
- [98] H. Hohl, P. G. Koutsoukos, and G. H. Nancollas, "The crystallization of hydroxyapatite and dicalcium phosphate dihydrate; representation of growth curves," *Journal of Crystal Growth*, vol. 57, pp. 325-335, 1982.

- [99] N. I. Ponomareva, T. D. Poprygina, M. V. Lesovoi, Y. V. Sokolov, and B. L. Agapov, "Crystal structure and composition of hydroxyapatite biocomposites prepared at excess of calcium ions," *Russian Journal of General Chemistry*, vol. 79, pp. 186-190, 2009.
- [100] R. Tang, Z. J. Henneman, and G. H. Nancollas, "Constant composition kinetics study of carbonated apatite dissolution," *Journal of Crystal Growth*, vol. 249, pp. 614-624, 2003.
- [101] S.-H. Rhee, "Synthesis of hydroxyapatite via mechanochemical treatment," *Biomaterials*, vol. 23, pp. 1147-1152, 2002.
- [102] C. Shu, W. Yanwei, L. Hong, P. Zhengzheng, and Y. Kangde, "Synthesis of carbonated hydroxyapatite nanofibers by mechanochemical methods," *Ceramics International*, vol. 31, pp. 135-138, 2005.
- [103] I. s. S. Neira, Y. V. Kolen'ko, O. I. Lebedev, G. Van Tendeloo, H. S. Gupta, F. Guitián, *et al.*, "An Effective Morphology Control of Hydroxyapatite Crystals via Hydrothermal Synthesis," *Crystal Growth & Design*, vol. 9, pp. 466-474, 2008.
- [104] K. Hosoi, T. Hashida, H. Takahashi, N. Yamasaki, and T. Korenaga, "New Processing Technique for Hydroxyapatite Ceramics by the Hydrothermal Hot-Pressing Method," *Journal of the American Ceramic Society*, vol. 79, pp. 2771-2774, 1996.
- [105] M. Leila, J. Jafar, S. Mohammad Ali, B. Shahin, and J. Sayfoddin, "Hydrothermal synthesis and characterization of hydroxyapatite and fluorhydroxyapatite nano-size powders," *Biomedical Materials*, vol. 5, p. 045004, 2010.
- [106] Y. Wang, S. Zhang, K. Wei, N. Zhao, J. Chen, and X. Wang, "Hydrothermal synthesis of hydroxyapatite nanopowders using cationic surfactant as a template," *Materials Letters*, vol. 60, pp. 1484-1487, 2006.
- [107] T. Hattori, Y. Iwadate, and T. Kato, "Hydrothermal synthesis of hydroxyapatite from calcium pyrophosphate," *Journal of Materials Science Letters*, vol. 8, pp. 305-306, 1989.
- [108] X. Zhang and K. S. Vecchio, "Hydrothermal synthesis of hydroxyapatite rods," *Journal of Crystal Growth*, vol. 308, pp. 133-140, 2007.
- [109] I. Neira, F. Guitián, T. Taniguchi, T. Watanabe, and M. Yoshimura, "Hydrothermal synthesis of hydroxyapatite whiskers with sharp faceted hexagonal morphology," *Journal of Materials Science*, vol. 43, pp. 2171-2178, 2008.
- [110] Y. Fujishiro, H. Yabuki, K. Kawamura, T. Sato, and A. Okuwaki, "Preparation of needle-like hydroxyapatite by homogeneous precipitation under hydrothermal conditions," *Journal of Chemical Technology & Biotechnology*, vol. 57, pp. 349-353, 1993.
- [111] E. Sada, H. Kumazawa, and Y. Murakami, "HYDROTHERMAL SYNTHESIS OF CRYSTALLINE HYDROXYAPATITE ULTRAFINE PARTICLES," *Chemical Engineering Communications*, vol. 103, pp. 57-64, 1991.
- [112] H. S. Liu, T. S. Chin, L. S. Lai, S. Y. Chiu, K. H. Chung, C. S. Chang, *et al.*, "Hydroxyapatite synthesized by a simplified hydrothermal method," *Ceramics International*, vol. 23, pp. 19-25, 1997.
- [113] F. Zhang, Z.-H. Zhou, S.-P. Yang, L.-H. Mao, H.-M. Chen, and X.-B. Yu, "Hydrothermal synthesis of hydroxyapatite nanorods in the presence of anionic starburst dendrimer," *Materials Letters*, vol. 59, pp. 1422-1425, 2005.
- [114] M. Yoshimura, H. Suda, K. Okamoto, and K. Ioku, "Hydrothermal synthesis of biocompatible whiskers," *Journal of Materials Science*, vol. 29, pp. 3399-3402, 1994.
- [115] A. A. Chaudhry, S. Haque, S. Kellici, P. Boldrin, I. Rehman, F. A. Khalid, *et al.*, "Instant nano-hydroxyapatite: a continuous and rapid hydrothermal synthesis," *Chemical Communications*, pp. 2286-2288, 2006.

- [116] S. Jinawath, D. Pongkao, and M. Yoshimura, "Hydrothermal synthesis of hydroxyapatite from natural source," *Journal of Materials Science: Materials in Medicine*, vol. 13, pp. 491-494, 2002.
- [117] J. Liu, X. Ye, H. Wang, M. Zhu, B. Wang, and H. Yan, "The influence of pH and temperature on the morphology of hydroxyapatite synthesized by hydrothermal method," *Ceramics International*, vol. 29, pp. 629-633, 2003.
- [118] P. G. Koutsoukos and G. H. Nancollas, "The morphology of hydroxyapatite crystals grown in aqueous solution at 37°C," *Journal of Crystal Growth*, vol. 55, pp. 369-375, 1981.
- [119] J. Arends, J. Christoffersen, M. R. Christoffersen, H. Eckert, B. O. Fowler, J. C. Heughebaert, *et al.*, "A calcium hydroxyapatite precipitated from an aqueous solution: An international multimethod analysis," *Journal of Crystal Growth*, vol. 84, pp. 515-532, 1987.
- [120] E. P. Paschalis, K. Wikiel, and G. H. Nancollas, "Dual constant composition kinetics characterization of apatitic surfaces," *J Biomed Mater Res*, vol. 28, pp. 1411-8, 1994.
- [121] D. G. A. Nelson, H. Salimi, and G. H. Nancollas, "Octacalcium phosphate and apatite overgrowths: A crystallographic and kinetic study," *Journal of Colloid and Interface Science*, vol. 110, pp. 32-39, 1986.
- [122] J. L. Meyer, J. D. Eick, G. H. Nancollas, and L. N. Johnson, "A scanning electron microscopic study of the growth of hydroxyapatite crystals," *Calcified Tissue Research*, vol. 10, pp. 91-102, 1972.
- [123] A. Ebrahimpour, M. Johnsson, C. F. Richardson, and G. H. Nancollas, "The Characterization of Hydroxyapatite Preparations," *Journal of Colloid and Interface Science*, vol. 159, pp. 158-163, 1993.
- [124] J. C. Heughebaert, S. J. Zawacki, and G. H. Nancollas, "The growth of nonstoichiometric apatite from aqueous solution at 37°C: I. Methology and growth at pH 7.4," *Journal of Colloid and Interface Science*, vol. 135, pp. 20-32, 1990.
- [125] M. S. Johnsson and G. H. Nancollas, "The role of brushite and octacalcium phosphate in apatite formation," *Crit Rev Oral Biol Med*, vol. 3, pp. 61-82, 1992.
- [126] P. G. Koutsoukos, Z. Amjad, and G. H. Nancollas, "The influence of phytate and phosphonate on the crystal growth of fluorapatite and hydroxyapatite," *Journal of Colloid and Interface Science*, vol. 83, pp. 599-605, 1981.
- [127] C. Liu, Y. Huang, W. Shen, and J. Cui, "Kinetics of hydroxyapatite precipitation at pH 10 to 11," *Biomaterials*, vol. 22, pp. 301-6, 2001.
- [128] I. Mobasherpour, M. S. Heshajin, A. Kazemzadeh, and M. Zakeri, "Synthesis of nanocrystalline hydroxyapatite by using precipitation method," *Journal of Alloys and Compounds*, vol. 430, pp. 330-333, 2007.
- [129] M. H. Santos, M. d. Oliveira, L. P. d. F. Souza, H. S. Mansur, and W. L. Vasconcelos, "Synthesis control and characterization of hydroxyapatite prepared by wet precipitation process," *Materials Research*, vol. 7, pp. 625-630, 2004.
- [130] M. Corno, A. Rimola, V. Bolis, and P. Ugliengo, "Hydroxyapatite as a key biomaterial: quantum-mechanical simulation of its surfaces in interaction with biomolecules," *Physical Chemistry Chemical Physics*, vol. 12, pp. 6309-6329, 2010.
- [131] L. Wang and G. H. Nancollas, "Calcium Orthophosphates: Crystallization and Dissolution," *Chemical Reviews*, vol. 108, pp. 4628-4669, 2008.

- [132] J. Rakovan, "Growth and Surface Properties of Apatite," *Reviews in Mineralogy and Geochemistry*, vol. 48, pp. 51-86, 2002.
- [133] H. Pan, X. Y. Liu, R. Tang, and H. Y. Xu, "Mystery of the transformation from amorphous calcium phosphate to hydroxyapatite," *Chemical Communications*, vol. 46, pp. 7415-7417, 2010.
- [134] T. P. Feenstra and P. L. De Bruyn, "Formation of calcium phosphates in moderately supersaturated solutions," *The Journal of Physical Chemistry*, vol. 83, pp. 475-479, 1979.
- [135] J. L. Meyer and E. D. Eanes, "A thermodynamic analysis of the amorphous to crystalline calcium phosphate transformation," *Calcified Tissue Research*, vol. 25, pp. 59-68, 1978.
- [136] M. Francis and N. Webb, "Hydroxyapatite formation from a hydrated calcium monohydrogen phosphate precursor," *Calcified Tissue Research*, vol. 6, pp. 335-342, 1970.
- [137] F. Betts, N. C. Blumenthal, A. S. Posner, G. L. Becker, and A. L. Lehninger, "Atomic structure of intracellular amorphous calcium phosphate deposits," *Proc Natl Acad Sci U S A*, vol. 72, pp. 2088-90, 1975.
- [138] J. C. Heughebaert and G. Montel, "Conversion of amorphous tricalcium phosphate into apatitic tricalcium phosphate," *Calcif Tissue Int*, vol. 34, pp. S103-8, 1982.
- [139] S. Dorozhkin, "A hierarchical structure for apatite crystals," *Journal of Materials Science: Materials in Medicine*, vol. 18, pp. 363-366, 2007.
- [140] F. Betts, N. C. Blumenthal, A. S. Posner, G. L. Becker, and A. L. Lehninger, "Atomic structure of intracellular amorphous calcium phosphate deposits," *Proceedings of the National Academy of Sciences*, vol. 72, pp. 2088-2090, 1975.
- [141] X. Yin and M. J. Stott, "Biological calcium phosphates and Posner's cluster," *The Journal of Chemical Physics*, vol. 118, pp. 3717-3723, 2003.
- [142] N. Kanzaki, G. Treboux, K. Onuma, S. Tsutsumi, and A. Ito, "Calcium phosphate clusters," *Biomaterials*, vol. 22, pp. 2921-2929, 2001.
- [143] A. Dey, P. H. H. Bomans, F. A. Müller, J. Will, P. M. Frederik, G. de With, *et al.*, "The role of prenucleation clusters in surface-induced calcium phosphate crystallization," *Nature Materials*, vol. 9, pp. 1010-1014, 2010.
- [144] W. J. E. M. Habraken, J. Tao, L. J. Brylka, H. Friedrich, L. Bertinetti, A. S. Schenk, *et al.*, "Ion-association complexes unite classical and non-classical theories for the biomimetic nucleation of calcium phosphate," *Nat Commun*, vol. 4, p. 1507, 2013.
- [145] A. C. Tas and S. B. Bhaduri, "Chemical Processing of CaHPO4·2H2O," *Journal of the American Ceramic Society*, vol. 87, pp. 2195-2200, 2004.
- [146] G. Williams and J. D. Sallis, "Structural factors influencing the ability of compounds to inhibit hydroxyapatite formation," *Calcif Tissue Int*, vol. 34, pp. 169-77, 1982.
- [147] J. D. Termine, R. A. Peckauskas, and A. S. Posner, "Calcium phosphate formation in vitro: II. Effects of environment on amorphous-crystalline transformation," *Archives of Biochemistry and Biophysics*, vol. 140, pp. 318-325, 1970.
- [148] T. A. Fuierer, M. LoRe, S. A. Puckett, and G. H. Nancollas, "A Mineralization Adsorption and Mobility Study of Hydroxyapatite Surfaces in the Presence of Zinc and Magnesium Ions," *Langmuir*, vol. 10, pp. 4721-4725, 1994.
- [149] J. L. Meyer and G. H. Nancollas, "The effect of pH and temperature on the crystal growth of hydroxyapatite," *Archives of Oral Biology*, vol. 17, pp. 1623-1627, 1972.
- [150] G. H. Nancollas and M. S. Mohan, "The growth of hydroxyapatite crystals," *Archives of Oral Biology*, vol. 15, pp. 731-745, 1970.

- [151] J. D. Termine and E. D. Eanes, "Calcium phosphate deposition from balanced salt solutions," *Calcified Tissue Research*, vol. 15, pp. 81-84, 1974.
- [152] H. Fleisch, R. G. G. Russell, and F. Straumann, "Effect of Pyrophosphate on Hydroxyapatite and Its Implications in Calcium Homeostasis," *Nature*, vol. 212, pp. 901-903, 1966.
- [153] W. N. Addison, F. Azari, E. S. Sørensen, M. T. Kaartinen, and M. D. McKee, "Pyrophosphate Inhibits Mineralization of Osteoblast Cultures by Binding to Mineral, Up-regulating Osteopontin, and Inhibiting Alkaline Phosphatase Activity," *Journal of Biological Chemistry*, vol. 282, pp. 15872-15883, 2007.
- [154] R. G. Russell and H. Fleisch, "Pyrophosphate, phosphonates and pyrophosphatases in the regulation of calcification and calcium homeostasis," *Proc R Soc Med*, vol. 63, p. 876, 1970.
- [155] B. Tomazic, M. Tomson, and G. H. Nancollas, "Growth of calcium phosphates on hydroxyapatite crystals: The effect of magnesium," *Archives of Oral Biology*, vol. 20, pp. 803-808, 1975.
- [156] T. Kobayashi, S. Ono, S. Hirakura, Y. Oaki, and H. Imai, "Morphological variation of hydroxyapatite grown in aqueous solution based on simulated body fluid," *CrystEngComm*, vol. 14, pp. 1143-1149, 2012.
- [157] C. E. Fowler, M. Li, S. Mann, and H. C. Margolis, "Influence of surfactant assembly on the formation of calcium phosphate materials-A model for dental enamel formation," *Journal of Materials Chemistry*, vol. 15, pp. 3317-3325, 2005.
- [158] S. Weiner and P. Dove, "An Overview of Biomineralization Processes and the Problem of the Vital Effect," *Reviews in Mineralogy and Geochemistry*, vol. 54, pp. 1-29, 2003.
- [159] C. Söllner, M. Burghammer, E. Busch-Nentwich, J. Berger, H. Schwarz, C. Riekel, *et al.*, "Control of Crystal Size and Lattice Formation by Starmaker in Otolith Biomineralization," *Science*, vol. 302, pp. 282-286, 2003.
- [160] D. M. Fekete, "Developmental biology. Rocks that roll zebrafish," *Science*, vol. 302, pp. 241-2, 2003.
- [161] M. M. Brzóska, K. Majewska, and J. Moniuszko-Jakoniuk, "Bone mineral density, chemical composition and biomechanical properties of the tibia of female rats exposed to cadmium since weaning up to skeletal maturity," *Food and Chemical Toxicology*, vol. 43, pp. 1507-1519, 2005.
- [162] S. Weiner and H. D. Wagner, "THE MATERIAL BONE: Structure-Mechanical Function Relations," *Annual Review of Materials Science*, vol. 28, pp. 271-298, 1998.
- [163] L. C. Palmer, C. J. Newcomb, S. R. Kaltz, E. D. Spoerke, and S. I. Stupp, "Biomimetic systems for hydroxyapatite mineralization inspired by bone and enamel," *Chem Rev*, vol. 108, pp. 4754-83, 2008.
- [164] N. Reznikov, R. Shahar, and S. Weiner, "Bone hierarchical structure in three dimensions," *Acta Biomater*, vol. 10, pp. 3815-26, 2014.
- [165] "Comparative study of nanohydroxyapatite microspheres for medical applications," *Journal of Biomedical Materials Research Part A*, 2007.
- [166] P. Zioupos, J. D. Currey, and A. J. Hamer, "The role of collagen in the declining mechanical properties of aging human cortical bone," *Journal of Biomedical Materials Research*, vol. 45, pp. 108-116, 1999.

- [167] E. A. McNally, H. P. Schwarcz, G. A. Botton, and A. L. Arsenault, "A Model for the Ultrastructure of Bone Based on Electron Microscopy of Ion-Milled Sections," *PLoS ONE*, vol. 7, p. e29258, 2012.
- [168] E. McNally, F. Nan, G. A. Botton, and H. P. Schwarcz, "Scanning transmission electron microscopic tomography of cortical bone using Z-contrast imaging," *Micron*, vol. 49, pp. 46-53, 2013.
- [169] A. Helebrant, L. Jonasova, L.Sanda, "The Influence of Simulated Body Fluid Composition on Carbonated Hydroxyapatite Formation", Ceramics -Silikaty, 2002, 46 (1), 9-14.
- [170] G. Boivin and P. J. Meunier, "The Degree of Mineralization of Bone Tissue Measured by Computerized Quantitative Contact Microradiography," *Calcified Tissue International*, vol. 70, pp. 503-511, 2002.
- [171] S. R. Elliott and R. A. Robinson, "The water content of bone. I. The mass of water, inorganic crystals, organic matrix, and CO2 space components in a unit volume of the dog bone," *J Bone Joint Surg Am*, vol. 39-a, pp. 167-88, 1957.
- [172] B. F. McEwen, M. J. Song, and W. J. Landis, "Quantitative determination of the mineral distribution in different collagen zones of calcifying tendon using high voltage electron microscopic tomography," *J Comput Assist Microsc*, vol. 3, pp. 201-10, 1991.
- [173] W. Traub, T. Arad, and S. Weiner, "Origin of mineral crystal growth in collagen fibrils," *Matrix*, vol. 12, pp. 251-5, 1992.
- [174] W. J. Landis, M. J. Song, A. Leith, L. McEwen, and B. F. McEwen, "Mineral and organic matrix interaction in normally calcifying tendon visualized in three dimensions by high-voltage electron microscopic tomography and graphic image reconstruction," *J Struct Biol*, vol. 110, pp. 39-54, 1993.
- [175] H. P. Wiesmann, U. Meyer, U. Plate, and H. J. Hohling, "Aspects of collagen mineralization in hard tissue formation," *Int Rev Cytol*, vol. 242, pp. 121-56, 2005.
- [176] H. C. Anderson, "Electron microscopic studies of induced cartilage development and calcification," *J Cell Biol*, vol. 35, pp. 81-101, 1967.
- [177] H. C. Anderson, "Mineralization by matrix vesicles," *Scan Electron Microsc*, vol. 2, pp. 953-64, 1984.
- [178] Z. Khavandgar and M. Murshed, "Sphingolipid metabolism and its role in the skeletal tissues," *Cellular and Molecular Life Sciences*, vol. 72, pp. 959-969, 2015.
- [179] E. E. Golub, "Role of matrix vesicles in biomineralization," *Biochim Biophys Acta*, vol. 1790, pp. 1592-8, 2009.
- [180] H. C. Anderson, "Matrix vesicles and calcification," *Curr Rheumatol Rep*, vol. 5, pp. 222-6, 2003.
- [181] D. Toroian, J. E. Lim, and P. A. Price, "The size exclusion characteristics of type I collagen: implications for the role of noncollagenous bone constituents in mineralization," *J Biol Chem*, vol. 282, pp. 22437-47, 2007.
- [182] F. Nudelman, K. Pieterse, A. George, P. H. H. Bomans, H. Friedrich, L. J. Brylka, *et al.*, "The role of collagen in bone apatite formation in the presence of hydroxyapatite nucleation inhibitors," *Nat Mater*, vol. 9, pp. 1004-1009, 2010.
- [183] F. H. Silver and W. J. Landis, "Deposition of apatite in mineralizing vertebrate extracellular matrices: A model of possible nucleation sites on type I collagen," *Connect Tissue Res*, vol. 52, pp. 242-54, 2011.

- [184] W. Landis and R. Jacquet, "Association of Calcium and Phosphate Ions with Collagen in the Mineralization of Vertebrate Tissues," *Calcified Tissue International*, vol. 93, pp. 329-337, 2013.
- [185] G. He, T. Dahl, A. Veis, and A. George, "Nucleation of apatite crystals in vitro by self-assembled dentin matrix protein 1," *Nat Mater*, vol. 2, pp. 552-8, 2003.
- [186] S. Ito, T. Saito, and K. Amano, "In vitro apatite induction by osteopontin: interfacial energy for hydroxyapatite nucleation on osteopontin," *J Biomed Mater Res A*, vol. 69, pp. 11-6, 2004.
- [187] J. D. Hartgerink, E. Beniash, and S. I. Stupp, "Self-assembly and mineralization of peptide-amphiphile nanofibers," *Science*, vol. 294, pp. 1684-8, 2001.
- [188] T. Saito, M. Yamauchi, Y. Abiko, K. Matsuda, and M. A. Crenshaw, "In vitro apatite induction by phosphophoryn immobilized on modified collagen fibrils," *J Bone Miner Res*, vol. 15, pp. 1615-9, 2000.
- [189] P. S. Rowe, "Regulation of bone-renal mineral and energy metabolism: the PHEX, FGF23, DMP1, MEPE ASARM pathway," *Crit Rev Eukaryot Gene Expr*, vol. 22, pp. 61-86, 2012.
- [190] W. N. Addison, F. Azari, E. S. Sorensen, M. T. Kaartinen, and M. D. McKee, "Pyrophosphate inhibits mineralization of osteoblast cultures by binding to mineral, upregulating osteopontin, and inhibiting alkaline phosphatase activity," *J Biol Chem*, vol. 282, pp. 15872-83, 2007.
- [191] A. Gericke, C. Qin, L. Spevak, Y. Fujimoto, W. T. Butler, E. S. Sorensen, *et al.*, "Importance of phosphorylation for osteopontin regulation of biomineralization," *Calcif Tissue Int*, vol. 77, pp. 45-54, 2005.
- [192] K. U. Ogbureke and L. W. Fisher, "Renal expression of SIBLING proteins and their partner matrix metalloproteinases (MMPs)," *Kidney Int*, vol. 68, pp. 155-66, 2005.
- [193] L. W. Fisher, D. A. Torchia, B. Fohr, M. F. Young, and N. S. Fedarko, "Flexible structures of SIBLING proteins, bone sialoprotein, and osteopontin," *Biochem Biophys Res Commun*, vol. 280, pp. 460-5, 2001.
- [194] E. Schad, L. Kalmar, and P. Tompa, "Exon-phase symmetry and intrinsic structural disorder promote modular evolution in the human genome," *Nucleic Acids Research*, vol. 41, pp. 4409-4422, 2013.
- [195] W. N. Addison, Y. Nakano, T. Loisel, P. Crine, and M. D. McKee, "MEPE-ASARM peptides control extracellular matrix mineralization by binding to hydroxyapatite: an inhibition regulated by PHEX cleavage of ASARM," *J Bone Miner Res*, vol. 23, pp. 1638-49, 2008.
- [196] P. S. Rowe, I. R. Garrett, P. M. Schwarz, D. L. Carnes, E. M. Lafer, G. R. Mundy, *et al.*, "Surface plasmon resonance (SPR) confirms that MEPE binds to PHEX via the MEPE-ASARM motif: a model for impaired mineralization in X-linked rickets (HYP)," *Bone*, vol. 36, pp. 33-46, 2005.
- [197] L. D. Quarles, "FGF23, PHEX, and MEPE regulation of phosphate homeostasis and skeletal mineralization," *Am J Physiol Endocrinol Metab*, vol. 285, pp. E1-9, 2003.
- [198] A. Martin, V. David, J. S. Laurence, P. M. Schwarz, E. M. Lafer, A. M. Hedge, *et al.*, "Degradation of MEPE, DMP1, and release of SIBLING ASARM-peptides (minhibins): ASARM-peptide(s) are directly responsible for defective mineralization in HYP," *Endocrinology*, vol. 149, pp. 1757-72, 2008.

- [199] B. Salmon, C. Bardet, M. Khaddam, J. Naji, B. R. Coyac, B. Baroukh, *et al.*, "MEPE-Derived ASARM Peptide Inhibits Odontogenic Differentiation of Dental Pulp Stem Cells and Impairs Mineralization in Tooth Models of X-Linked Hypophosphatemia," *PLoS ONE*, vol. 8, p. e56749, 2013.
- [200] W. N. Addison, D. L. Masica, J. J. Gray, and M. D. McKee, "Phosphorylation-dependent inhibition of mineralization by osteopontin ASARM peptides is regulated by PHEX cleavage," *J Bone Miner Res*, vol. 25, pp. 695-705, 2010.
- [201] N. Almora-Barrios and N. H. de Leeuw, "A density functional theory study of the interaction of collagen peptides with hydroxyapatite surfaces," *Langmuir*, vol. 26, pp. 14535-42, 2010.
- [202] D. A. Pampena, K. A. Robertson, O. Litvinova, G. Lajoie, H. A. Goldberg, and G. K. Hunter, "Inhibition of hydroxyapatite formation by osteopontin phosphopeptides," *Biochem J*, vol. 378, pp. 1083-7, 2004.
- [203] Y. Yang, Q. Cui, and N. Sahai, "How does bone sialoprotein promote the nucleation of hydroxyapatite? A molecular dynamics study using model peptides of different conformations," *Langmuir*, vol. 26, pp. 9848-59, 2010.
- [204] B. Christensen, M. S. Nielsen, K. F. Haselmann, T. E. Petersen, and E. S. Sorensen, "Post-translationally modified residues of native human osteopontin are located in clusters: identification of 36 phosphorylation and five O-glycosylation sites and their biological implications," *Biochem J*, vol. 390, pp. 285-92, 2005.
- [205] C. E. Tye, K. R. Rattray, K. J. Warner, J. A. R. Gordon, J. Sodek, G. K. Hunter, *et al.*, "Delineation of the Hydroxyapatite-nucleating Domains of Bone Sialoprotein," *Journal of Biological Chemistry*, vol. 278, pp. 7949-7955, March 7, 2003.
- [206] G. K. Hunter and H. A. Goldberg, "Modulation of crystal formation by bone phosphoproteins: role of glutamic acid-rich sequences in the nucleation of hydroxyapatite by bone sialoprotein," *Biochem J*, vol. 302, pp. 175-9, 1994.
- [207] L. Malaval, N. M. Wade-Gueye, M. Boudiffa, J. Fei, R. Zirngibl, F. Chen, *et al.*, "Bone sialoprotein plays a functional role in bone formation and osteoclastogenesis," *J Exp Med*, vol. 205, pp. 1145-53, 2008.
- [208] R. M. Wazen, C. E. Tye, H. A. Goldberg, G. K. Hunter, C. E. Smith, and A. Nanci, "In Vivo Functional Analysis of Polyglutamic Acid Domains in Recombinant Bone Sialoprotein," *Journal of Histochemistry & Cytochemistry*, vol. 55, pp. 35-42, 2007.
- [209] G. K. Hunter and H. A. Goldberg, "Modulation of crystal formation by bone phosphoproteins: role of glutamic acid-rich sequences in the nucleation of hydroxyapatite by bone sialoprotein," *Biochem J*, vol. 302 (Pt 1), pp. 175-9, 1994.
- [210] H. A. Goldberg, K. J. Warner, M. J. Stillman, and G. K. Hunter, "Determination of the hydroxyapatite-nucleating region of bone sialoprotein," *Connect Tissue Res*, vol. 35, pp. 385-92, 1996.
- [211] N. L. Harris, K. R. Rattray, C. E. Tye, T. M. Underhill, M. J. Somerman, J. A. D'Errico, *et al.*, "Functional analysis of bone sialoprotein: identification of the hydroxyapatite-nucleating and cell-binding domains by recombinant peptide expression and site-directed mutagenesis," *Bone*, vol. 27, pp. 795-802, 2000.
- [212] G. K. Hunter and H. A. Goldberg, "Nucleation of hydroxyapatite by bone sialoprotein," *Proc Natl Acad Sci U S A*, vol. 90, pp. 8562-5, 1993.
- [213] B. Ganss, R. H. Kim, and J. Sodek, "Bone sialoprotein," *Crit Rev Oral Biol Med*, vol. 10, pp. 79-98, 1999.

- [214] A. George, L. Bannon, B. Sabsay, J. W. Dillon, J. Malone, A. Veis, *et al.*, "The carboxylterminal domain of phosphophoryn contains unique extended triplet amino acid repeat sequences forming ordered carboxyl-phosphate interaction ridges that may be essential in the biomineralization process," *J Biol Chem*, vol. 271, pp. 32869-73, 1996.
- [215] A. Guweidhi, J. Kleeff, H. Adwan, N. A. Giese, M. N. Wente, T. Giese, *et al.*, "Osteonectin Influences Growth and Invasion of Pancreatic Cancer Cells," *Annals of Surgery*, vol. 242, pp. 224-234, 2005.
- [216] X. C. Villarreal, K. G. Mann, and G. L. Long, "Structure of human osteonectin based upon analysis of cDNA and genomic sequences," *Biochemistry*, vol. 28, pp. 6483-6491, 1989.
- [217] P. Maurer, C. Hohenadl, E. Hohenester, W. Göhring, R. Timpl, and J. Engel, "The Cterminal Portion of BM-40 (SPARC/Osteonectin) is an Autonomously Folding and Crystallisable Domain that Binds Calcium and Collagen IV," *Journal of Molecular Biology*, vol. 253, pp. 347-357, 1995.
- [218] R. Fujisawa, Y. Wada, Y. Nodasaka, and Y. Kuboki, "Acidic amino acid-rich sequences as binding sites of osteonectin to hydroxyapatite crystals," *Biochim Biophys Acta*, vol. 1292, pp. 53-60, 1996.
- [219] R. Pankov and K. M. Yamada, "Fibronectin at a glance," *Journal of Cell Science*, vol. 115, pp. 3861-3863, 2002.
- [220] G. Daculsi, P. Pilet, M. Cottrel, and G. Guicheux, "Role of fibronectin during biological apatite crystal nucleation: Ultrastructural characterization," *Journal of Biomedical Materials Research*, vol. 47, pp. 228-233, 1999.
- [221] K. E. Watson, F. Parhami, V. Shin, and L. L. Demer, "Fibronectin and Collagen I Matrixes Promote Calcification of Vascular Cells in Vitro, Whereas Collagen IV Matrix Is Inhibitory," *Arteriosclerosis, Thrombosis, and Vascular Biology*, vol. 18, pp. 1964-1971, 1998.
- [222] A. L. Boskey, "Noncollagenous matrix proteins and their role in mineralization," *Bone Miner*, vol. 6, pp. 111-23, 1989.
- [223] R. V. Iozzo and A. D. Murdoch, "Proteoglycans of the extracellular environment: clues from the gene and protein side offer novel perspectives in molecular diversity and function," *Faseb J*, vol. 10, pp. 598-614, 1996.
- [224] P. V. Hauschka, "Osteocalcin: the vitamin K-dependent Ca2+-binding protein of bone matrix," *Haemostasis*, vol. 16, pp. 258-72, 1986.
- [225] R. A. Atkinson, J. S. Evans, P. V. Hauschka, B. A. Levine, R. Meats, J. T. Triffitt, *et al.*, "Conformational studies of osteocalcin in solution," *Eur J Biochem*, vol. 232, pp. 515-21, 1995.
- [226] Q. Q. Hoang, F. Sicheri, A. J. Howard, and D. S. C. Yang, "Bone recognition mechanism of porcine osteocalcin from crystal structure," *Nature*, vol. 425, pp. 977-980, 2003.
- [227] C. Chenu, S. Colucci, M. Grano, P. Zigrino, R. Barattolo, G. Zambonin, *et al.*, "Osteocalcin induces chemotaxis, secretion of matrix proteins, and calcium-mediated intracellular signaling in human osteoclast-like cells," *J Cell Biol*, vol. 127, pp. 1149-58, 1994.
- [228] P. V. Bodine and B. S. Komm, "Evidence that conditionally immortalized human osteoblasts express an osteocalcin receptor," *Bone*, vol. 25, pp. 535-43, 1999.
- [229] A. N. Kapustin and C. M. Shanahan, "Osteocalcin: a novel vascular metabolic and osteoinductive factor?," *Arterioscler Thromb Vasc Biol*, vol. 31, pp. 2169-71, 2011.

- [230] A. Idelevich, Y. Rais, and E. Monsonego-Ornan, "Bone Gla protein increases HIF-lalpha-dependent glucose metabolism and induces cartilage and vascular calcification," *Arterioscler Thromb Vasc Biol*, vol. 31, pp. e55-71, 2011.
- [231] Y. Yao, M. Jumabay, A. Ly, M. Radparvar, M. R. Cubberly, and K. I. Boström, "A Role for the Endothelium in Vascular Calcification," *Circulation research*, vol. 113, pp. 495-504, 2013.
- [232] G. Luo, P. Ducy, M. D. McKee, G. J. Pinero, E. Loyer, R. R. Behringer, *et al.*, "Spontaneous calcification of arteries and cartilage in mice lacking matrix GLA protein," *Nature*, vol. 386, pp. 78-81, 1997.
- [233] S. K. Nishimoto and M. Nishimoto, "Matrix Gla Protein Binds to Fibronectin and Enhances Cell Attachment and Spreading on Fibronectin," *International Journal of Cell Biology*, vol. 2014, p. 13, 2014.
- [234] P. A. Marques, A. P. Serro, B. J. Saramago, A. C. Fernandes, M. C. Magalhaes, and R. N. Correia, "Mineralisation of two phosphate ceramics in HBSS: role of albumin," *Biomaterials*, vol. 24, pp. 451-60, 2003.
- [235] S. Areva, T. Peltola, E. Säilynoja, K. Laajalehto, M. Lindén, and J. B. Rosenholm, "Effect of Albumin and Fibrinogen on Calcium Phosphate Formation on Sol-Gel-Derived Titania Coatings in Vitro," *Chemistry of Materials*, vol. 14, pp. 1614-1621, 2002.
- [236] C. Schäfer and W. Jahnen-Dechent, "The Biological and Cellular Role of Fetuin Family Proteins in Biomineralization," in *Handbook of Biomineralization*, ed: Wiley-VCH Verlag GmbH, 2008, pp. 317-328.
- [237] L. Brylka and W. Jahnen-Dechent, "The Role of Fetuin-A in Physiological and Pathological Mineralization," *Calcified Tissue International*, vol. 93, pp. 355-364, 2013.
- [238] P. A. Price, D. Toroian, and J. E. Lim, "Mineralization by inhibitor exclusion: the calcification of collagen with fetuin," *J Biol Chem*, vol. 284, pp. 17092-101, 2009.
- [239] R. A. Terkeltaub, "Inorganic pyrophosphate generation and disposition in pathophysiology," *American Journal of Physiology Cell Physiology*, vol. 281, pp. C1-C11, 2001.
- [240] A. M. Ho, M. D. Johnson, and D. M. Kingsley, "Role of the mouse ank gene in control of tissue calcification and arthritis," *Science*, vol. 289, pp. 265-70, 2000.
- [241] F. Cailotto, A. Bianchi, S. Sebillaud, N. Venkatesan, D. Moulin, J.-Y. Jouzeau, *et al.*, "Inorganic pyrophosphate generation by transforming growth factor-beta-1 is mainly dependent on ANK induction by Ras/Raf-1/extracellular signal-regulated kinase pathways in chondrocytes," *Arthritis Research & Therapy*, vol. 9, pp. R122-R122, 2007.
- [242] L. M. Ryan, R. L. Wortmann, B. Karas, M. P. Lynch, and D. J. McCarty, "Pyrophosphohydrolase activity and inorganic pyrophosphate content of cultured human skin fibroblasts. Elevated levels in some patients with calcium pyrophosphate dihydrate deposition disease," *J Clin Invest*, vol. 77, pp. 1689-93, 1986.
- [243] C. Thouverey, G. Bechkoff, S. Pikula, and R. Buchet, "Inorganic pyrophosphate as a regulator of hydroxyapatite or calcium pyrophosphate dihydrate mineral deposition by matrix vesicles," *Osteoarthritis Cartilage*, vol. 17, pp. 64-72, 2009.
- [244] A. Jung, S. Bisaz, P. Bartholdi, and H. Fleisch, "Influence of pyrophosphate on the exchange of calcium and phosphate ions on hydroxyapatite," *Calcified Tissue Research*, vol. 13, pp. 27-40, 1973.

- [245] W. W. Souba and A. J. Pacitti, "How amino acids get into cells: mechanisms, models, menus, and mediators," *JPEN J Parenter Enteral Nutr*, vol. 16, pp. 569-78, 1992.
- [246] C. Bolton and G. P. Wright, "The Absorption of amino acids and their distribution in the body fluids," *The Journal of Physiology*, vol. 89, pp. 269-286, 1937.
- [247] Y. Ishikawa, J. E. Chin, H. L. Hubbard, and R. E. Wuthier, "Utilization and formation of amino acids by chicken epiphyseal chondrocytes: comparative studies with cultured cells and native cartilage tissue," *J Cell Physiol*, vol. 123, pp. 79-88,1985.
- [248] Y. Ishikawa, J. E. Chin, E. M. Schalk, and R. E. Wuthier, "Effect of amino acid levels on matrix vesicle formation by epiphyseal growth plate chondrocytes in primary culture," *J Cell Physiol*, vol. 126, pp. 399-406, 1986.
- [249] R. E. Wuthier, "A review of the primary mechanism of endochondral calcification with special emphasis on the role of cells, mitochondria and matrix vesicles," *Clin Orthop Relat Res*, pp. 219-42, 1982.
- [250] H. Pan, J. Tao, X. Xu, and R. Tang, "Adsorption Processes of Gly and Glu Amino Acids on Hydroxyapatite Surfaces at the Atomic Level," *Langmuir*, vol. 23, pp. 8972-8981, 2007.
- [251] J. Tao, H. Pan, Y. Zeng, X. Xu, and R. Tang, "Roles of Amorphous Calcium Phosphate and Biological Additives in the Assembly of Hydroxyapatite Nanoparticles," *The Journal of Physical Chemistry B*, vol. 111, pp. 13410-13418, 2007.
- [252] E. V. Rosseeva, O. A. Golovanova, and O. V. Frank-Kamenetskaya, "The influence of amino acids on the formation of nanocrystalline hydroxyapatite," *Glass Physics and Chemistry*, vol. 33, pp. 283-286, 2007.
- [253] M. Kresak, E. C. Moreno, R. T. Zahradnik, and D. I. Hay, "Adsorption of amino acids onto hydroxyapatite," *Journal of Colloid and Interface Science*, vol. 59, pp. 283-292, 1977.
- [254] Y. Cai and R. Tang, "Calcium phosphate nanoparticles in biomineralization and biomaterials," *Journal of Materials Chemistry*, vol. 18, pp. 3775-3787, 2008.
- [255] J. Aizenberg, A. J. Black, and G. M. Whitesides, "Oriented Growth of Calcite Controlled by Self-Assembled Monolayers of Functionalized Alkanethiols Supported on Gold and Silver," *Journal of the American Chemical Society*, vol. 121, pp. 4500-4509, 1999.
- [256] G. K. Toworfe, S. Bhattacharyya, R. J. Composto, C. S. Adams, I. M. Shapiro, and P. Ducheyne, "Effect of functional end groups of silane self-assembled monolayer surfaces on apatite formation, fibronectin adsorption and osteoblast cell function," *Journal of Tissue Engineering and Regenerative Medicine*, vol. 3, pp. 26-36, 2009.
- [257] S. Cavalli, D. C. Popescu, E. E. Tellers, M. R. J. Vos, B. P. Pichon, M. Overhand, *et al.*, "Self-Organizing β-Sheet Lipopeptide Monolayers as Template for the Mineralization of CaCO3," *Angewandte Chemie International Edition*, vol. 45, pp. 739-744, 2006.
- [258] Y.-Y. Hu, Y. Yusufoglu, M. Kanapathipillai, C.-Y. Yang, Y. Wu, P. Thiyagarajan, *et al.*, "Self-assembled calcium phosphate nanocomposites using block copolypeptide templates," *Soft Matter*, vol. 5, pp. 4311-4320, 2009.
- [259] P. Zhu, Y. Masuda, and K. Koumoto, "The effect of surface charge on hydroxyapatite nucleation," *Biomaterials*, vol. 25, pp. 3915-3921, 2004.
- [260] H. Li, W. Huang, Y. Zhang, and M. Zhong, "Biomimetic synthesis of enamel-like hydroxyapatite on self-assembled monolayers," *Materials Science and Engineering: C*, vol. 27, pp. 756-761, 2007.

- [261] Q. Liu, J. Ding, F. K. Mante, S. L. Wunder, and G. R. Baran, "The role of surface functional groups in calcium phosphate nucleation on titanium foil: a self-assembled monolayer technique," *Biomaterials*, vol. 23, pp. 3103-11, 2002.
- [262] M. Tanahashi and T. Matsuda, "Surface functional group dependence on apatite formation on self-assembled monolayers in a simulated body fluid," *Journal of Biomedical Materials Research*, vol. 34, pp. 305-315, 1997.
- [263] T. Miyazaki, C. Ohtsuki, Y. Akioka, M. Tanihara, J. Nakao, Y. Sakaguchi, *et al.*, "Apatite deposition on polyamide films containing carboxyl group in a biomimetic solution," *J Mater Sci Mater Med*, vol. 14, pp. 569-74, 2003.
- [264] L. J. Zhang, H. G. Liu, X. S. Feng, R. J. Zhang, L. Zhang, Y. D. Mu, *et al.*, "Mineralization mechanism of calcium phosphates under three kinds of Langmuir monolayers," *Langmuir*, vol. 20, pp. 2243-9, 2004.
- [265] J. R. Long, J. L. Dindot, H. Zebroski, S. Kiihne, R. H. Clark, A. A. Campbell, et al., "A peptide that inhibits hydroxyapatite growth is in an extended conformation on the crystal surface," Proceedings of the National Academy of Sciences, vol. 95, pp. 12083-12087, October 13, 1998.
- [266] M. D. Roy, S. K. Stanley, E. J. Amis, and M. L. Becker, "Identification of a Highly Specific Hydroxyapatite-binding Peptide using Phage Display," *Advanced Materials*, vol. 20, pp. 1830-1836, 2008.
- [267] E. C. Moreno, M. Kresak, and D. I. Hay, "Adsorption of two human parotid salivary macromolecules on hydroxy-, fluorhydroxy-and fluorapatites," *Archives of Oral Biology*, vol. 23, pp. 525-533, 1978.
- [268] K. Wikiel, E. M. Burke, J. W. Perich, E. C. Reynolds, and G. H. Nancollas, "Hydroxyapatite mineralization and demineralization in the presence of synthetic phosphorylated pentapeptides," *Archives of Oral Biology*, vol. 39, pp. 715-721, 1994.
- [269] N. Almora-Barrios, K. F. Austen, and N. H. de Leeuw, "Density Functional Theory Study of the Binding of Glycine, Proline, and Hydroxyproline to the Hydroxyapatite (0001) and (0110) Surfaces," *Langmuir*, vol. 25, pp. 5018-5025, 2009.
- [270] S. Koutsopoulos and E. Dalas, "The Crystallization of Hydroxyapatite in the Presence of Lysine," *J Colloid Interface Sci*, vol. 231, pp. 207-212, 2000.
- [271] W. N. Addison, S. J. Miller, J. Ramaswamy, A. Mansouri, D. H. Kohn, and M. D. McKee, "Phosphorylation-dependent mineral-type specificity for apatite-binding peptide sequences," *Biomaterials*, vol. 31, pp. 9422-30, 2010.
- [272] R. M. Hazen, T. R. Filley, and G. A. Goodfriend, "Selective adsorption of l- and d-amino acids on calcite: Implications for biochemical homochirality," *Proceedings of the National Academy of Sciences*, vol. 98, pp. 5487-5490, 2001.
- [273] C. A. Orme, A. Noy, A. Wierzbicki, M. T. McBride, M. Grantham, H. H. Teng, *et al.*, "Formation of chiral morphologies through selective binding of amino acids to calcite surface steps," *Nature*, vol. 411, pp. 775-9, 2001.
- [274] S. Albeck, J. Aizenberg, L. Addadi, and S. Weiner, "Interactions of various skeletal intracrystalline components with calcite crystals," *Journal of the American Chemical Society*, vol. 115, pp. 11691-11697, 1993.
- [275] V. Nelea, Y.-C. Chien, J. Paquette, and M. D. McKee, "Effects of Full-Length Phosphorylated Osteopontin and Constituent Acidic Peptides and Amino Acids on Calcite Dissolution," *Crystal Growth & Design*, vol. 14, pp. 979-987, 2014.

- [276] M. Ukrainczyk, M. Gredičak, I. Jerić, and D. Kralj, "Interactions of Scalenohedral Calcite Crystals with Acidic Amino Acid Derivatives of Salicylic Acid," *Crystal Growth & Design*, vol. 14, pp. 4335-4346, 2014.
- [277] D. L. Masica, S. B. Schrier, E. A. Specht, and J. J. Gray, "De novo design of peptide-calcite biomineralization systems," *J Am Chem Soc*, vol. 132, pp. 12252-62, 2010.
- [278] M. B. Dickerson, K. H. Sandhage, and R. R. Naik, "Protein- and Peptide-Directed Syntheses of Inorganic Materials," *Chemical Reviews*, vol. 108, pp. 4935-4978, 2008.
- [279] J. Song, M. Viengkham, and C. R. Bertozzi, "Mineralization of Synthetic Polymer Scaffolds: A Bottom-up Approach for the Development of Artificial Bone," ed, 2004.
- [280] N. Almora-Barrios, K. F. Austen, and N. H. de Leeuw, "Density Functional Theory Study of the Binding of Glycine, Proline, and Hydroxyproline to the Hydroxyapatite (0001) and (0110) Surfaces," *Langmuir : the ACS journal of surfaces and colloids*, vol. 25, pp. 5018-5025, 2009.
- [281] L. D. Stegink, L. J. Filer, M. C. Brummel, G. L. Baker, W. L. Krause, E. F. Bell, *et al.*, "Plasma amino acid concentrations and amino acid ratios in normal adults and adults heterozygous for phenylketonuria ingesting a hamburger and milk shake meal," *The American Journal of Clinical Nutrition*, vol. 53, pp. 670-5, 1991.
- [282] H. Pan, J. Tao, X. Xu, and R. Tang, "Adsorption processes of Gly and Glu amino acids on hydroxyapatite surfaces at the atomic level," *Langmuir : the ACS journal of surfaces and colloids*, vol. 23, pp. 8972-81, 2007.
- [283] H. McDowell, T. M. Gregory, W. E. Brown, "Solubility of Ca5(PO4)3OH in the system Ca(OH)2-H3PO4-H2O at 5, 15, 25 and 37° C," *Journal of Research of the National Bureau of Standards A. Physics and Chemistry*, vol. 81A, pp. 273-281, 1977.
- [284] K. Venkateswarlu, A. Chandra Bose, and N. Rameshbabu, "X-ray peak broadening studies of nanocrystalline hydroxyapatite by Williamson-Hall analysis," *Physica B: Condensed Matter*, vol. 405, pp. 4256-4261, 2010.
- [285] (26) Gregg, S. J.; Sing, K. S.W.Adsorption, Surface AreaandPorosity, 2nd ed.; Academic Press: London, 1982.
- [286] S. Brunauer, P. H. Emmett, and E. Teller, "Adsorption of Gases in Multimolecular Layers," *Journal of the American Chemical Society*, vol. 60, pp. 309-319, 1938.
- [287] B. C. Lippens and J. H. de Boer, "Studies on pore systems in catalysts: V. The t method," *Journal of Catalysis*, vol. 4, pp. 319-323, 1965.
- [288] Y. P. Lee and T. Takahashi, "An improved colorimetric determination of amino acids with the use of ninhydrin," Analytical Biochemistry, vol. 14, pp. 71-77, 1966.
- [289] P. Duggan, D. Donnelly, and D. Melody, "The reaction of glyoxylate with tris buffer under physiological conditions," *Irish Journal of Medical Science (1926-1967)*, vol. 39, pp. 163-168, 1964.
- [290] T. Kokubo and H. Takadama, "How useful is SBF in predicting in vivo bone bioactivity?," Biomaterials, vol. 27, pp. 2907-15, 2006.
- [291] A. A. El-Harakany, F. M. Abdel Halim, and A. O. Barakat, "Dissociation constants and related thermodynamic quantities of the protonated acid form of tris-(hydroxymethyl)-aminomethane in mixtures of 2-methoxyethanol and water at different temperatures," *Journal of Electroanalytical Chemistry and Interfacial Electrochemistry*, vol. 162, pp. 285-305, 1984.
- [292] M. S. Silberberg, Chemistry, 5th edition, McGraw-Hill, 2009.

- [293] Z. H. Cheng, A. Yasukawa, K. Kandori, and T. Ishikawa, "FTIR Study of Adsorption of CO2 on Nonstoichiometric Calcium Hydroxyapatite," Langmuir: the ACS journal of surfaces and colloids, vol. 14, pp. 6681-6686, 1998.
- [294] S. A. Hutchens, R. S. Benson, B. R. Evans, H. M. O'Neill, and C. J. Rawn, "Biomimetic synthesis of calcium-deficient hydroxyapatite in a natural hydrogel," Biomaterials, vol. 27, pp. 4661-4670, 2006.
- [295] B. O. Fowler, M. Markovic, and W. E. Brown, "Octacalcium phosphate. 3. Infrared and Raman vibrational spectra," *Chemistry of Materials*, vol. 5, pp. 1417-1423, 1993.
- [296] N. Pleshko, A. Boskey, and R. Mendelsohn, "Novel infrared spectroscopic method for the determination of crystallinity of hydroxyapatite minerals," B*iophysical Journal*, vol. 60, pp. 786-793, 1991.
- [297] L. J. Webb, S. Rivillon, D. J. Michalak, Y. J. Chabal, and N. S. Lewis, "Transmission Infrared Spectroscopy of Methyl- and Ethyl-Terminated Silicon(111) Surfaces," *The Journal of Physical Chemistry B*, vol. 110, pp. 7349-7356, 2006.
- [298] L. Bertinetti, A. Tampieri, E. Landi, C. Ducati, P. A. Midgley, S. Coluccia, *et al.*, "Surface Structure, Hydration, and Cationic Sites of Nanohydroxyapatite: UHR-TEM, IR, and Microgravimetric Studies," *The Journal of Physical Chemistry C*, vol. 111, pp. 4027-4035, 2007.
- [299] E. R. Clarke and A. E. Martell, "Metal chelates of arginine and related ligands," *Journal of Inorganic and Nuclear Chemistry*, vol. 32, pp. 911-926, 1970.
- [300] P. G. Daniele, C. Foti, A. Gianguzza, E. Prenesti, and S. Sammartano, "Weak alkali and alkaline earth metal complexes of low molecular weight ligands in aqueous solution," *Coordination Chemistry Reviews*, vol. 252, pp. 1093-1107, 2008.
- [301] R. F. Lumb and A. E. Martell, "Metal Chelating Tendencies of Glutamic and Aspartic Acids," *The Journal of Physical Chemistry*, vol. 57, pp. 690-693, 1953.
- [302] De Stefano C, Foti C, Gianguzza A. 1995 Ligand-ligand complexes of ethylenediaminetetracetic acid and histidine or ethylenediamine. Ann. Chim. 85, 69–75.
- [303] C. W. Davies, "56. The extent of dissociation of salts in water. Part VI. Some calcium salts of organic acids," Journal of the Chemical Society (Resumed), pp. 277-281, 1938.
- [304] Y.-P. Ho, M.-W. Yang, L.-T. Chen, and Y.-C. Yang, "Relative calcium-binding strengths of amino acids determined using the kinetic method," Rapid *Communications in Mass Spectrometry, vol.* 21, pp. 1083-1089, 2007.
- [305] G. Lancelot and C. Hélène, "Selective recognition of nucleic acids by proteins: the specificity of guanine interaction with carboxylate ions," Proceedings of the National Academy of Sciences, vol. 74, pp. 4872-4875, 1977.
- [306] G. Lancelot, R. Mayer, and C. Hélène, "Models of interaction between nucleic acids and proteins Hydrogen bonding of arginine with nucleic acid bases, phosphate groups and carboxylic acids," Biochimica et Biophysica Acta (BBA) Nucleic Acids and Protein Synthesis, vol. 564, pp. 181-190, 1979.
- [307] N. M. Luscombe, R. A. Laskowski, and J. M. Thornton, "Amino acid-base interactions: a three-dimensional analysis of protein–DNA interactions at an atomic level," Nucleic *Acids Research*, vol. 29, pp. 2860-2874, 2001.
- [308] K. Skartsila and N. Spanos, "Surface characterization of hydroxyapatite: Potentiometric titrations coupled with solubility measurements," Journal of Colloid and Interface Science, vol. 308, pp. 405-412, 2007.

- [309] P. W. Brown and R. I. Martin, "An Analysis of Hydroxyapatite Surface Layer Formation," The *Journal of Physical Chemistry B, vol.* 103, pp. 1671-1675, 1999.
- [310] D. N. Misra, "Interaction of Citric or Hydrochloric Acid with Calcium Fluorapatite: Precipitation of Calcium Fluoride," Journal of Colloid and Interface Science, vol. 220, pp. 387-391, 1999.
- [311] A. Rimola, M. Corno, C. M. Zicovich-Wilson, and P. Ugliengo, "Ab Initio Modeling of Protein/Biomaterial Interactions: Glycine Adsorption at Hydroxyapatite Surfaces," Journal of the American Chemical Society, vol. 130, pp. 16181-16183, 2008.
- [312] M. Corno, A. Rimola, V. Bolis, and P. Ugliengo, "Hydroxyapatite as a key biomaterial: quantum-mechanical simulation of its surfaces in interaction with biomolecules," Physical chemistry chemical physics: PCCP, vol. 12, pp. 6309-29, 2010.
- [313] Q. J. He and Z. L. Huang, "Controlled growth and kinetics of porous hydroxyapatite spheres by a template-directed method," Journal of Crystal Growth, vol. 300, pp. 460-466, 2007.
- [314] K. Teshima, M. Sakurai, S. Lee, K. Yubuta, S. Ito, T. Suzuki, et *al., "Morphologically Controlled Fibrous Spherulites of an Apatite Precursor Biocrystal," Crystal Growth & Design, vol.* 9, pp. 650-652, 2008.
- [315] L. Granasy, T. Pusztai, G. Tegze, J. A. Warren, and J. F. Douglas, "Growth and form of spherulites," Phys *Rev E Stat Nonlin Soft Matter Phys, vol.* 72, p. 19, 2005.
- [316] R. Beck and J.-P. Andreassen, "Spherulitic Growth of Calcium Carbonate," Crystal Growth & Design, vol. 10, pp. 2934-2947, 2010.
- [317] H. D. Keith and F. J. Padden, "A Phenomenological Theory of Spherulitic Crystallization," Journal of Applied Physics, vol. 34, pp. 2409-2421, 1963.
- [318] J.-P. Andreassen and M. J. Hounslow, "Growth and aggregation of vaterite in seeded-batch experiments," AICh*E Journal*, vol. 50, pp. 2772-2782, 2004.
- [319] T. N. Bhat and M. Vijayan, "X-ray studies of crystalline complexes involving amino acids. II. The crystal structure of l-arginine l-glutamate," Acta *Crystallographica Section B, vol.* 33, pp. 1754-1759, 1977.
- [320] G. Lancelot and H. Claude, "Model studies of interactions between nucleic acids and proteins: hydrogen bonding of amides with nucleic acid bases," Nucleic Acids Research, vol. 6, pp. 1063-1072, 1979.
- [321] D. Quigley and P. M. Rodger, "Free energy and structure of calcium carbonate nanoparticles during early stages of crystallization," J Chem Phys, vol. 128, p. 221101, 2008.
- [322] A. F. Wallace, L. O. Hedges, A. Fernandez-Martinez, P. Raiteri, J. D. Gale, G. A. Waychunas, et *al.*, "Microscopic Evidence for Liquid-Liquid Separation in Supersaturated CaCO3 Solutions," Science, vol. 341, pp. 885-889, August 23, 2013.
- [323] A. Dey, P. H. H. Bomans, F. A. Müller, J. Will, P. M. Frederik, G. de With, et *al.*, "The role of prenucleation clusters in surface-induced calcium phosphate crystallization," Nat *Mater, vol.* 9, pp. 1010-1014, 2010.
- [324] A. Jawor-Baczynska, J. Sefcik, and B. D. Moore, "250 nm Glycine-Rich Nanodroplets Are Formed on Dissolution of Glycine Crystals But Are Too Small To Provide Productive Nucleation Sites," Crystal Growth & Design, vol. 13, pp. 470-478, 2012.
- [325] B. Clarke, "Normal Bone Anatomy and Physiology," Clinical Journal of the American Society of Nephrology, vol. 3, pp. S131-S139, 2008.

- [326] E. Bonucci, The Mineralization of Bone and Its Analogies with Other Hard Tissues, 2013.
- [327] S. Weiner and P. M. Dove, "An Overview of Biomineralization Processes and the Problem of the Vital Effect," Reviews in Mineralogy and Geochemistry, vol. 54, pp. 1-29, 2003.
- [328] M. Kerschnitzki, P. Kollmannsberger, M. Burghammer, G. N. Duda, R. Weinkamer, W. Wagermaier, et *al.*, "Architecture of the osteocyte network correlates with bone material quality," J Bone Miner Res, vol. 28, pp. 1837-45, 2013.
- [329] M. Rumpler, T. Wurger, P. Roschger, E. Zwettler, I. Sturmlechner, P. Altmann, et *al.*, "Osteoclasts on bone and dentin in vitro: mechanism of trail formation and comparison of resorption behavior," Calcif Tissue Int, vol. 93, pp. 526-39, 2013.
- [330] A. George and A. Veis, "Phosphorylated proteins and control over apatite nucleation, crystal growth, and inhibition," Chem *Rev*, *vol.* 108, pp. 4670-93, 2008.
- [331] M. T. Jahromi, G. Yao, and M. Cerruti, "The importance of amino acid interactions in the crystallization of hydroxyapatite," Journal of The Royal Society Interface, vol. 10, 2013.
- [332] J. Reyes-Gasga, R. Garcia-Garcia, and E. Brès, "Electron beam interaction, damage and reconstruction of hydroxyapatite," Physica B: Condensed Matter, vol. 404, pp. 1867-1873, 2009.
- [333] A. Meldrum, L. M. Wang, and R. C. Ewing, "Electron-irradiation-induced phase segregation in crystalline and amorphous apatite; a TEM study," American Mineralogist, vol. 82, pp. 858-869, 1997.
- [334] G. Daculsi, R. Z. LeGeros, and D. Mitre, "Crystal dissolution of biological and ceramic apatites," Calcif Tissue Int, vol. 45, pp. 95-103, 1989.
- [335] Y.-Y. Kim, A. S. Schenk, J. Ihli, A. N. Kulak, N. B. J. Hetherington, C. C. Tang, et *al.*, "A critical analysis of calcium carbonate mesocrystals," Nat *Commun*, vol. 5, 2014.
- [336] R. F. Egerton, P. Li, and M. Malac, "Radiation damage in the TEM and SEM," Micron, vol. 35, pp. 399-409, 2004.
- [337] D. Hagmeyer, J. Ruesing, T. Fenske, H.-W. Klein, C. Schmuck, W. Schrader, et *al.*, "Direct experimental observation of the aggregation of [small alpha]-amino acids into 100-200 nm clusters in aqueous solution," RSC *Advances*, vol. 2, pp. 4690-4696, 2012.
- [338] I. Ben Shir, S. Kababya, I. Katz, B. Pokroy, and A. Schmidt, "Exposed and Buried Biomineral Interfaces in the Aragonitic Shell of Perna canaliculus Revealed by Solid-State NMR," Chemistry of Materials, vol. 25, pp. 4595-4602, 2013.
- [339] M. Weaver, S. R. Qiu, J. Hoyer, W. Casey, G. Nancollas, and J. De Yoreo, "Surface Aggregation of Urinary Proteins and Aspartic Acid-Rich Peptides on the Faces of Calcium Oxalate Monohydrate Investigated by In Situ Force Microscopy," Calcified *Tissue International*, vol. 84, pp. 462-473, 2009.
- [340] S. Dharmayat, J. Calderon De Anda, R. B. Hammond, X. Lai, K. J. Roberts, and X. Z. Wang, "Polymorphic transformation of l-glutamic acid monitored using combined online video microscopy and X-ray diffraction," Journal of Crystal Growth, vol. 294, pp. 35-40, 2006.
- [341] C. Holt, E. S. Sørensen, and R. A. Clegg, "Role of calcium phosphate nanoclusters in the control of calcification," FEBS *Journal*, vol. 276, pp. 2308-2323, 2009.
- [342] C.-L. Chen, K. M. Bromley, J. Moradian-Oldak, and J. J. DeYoreo, "In situ AFM Study of Amelogenin Assembly and Disassembly Dynamics on Charged Surfaces Provides

- Insights on Matrix Protein Self-Assembly," Journal of the American Chemical Society, vol. 133, pp. 17406-17413, 2011.
- [343] S. Mann, "Biomineralization: the form(id)able part of bioinorganic chemistry! \*," Journal of the Chemical Society, Dalton Transactions, pp. 3953-3962, 1997.
- [344] L. Wang and M. Nilsen-Hamilton, "Biomineralization proteins: from vertebrates to bacteria," Frontiers in Biology, vol. 8, pp. 234-246, 2013.
- [345] S. J. Parikh, J. D. Kubicki, C. M. Jonsson, C. L. Jonsson, R. M. Hazen, D. A. Sverjensky, et *al.*, "Evaluating glutamate and aspartate binding mechanisms to rutile (alpha-TiO2) via ATR-FTIR spectroscopy and quantum chemical calculations," Langmuir, vol. 27, pp. 1778-87, 2011.
- [346] A. Barth, "The infrared absorption of amino acid side chains," Prog *Biophys Mol Biol*, vol. 74, pp. 141-73, 2000.
- [347] L. J. Webb, S. Rivillon, D. J. Michalak, Y. J. Chabal, and N. S. Lewis, "Transmission infrared spectroscopy of methyl- and ethyl-terminated silicon(111) surfaces," J Phys *Chem B, vol.* 110, pp. 7349-56, 2006.
- [348] J. T. L. Navarrete, L. Bencivenni, F. Ramondo, V. Hernández, and F. J. Ramírez, "Structural and spectroscopical study of glutamic acid in the nonzwitterionic form," Journal of Molecular Structure: THEOCHEM, vol. 330, pp. 261-266, 1995.
- [349] S. Goenka, V. Sant, and S. Sant, "Graphene-based nanomaterials for drug delivery and tissue engineering," Journal of Controlled Release, vol. 173, pp. 75-88, 2014.
- [350] C. Chung, Y.-K. Kim, D. Shin, S.-R. Ryoo, B. H. Hong, and D.-H. Min, "Biomedical Applications of Graphene and Graphene Oxide," Accounts of Chemical Research, vol. 46, pp. 2211-2224, 2013.
- [351] Z. Fan, J. Wang, Z. Wang, H. Ran, Y. Li, L. Niu, et *al., "One-pot synthesis of graphene/hydroxyapatite nanorod composite for tissue engineering," Carbon, vol.* 66, pp. 407-416, 2014.
- [352] S. Kim, S. H. Ku, S. Y. Lim, J. H. Kim, and C. B. Park, "Graphene–Biomineral Hybrid Materials," Advanced Materials, vol. 23, pp. 2009-2014, 2011.
- [353] M. Li, Y. Wang, Q. Liu, Q. Li, Y. Cheng, Y. Zheng, et *al.*, "In situ synthesis and biocompatibility of nano hydroxyapatite on pristine and chitosan functionalized graphene oxide," Journal of Materials Chemistry B, vol. 1, pp. 475-484, 2013.
- [354] Y. Li, C. Liu, H. Zhai, G. Zhu, H. Pan, X. Xu, et *al.*, "Biomimetic graphene oxide-hydroxyapatite composites via in situ mineralization and hierarchical assembly," RSC *Advances*, vol. 4, pp. 25398-25403, 2014.
- [355] H. Liu, J. Cheng, F. Chen, D. Bai, C. Shao, J. Wang, et *al.*, "Gelatin functionalized graphene oxide for mineralization of hydroxyapatite: biomimetic and in vitro evaluation," Nanoscale, vol. 6, pp. 5315-22, 2014.
- [356] G. M. Neelgund, A. Oki, and Z. Luo, "In situ deposition of hydroxyapatite on graphene nanosheets," Materials Research Bulletin, vol. 48, pp. 175-179, 2013.
- [357] R. Deepachitra, M. Chamundeeswari, B. Santhosh kumar, G. Krithiga, P. Prabu, M. Pandima Devi, et *al.*, "Osteo mineralization of fibrin-decorated graphene oxide," Carbon, vol. 56, pp. 64-76, 2013.
- [358] X. Sun, Z. Liu, K. Welsher, J. Robinson, A. Goodwin, S. Zaric, et *al.*, "Nano-graphene oxide for cellular imaging and drug delivery," Nano *Research*, vol. 1, pp. 203-212, 2008.
- [359] T. Kokubo and H. Takadama, "How useful is SBF in predicting in vivo bone bioactivity?," Biomaterials, vol. 27, pp. 2907-2915, 2006.

- [360] D. C. Marcano, D. V. Kosynkin, J. M. Berlin, A. Sinitskii, Z. Sun, A. Slesarev, et *al.*, "Improved Synthesis of Graphene Oxide," ACS Nano, vol. 4, pp. 4806-4814, 2010.
- [361] X. Zhang, K. Li, H. Li, and J. Lu, "Dipotassium hydrogen phosphate as reducing agent for the efficient reduction of graphene oxide nanosheets," J Colloid Interface Sci, vol. 409, pp. 1-7, 2013.
- [362] P. Han, H. Wang, Z. Liu, X. Chen, W. Ma, J. Yao, et *al.*, "Graphene oxide nanoplatelets as excellent electrochemical active materials for VO2+/ and V2+/V3+ redox couples for a vanadium redox flow battery," Carbon, vol. 49, pp. 693-700, 2011.
- [363] N. Hellgren, J. Guo, Y. Luo, C. Såthe, A. Agui, S. Kashtanov, et *al.*, "Electronic structure of carbon nitride thin films studied by X-ray spectroscopy techniques," Thin *Solid Films*, *vol.* 471, pp. 19-34, 2005.
- [364] E. Sardella, F. Liuzzi, R. Comparelli, N. Depalo, M. Striccoli, A. Agostiano, et *al.*, "Functionalized luminescent nanocrystals on patterned surfaces obtained by radio frequency glow discharges," Nanotechnology, vol. 24, pp. 0957-4484, 2013.
- [365] H. Awada, D. Montplaisir, and C. Daneault, "Growth of polyelectrolyte on lignocellulosic fibers: study by zeta potential, FTIR, and XPS," BioResources, *vol* 7, pp. 2090-2104, 2012.
- [366] A. Bagri, C. Mattevi, M. Acik, Y. J. Chabal, M. Chhowalla, and V. B. Shenoy, "Structural evolution during the reduction of chemically derived graphene oxide," Nat *Chem, vol.* 2, pp. 581-587, 2010.
- [367] A. Ganguly, S. Sharma, P. Papakonstantinou, and J. Hamilton, "Probing the Thermal Deoxygenation of Graphene Oxide Using High-Resolution In Situ X-ray-Based Spectroscopies," The *Journal of Physical Chemistry C, vol.* 115, pp. 17009-17019, 2011.
- [368] M. Acik, G. Lee, C. Mattevi, M. Chhowalla, K. Cho, and Y. J. Chabal, "Unusual infrared-absorption mechanism in thermally reduced graphene oxide," Nat *Mater, vol.* 9, pp. 840-845, 2010.
- [369] T. Szabó, O. Berkesi, P. Forgó, K. Josepovits, Y. Sanakis, D. Petridis, et al., "Evolution of Surface Functional Groups in a Series of Progressively Oxidized Graphite Oxides," Chemistry of Materials, vol. 18, pp. 2740-2749, 2006.
- [370] T. Classen, M. Lingenfelder, Y. Wang, R. Chopra, C. Virojanadara, U. Starke, et *al.*, "Hydrogen and Coordination Bonding Supramolecular Structures of Trimesic Acid on Cu(110)†," The *Journal of Physical Chemistry A, vol.* 111, pp. 12589-12603, 2007.
- [371] B. L. Frey and R. M. Corn, "Covalent Attachment and Derivatization of Poly(1-lysine) Monolayers on Gold Surfaces As Characterized by Polarization–Modulation FT-IR Spectroscopy," Analytical Chemistry, vol. 68, pp. 3187-3193, 1996.
- [372] R. G. Chapman, E. Ostuni, L. Yan, and G. M. Whitesides, "Preparation of Mixed Self-Assembled Monolayers (SAMs) That Resist Adsorption of Proteins Using the Reaction of Amines with a SAM That Presents Interchain Carboxylic Anhydride Groups," Langmuir, vol. 16, pp. 6927-6936, 2000.
- [373] Y. Zhang, H.-L. Ma, Q. Zhang, J. Peng, J. Li, M. Zhai, et *al.*, "Facile synthesis of well-dispersed graphene by [gamma]-ray induced reduction of graphene oxide," Journal of Materials Chemistry, vol. 22, pp. 13064-13069, 2012.
- [374] F. P. Du, J. J. Wang, C. Y. Tang, C. P. Tsui, X. P. Zhou, X. L. Xie, et *al.*, "Water-soluble graphene grafted by poly(sodium 4-styrenesulfonate) for enhancement of electric capacitance," Nanotechnology, vol. 23, pp. 0957-4484, 2012.

- [375] K. Haubner, J. Murawski, P. Olk, L. M. Eng, C. Ziegler, B. Adolphi, et *al.*, "The Route to Functional Graphene Oxide," Chem*PhysChem*, vol. 11, pp. 2131-2139, 2010.
- [376] R. Rastogi, N. Gulati, R. K. Kotnala, U. Sharma, R. Jayasundar, and V. Koul, "Evaluation of folate conjugated pegylated thermosensitive magnetic nanocomposites for tumor imaging and therapy," Colloids and Surfaces B: Biointerfaces, vol. 82, pp. 160-167, 2011.
- [377] M. Neo, T. Nakamura, C. Ohtsuki, T. Kokubo, and T. Yamamuro, "Apatite formation on three kinds of bioactive material at an early stage in vivo: a comparative study by transmission electron microscopy," J Biomed Mater Res, vol. 27, pp. 999-1006, 1993.
- [378] A. Paz, D. Guadarrama, M. López, J. E. González, N. Brizuela, and J. Aragón, "A comparative study of hydroxyapatite nanoparticles synthesized by different routes," Quím*ica Nova, vol.* 35, pp. 1724-1727, 2012.
- [379] C. Y. Kim, A. E. Clark, and L. L. Hench, "Compositional dependence of calcium phosphate layer formation in fluoride Bioglasses," J Biomed Mater Res, vol. 26, pp. 1147-61, 1992.
- [380] C. Combes and C. Rey, "Amorphous calcium phosphates: synthesis, properties and uses in biomaterials," Acta *Biomater*, vol. 6, pp. 3362-78, 2010.
- [381] S. Raynaud, E. Champion, D. Bernache-Assollant, and P. Thomas, "Calcium phosphate apatites with variable Ca/P atomic ratio I. Synthesis, characterisation and thermal stability of powders," Biomaterials, vol. 23, pp. 1065-72, 2002.
- [382] R. A. Terpstra and F. C. M. Driessens, "Magnesium in tooth enamel and synthetic apatites," Calcified Tissue International, vol. 39, pp. 348-354, 1986.
- [383] P. A. A. P. Marques, G. Gonçalves, S. Cruz, N. Almeida, M. K. Singh, J. Grácio, et al., Functionalized Graphene Nanocomposites, 2011.